Jonas van Ouwerkerk

Integrating a battery value stacking approach into an energy system modelling framework to decarbonise a glassworks

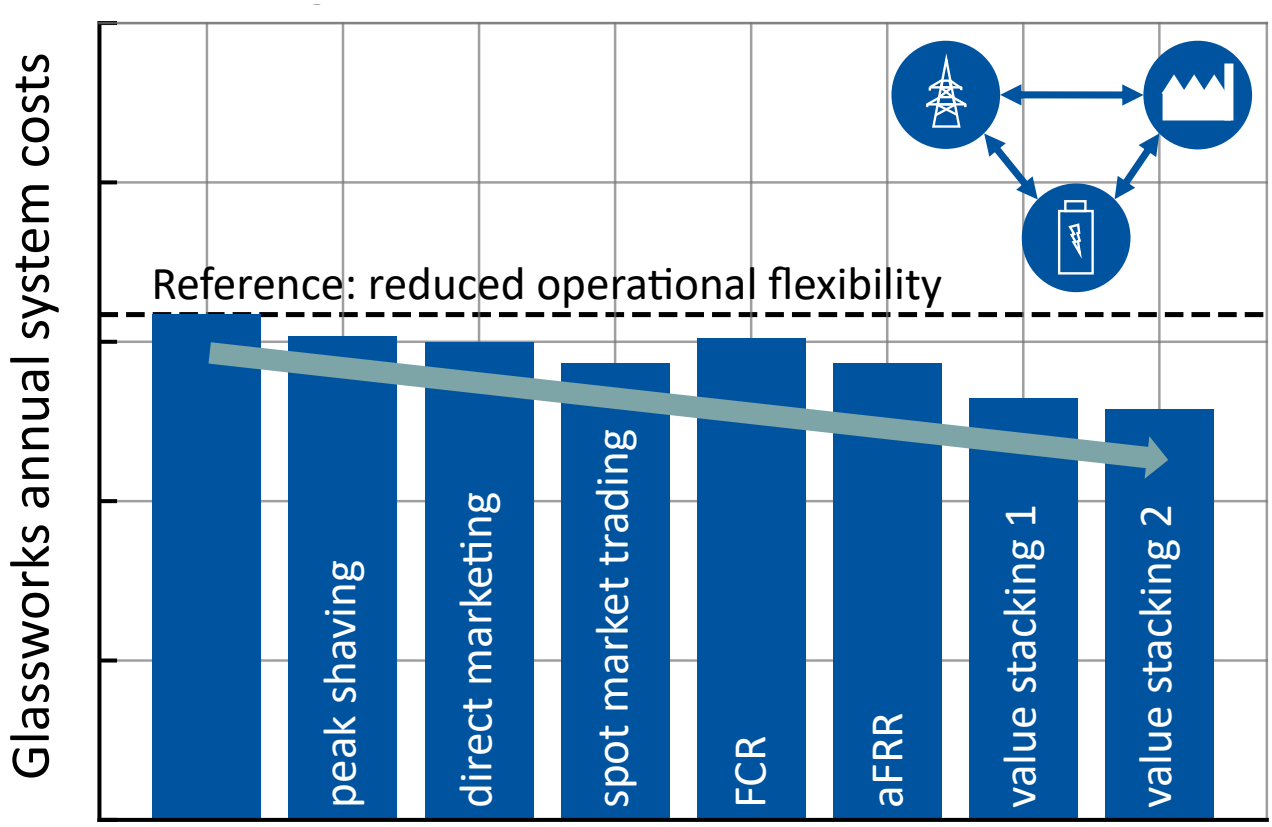

Aachener Beiträge des ISEA Band 198

Integrating a battery value stacking approach into an energy system modelling framework to decarbonise a glassworks

Von der Fakultät für Elektrotechnik und Informationstechnik
der Rheinisch-Westfälischen Technischen Hochschule Aachen
zur Erlangung des akademischen Grades eines Doktors der
Ingenieurwissenschaften genehmigte Dissertation

vorgelegt von
Jonas van Ouwerkerk, M. Sc.
aus Malsch Kreis Karlsruhe

Berichter:
Univ.-Professor Dr. rer. nat. Dirk Uwe Sauer
Univ.-Professor Dr.-Ing. Niklas von der Aßen

Tag der mündlichen Prüfung: 10. Juli 2025

AACHENER BEITRÄGE DES ISEA
Vol. 198

Editor:
Univ.-Prof. Dr. ir. Dr. h. c. Rik W. De Doncker
Director of the Institute for Power Electronics and Electrical Drives (ISEA)
RWTH Aachen University

ISSN 1437-675X

Institute for Power Electronics and Electrical Drives (ISEA)
RWTH Aachen University
Campus-Boulevard 89 • 52074 Aachen • Germany
Tel: +49 (0)241 80-96920
post@isea.rwth-aachen.de

"… industry and global institutions must appreciate that ensuring economic justice, equity and ecological integrity are of greater value than profits at any cost. The extreme global inequities and prevailing consumption patterns continue at the expense of the environment and peaceful co-existence."

Wangari Muta Maathai (1940 - 2011)
Laureate for the Nobel Peace Prize in 2004, Oslo

Preface

Die vergangenen Jahre waren geprägt von globalen Krisen wie der COVID-19-Pandemie und dem russischen Angriffskrieg gegen die Ukraine. Die zunehmende Verunsicherung der Bevölkerung spiegelt sich insbesondere im Erstarken radikaler Parteien wider. Saubere, grüne Energie ist der Schlüssel, um die größten Herausforderungen der Menschheitsgeschichte in den kommenden Jahren zu bewältigen und die Auswirkungen der Klimakrise zu begrenzen. Gleichzeitig kann eine dezentralere Energieversorgung die geopolitischen Konflikte reduzieren, deren Kern zumeist der Kampf um fossile Ressourcen ist.

Die vorliegende Dissertation soll einen Beitrag zur Transformation hin zu einem nachhaltigen Energiesystem leisten. Der Fokus liegt dabei auf der Schwerindustrie, in der die Dekarbonisierung als besonders herausfordernd gilt. Dies liegt zum einen am hohen Energieeinsatz und den hohen Prozesstemperaturen sowie am Preisdruck globaler Märkte. Am Beispiel eines bestehenden Glasswerks werden unterschiedliche Dekarbonisierungs-optionen verglichen und bewertet. Zentrale Rolle spielen dabei der Energieträger Wasserstoff und eine möglichst hohe Elektrifizierung der Schmelzwanne. Bestandteil der Untersuchungen ist, wie grüner Strombezug und das Ausschöpfen von Flexibilitäten mithilfe von Batteriespeichern zu kompetitiven Kosten führen können.

Ich möchte insbesondere Prof. Dirk Uwe Sauer danken, der es mir ermöglicht hat, an seinem Lehrstuhl zu forschen und mir stets das größte Vertrauen entgegengebracht hat. Zudem danke ich Prof. von der Aßen für die Übernahme des Korreferats. Auf meinem Weg begleitet haben mich unter anderem eine Vielzahl von Kolleg:innen, die mit mir an denselben Themen geforscht und mich stets unterstützt haben. Insbesondere danke ich Dr. Jan Figgener, Dr. Christian Bußar, Sebastian Zurmühlen, Mauricio Celi Cortés, Dr. Lucas Koltermann und allen weiteren Kolleg:innen aus der Abteilung für die Netzintegration von Speichersystemen am ISEA. Auch den studentischen Hilfskräften und Abschlussarbeitern Joschka Krause, Laszlo Hartung und Ole Krause möchte ich für die hervorragenden Vorarbeiten danken, die zum Gelingen der Dissertation beigetragen haben.
Die Forschung in der vorliegenden Dissertation wurde zudem durch die Projekte COSiMa (FKZ EFO 0133E) und InEEd-DC (FKZ 03SF0597) ermöglicht. Ich danke insbesondere den Ansprechpartner:innen auf Seiten des Glasswerks sowie den Kolleg:innen der RWTH Aachen für ihre wertvollen Beiträge und Einblicke im Rahmen der Projekte.

Ich bin überzeugt, dass die Vorteile eines nachhaltigen Energiesystems erdrückend sind und zu mehr Wohlstand führen. Das Gelingen der Energiewende ist für mich eine Herzensangelegenheit, zu der ich mich auch zukünftig verpflichtet fühle und für die ich mich mit voller Kraft einsetzen möchte.

Jonas van Ouwerkerk - Aachen den 10.07.2025

Abstract

Achieving climate neutrality requires decarbonisation across all sectors. While emissions from the German electric power sector show a promising trajectory, other sectors are progressing more slowly. This includes the industrial sector, where energy-intensive applications are particularly challenging due to the need for high-temperature process heat. The primary approach to decarbonising these applications is to maximise electrification where possible and to substitute the remaining demand for fossil energy carriers with renewable hydrogen or its derivatives. This usually comes with increased renewable power installations, including photovoltaic and wind power, which require redesign and operational adjustments to existing industrial energy systems. This may include battery storage systems to increase flexibility and align with the variable nature of renewable power generation.

A challenging industrial application for decarbonisation is glassworks for automotive products. The main challenge is to increase the furnace's electrification and replace the primary energy carrier, natural gas, with hydrogen. One option for supplying renewable hydrogen is via pipeline as part of the planned hydrogen core network in Germany. The basic concept for this core network was already approved by the German Federal Network Agency in 2024, with phased commissioning until 2032. An alternative solution that can be realised in the short term is on-site production of green hydrogen via electrolysis. Supplying the electrolysis system with green electricity requires power purchase agreements that comply with the high legal requirements of the EU Renewable Energy Directive.

Finding the most cost-efficient solution for industrial sites requires a sophisticated energy system modelling framework that can benchmark different solutions. There is a variety of frameworks featuring multiple approaches. The majority of frameworks are designed to model national or smaller regional grid-scale energy systems. Only a few frameworks focus on industrial scale. Therefore, a framework is developed specifically for local industrial flexumer applications. This includes integrating a value stacking approach for battery storage systems to demonstrate cost-reduction potential by leveraging additional flexibility.

The developed framework is applied to a glassworks use case in Germany. The results show that, despite a decreasing trend towards 2037, decarbonisation choices lead to higher annual costs than rebuilding a natural gas-based furnace, by at least 18.3%. The most cost-competitive decarbonisation is achieved through high furnace electrification, which reduces hydrogen demand. By utilising low-cost renewable generation through power purchase agreements and battery storage, operating an on-site electrolysis system can be a competitive choice compared to connecting to a future hydrogen pipeline. Furthermore, in 2024, substantial additional cost reductions of up to 30.1% can be achieved when exploiting the flexibility of the electrolysis system and stacking multiple use cases for the battery storage system. Although the evaluation focuses on one specific glassworks use case, the results act as a blueprint for decarbonisation concepts for other industrial sites.

Table of contents

1. Introduction

Energy systems worldwide face profound challenges as the energy transition progresses. The acceleration of the climate crisis requires a fast transformation towards net-zero. In 2023, global annual greenhouse gas (GHG) emissions reached a new record-high of 53 Gt of CO_2 equivalents [1]. At the same time, in 2024, the global average temperature has increased by 1.6°C compared to pre-industrial levels, exceeding the 1.5 °C target of the Paris Agreement [2]. The increased anthropogenic warming of the atmosphere is causing extreme weather events to occur more frequently [2] threatening the living conditions of humans worldwide. At the same time, increasing geopolitical tensions pose a challenge to energy security. With the ongoing invasion of Ukraine by Russia since February 24, 2022, the supply of natural gas (NG) to especially Europe abruptly decreased, which led to disruptions in the global energy markets [3].

The acceleration of the climate crisis and the rise in geopolitical conflicts demand a faster transition to sustainable energy sources. Achieving climate neutrality requires decarbonisation across all sectors. While emissions for the electric power sector in Germany show a promising trajectory substantially below the political targets, other sectors show slower progress [4, 5]. This includes the industrial sector, which is particularly challenging when it comes to energy-intensive applications that require high-temperature process heat and large amounts of energy at a global competitive price [4, 6]. For most of these industries, today, the largest share of energy comes from fossil fuels [5]. The primary and most efficient solution to decarbonise heavy industry applications is to aim for higher rates of electrification [5–7], when technically possible, in combination with the utilisation of green electricity. Higher electrification is enabled by the coupling of energy sectors, including electricity, heat, and gas [7]. Moreover, switching to green electricity provides the chance for a low-cost energy supply. The levelised costs of energy (LCOEs) for photovoltaics (PV) and wind power plants (WPP) in Germany have substantially reduced over the last decade and reach levels as low as 4.1 $EURct_{2024}$/kWh and 4.3 $EURct_{2024}$/kWh (2024), respectively [8]. For many industrial sites, on-site renewable installations can be a quick and simple way to generate their own green electricity and transition from consumers to prosumers. However, space requirements, among others, can potentially be a limiting factor that demands additional renewable external generation. A prominent form of contracting renewable electricity is via power purchase agreements (PPAs), which show increasing volumes in Germany [9, 10].

Another important step towards climate neutrality for the industry sector is to exploit possible flexibility. This may include battery storage systems that balance the variable nature of renewable power generation and provide additional flexibility-related services, thereby enhancing revenue potential. The market for industrial and large-scale storage systems in Germany is continuously growing, with a cumulated installed capacity of almost 3 GWh at the

beginning of 2025 [11]. Currently, battery storage systems in the industrial sector are mainly used for behind-the-meter (BTM) services, e.g. peak-shaving (PS) and self-consumption increase (SCI) [12, 13]. New concepts, as shown by Englberger, aim at combining them with front-of-the-meter (FTM) services [14]. Industrial prosumers that exploit these additional flexibilities are referred to as flexumers [15].

A challenging industrial application for decarbonisation is glassworks for automotive products. Typical glass furnaces for this application have comparatively long lifetimes of 20-30 years, which requires sufficient lead-time for the transformation to net-zero [16]. A holistic life-cycle assessment (LCA) by Jost et al. [17] compares different measures to reduce GHG emissions in the glass industry and concludes that reductions of 75% are possible. Another study by Zier et al. [18] shows possible decarbonisation pathways for this industry, discussing various options for substituting fossil fuels. From the perspective of the energy supply and consumption, the most promising concept for decarbonisation is to increase the electrification/efficiency of the melting furnace and substitute the primary energy carrier of NG with renewable hydrogen [18, 19]. One option for supplying renewable hydrogen is via pipeline as part of the planned German hydrogen core network. The basic concept for this core network has already been approved by the Federal Network Agency in 2024, with phased commissioning until 2032 [20]. An alternative solution that can be realised in the short term is the on-site production of green hydrogen through electrolysis. However, supplying the electrolysis system with green electricity usually requires adequate contracting of PPAs to comply with the high legal requirements of the EU Renewable Energy Directive (RED II) [21, 22]. This particularly includes the requirements for the geographical and temporal correlation between renewable generation and electrolyser system consumption. Optimising PPA portfolios for industrial use cases under consideration of mitigating financial risks can be achieved with stochastic optimisation [23, 24]. Figure 1 presents the concept of a decarbonised industrial flexumer applied to the glassworks use case, which serves as the foundation for the methods developed in this thesis.

1.1. Research objective

This dissertation aims to develop an energy system modelling framework capable of benchmarking different decarbonisation options for a glassworks use case in Herzogenrath, Germany. Finding the most cost-efficient solution for the industrial site requires a sophisticated energy system modelling framework. The developed model should be a realistic technical representation of a future energy supply system for the use case, including electricity, heating, and gas systems, as well as generation, storage, and hydrogen use. There is a variety of different energy system modelling frameworks featuring multiple approaches [25–28]. The majority of frameworks are designed to model national or smaller regional grid-

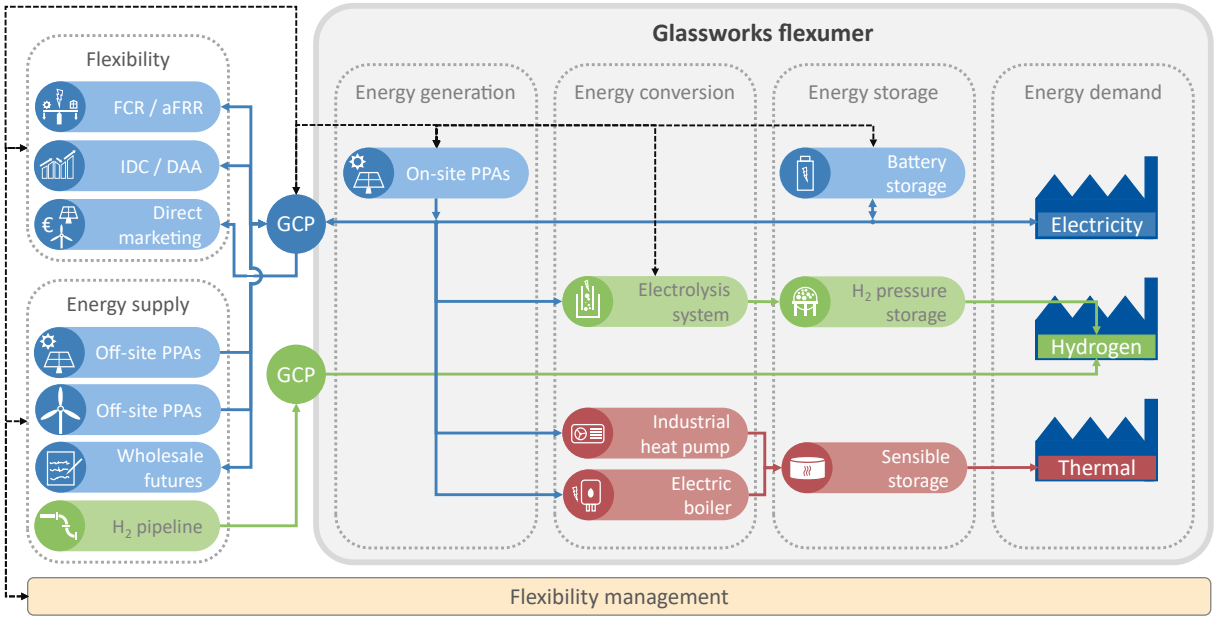

Figure 1: Concept for the decarbonised energy system of an industrial flexumer with sector coupling, applied to the use case of a glassworks. Own illustration. Abbreviations: grid connection point (GCP), power purchase agreements (PPA), frequency containment reserve (FCR), automatic frequency restoration reserve (aFRR), intraday-continuous (IDC), day-ahead auction (DAA).

scale energy systems. Fewer frameworks focus specifically on the industrial scale, as shown in [15]. In this dissertation, a framework is developed specifically for local industrial flexumer applications. The approach is based on mixed-integer linear programming (MILP) and combines best-practice implementations from various existing frameworks. This includes a separation into a sizing and an operation problem, and methods to improve solvability, including time series aggregation and a rolling horizon approach [29–31]. Moreover, the modular structure of the approach enables flexible integration of any required energy sectors, technical components for energy conversion and storage, and regulatory constraints. This allows the framework to be applied to a wide range of industrial energy systems.

The core element of the developed framework is a value stacking approach for industrial battery storage. The approach enables combining behind-the-meter (BTM) and front-of-the-meter (FTM) services. For BTM services, it considers peak shaving and increased self-consumption from on-site renewable generation. The main application for FTM services is the integration of PPAs, which separates the value stacking approach from most other methods in the literature. There are only a few studies on the optimisation of PPAs with battery storage that primarily focus on installing the battery storage at the site of the renewable asset [32]. In addition, the model includes implementations for spot market trading and for detailed representations of ancillary services. This includes frequency containment reserve (FCR) and automatic frequency restoration reserve (aFRR). One major contribution of the implemented approach is its aggregation method for accurately integrating ancillary services. These services are based on second-to-second decisions that are converted into the 15-minute resolution of the energy system modelling framework. Overall, the approach in this dissertation aims at

closing the gap between stand-alone battery revenue models and state-of-the-art energy system models. **Section 3** provides the methodology for the developed industry flexumer decarbonisation framework.

With the developed framework for industry decarbonisation, we conduct an extensive analysis of decarbonisation options for the existing glassworks in Herzogenrath, Germany. The site operator provides extensive measurement data to feed the energy system model. Based on all model input parameters, we develop a scenario setup to capture the relevant sensitivities and adequately evaluate the use case (see **Section 4**). The evaluation compares different years for the transformation of the glassworks' energy system, including 2024, 2030, and 2037. The evaluation section is split into three major subsections. **Subsection 5.1** features a high-level analysis of decarbonisation options for the glassworks. Overall, the results show that, despite a decreasing trend towards 2037, decarbonisation choices lead to higher annual costs than rebuilding an NG-based furnace, by at least 18.3%. The most cost-competitive decarbonisation is achieved through high furnace electrification. In **Subsection 5.2**, the most promising setups are further evaluated in more detail. The evaluation highlights that operating an on-site electrolysis system can be a competitive option compared to connecting to a future hydrogen pipeline network. Finally, in **Subsection 5.3,** additional benefits of leveraging flexibility potentials are analysed. The results indicate that in 2024, substantial cost reductions of up to 30.1% can be achieved when exploiting the flexibility of the electrolysis system and stacking multiple use cases for the industrial battery storage system. Although the evaluation focuses on the specific glassworks use case in Herzogenrath, the results act as a blueprint for decarbonisation concepts for other industrial sites.

2. Fundamentals

This section provides the theoretical foundation for the development of necessary models and parameterisation of use cases in this dissertation. This includes the basics of energy system modelling. Section 2.1 gives an overview of typical methods and compares various techniques. A prominent characteristic of renewable energy systems is the volatile nature of generation. Therefore, the key challenge is to balance intermittent renewable generation and demand. One key asset that provides the necessary flexibility is energy storage, particularly battery storage systems. Section 2.2 summarises the basics of industrial battery storage systems and their typical applications, including self-consumption increase, peak shaving, arbitrage, and frequency control. Moreover, to decarbonise industrial energy systems, it is essential to consider the coupling of different end-energy sectors, including electricity, heat, and gas. Section 2.3 gives an overview of the relevant sector-coupling technologies. Furthermore, regulations impose many additional constraints on renewable energy systems. Therefore, Section 2.3.3 summarises all relevant regulatory aspects for the glassworks use case of this dissertation.

2.1. Energy system modelling

Finding solutions to decarbonise energy systems requires advanced energy system modelling techniques. They enable sophisticated optimisation of renewable energy systems to find the best configuration and operation. While the term framework describes a modelling toolbox that contains the mathematical implementations and constraints, a model is the application of a framework to a specific use case [33]. The diversity of energy system structures has led to a wide range of approaches for different frameworks and models.

2.1.1. State-of-the-art

A large number of energy system models and frameworks exist, and multiple reviews aim to categorise them by their features. Typically, reviews distinguish between top-down, bottom-up, or hybrid models [25, 34]. Top-down models are often used to analyse the impact of energy or climate policies on macroeconomic sectors and therefore feature a simpler representation of the energy system and its components [25, 34]. On the contrary, bottom-up models focus on the detailed modelling of technical components and the interdependencies of energy systems, allowing for identifying the best system configuration from a techno-economic perspective [25, 34]. Hybrid models, however, aim to combine top-down and bottom-up approaches to leverage the advantages of both [25]. In this dissertation, the bottom-up approach is the sole relevant approach, as the focus is on detailed modelling of industrial energy systems and their components.

Bottom-up models are further split into short- and long-term models, as described in detail by Prina et al. [25] and summarised in the following. While short-term models typically feature shorter time horizons of single target years, long-duration models consider the transition of an energy system over several years. On the one hand, long-term models can be classified as intertemporal models, consisting of a single optimisation problem over the full horizon. On the other hand, another approach for long-term models is the myopic approach, in which the horizon is divided into sub-problems and results are recursively transferred from one to the next. Moreover, considering a longer temporal horizon enables the formulation of additional constraints, such as the (de-)commissioning of components or life-cycle considerations. [25]
Apart from the top-level overview of energy system models, we identify five main categories in the literature (see Table 1) to achieve a finer granularity of categorisation based on [25, 27, 28]. While all models feature a high temporal resolution, spatial resolution and modelling detail vary substantially between models, and no model achieves the highest rating for all categories [25]. This highlights that there is no one-size-fits-all model that can solve all problems, as the complexity of energy systems requires models to focus on very specific research questions and sub-problems.

Table 1: Categorisation of energy system models and frameworks based on [25, 27, 28], with own adaptations to improve consistency.

Optimisation techniques	**Solution objective**	**Temporal scope**	**Geographical scope**	**Sectors**
Structural approach • Component-based • Rule-based • Agent-based Mathematical approach • Linear programming (LP) • Mixed-integer LP (MILP) • Non-linear (e.g., quadratic) • Dynamic • Stochastic/robust • Heuristic • Artificial intelligence Modelling language • Python • GAMS (The General Algebraic Modelling Language)	Overall classification • Optimisation • Forecasting • Backcasting Specific objectives • Simulation • Dispatch optimisation/ Unit commitment • Single-objective investment optimisation • Multi-objective investment optimisation	Time resolution • Seconds • 15 minutes • Hourly Time horizon • Typical days/weeks • One year • Multi years (pathway)	Model structure • Single-node • Multi-node Geographical region • Single (industrial) plant • Local energy system • National energy system • Multi-national energy system • Continental energy system	End-use sectors • Electricity • Building • Transport • District heating • Industry Commodities: • Electricity • Heat • Cooling • Gas • Hydrogen • Liquid fuels

Optimisation techniques: Formulating optimisation problems requires a set of optimisation variables, equality and inequality constraints, and one or multiple objectives [35]. The objective defines the problem and is formulated as a mathematical function (the objective function) that can be minimised or maximised. There are many available numerical optimisation techniques to set up and solve an energy system simulation or optimisation model [25, 36]. A very common technique is linear programming (LP) [36, 37]. In this case, the

objective function and all constraints for relationships between energy flows and component behaviour are linear. To add more flexibility to the optimisation problem, mixed-integer linear programming (MILP) [37] introduces the possibility of binary decision variables that enable a higher modelling detail, for instance, for component behaviour by piecewise linearisation of efficiencies or switching components on and off [38]. One benefit of MILP-based models is that when the solver used finds a solution, it is always guaranteed to be the global optimum [39]. Moreover, fast commercial solvers for LP and MILP are widely available [39]. In contrast to LP and MILP, quadratic programming (QP) is less commonly used. However, there are applications, especially in the smart and micro-grid domain, that use the principle [40, 41]. When modelling highly complex energy systems with multiple sectors and components, even for LP or MILP problems, solving can become challenging. Therefore, other mathematical approaches exist that aim to improve solvability. In dynamic programming, the optimisation problem can be divided into sub-problems that are simpler and therefore easier to solve [42, 43]. Another possibility is to apply heuristic approaches. This is a group of methods based on the principle of searching for a near-optimal [36] solution by iteratively evaluating different system configurations [35, 44]. This requires a very fast calculation time for each single system solution, which can, for instance, be achieved with rule-based formulations for energy distribution [35, 44]. Common methods for heuristic optimisation make use of the evolutionary strategy concept [44]. Apart from rule-based methods, another way to structure and simplify optimisation problems is to use agent-based approaches [36, 45]. This requires identifying entities, e.g., consumers or prosumers, that exhibit their own behaviour and can therefore be isolated from other parts of the model [36].

One issue with all deterministic modelling approaches is that they do not account for uncertainties, for instance, in renewable generation and demand. However, in stochastic and robust optimisation, there are two techniques for incorporating uncertainty into energy system modelling: assigning a probability of occurrence to certain parameters, or treating uncertainty as a mathematical space, respectively [39, 46]. Furthermore, a possible method to account for uncertainties, though computationally complex, is the Monte Carlo optimisation [46]. Another large field of energy system modelling optimisation techniques can be categorised under the generic term of artificial intelligence [27]. This includes fuzzy logic, particle swarm, and neural networks, among others [27]. From a programming perspective, many programming languages are suited for energy system modelling. However, while in the 2000s the majority of models relied on the programming language “General Algebraic Modelling System (GAMS)”, since 2010, Python has become the new standard [47].

Based on current methods and literature reviews of optimisation techniques, we conclude that the MILP modelling approach is well-suited for the industrial prosumer use case we aim to evaluate in terms of solvability, preliminary work, available tools, and software support.

Solution objective: Depending on the use case, the objective of what to optimise varies. It can be distinguished between optimisation, forecasting, and back-casting [27]. The aim with optimisation models is to identify the optimal investment decision for a given portfolio of possible technologies or operational decisions for optimal energy flows within an energy system [27]. Optimisation models are further separated into single or multi-objective [25]. For multi-objective optimisation, also referred to as multi-criterial optimisation, more than one objective is formulated, which allows for optimising, for instance, costs and CO_2 emissions at the same time [48]. In contrast to optimisation models, forecasting models are simulation models that analyse a pre-defined system under future conditions to identify, for instance, renewable energy demands [27]. Another approach is backcasting, where a future condition is specified and the optimisation model provides the best possible pathway to reach that future state [27]. One specific and common objective in electric power system modelling is the optimal planning of the operation of existing power plant resources, referred to as dispatch. Mathematically, this can be formulated as an LP model (unit commitment problem) or rule-based, considering the merit order list of power plants [38].

Temporal scope: Two main characteristics of an energy system model are the time resolution and the time horizon. The time resolution refers to the granularity of the modelling, thus the length of each time step (time-slice) [25], which is usually identical within one model. However, there are concepts where individual time steps can have different lengths [30]. On the contrary, the optimisation horizon measures the full timespan a model covers. For long-term models, the optimisation horizon of multiple years further separates into single simulation years [25]. The majority of energy system models feature an hourly time resolution and an optimisation horizon of one year or more [28].

Geographical scope: One important characteristic to distinguish is the geographical coverage of energy system models, which can vary widely. Typically, on a higher geographical level, models are classified as one- or multi-node models. A one-node model aggregates a specific geographical region into a single node, assuming ideal transmission or distribution conditions without losses or bottlenecks [25]. In the electricity sector, this is known as the copper plate model [49]. On the contrary, multi-node models consist of more than one node, with distribution or transmission capacities modelled between them [25]. Regarding geographical coverage, models further differentiate by the size of the energy system and the area they cover. This can include single (industrial) plants or areas covering local, national, multi-national, or continental energy systems [25, 27].

Energy sectors: There are several end-use energy sectors, for instance, electricity or industry [25]. Within the end-use sectors, it can further be distinguished between energy commodities, including electricity, heat, and hydrogen, among others [25]. Most models mainly cover the

electricity sector with limited options of sector coupling, while industrial applications are only considered by one-third of the models [28]. Moreover, to the best of our knowledge, a sophisticated framework specifically designed to decarbonise industrial applications does not exist. However, a few studies use MILP-based approaches customised to optimise single energy-intensive industrial applications. In Fleschutz et al., a beverage company is turned into a so-called flexumer by leveraging flexibility potentials, including demand response (DR), peak shaving, and self-consumption increase [15]. Other studies evaluate the potential for demand side management (DSM) for a cement plant [50] and DR for copper production [51].

While categorisation is a main motivation for comparing energy system modelling frameworks, qualitative comparisons can yield further insights. A qualitative comparison can be achieved by feeding energy system models with the same harmonised input data and comparing the results. One of the first so-called model experiments presented by Gils et al. reveals that, despite similar results for the energy balance of dispatchable power plants and flexibility, the technologies used across the models can differ significantly [52]. However, the reasons for differences in the study remain unclear, as modelling differences are not evaluated [52]. Therefore, a range of follow-up studies aims to provide better insights by focusing specifically on modelling details and harmonising input data through simplified test cases [26, 53, 54]. In the first study, only basic technologies and the flexibilities with fixed capacities (dispatch) of the power sector are compared, and despite very different mathematical concepts in the models, the results are very similar due to high data harmonisation [53]. However, when comparing capacity expansion, deviations in results increase, especially for long-duration storage and transmission [54]. The deviations become even higher when more individual technologies are introduced, especially for sector coupling, as some models can only consider them rudimentarily [26]. In this group of studies, harmonised data and simplified test cases lead to a better understanding of the differences in results. However, the results' relevance is limited. Therefore, another comparative study focuses on scenarios that include variations in policy parameters that are relevant to the German energy transition [55]. The insights reveal that significant deviations can occur in crucial technologies such as battery storage investments. Therefore, it is important for political actors to distinguish between different modelling approaches and their impacts on results.

As energy systems become increasingly complex, a common question is how to reduce model size without sacrificing accuracy. An analysis by Priesmann et al. [49] concludes that a certain complexity is necessary and that a good practice is to use different formulations for dispatch/operation and investment decision problems. Another common issue of energy system models with longer continuous optimisation horizons is that the model knows all its input parameters, which is known under the term of perfect foresight [25]. This can lead to unrealistic results compared with real systems, especially for flexible components like storage

systems, whose operation depends primarily on time-series characteristics that are usually unknown beforehand. One possible solution to this problem is the so-called rolling horizon (RH) approach that is commonly used, especially for system dispatch simulation [56] and micro-grid applications [57]. It uses a rolling window to split the full optimisation problem into smaller sub-problems on a temporal scale. For instance, Marquant et al. [31] apply the approach to Urban Energy Hubs, while Silvente et al. [29] use it for energy supply and demand planning in micro-grids.

With the number of energy system models and approaches rising, one of the main issues remains transparency [58]. There are attempts to solve this problem, especially through open-source initiatives. This especially includes the Open Energy Modelling Initiative (Openmod) [59] that features a large database of existing energy system models and energy modelling data. In addition, few studies have examined the quality of open-source energy system models in depth. A study by Candas et al. looks more closely at implementations of open source models and finds that, despite similarities, there is a variety of unique features for some models [60]. Furthermore, a comparison of open source frameworks by Berendes et al. reveals that the usability of open source can still be increased [61]. Nevertheless, recent research indicates that, despite a growing number of open models and frameworks, many models are still not publicly available, and that reproducibility is often not possible [25, 27].

2.1.2. Battery storage system modelling

There is a wide range of electrochemical, electrical, and machine learning models for battery storage systems and a deep understanding of the underlying effects and insight into battery cells [62–64]. However, a majority of energy system modelling frameworks focus on larger system scopes, for instance, nationwide energy systems and therefore typically feature rudimentary representation for battery storage systems [53, 60]. While this might be sufficient for national energy system models, for local energy systems, the development of different operating strategies for battery storage, including combinations of several use cases (multi-use or value stacking) (see definition in Subsection 2.2.2) [12] comes with the necessity of a greater detail in modelling. In the literature, there are few sophisticated value-stacking models, mostly for stand-alone applications. One of the most prominent stand-alone models that considers peak shaving (PS), frequency containment reserve (FCR), and spot market trading (SMT) is presented by Englberger et al. [13]. However, only a few multi-use models are integrated into state-of-the-art energy system modelling tools that can investigate optimal energy system configuration and storage use for prosumer/flexumer applications simultaneously. One study integrates ageing characteristics of energy storage into a so-called zero-carbon multi-energy system [65]. The approach in this dissertation aims at closing the gap between stand-alone battery models and state-of-the-art energy system models.

2.2. Stationary battery storage systems

The market for stationary battery storage systems in Germany shows increasing growth [11, 12]. As of the end of 2024, about 18 GWh of stationary battery storage systems were installed in Germany [11]. Figure 2 shows the development of stationary battery storage in Germany since 2015.

Most of the market growth for stationary battery storage comes from the residential segment (home storage). The industrial segment accounts for only about 4% of installations, although the growth rate was over 30% in 2024. Nevertheless, there are high expectations for future growth in this sector, considering especially popularity of behind-the-meter applications [66]. For all installed battery storage systems in Germany, the dominating technology is lithium-ion [12]. Although lead-acid batteries still play a role, they are predominantly used for an uninterruptible power supply [12]. Therefore, for the use case of this dissertation, we focus on the lithium-ion technology.

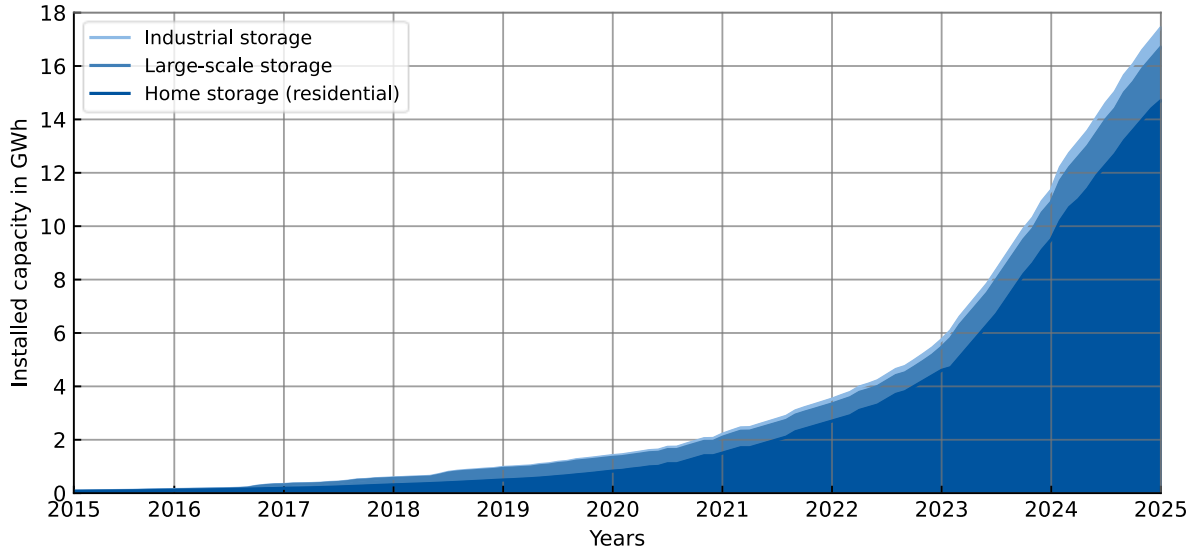

Figure 2: Development of the market for stationary battery storage systems in Germany based on data from [11]. Own illustration.

2.2.1. Battery fundamentals

The lithium-ion battery technology is based on the “Rocking-Chair” principle (see Figure 3) as described in the following by summarising descriptions in [67, 68]. It consists of two electrodes, the anode and cathode, as well as separators in between. The cathode consists of a lithium metal oxide that can be substantially different depending on the type of lithium-ion battery. The anode material is usually based on carbon, such as graphite. The separator is a porous membrane that is permeable to lithium ions and electrically isolates the electrodes.

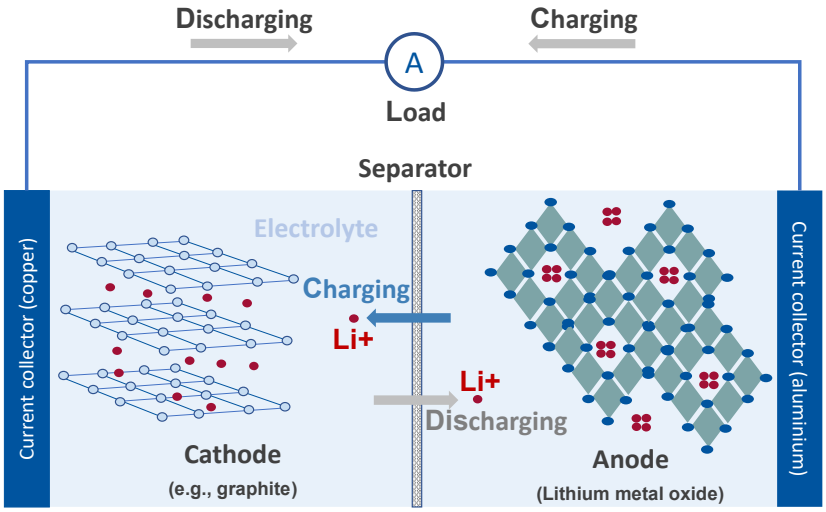

Figure 3: Illustration of the basic structure and working principle of a lithium-ion battery, reffered to as “Rocking-Chair” concept. Own illustration based on [67, 68].

All elements are surrounded by an organic liquid electrolyte that conducts lithium ions. During discharge, lithium ions deintercalate from the anode carbon structure and travel to the cathode, where they intercalate into the metal oxide. The electron that has been separated from the lithium atom, however, travels outside the cell via the electric circuit from anode to cathode. For charging, the process reverses in the opposite direction. [67, 68]

Based on the principle of lithium-ion batteries, various material combinations for the anode and cathode exist [69, 70]. While the anode typically consists of a graphite-based material, the cathode features different metal oxides, which commonly include nickel manganese cobalt oxide (NMC) and lithium-iron phosphate (LFP) [70]. Despite lower energy density, battery storage systems with LFP chemistry are particularly suited for stationary applications as they are based on low-cost materials and promise long lifetimes [70, 71]. In 2021, LFP batteries accounted for 50% of global newly installed capacity in the stationary segment, which is expected to increase in the coming years [71].

In the performance of a lithium-ion battery, its ageing characteristics play a key role. It can be mainly distinguished between calendar and cyclic ageing [72]. Calendar ageing describes ageing over time through ongoing chemical processes. It depends highly on the state-of-charge (SOC) and temperature of the battery [72]. Avoiding high SOC and temperatures reduces the ageing rate. The other type of ageing is cyclic ageing, which occurs during charging or discharging. Its main influences are current rate, depth-of-discharge (DOD), and temperature [72]. The DOD describes the depth of one cycle. For instance, charging from 10% to 90% SOC corresponds to a DOD of 80%. Adjusting the battery's operation and avoiding high DODs significantly reduces the ageing rate. Another important performance indicator for different use cases is equivalent full cycles (EFC) of a battery storage system, which is the cumulative energy throughput divided by the nominal capacity [73].

Another more general characteristic of storage systems that can be a limitation for many applications is the energy-to-power ratio (EPR). It is calculated by dividing the energy capacity by the storage asset's maximum power capability. For battery storage systems, limiting factors can be the battery cells or the inverters. The EPR can be designed specifically for an anticipated use case by choosing battery and inverter capacity accordingly. For stationary battery storage systems in Germany, typical EPRs are between 1-4 hours [12].

2.2.2. Typical use cases for battery storage systems

There is a wide range of use cases for stationary battery storage systems [13, 74, 75]. They are separated into front-of-the-meter (FTM) and behind-the-meter (BTM) services. FTM services affect the exchange with the electric power grid and typically include either grid-stabilising services (ancillary services) or energy exchange through wholesale markets [14]. The most common FTM use case in Germany until 2019 was frequency control (see Subsection 2.2.3); however, the range of possible applications has expanded since then [12]. For megawatt-scale systems, trading energy on spot markets at power exchanges (arbitrage) is becoming increasingly popular, as are renewable integration and multi-use concepts [12, 13]. On the contrary, battery storage systems with sizes of several hundred kilowatt-hours are typically designed to provide BTM services. This includes increasing self-consumption from, for instance, PV or WPP, peak shaving of the load, EV charging, or backup power supply [12]. While technically possible, combining FTM and BTM services in Germany has been difficult due to regulatory constraints aimed at preventing the mixing of subsidised renewable generation and fossil electricity from the electric power grid [76]. However, with the new regulations of the 2023 German Renewable Energy Act (EEG 2023), this has changed, although questions remain regarding the implementation of required measurement concepts [77]. In the following, we describe in more detail the use cases for battery storage relevant to the modelling in this dissertation.

Self-consumption increase (SCI)

This concept refers to an application where battery storage systems are used to increase the self-consumption rate of self-generated renewable electricity from typically PV [14]. This is beneficial when self-generated renewable electricity is cheaper than grid electricity. Common applications for SCI are residential home storage systems that typically are designed with an EPR of 2 hours and show 200-300 EFCs per year [12, 78, 79]. For industrial battery storage systems in Germany, this is also the dominating use case that (as of 2022) applies to over 50% of installations [12].

Peak-shaving (PS)

Commercial and industrial consumers in Germany connected to the public electric power grid have to pay grid fees, which include energy- and power-related tariffs [80, 81]. The power-related tariff, known as peak power costs, is charged for the highest 15-minute load peak within a year [81, 82]. This motivates companies to reduce their peak load to reduce costs. Battery storage systems can be used to reduce peak load. This requires charging the battery before the peak to take over the load's supply when the peak occurs. The challenge with this use case is that precise prediction of load peaks is necessary. This can, for instance, be achieved with probabilistic forecasting approaches [83]. In addition to the regular PS concept, there are other regulations to reduce grid fees. The atypical grid usage concept incentivises companies to shift their consumption from periods of high power grid utilisation to periods of lower utilisation to obtain individual grid fees with reductions of up to 80% [81, 82]. Battery storage systems can be used to take advantage of this regulation.

Spot market trading (ST)

There are different spot market power trading platforms in Europe, with the European Power Exchange (EPEX SPOT) in Leipzig trading over 90% of volume in Germany (status 2021), followed by Nord Pool [84]. Spot markets at EPEX SPOT can be divided into day-ahead auctions (DAA) and intraday continuous (IDC) trading. The DAA features a product length of 1 hour, and the auction closes at 12 pm the day before delivery [85]. On the contrary, IDC products can be traded until 5 minutes before delivery with 15-minute granularity [85]. With a battery storage system, price spreads within or between those markets can be utilised, which is referred to as arbitrage trading [14]. It can be distinguished between regular trading, when the battery is actually charged or discharged, and virtual (financial) trading [86] without any physical energy flows when positive and negative bids balance each other out. Table 2 summarises the most relevant characteristics of the DAA and IDC spot markets at the EPEX SPOT.

Table 2: Characteristics of the day-ahead auction and intraday continuous trading spot markets at the EPEX SPOT, based on information in [85].

EPEX SPOT market	**Day-ahead auction (DAA)**	**Intraday continuous trading (IDC)**
Product length	1 hour	15 minutes
Gate opening	-	3 pm the day before delivery
Gate closing	12 pm the day before delivery	5 minutes before delivery
Type of auction	Pay-as-bid	Pay-as-bid
Minimum trade quantity	0.1 MWh	0.1 MWh

2.2.3. Frequency control markets in Germany

The German power grid is part of the largest synchronous electric power grid in the world, known as the Continental Europe Synchronous Area (CESA) [87]. It covers more than 20 countries and multiple transmission grid operators (TSOs) across continental Europe [88].

Most European countries are part of the association of the European Network of Transmission System Operators for Electricity (ENTSO-E), which ensures coordinated operation of the large electric power grid [85, 89]. The synchronous grid frequency of the CESA is 50 Hz [85]. Maintaining the frequency requires a mechanism to balance demand and supply. Frequency control markets are designed for this purpose. Several frequency control markets exist with different requirements regarding response times and duration of provision [85, 90]. This ensures that the most suitable assets activate at the right time. Figure 4 illustrates the frequency control market products in Germany and their respective response times.

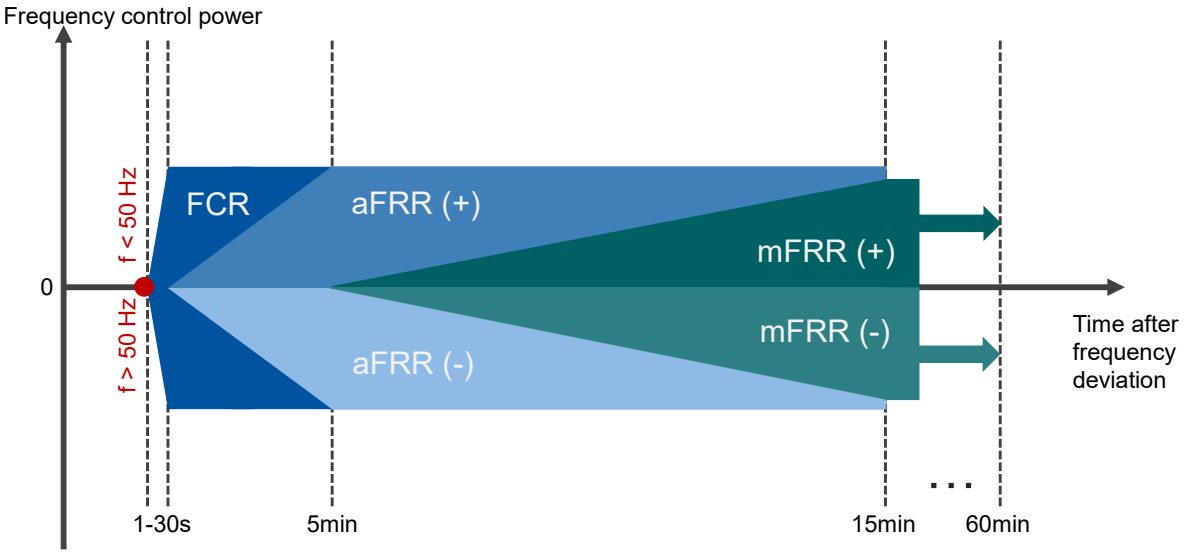

Figure 4: Schematic illustration of frequency control market products in Germany (2024), with their corresponding ramping requirements. Own illustration based on data from [85, 90].

In the following three paragraphs, we summarise the market characteristics and design of control markets in Germany that are described in detail on *regelleistung.net* [90]. The market with the fastest response to frequency deviations is the frequency containment reserve (FCR) market, also known as the primary frequency control reserve. In 2007, FCR cooperation was established through joint procurement among German TSOs. Over time, TSOs from eight other countries joined this collaboration, covering more than 50% of the FCR demand of ENTSO-E members, corresponding to over 1,500 MW of provision. The activation of FCR is decentralised and occurs as a direct response to frequency deviations from 50 Hz, and must be initiated within 30 seconds. The maximum power has to be activated at a deviation of 200 mHz, which typically does not occur [91]. Asset operators providing FCR are compensated solely for the reservation of capacity, not for activation. Participation in the FCR capacity market is possible via a pay-as-cleared auction that closes at 8 am the day before delivery. The auction features FCR products in 1 MW steps for reserving capacity with a length of 4 hours starting at midnight. Each product is symmetrical, which requires equal amounts of positive and negative control power. [90]

The market that gradually replaces FCR over time is the automatic frequency restoration reserve (aFRR), also known as the secondary frequency control reserve. For aFRR, since 2017, a collaboration among European countries has existed through the Platform for the International Coordination of Automated Frequency Restoration and Stable System Operation (PICASSO). Activation of aFRR occurs via a setpoint specified by the responsible TSO. The ramp-up requires a first response within 30 seconds, with full activation 5 minutes after the frequency deviation. For activation signal processing by the TSOs, the clearing price and, thus, the list of activated assets are calculated every few seconds based on the merit order list established every 15 minutes [90, 92, 93]. In contrast to FCR, participants in the auction can choose between aFRR capacity products, compensating for the reservation of capacity, and aFRR energy products, compensating for activated energy. All capacity auctions are based on the pay-as-bid principle, and products are separated into negative and positive provision. On the contrary, the aFRR energy market applies the pay-as-cleared principle to both positive and negative products. [90]

The third and final market is the manual Frequency Restoration Reserve (mFRR), also known as tertiary frequency control. The mFRR activates after 5 minutes and gradually replaces aFRR. It has to be active latest 12.5 minutes after the occurrence of the frequency deviation. The market design and products are similar to aFRR. However, activation is executed manually by the asset operator. Table 3 summarises the most relevant characteristics of the frequency control reserve markets in Germany. [90]

Table 3: Characteristics of the frequency control reserve markets in Germany, based on information in [90].

	Frequency containment reserve **(FCR)**	Automatic frequency restoration reserve **(aFRR)**		Manual frequency restoration reserve **(mFRR)**	
		aFRR capacity	**aFRR energy**	**mFRR capacity**	**mFRR energy**
Activation procedure	Decentralised based on frequency deviation	Activation signal by TSO		Manual activation by asset operator	
Direction	Positive and negative (symmetrical)	Positive or negative	Positive or negative	Positive or negative	Positive or negative
Product length	4 hours	4 hours	15 minutes	4 hours	15 minutes
Minimum quantity	1 MW	1 MW	1 MW	1 MW	1 MW
Gate closing	8 am the day before delivery	9 am the day before delivery	25 minutes before delivery	10 am the day before delivery	25 minutes before delivery
Minimum provision	15 minutes	1 hour	15 minutes	4 hours	15 minutes
Market mechanism	Pay-as-cleared	Pay-as-bid	Pay-as-cleared	Pay-as-bid	Pay-as-cleared

Participation in auctions for the German frequency control markets requires successful prequalification (PQ). With this procedure, asset owners prove to the responsible TSO that they can provide FCR or aFRR with the desired performance. The technical requirements are summarised in a document called PQ-conditions [94]. For assets with reduced energy capacity, such as battery storage systems, specific conditions must be met.

For large-scale battery energy storage systems (BESS) in Germany, FCR has been the most relevant market for the past years, as it is well suited for 1-hour systems with maximum activation times of 15 minutes [94, 95]. In contrast, the aFRR capacity and energy market featured maximum activation times of 4 hours until 2022, which were not attractive, especially for the first large-scale battery storage systems with comparatively lower energy-to-power ratios (EPR) [12, 85, 95]. However, in 2022, the market design for aFRR energy was changed from 4-hour to 15-minute products [85]. In combination with the ongoing saturation of the FCR market, aFRR products have become more attractive to battery storage operators [95].

2.3. Sector Coupling

The concept of sector coupling has many ambiguous definitions in the literature [7]. Nevertheless, most definitions agree that sector coupling is an instrument to increase the use of variable renewable energy (VRE) generation to decarbonise end-use demand sectors like electricity and industry [7]. When coupling sectors, energy flows must be adequately tracked to assign corresponding emissions. For emissions, it must be distinguished between those that directly occur on-site (scope 1), emissions from imported energy and fuels (scope 2), as well as other upstream and downstream emissions (scope 3) [96].

Industrial sites often have energy demands across multiple sectors, including electricity, heat, and gas. Depending on the industry sector, the electrification level for German industrial sites is only between 13-66% [97]. Primary energy carriers, including NG, coal, oil, and others, provide the remaining share of energy demand [97, 98]. The deep decarbonisation of the industry sector requires a higher electrification and substitution of fossil fuels by green energy carriers, in particular hydrogen [98, 99]. Reaching higher electrification levels is possible through the coupling of energy sectors. This typically requires technical components that can convert electricity into other forms of energy. In particular, the coupling of electricity and heat is key for many applications, with many technologies available to achieve this [100]. For this dissertation, this includes the coupling of electricity and heat by industrial heat pumps (HPs) and an electrolysis system. On the one side, HPs can serve industrial heat demand for low temperature levels in the range of up to 200°C by utilising lower temperature waste heat [101]. On the other hand, the purpose of the electrolysis system is to produce green hydrogen that can be used to generate high-temperature industrial heat for melting raw materials. For the use case of the glass industry in this dissertation, this corresponds with temperatures around 1200°C [18, 102]. To add flexibility to the sector-coupled industrial energy system, energy storage can play a key role [7]. In the following, we describe the relevant sector coupling components and their technical characteristics for the use case of the glassworks in this dissertation in more detail.

2.3.1. Industrial heat pumps

Many industrial sites produce vast amounts of waste heat that is often unused [103]. With high-temperature HPs, it is possible to utilise waste heat and reuse it for low-temperature industrial heating demands [101]. Typically, this is suitable for industrial heating demands with temperatures of up to 200°C [101, 104].

The working principle of an HP is to extract thermal energy from a lower temperature heat source (T_{source}), for instance, from waste heat, and convert it to a higher temperature (T_{sink}). The coefficient of performance (COP) in Eq. (2.1) defines the efficiency that depends on source and sink temperatures [104]. Different models of high-temperature HPs can serve different temperature levels for source (0-100°C) and sink (35-180°C) with COPs between 1.9 and 6.0 [104].

$$COP_t = \frac{T_{sink,t} + 273.15°C}{T_{sink,t} - T_{source,t}} * \eta_{HP} \tag{2.1}$$

High-temperature HPs are often combined with thermal energy storage (TES) to better size the system and increase flexibility and operational efficiency. For TES, it can be distinguished between sensible, latent, and thermochemical heat thermal energy storage [105]. The most common thermal storage type with low-cost materials like water is sensible heat thermal energy storage (SHTES), which is well suited for low temperature industrial heat (<150°C) [105, 106]. However, it has a 3-4 times lower energy density than latent heat thermal energy storage [105]. For the glassworks use case in this dissertation, we consider only SHTES for modelling waste heat utilisation, as cost considerations are most important.

2.3.2. Electrolysis systems

Water electrolysis enables the production of green hydrogen with renewable electricity by splitting water into its two components, hydrogen and oxygen [107]. There are three main existing electrolysis technologies that have different characteristics. This includes alkaline water electrolysis (AWE), Proton Exchange Membrane (PEM) electrolysis, and high-temperature electrolysis, as described in detail in [107]. They differ mainly in their use of electrolytes and in temperature levels. While AWE systems have been commercially used for several decades, the PEM technology started development in the 1960s [107]. For high-temperature electrolysis, several technologies exist, with solid oxide electrolysis (SOE) among the prominent candidates [108]. However, SOEs are still in a developmental and research stage [107, 108], which is why we focus on low-temperature technologies for application in this work. Figure 5 illustrates the typical structure and working principles of AWE and PEM

electrolysis cells based on [107, 109]. Furthermore, we illustrate the setup of an electrolysis system that requires additional electrical components, as shown in [110]. In the remainder of this dissertation, we model the entire electrolysis system as a single component.

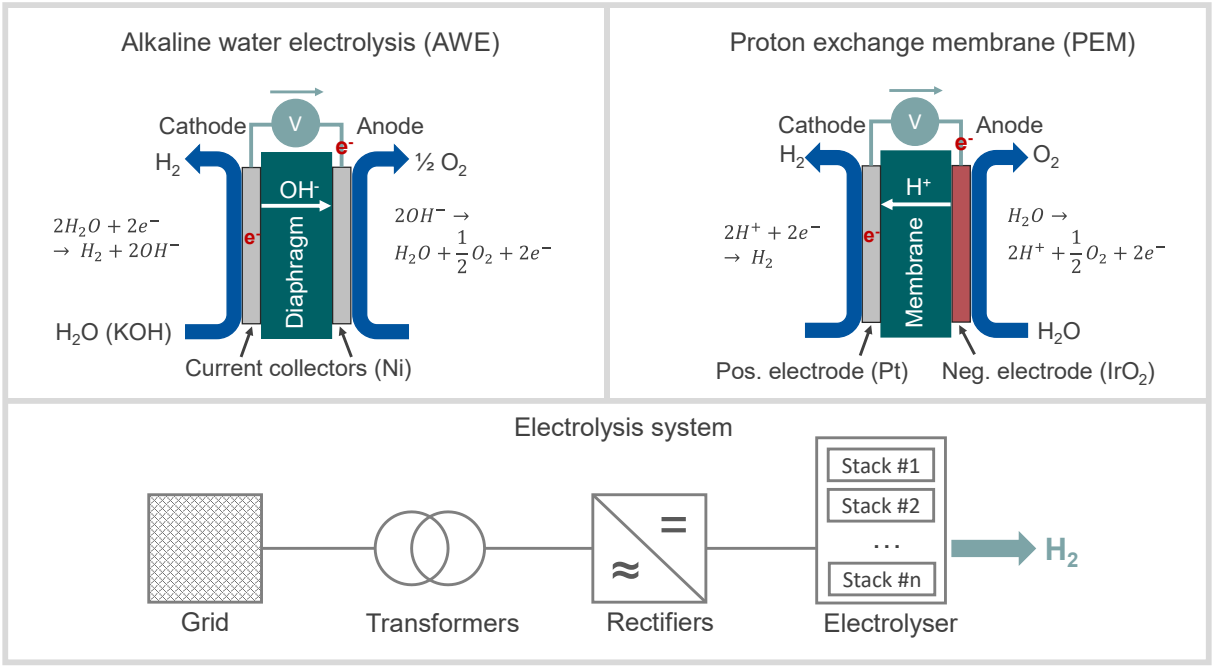

Figure 5: Visualisation of the basic structure and working principle of AWE and PEM electrolysis cells, as well as illustration of an exemplary setup of an electrolysis system. Own illustration based on [107, 109, 110].

The following two paragraphs summarise the working principle of the AWE and PEM technology as described in [107]. The AWE is operated with an alkaline electrolyte consisting of potassium hydroxide (KOH) and operates at temperatures between 40-90°C, with a typical operating temperature of 80°C. It is a well-established technology with modules available in the megawatt range at comparatively low costs of 1000€/kW. The technology is also characterised by a high degree of cyclic stability with stack lifetimes of up to 90,000 h. The efficiencies of AWE systems are between 60-85%. The main disadvantage is a low current density, resulting in a comparatively low power density. Moreover, the minimum part load is at 20-40% of the nominal capacity. [107]

Similar to AWE technology, PEM electrolysis operates at temperatures between 20-80°C. Its main features are the proton-conducting membrane and platinum-group metals on the electrodes, required by the high anode overvoltage. This leads to current densities that are 2-3 times higher than for the AWE. Equally, the power density increases, making PEM electrolyser systems more compact than AWE systems. Moreover, PEM electrolysis systems can operate in standby mode, with part loads of approximately 5% of nominal power, where power is mostly supplied to the periphery. One of the major challenges is the shorter lifetime of the stack (20,000-50,000 h) and the comparatively high cost of the noble platinum-based electrodes. [107]

Table 4: Comparison of state-of-the-art technological characteristics of AWE and PEM electrolyser systems.

Technical parameters	AWE system	PEM system	Sources
Current density in A/cm²	0.2-1.3	<2.0	[107, 111]
Operating temperature in °C	40-90	20-80	[107, 112]
Operating pressure in MPa	0.1-3	3-8	[112]
Stack lifetime in hours	60,000 - 90,000	20,000 - 90,000	[107, 112]
Electrical efficiency in %	63-70	56-64	[107, 108, 112]
Lower power threshold in % of nominal power	12-22	3-7	[107, 108, 113]
Hydrogen purity in %	>99.8	>99.999	[108]
Ramp up time (warm start) in min	5.9	2	[113]

One further important aspect of modelling an electrolyser is that its efficiency curve reaches its maximum at part load. The efficiency curve for the AWE system differs substantially from the PEM electrolyser, with the highest part load at around half of the nominal power [114]. On the contrary, the PEM electrolysis system has the highest part load at one-third of the nominal power [115]. Based on [114, 115] and reported efficiencies as well as power thresholds in [112] we approximate exemplary efficiency curves for AWE and PEM electrolysers systems in 2024 as illustrated in Figure 6.

Hydrogen storage

There are several possibilities for storing hydrogen, as summarised in the following two paragraphs, based on information from [116]. These can initially be categorised into material-based and physical-based storage technologies. For material-based hydrogen storage, it can be further distinguished between chemical and physical sorption. Chemical sorption includes all types of storage in which hydrogen is chemically bound within a different material, for instance, ammonia or liquid organic hydrogen carriers (LOHC). This comes with the disadvantages of high investments for conversion plants from hydrogen to other chemical energy carriers and vice versa, as well as comparatively low efficiencies. On the contrary, physical sorption refers to storing hydrogen in porous structures, including carbon-based materials, which shows a high potential for low-cost materials. However, the technology still faces challenges in energy density, pressure, and temperature, and is currently in a development and research phase. [116]

Physical-based hydrogen storage includes either liquefied/cryogenic or compressed hydrogen storage. Compression-based systems use pressure vessels capable of handling up to 100 MPa, while cryogenic systems require temperatures of -250°C. In particular, for cryogenic hydrogen storage systems, this results in additional cooling energy consumption, leading to energy losses of around 40%. Similarly, compression-based hydrogen storage requires additional energy. Nevertheless, with only approximately 10% of energy losses, the efficiency is substantially higher. [116]

For the glassworks use case in this dissertation, investment costs and efficiency are the most important requirements for hydrogen storage. Therefore, for modelling purposes, we

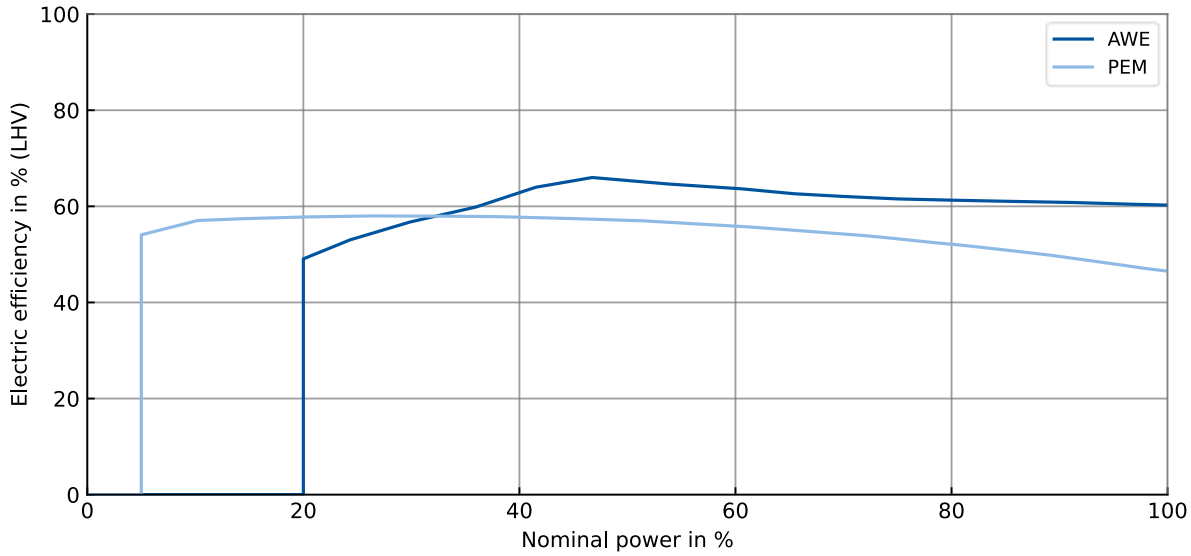

Figure 6: Approximation of exemplary electrical efficiency curves for AWE and PEM electrolysis systems in 2024, based on data in [112, 114, 115].

consider only compressed hydrogen storage. Specifically, we focus on Type I steel or aluminium pressure vessels, typically operating at 20-30 MPa, which is the most conventional and cost-competitive technology [116, 117].

2.3.3. Levelised costs of hydrogen

For industrial energy systems that require hydrogen for decarbonisation, the competitiveness of different technological choices largely depends on the overall costs for producing or importing green hydrogen. A measure to make these costs more transparent and better to compare is the levelised cost of hydrogen (LCOH). The LCOH is typically calculated by dividing all accumulating costs for hydrogen production by the total amount of hydrogen produced in kilograms [118, 119]. The most important cost drivers for green hydrogen production in Europe are electricity costs and capital expenditures (CAPEX) for required components, while water costs play a negligible role [119]. The best-case LCOH for hydrogen production in Germany is above 6 EUR/kgH_2, with the AWE having a cost advantage over PEM technology [118].

2.4. Regulatory framework

The integration of RE generation and green hydrogen production for modelling industrial energy systems requires consideration of numerous regulatory requirements. For Germany, this includes mainly the Renewable Energy Act (German: Erneuerbares Energien Gesetz - (EEG)) on the national level [120] as well as the Renewable Energy Directive (RED) at the

European level [22] that both were updated in 2023. This Subsection summarises the relevant regulatory requirements for the glassworks use case in this dissertation.

2.4.1. Feed-in compensation for renewable generation

For renewable generation, the EEG regulation [120] provides a mechanism that compensates for feeding potential surplus to the electric power grid, which is also described in detail in [121] and summarised in the following. While the EEG compensates small residential power plants (<100kW) with a fixed feed-in tariff, larger industrial and utility-scale plants must participate in the so-called direct marketing (DM) mechanism (German: Direktvermarktung). This means that larger renewable plants are listed on the stock exchange, and the state pays a market premium to compensate for the difference from a fair feed-in value. The fair feed-in value of the renewable energy (RE) plant is typically determined in a tender process and is guaranteed for 20 years [120]. For most RE power plants, the fair feed-in value is identified in a tender that regularly takes place. For each type of RE power plant, the regulator defines upper caps for the volume and price within the tenders [120]. Figure 7 illustrates the German DM mechanism. [121]

For the calculation of the market premium, monthly market values for different types of RE generators are published by the network transparency platform [122]. Table 5 shows the market values of utility-scale PV for 2023 and 2024. The trend shows that the market value has been decreasing since the beginning of 2023, similar to wholesale electricity prices after the 2022 energy crisis [123]. The monthly market premium is then calculated by subtracting the monthly market value from the fair value [121].

Table 5: Monthly market value of utility-scale PV for 2023 and 2024 in EURct/kWh. Values taken from [122].

RE generator	Year	Jan	Feb	Mar	Apr	May	Jun	Jul	Aug	Sep	Oct	Nov	Dec
Utility-scale PV	**2023**	12.291	12.343	8.883	8.002	5.356	7.124	5.173	7.533	7.447	6.763	8.525	6.592
	2024	7.535	5.875	4.965	3.795	3.161	4.635	3.554	4.263	4.512	6.752	10.067	11.171

2.4.2. Production of green hydrogen

Most hydrogen produced today is not green, with the majority of production utilising steam reforming, which splits fossil methane into its compounds, hydrogen and carbon dioxide (CO_2) [124]. This form of hydrogen is referred to as grey hydrogen [21, 124]. Another possibility is coal gasification, referred to as brown hydrogen (lignite) or black hydrogen (hard coal) [21, 124]. All fossil fuel-based production has in common that it comes with high CO_2 emissions. One possibility to reduce emissions is to use carbon capture and storage (CCS), which literature often refers to as blue hydrogen [21, 124]. In electrolysis systems, the colour of the

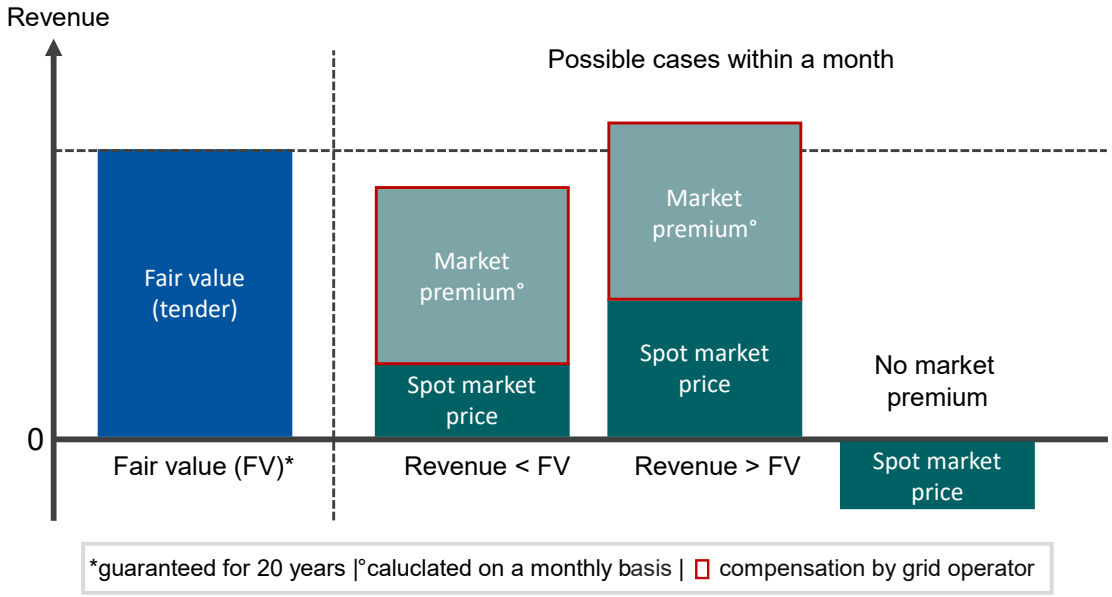

Figure 7: Visualisation of the German direct marketing (DM) concept for the compensation of the feed-in of RE generation plants. Own illustration based on [121] and information in [120].

produced hydrogen depends on the source of the electricity used. However, in literature, there are different definitions. One common definition is to mark hydrogen from nuclear energy in purple and hydrogen produced from grid electricity in yellow [124]. Reaching the climate targets, however, in the long term requires most hydrogen production to be green, utilising RE sources. In the European Union, the Renewable Energy Directive (RED) provides the regulatory framework for green hydrogen production [22]. The revised directive (RED III) following the former version (RED II) entered into force on 20th of November 2023. One of the main changes introduced by RED III is the introduction of renewable targets for fuels of non-biological origin (RFNBO), including hydrogen. The renewable share of RFNBO (based on energy content) must be at 42% and 60% until 2030 and 2035, respectively [22, 125].

The most important regulations for the production of hydrogen were already included in RED II and are adopted in RED III [22]. Among the last adoptions of the RED II are regulations on how to produce green hydrogen and definitions for renewable electricity for hydrogen production, as described in detail in [21] and summarised in the following. The simplest implementation of green hydrogen production from a regulatory perspective is an off-grid or co-located island setup. This means there is a direct connection between RE generation and the electrolyser system, allowing for a simple calculation of the share of renewable electricity. One restriction of the RED II for the off-grid concept is that the RE generators must not have been in operation for more than 3 years prior to the electrolysis system. Another possible setup for green hydrogen production is the grid-connected approach. This, however, poses challenges in accounting for the renewable share of electricity. Therefore, the RED II defines three criteria: additionality, geographical correlation, and temporal correlation. They define the circumstances under which electricity generation for hydrogen production is recognised

as green. The main purpose of additionality is to ensure that sufficient RE generation is installed to power the electrolyser and to avoid a reduction in renewable electricity for other sectors. When it is not possible to install RE generation on-site of the hydrogen production, contracting of power purchase agreements (PPA) (see Subsection 2.4.3) in the same geographical area (geographical correlation) is necessary. Moreover, for all renewable electricity, it must be ensured that generation and demand match in the temporal domain, with monthly or hourly correlation, depending on the date of installation of the electrolyser system. Table 6 summarises the most important characteristics of these three criteria. [21]

Table 6: Criteria for green electricity for hydrogen production in accordance with the regulations of the RED II, based on information from [21].

	Additionality	**Geographical correlation**	**Temporal correlation**
Purpose	Proof that enough additional RE generation is set up to cover the additional demand for hydrogen production	Proof that additional RE generation is within the same geographical area as the hydrogen production	Proof that additional RE generation correlates in the temporal domain with the demand for hydrogen production
Valid from	H_2 installations before 2028: 1st January 2038 New H_2 installations from 2028: 1st January 2028	Immediately	Monthly correlation until: 31st December 2029 Hourly correlation from: 1st January 2030 (EU) 1st July 2027 (member states)
Criteria	One to be fulfilled: • VRE installed together with the hydrogen plant • Installations from power purchase agreements (PPA) For all to be fulfilled: • VRE installation not older than 3 years at the start of hydrogen production	One or more to be fulfilled: • VRE in the same bidding zone as the electrolyser • VRE in interconnected bidding zone (same or higher DA prices than in bidding zone of electrolyser) • VRE in the offshore zone connected to the electrolysers bidding zone	One to be fulfilled: • VRE generation matches the demand of the electrolyser in the same calendar month (or hour), possibly with storage • DA clearing price of electricity is below the threshold (20€/MWh or 0.36 times of CO_2 price)

For geographical correlation, geographical areas are mainly defined through price or bidding zones that depend on grid bottlenecks that typically occur between EU neighbouring countries [126]. Germany, as of today, is one bidding zone and therefore counts as one geographical area, although there are grid bottlenecks from north to south that fuel debates on splitting Germany into several bidding zones [127].

There are a few exceptions in the RED [22] where the criteria for green hydrogen production are not mandatory, as described in [21] and summarised below. This includes bidding zones with a very high share of renewable electricity, where the share exceeds 90% in a calendar year. Another exception is bidding zones where the electricity emission factor is less than 18 gCO_2e/MJ. However, this applies only when hydrogen producers have contracted for at least one renewable PPA. Furthermore, the regulation allows the electrolyser system to

consume grid power when this reduces the need for redispatch during temporary grid bottlenecks. [21]

2.4.3. Power purchase agreements

When it is not possible to install RE generation at the hydrogen production site, PPA contracting becomes inevitable. This type of contracting takes place outside organised markets and describes bilateral, medium- or long-term contracting for electricity, typically between large consumers and suppliers (corporate PPAs) [126, 128, 129]. This has become especially popular recently for contracting of RE generation (green PPAs) to gain greater independence from volatile energy markets and ensure price security for both parties over a longer period [128–130]. The main characteristics of PPA contracts are quantity, duration, price, and individual agreements [129]. For power purchase agreements, there are different contracting types. They can be separated into two main categories: physical on-site and physical off-site PPAs [126, 128, 129]. For physical on-site PPAs, the (RE) generators are at the same location as the consumer and physically connected behind GCP. On the contrary, for off-site PPAs, the generation unit and consumption are geographically separated and only connect physically via the public electric power grid, which results in additional grid charges. For off-site PPAs, it can be further distinguished between sleeved and financial PPAs (virtual PPAs). In the case of sleeved PPAs, an intermediary, e.g., an energy trading or utility company, stands between the energy supplier and the consumer to take over administrative tasks, including the management of balancing groups or green electricity certificates [126, 129]. In the case of financial PPAs, financial transactions and physical electricity delivery are decoupled [126, 129]. This type of PPA contracting ensures a certificate of origin for green power supply on the balancing sheet.

For green PPAs, the power supply profile can vary significantly, especially depending on the type of RE power plant. One type of green PPA is the so-called pay-as-produced, which refers to a supply profile that is equal or very similar to the production of the RE power plant [126, 129]. For PV pay-as-produced PPAs, the supply profile corresponds to a typical PV generation curve that peaks at noon and is zero at night. Another type of PPA is the baseload PPA [129]. It ensures a fixed supply profile either for a year or each month.

PPA contracts require the supplier and consumer to agree on a purchase price that is mutually beneficial. The calculation of a fair price for a PPA involves several components, as described in [126] and summarised below. The base load prices on the stock exchange serve as a comparative value from which a profile factor, depending on the type of RE generation technology, is deducted, taking into account the effects of future RE installation capacity. Other deductions include marketing costs for RE prognosis errors or for balancing energy

demands, as well as costs for production risks associated with VRE generation. On the contrary, the characteristics of green electricity positively influence prices and can be quantified through the price of certificates of origin. [126]

3. Methodology

The focus of this dissertation is to identify energy system configurations for decarbonised power supply for industrial flexumer applications, utilising flexibility options such as battery storage. At its core, this requires a framework to model industrial energy systems and optimise their energy flows. For this purpose, we develop the **F**ramework for **O**ptimising Sector-**C**oupled **U**rban Energy **S**ystems (FOCUS). It uses the principle of mixed-integer linear programming (MILP) and the Python programming language. For designing the optimisation problem, we specifically use the Pyomo package [131]. Gong et al. describe the basic concept of the FOCUS framework that aims at building models from the prosumer to the city district scale [132]. However, in the scope of this dissertation, we solely focus on the prosumer level. Section 3.1 presents the development of the basic prosumer model, which can be applied to any prosumer application. In Section 3.2, we transform the prosumer into a flexumer model by implementing a value stacking model for battery storage systems. Section 3.3 contains implementations of additional tools required by the FOCUS framework.

3.1. FOCUS - prosumer model

The prosumer model of the FOCUS framework features a modular structure. The structure is based on the concept of object-oriented programming. This includes a class structure that uses inheritance to create objects with different characteristics. Figure 8 provides an overview of the prosumer model's structure. The prosumer class forms the core of the model. Its objects define the main characteristics of a prosumer and process the input data. Implemented characteristics include the prosumer configuration, comprising installed technical components, their interconnections, and the overall optimisation strategy and settings. After creating a prosumer object, it instantiates the component classes and the energy management system (EMS) class. Component classes can be used to model any energy conversion or storage components, as well as structural components required by a prosumer. The component library in Subsection 3.1.2 gives an overview of available component classes. The EMS class is the central element of the optimisation. It contains the objective function, which defines the quantity to be minimised or maximised. In a last step, we pass the prosumer model to a solver. For all optimisations in this dissertation, the GUROBI solver [133] with academic licence is used. The solver returns the optimal solution, including optimised component sizes and energy flows between components.

In the following, we use the structure shown in Figure 8 to set up a realistic optimisation procedure that accounts for the temporal component. When it comes to complex industrial prosumers, solving the entire optimisation problem as a single entity is challenging, given limited computational power. Therefore, we choose to implement a two-layer approach,

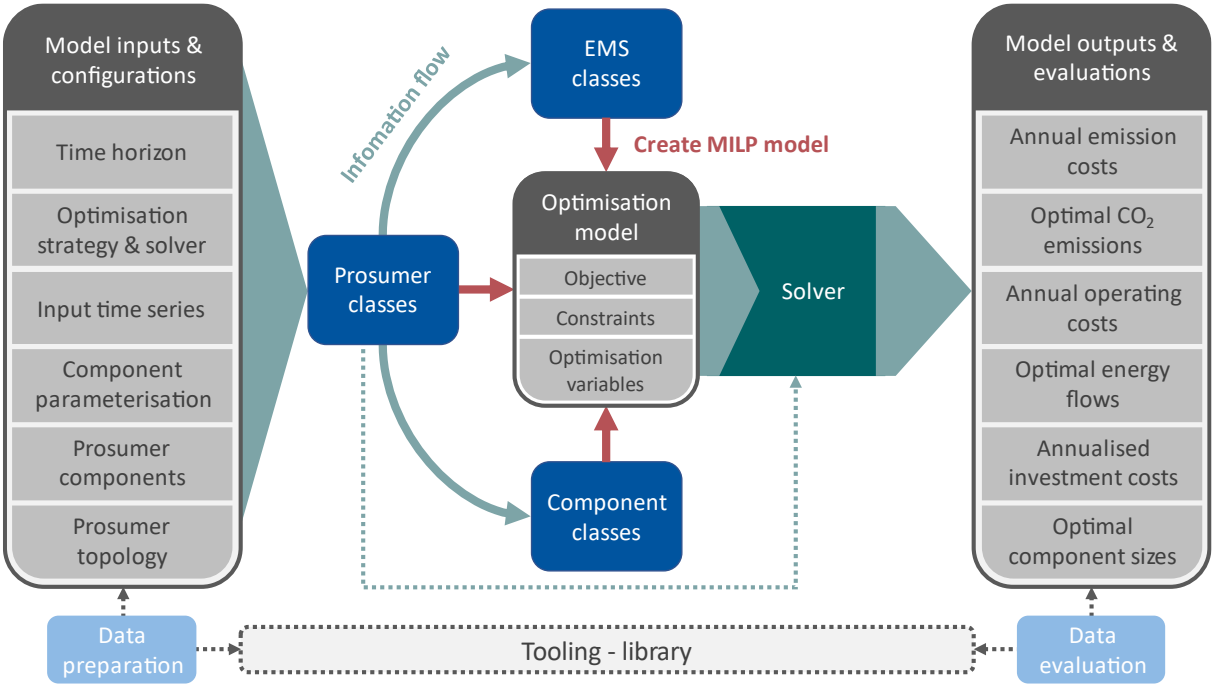

Figure 8: Visualisation of the basic structure of the FOCUS prosumer model, including information flows and creation of the optimisation model by using the Pyomo package. Own illustration based on [123].

separating component sizing from the operation of the energy system (see Figure 9). In the following, we refer to the sizing and operating layer.

The output of the sizing layer is the optimised sizes of components, which include energy conversion and storage components. To obtain realistic results, especially for long-duration storage sizing, it is necessary to optimise over a 1-year period. This is highly complex, as the size of the optimisation problem increases linearly with the number of time steps. Therefore, we take several measures to reduce complexity. On the one hand, simplified component models are used whenever possible. This includes the fact that most components have only one fixed efficiency. On the other hand, we try to increase the model time step length by aggregating timesteps whenever possible. Subsection 3.3.2 describes the algorithm for time step aggregation.

The operating layer receives the optimised component sizes and storage levels from the sizing layer. In contrast to the sizing layer, which assumes simplified conditions, the operating layer aims to produce results closer to real operation. Therefore, a so-called rolling horizon (RH) approach is implemented as described in Subsection 3.1.5. This approach cuts the one-year optimisation problem into multiple smaller sub-problems and solves them individually. This reduction in model size enables the use of more detailed component models.

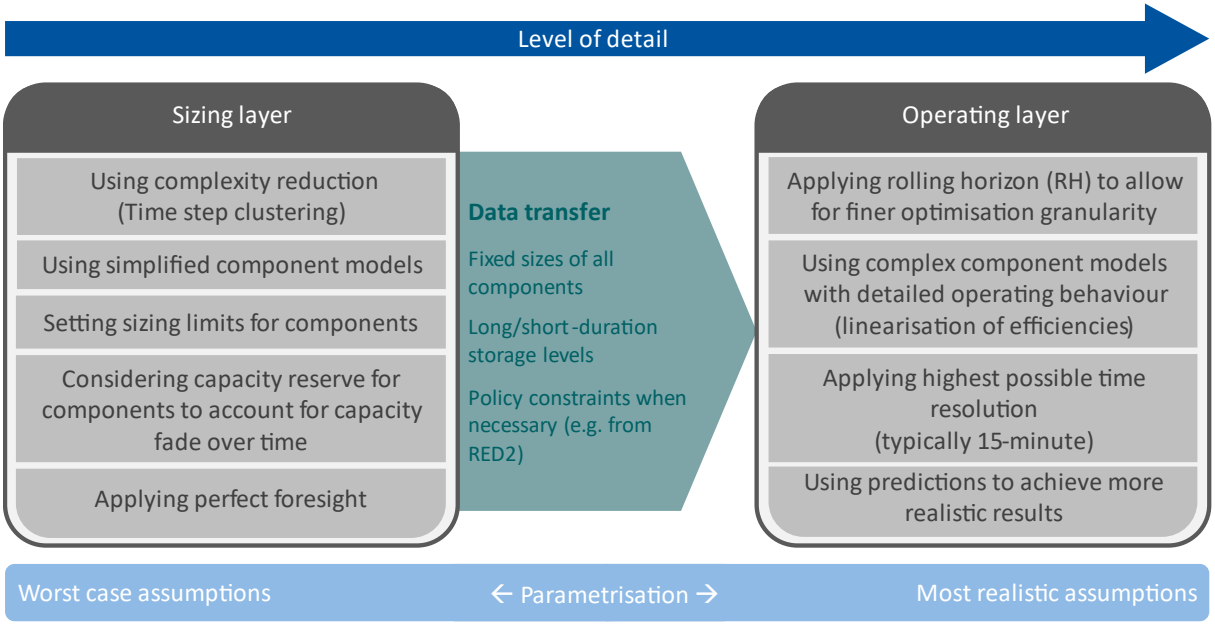

Figure 9: Comparison of the sizing and operating layer of the FOCUS prosumer model. The sizing layer is always optimised before the operating layer to determine component sizes, among others.

3.1.1. Prosumer class

The prosumer class provides the basic structure to model any kind of prosumer application. It consists of several methods that are summarised in Table 7. The creation of a prosumer class object activates the initialisation method *(__init__)*. As input, it receives the following list of variables:

- *name*: unique identifier for each prosumer object/scenario
- *configuration*: prosumer layout consisting of several dictionaries and variables
- *profiles*: dictionary containing time series for all required profiles
- *t_start*: time stamp for starting date (format: “YYYY-MM-DD hh:mm:ss”)
- *t_step*: list of all time step lengths for the optimisation
- *mode*: string that distinguishes between sizing or operating layer (see Figure 9)

From the *configuration* variable, the initialisation function extracts *components*, *connections*, global variables, and *services*. The *components* dictionary includes one entry for each installed component. Each component must have the following standard parameters:

- *type*: name of the implemented component type
- *model*: name of the predefined parameterisation model for the specified type
- *min_size*: minimal size of the component in kW (converters) or kWh (storage)
- *max*_size: maximum size of the component in kW (converters) or kWh (storage)

Table 7: Relevant methods of the FOCUS prosumer class that contain the core implementations to create any kind of prosumer object.

Call hierarchy	**Name**	**Input variables**	**Purpose**
1	__init__()	*name = {str}:* unique identifier *configuration = {dict}:* prosumer layout *profiles = {dict}*: input time series *t_start = {timestamp}*: starting date *t_step = {list}*: length of time steps *mode = {str}*: sizing or operation mode	Initialisation of the Prosumer class object
2	optimise_sizing()	*strategy_name = {str}*: optimisation strategy *solver_name = {str}*: name of solver *mip_gap = {float}:* min. quality of solution *presolve = {int}:* use presolve model *int_feas_tol = {float}:* feasible tolerance *time_limit = {int}:* time limit in seconds	Controls/executes the optimisation of the sizing layer
2	optimise_operation()	*strategy = {str}*: optimisation strategy *solver_name = {str}*: name of solver *mip_gap = {float}:* min. quality of solution *presolve = {int}:* use presolve model *int_feas_tol = {float}:* feasible tolerance *time_limit = {int}:* time limit in seconds *t_overlap_default = {int}*: overlap RH *t_interval_default = {int}*: length RH interval *t_perfect_foresight = {int}*: steps with perfect foresight for RH *initial_rsl = {Dataframe}*: results from sizing	Controls/executes the optimisation of the operating layer
3	build_sizing_model()	*strategy_list = {list}*: optimisation strategies	Controls the creation of the sizing model
3	build_rolling_model()	*time_steps = {list}*: time steps of RH interval *t_perfect_foresight = {int}*: steps with perfect foresight for RH *initial_rsl = {Dataframe}*: results from sizing *fixed_rsl = {Dataframe}*: RH results from previous interval *strategy = {list}*: optimisation strategies	Controls the creation of the operation model
4	add_flow_variables()	*model = {ConcreteModel}*: Pyomo model *var_dict = {dict}*: optimisation variables *prefix = {tuple}*: prefix to name constraint	Adds optimisation variables for all connections between components
4	add_connection_ constraints()	*model = {ConcreteModel}*: Pyomo model *var_dict = {dict}*: optimisation variables *prefix = {tuple}*: prefix to name constraint	Adds optimisation constraints for all connections between components
5	_extract_results()	*var_dict = {dict}*: optimisation variables *time_steps = {list}*: optimisation time steps	Generates a dataframe with the results of the optimisation
6	save_results()	*strategy = {str}*: optimisation strategy	Controls the saving of results to pkl and csv formats

In addition to these standard parameters, components can also have unlimited individual parameters (see Subsection 3.1.2). To create an energy system, components must be interconnected. All connections are specified in a *connections* list. A dictionary containing the following parameters describes each one-way connection:

- *from*: name of origin component
- *output*: integer that defines the origin component output connector to connect from
- *to*: name of destination component
- *input*: integer that defines the destination component input connector to connect to

To set up a complete prosumer model, additional global variables are needed. This can include financial constraints, prices, or emission factors. Mandatory constraints are the interest rate (*yearly_interest*) and the planning horizon (*planning_horizon*), which are required to calculate the annuities of components.
In contrast to all the previously mentioned configurations, the *services* dictionary is optional. Services include flexibility components, such as markets, to provide ancillary services to the electric power grid. In the *services* dictionary, single components can be linked to those services.

Once the prosumer class is initialised, we call its methods, shown in Table 7, in a defined order. First, the function *optimise_sizing()* is called, which controls the optimisation of the sizing layer. It calls the method *build_sizing_model(),* which is responsible for controlling the creation of the sizing model. This includes calling respective building functions within the component and energy management classes. Moreover, the flows between components are established in the optimisation model by calling the Prosumer methods *add_flow_variables()* and *add_connection_constraints()*. When the optimisation model is finalised, the method *optimise_sizing()* passes the model to the solver. Once we receive the optimal sizing result from the solver, the method *optimise_sizing()* calls the method *_extract_results()* that converts the solver results into a Pandas dataframe. This marks the end of the sizing layer and the beginning of the operating layer, which is started by calling the method *optimise_operation()*. This method receives the optimal sizing results and controls the operating layer. At its core, it cuts the optimisation problem into smaller pieces by applying the RH procedure. For each RH interval, it calls the method *build_rolling_model()* that creates the operation models equivalent to the procedure described for the sizing layer. In parallel, *optimise_operation()* continuously collects all RH operation results into a single Pandas dataframe. In the last step, the method *save_results()* separately converts the sizing and operation results to pkl or csv format and saves them to the desired path.

3.1.2. Component library

One core element of modelling prosumer behaviour is enabling realistic modelling of technical components. The FOCUS framework's component library serves this purpose. The modular structure of the library is designed to allow for the modelling of all relevant energy conversion, energy storage, or structural components. We achieve modularity by applying the inheritance principle, the main principle of object-oriented programming. The parent component class is called *AbstractComponent* (inheritance level 0). It serves as a basic building block for all other component classes that inherit from it. When creating any component object, the *AbstractComponent* class initialises the following list of variables:

- *name*: unique identifier of component
- *type*: component type
- *input_commodity_1/2*: commodities are allocated to inputs 1 and 2
- *output_commodity_1/2*: commodities are allocated to outputs 1 and 2
- *min_size*: minimum size of component
- *max_size*: maximum size of component
- *predictions*: dictionary with predictions for time series

The core method of the *AbstractComponent* class is *build_model()*. It calls the methods *_add_variables()* and *_add_constraints*, which exist in any component class, to add optimisation variables and constraints, respectively. From the *AbstractComponent* class, we inherit the base component classes (inheritance level 1). From the base classes, more specific component classes can be inherited (inheritance level 2). Figure 10 gives an overview of the implemented inheritance levels and component classes.
The most commonly used base component class is *BaseComponent*. All generation and energy conversion components inherit from this class. Its main characteristic is that it features at least one input and one output variable linked by a mathematical equation that replicates the physical behaviour of the corresponding component. On the contrary, the *BaseConsumption* component class has no output variable and acts as a sink with an underlying demand characteristic. Moreover, to connect the prosumer to any external energy supply network, such as public grids, we introduce a *BaseGrid* class. This class usually has one input and one output variable and enables buying or selling energy to the external supply network at different prices. The remaining two classes are a balancing node, represented by the *BaseBusBar* class, and the *BaseStorage* class, which we use for modelling any kind of storage component. In contrast to the *BaseComponent* class, the *BaseStorage* class has only one input and one output variable, with a possible time lag between them, depending on the storage's energy capacity.

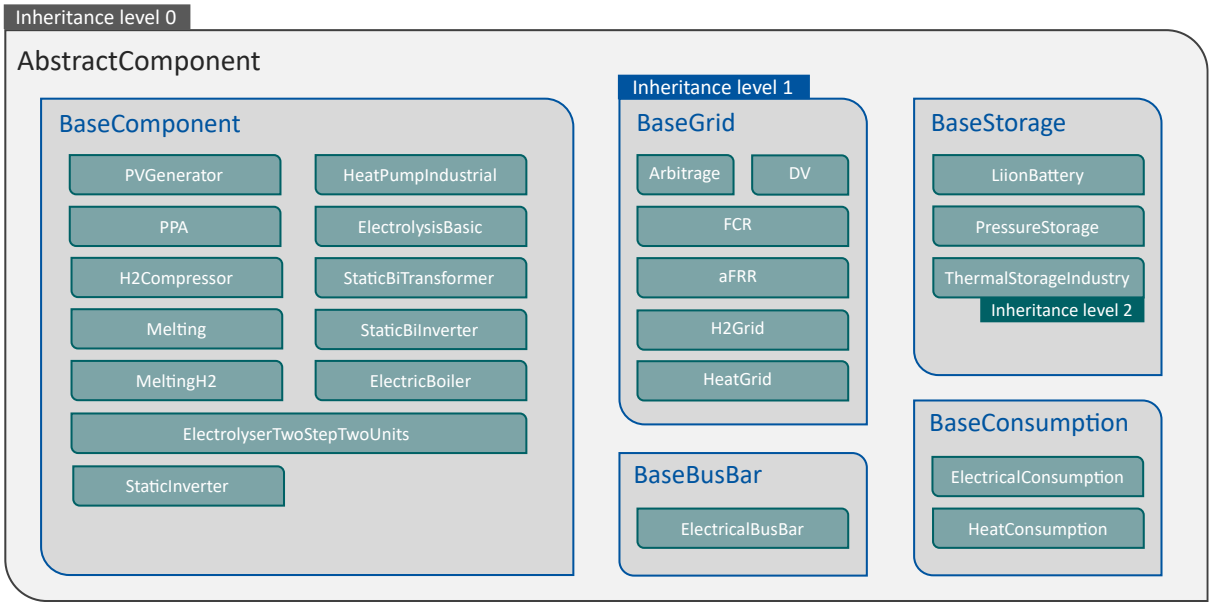

Figure 10: Inheritance structure of the component library of the FOCUS framework consisting of three levels. The illustrated boxes all represent individual class structures. EMS components are not part of the inheritance structure and function as independent components.

From the component base classes, we inherit the specific component classes, which are referred to as component types in the following. The component types are classified by sector/commodity, with the output variable determining which sector they are assigned to. While this dissertation focuses on the electricity, hydrogen, heat, and gas sectors, other sectors can be added to the component library. The component types can be understood as envelopes that have to be filled with parameterisation data. Therefore, for each component type, multiple parameterisations (models) exist that can differently shape the components' characteristic behaviour. For many components, a simplified model is used in the sizing layer to reduce complexity. The full model is typically used for the operating layer. Table 8 summarises all relevant component classes that inherit from the base classes.

In the following, we describe in detail the most important mathematical equations of component classes. In the programme code, the naming of optimisation variables and constraints follows a clear structure. In this dissertation, however, to be as compact as possible, we use simple formula letters for the variable names. Therefore, Table 22 in Appendix A provides a translation between programme code optimisation variable names and the formula letters used in the following for the mathematical description of components. In addition, the table lists all other modelling variables we use to formulate the constraints.

Table 8: List of implemented relevant component types that are part of the FOCUS framework component library. With the component types, specific component models can be parameterised, some of which are listed as examples.

Base class	**Component classes (types)**	**Component parameterisations (models) - exemplary**	**Input/output commodities** Input 1: commodity_1 (In1) Input 2: commodity_2 (In2) Output 1: commodity_3 (Out1) Output 2: commodity_4 (Out2)			
			electricity	*hydrogen*	*heat*	*gas*
Base Component	PVGenerator	PV_ROOF_L	Out1			
	PPA	PPA_PAP_PV PPA_PAP_WIND_OFFSHORE PPA_PAP_WIND_ONSHORE PPA_BASELOAD	Out1			
	GridConnectionPointMV	GCPMW	1,2 | 2,1			
	StaticInverter	INVPV	1 | 1			
	StaticBiInverter	INVBAT, INVBAT_SIMPLE	1,2 | 2,1			
	StaticBiTransformer	TR1	1,2 | 2,1			
	ElectrolysisBasic	PEM_BASIC, AWE_BASIC	In1	Out1	Out2	
	Electrolyzer2Step2Units	PEM_2STEP, AWE_2STEP	In1	Out1	Out2	
	H2Compressor	H2COMP	In1	Out1		
	HeatPumpIndustrial	INDUSTRY_HP	In1		Out1	
	Melting	MELT	In1			In2
	Melting_H2	MELT_H2_8MWel, MELT_H2_12MWel, MELT_H2_20MWel	In1	In2		
	ElectricBoiler	BOI2	In1		Out2	
Base Consumption	ElectricalConsumption	CNS1	In1			
	HeatConsumption	TDS			In1	
Base Grid	Arbitrage	ARB_SIMPLE_BUY_FIX	1 | 1			
	DirectMarketing	DM	1 | 1			
	FCR	FCR, FCR_SIMPLE	1 | 1			
	aFRR	aFRR, aFRR_SIMPLE	1 | 1			
	H2Grid	H2G1, H2_SLACK		1 | 1		
	HeatGrid	HG1			1 | 1	
	GasGrid	GAS1				1 | 1
BaseBusBar	ElectricalBusBar	ELEC_BUSBAR, BLCE_GROUP_SIMPLE	1 | 1			
Base Storage	LiionBattery	LFP	1 | 1			
	PressureStorage	PST1		1 | 1		
	ThermalStorageIndustry	THERM_STORAGE			1 | 1	

BaseComponent

This class adds three main optimisation variables. This includes two unbounded variables for each input and output power, as well as a nominal power variable (P_N). Two basic optimisation constraints are added. The first constraint in Eq. (3.1) ensures that the input is no greater than the maximum capacity. For the sizing layer of the model, a capacity reserve ($r_{cap,res}$) can be optionally added. The second constraint in Eq. (3.2) connects the input and output power with a simple efficiency η. Another optional constraint allows for discrete sizing (3.3). Apart from energy-related constraints, we need to factor in component investment costs as indicated by Eq. (3.4). The *BaseComponent* class features capital costs, which include annuities for the investment and fixed operational costs with a factor ($f_{fix,op}$) of investment costs (3.5). For annuities, we calculate the annuity factor (ANF) that is multiplied by the net present value of the investment. Moreover, additional factors for replacement and residual values are taken into account. Appendix E contains a more detailed description of financial calculations.

$$P_{in1,t}^{m1} \leq P_N^{m1} \;\Big|\; P_{in1,t}^{m1} \leq P_N^{m1} * \left(1 + r_{cap,res}\right) \quad \forall t \in T \tag{3.1}$$

$$P_{out1,t}^{m2} = P_{in1,t}^{m1} * \eta \quad \forall t \in T \tag{3.2}$$

$$P_N^{m1} = n_{discr} * P_{discr} \tag{3.3}$$

$$\kappa_{capex} = \kappa_{inv} * P_N^{m1} * \left(ANF + f_{fix,op} + f_{replace} + f_{residual}\right) \tag{3.4}$$

BaseConsumption

Consumption components require only one optimisation variable for their input. Eq. (3.5) describes the constraint that links the input to the time series for consumption. The class does not feature any cost-related constraints.

$$P_{in1,t}^{m1} = P_{load,t}^{m1} \quad \forall t \in T \tag{3.5}$$

BaseGrid

Grid connections for prosumers should be bidirectional, allowing them to draw power from the grid or inject power into it. As with the *BaseComponent* class, we define two unbounded optimisation variables for input and output power, and one bounded optimisation variable for the nominal power capacity. One condition is that the input and output variables must have the same commodity. For constraints, we use the identical formula as in Eq. (3.1) and add another constraint for the output in Eq. (3.6) to account for the possibility of flows in both directions. In addition, the model must prevent flows in opposite directions simultaneously (bidirectional flows), which is physically impossible. Therefore, the constraints in Eq. (3.7) and Eq. (3.8) add a limitation on bidirectional flows by using a set of two binary variables. Eq. (3.7)

ensures that only one binary variable is in an active state (equalling 1) at the same time. The global variable M describes a large number, referred to as big-M [134], which ensures unambiguousness. Finally, we consider cost constraints for the *BaseGrid* class. For capital costs, it uses the same implementation as in the *BaseComponent* class, as described in Eq. (3.9). However, the most relevant costs are the operating costs associated with purchasing energy from and selling energy to the grid. As an alternative to fixed prices, time-dependent variable prices can be used by passing a Pandas Series of prices instead of a float value.

$$P_{out1,t}^{m1} \leq P_N^{m1} \quad \forall t \in T \tag{3.6}$$

$$z_{in1,t} + z_{out1,t} \leq 1 \quad z \in \{0,1\}, \forall t \in T \tag{3.7}$$

$$P_{in1,t}^{m1} \leq z_{in1,t} * M * P_{N,max} \mid P_{out1,t}^{m1} \leq z_{out1,t} * M * P_{N,max} \quad \forall t \in T \tag{3.8}$$

$$\kappa_{opex,buy,sell,fix} = P_{out1,t}^{m1} * \pi_{buy}^{m1} + P_{in1,t}^{m1} * \pi_{sell}^{m1} \tag{3.9}$$

$$\kappa_{opex,buy,sell,var} = P_{out1,t}^{m1} * \pi_{buy,t}^{m1} + P_{in1,t}^{m1} * \pi_{sell,t}^{m1} \tag{3.10}$$

BaseStorage

To add flexibility to the prosumer energy system, we implement a basic class for storage components. Equivalent to the *BaseComponent* and *BaseGrid* classes, the *BaseStorage* class includes two unbounded optimisation variables for input and output. For capacity, however, we add a bounded variable for nominal energy capacity instead of power capacity. In addition, the storage model requires an additional unbounded optimisation variable for the storage level, referred to as the state-of-energy (SOE). In Eq. (3.9), we formulate the power capacity constraints on the storage's input and output powers. They ensure that input and output power remain within the specified limits. The calculation of the boundaries accounts for limitations imposed by efficiencies (η) and energy-to-power ratios (EPR). On the contrary, the constraints in Eq. (3.12) ensure that the SOE is always above a lower (SOE_{min}) and below an upper (SOE_{max}) threshold. Another mandatory constraint for energy storage is the energy conservation constraint in (3.13), which calculates the SOE at each time step based on input and output energy flows and the self-discharge rate ($\eta_{self,dch}$). To ensure that the storage is not charged and discharged at the same time, the constraints in Eq. (3.7) and (3.8) of the *BaseGrid* class are equally implemented. In addition, we add an optional negative penalty to maximise the storage level at each time step, as in Eq. (3.14), which is used only for hydrogen pressure and thermal storage in this dissertation. For capital cost, the class features the identical implementation as in the *BaseComponent* class, as described in Eq. (3.9).

$$P_{in1,t}^{m1} * \eta_{in} \leq \frac{C_N^{m1}}{EPR_{in}} \quad | \quad \frac{P_{out1,t}^{m1}}{\eta_{out}} \leq \frac{C_N^{m1}}{EPR_{in}} \quad \forall t \in T \tag{3.11}$$

$$E_t \geq E_{min} = SOE_{min} * C_N^{m1} \quad | \quad E_t \leq E_{max} = SOE_{max} * C_N^{m1} \quad \forall t \in T \tag{3.12}$$

$$E_t = E_{t-1} * \eta_{self,dch} + P_{in1,t}^{m1} * \eta_{in} * t_{\Delta,t} - P_{out1,t}^{m1} * \frac{1}{\eta_{out}} * t_{\Delta,t} \quad \forall t \in T \tag{3.13}$$

$$\kappa_{opex,pen,t} = -E_t \tag{3.14}$$

With this basic implementation of the *BaseStorage* class, we can realistically model a wide range of storage applications. However, the performance of many storage technologies, for instance battery storage, depends on degradation behaviour. Calendar ageing can already be reduced by setting appropriate parameters for the introduced SOE limits (3.12). However, the model does not yet consider cyclic ageing. Therefore, we implement an additional cycle limitation constraint according to Eq. (3.15). It limits the cycles by calculating the available share of possible cycles from the total available cycles (L_{cycle}). This share is proportional to the duration of the optimisation horizon with respect to the total available calendar lifetime ($L_{calendar}$). In addition to the regular cycling of the storage, we optionally add a variable for hidden cycling for ancillary services (P_{hidden}) as defined in Subsection 3.2.4.

$$\frac{L_{cycle}}{L_{calender}} * \frac{\sum t_{\Delta,t}}{8760\ h} * 2C_N^{m1} \geq \sum_{t \in T} \left(P_{in1,t}^{m1} * \eta_{in} + P_{out1,t}^{m1} * \frac{1}{\eta_{out}} + P_{hidden,t}^{\pm} \right) * t_{\Delta,t} \tag{3.15}$$

BaseBusBar

This component class serves as a structural element, aggregating multiple components into a single entity. It is similar to the *BaseGrid* class and features one input and output optimisation variable that requires the same commodity. The difference, however, is that pricing on the input and output is not possible, and there is no clear definition of the direction of the flows.

$$P_{out1,t}^{m1} = P_{in1,t}^{m1} \quad \forall t \in T \tag{3.16}$$

3.1.3. Detailed component modelling

From the basic components in Subsection 3.1.2, we can derive more detailed and specific component classes. However, all specific components inherit from a basic component and thus inherit its functionality until overwritten. For most specific components, this only includes small, relevant changes to adjust component behaviour to the desired output. In the following, we show the detailed modelling for only those specific component classes that feature relevant changes compared to the base component classes. Furthermore, in this subsection, we exclude the ancillary service classes *FCR* and *aFRR* as well as the wholesale *arbitrage* class, as Section 3.2 focuses specifically on those components.

PVGenerator (BaseComponent)

This class features different implementations for PV systems. In the scope of this dissertation, we do not consider the irradiance-based model and solely use the capacity factor (CF)-based model. The CF-based model requires the equivalent relationship between output and nominal capacity as described in Eq. (3.6). In addition, the constraint in Eq. (3.17) defines how the output energy depends on the CFs. This definition allows for curtailment of generated PV electricity.

$$P^{el}_{gen,PV,t} = P^{el}_{out1,t} \leq P^{el}_{N} * CF_{PV,t} \quad \forall t \in T \tag{3.17}$$

PPA (BaseComponent)

PPAs are one contracting option for industrial prosumers to exploit green renewable electricity directly from external PV, WPP, hydropower, or other RE generators. The *PPA* class allows for the inclusion of such external renewable electricity generation. The implementation is similar to the *PVGenerator* class. However, we need to account for an efficiency loss in electricity transmission and distribution and introduce a pricing option. Eq. (3.18) describes the efficiency loss (a modification of Eq. (3.17)), while Eq. (3.19) models a constant purchase price for generation from PPAs. Furthermore, unlike the *PVGenerator* class, the constraint in Eq. (3.18) does not allow any PPA curtailment; however, the PPA's availability can be varied with the CF parameter.

$$P^{elec}_{gen,PPA,t} = P^{el}_{out1,t} = P^{el}_{N} * CF^{el}_{t} * \eta_{tr,distr} \quad \forall t \in T \tag{3.18}$$

$$\kappa_{opex,contr,PPA} = P^{el}_{out1,t} * \pi_{PPA,contr} * t_{\Delta,t} \quad \forall t \in T \tag{3.19}$$

StaticBiInverter and GridConnectionPointMV (BaseComponent)

In prosumers with RE generators, often a conversion between direct current (DC) and alternating current (AC) is necessary. Inverters serve this purpose. In the *StaticBiInverter* class, we add a bidirectional inverter to the component library for use with battery storage. The class features two inputs and two outputs. The constraints in Eq. (3.20) connect inputs and outputs with a fixed efficiency. Other constraints equivalent to those in *BaseGrid* in Eq. (3.8) impose a bidirectional flow limitation, ensuring that we can use the inverter in only one direction at a time. The same model is used for the *GridConnectionPointMV* class, which allows for modelling a GCP. It also requires limiting bidirectional flows to avoid circular energy flows in the model.

$$P^{el}_{out1,t} = P^{el}_{in2,t} * \eta_{inv} \mid P^{el}_{out2,t} = P^{el}_{in1,t} * \eta_{inv} \quad \forall t \in T \tag{3.20}$$

ElectrolysisBasic and Electrolyser2Step2Units (BaseComponent)

The decarbonisation of industrial prosumers often comes with a fuel switch from NG to hydrogen. This, for instance, is necessary for the glassworks use case in this dissertation, which requires high melting temperatures and thus a high energy density of the energy carrier used. As hydrogen is not widely available today, electrolysis systems can be a solution to produce green hydrogen. Therefore, with a more simplistic approach in class *ElectrolysisBasic* and a more detailed approach in class *Electrolyser2Step2Units,* we implement two models for electrolyser systems. The simplistic model requires only a few constraints. The constraint in Eq. (3.21) adds a calculation for hydrogen output using a simple efficiency factor applied to the electricity input. Equally, the constraint in Eq. (3.22) defines the waste heat output as the difference between the total and hydrogen efficiencies. Another particularity of the electrolysis system models is that, for capital expenditures, we separate costs into periphery and stack-related components, as they have different lifetimes. The stack's lifetime in years is calculated according to Eq. (3.23). This leads to different annuity factors, replacement costs, and residual values as indicated by Eq. (3.24).

$$P_{out1,t}^{H2} = P_{in1,t}^{el} * \eta_{el,H2} \tag{3.21}$$

$$P_{out2,t}^{Heat} = P_{in1,t}^{el} * \left(\eta_{el} - \eta_{el,H2}\right) \tag{3.22}$$

$$L_{stack} = \frac{T_{stack,life,hours}}{8760 * (1 - p_{off,min})} \tag{3.23}$$

$$\begin{aligned} \kappa_{capex} &= \kappa_{capex,periphery} + \kappa_{capex,stack} \\ &= \kappa_{inv,periphery} * P_N^{m1} * \left(ANF_p + f_{fix,op,p} + f_{replace,p} + f_{residual,p}\right) \\ &\quad + \kappa_{inv,stack} * P_N^{m1} * \left(ANF_s + f_{fix,op,s} + f_{replace,s} + f_{residual,s}\right) \end{aligned} \tag{3.24}$$

Based on the simplistic electrolyser system model used for the sizing layer of the optimisation, the class *Electrolyser2Step2Units* adds a more complex approach for the operating layer. More detailed modelling is required to account for the comparatively slow dynamics and the specific efficiency curves of electrolysers in real operation. For the more complex approach, we follow the recommendations of Baumhof et al. [135]. In a first step, using three binary variables, we define three possible operational states: off-mode, standby-mode, and on-mode. Eq. (3.25) ensures that the electrolyser system can only be in one state at a time. Eq. (3.26) defines valid power states or ranges for the respective mode. The constraints in (3.27)-(3.30) ensure that the binary variables take on the desired power states and ranges. Moreover, to account for the modularity of an electrolysis system, we model two identical units. All equations below are only describing one of the two identical units, which is why the nominal system power is always divided by two.

$$z_{off,t} + z_{standby,t} + z_{on1,t} + z_{on2,t} = 1 \quad z \in \{0,1\}, \forall t \in T \tag{3.25}$$

$$P_{off} = 0 \quad \Big| \quad P_{standby} = \frac{P_N^{el}}{2} * p_{standby} \quad \Big| \quad P_{on,startup} = \frac{P_N^{el}}{2} * p_{on,startup}$$
$$P_{on,upper} = \frac{P_N^{el}}{2} * p_{on,upper} \quad \Big| \quad P_{on,lower} = \frac{P_N^{el}}{2} * p_{on,lower} \tag{3.26}$$

$$z_{off,t} \leq \frac{-P_{in1,t}^{el}}{M} + 1 \quad \forall t \in T \tag{3.27}$$

$$z_{standby,t} \leq \frac{P_{in1,t}^{el} - P_{standby}}{M} + 1 \;\mid\; z_{standby,t} \leq \frac{P_{standby} - P_{in1,t}^{el}}{M} + 1 \quad \forall t \in T \tag{3.28}$$

$$z_{on1,t} \leq \frac{P_{in1,t}^{el} - P_{on,upper}}{M} + 1 \;\mid\; z_{on1,t} \leq \frac{P_{on,startup} - P_{in1,t}^{el}}{M} + 1 \quad \forall t \in T \tag{3.29}$$

$$z_{on2,t} \leq \frac{P_{in1,t}^{el} - P_{on,lower}}{M} + 1 \;\mid\; z_{on2,t} \leq \frac{P_{on,upper} - P_{in1,t}^{el}}{M} + 1 \quad \forall t \in T \tag{3.30}$$

For the defined operating modes, we can define the hydrogen output of the electrolysis system. For off- and standby-mode, we define the hydrogen output as zero as indicated in Eq. (3.31). In on-mode, in contrast to the implementation in class *ElectrolysisBasic*, the class *Electrolyser2Step2Units* features a linearised efficiency with three interpolation points, resulting in two linearisation areas, as illustrated in Figure 11. We calculate the slopes $(m1, m2)$ according to Eq. (3.32) and Eq. (3.33) and use them to formulate the linearisation constraints to obtain electrolysis system hydrogen output (3.34).

$$P_{out1,t}^{H2} * z_{off,t} = 0 \;\mid\; P_{out1,t}^{H2} * z_{standby,t} = 0 \quad \forall t \in T \tag{3.31}$$

$$m1 = \frac{P_{on,startup} * \eta_{on,startup} - P_{on,upper} * \eta_{on,upper}}{P_{on,startup} - P_{on,upper}} \tag{3.32}$$

$$m2 = \frac{P_{on,upper} * \eta_{on,upper} - P_{on,lower} * \eta_{on,lower}}{P_{on,upper} - P_{on,lower}} \tag{3.33}$$

$$P_{out1,t}^{H2} \leq \left(P_{in1,t}^{el} * m1 + P_{on,startup} * \eta_{on,startup}\right) * \eta_{on,N} * z_{on1,t} \quad \forall t \in T$$
$$P_{out1,t}^{H2} \leq \left(P_{in1,t}^{el} * m2 + P_{on,lower} * \eta_{on,lower}\right) * \eta_{on,N} * z_{on2,t} \quad \forall t \in T \tag{3.34}$$

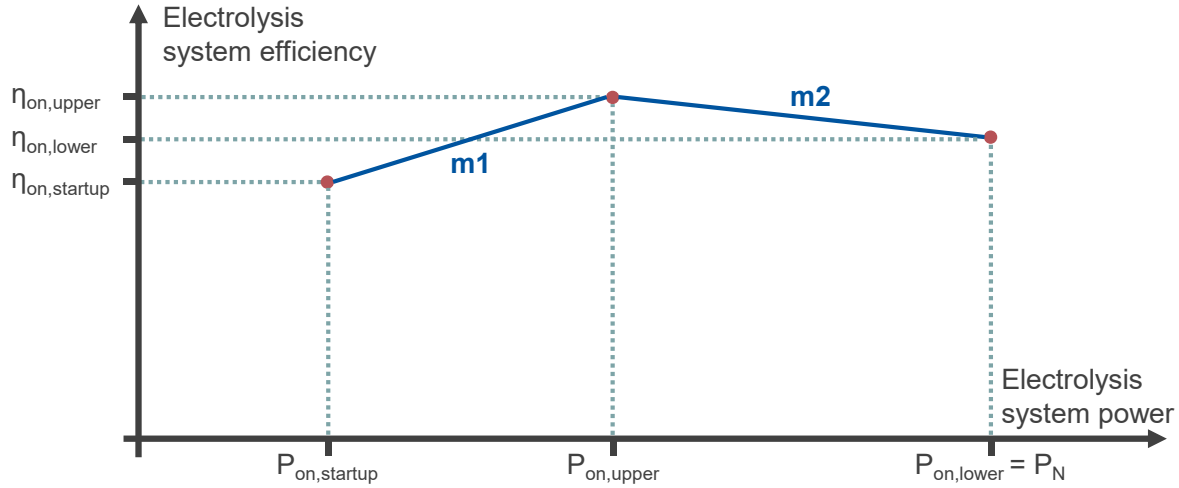

Figure 11: Schematic illustration of the linearisation process for the electrolysis system efficiency curve during on-mode in the FOCUS framework. The method considers three characteristic efficiency points similar to the description in [135].

Another important characteristic of an electrolyser system is the cold-start behaviour from off-mode to on-mode. To detect the cold start state, we introduce an additional binary variable. The variable is potentially activated when the electrolyser system is switched on and has not been in on- or standby-mode in the previous time step (3.35). The constraints in Eq. (3.36) narrow this down by ensuring that, before a cold start, the electrolyser system is tuned off. Moreover, they ensure that an off and cold start mode cannot occur simultaneously, and that it is not possible to go from off to standby mode. Finally, we consider an increased ramp-up time for electrolyser systems with the constraint in Eq. (3.37) that limits the input power during cold start to a percentage ($p_{ramp,cold}$) of nominal input power.

$$z_{cold,t} \geq z_{on1,t} + z_{on2,t} - z_{on1,t-1} - z_{on2,t-1} - z_{standby,t-1} \qquad z \in \{0,1\}, \forall t \in T \qquad (3.35)$$

$$z_{cold,t} \leq z_{off,t-1} \mid z_{cold,t} + z_{off,t} \leq 1 \mid z_{standby,t} + z_{off,t-1} \leq 1 \quad \forall t \in T \qquad (3.36)$$

$$\frac{P_N^{el}}{2} - P_{in1,t}^{el} \geq z_{cold,t} * p_{ramp,cold} * \frac{P_N^{el}}{2} \quad \forall t \in T \qquad (3.37)$$

Furthermore, electrolysers have downtime that needs to be accounted for. The constraint in Eq. (3.38) ensures that the sum of time steps for off- and standby-mode is at least as high as the sum of availability (A) of the electrolysis system.

$$\sum_{t \epsilon T} z_{off,t} + \sum_{t \epsilon T} z_{standby,t} \geq \sum_{t \epsilon T} A_t \qquad (3.38)$$

Another modification in the *Electrolyser2Step2Units* class compared to the *ElectrolysisBasic* class is the calculation for waste heat output. The assumption with constraint (3.39) is that a certain percentage of waste heat ($p_{heat,loss}$) is non-recoverable. Furthermore, when the electrolyser system is not in on-mode, no heat output is possible according to the constraint in Eq. (3.40).

$$P_{out2,t}^{Heat} \leq P_{in1,t}^{el} * \left(1 - p_{heat,loss}\right) - P_{out1,t}^{H2} \quad \forall t \in T \tag{3.39}$$

$$P_{out2,t}^{Heat} \leq M * (z_{on1,t} + z_{on2,t}) \quad \forall t \in T \tag{3.40}$$

$$P_{out2,t}^{Heat} \geq M * \left(z_{on1,t} + z_{on2,t} - 1\right) + P_{in1,t}^{el} * \left(1 - p_{heat,loss}\right) - P_{out1,t}^{H2} \quad \forall t \in T \tag{3.41}$$

The last remaining implementation for the *Electrolyser2Step2Units* model concerns operational costs. Under current regulations, the electric power grid fees, levies, and taxes for the electrolysis system can be reimbursed, as we account for in Eq. (3.42). However, the reimbursement is only applied to selected scenarios as defined in Subsection 4.2.

$$\kappa_{opex,levy,tax} = -P_{in1,t}^{el} * \pi_{fee,levy,tax}^{el} \tag{3.42}$$

H2Compressor (BaseComponent)

Efficient storage of green hydrogen produced by the electrolyser system requires a compression unit to increase the energy carrier's volumetric energy density. For this purpose, the class *H2Compressor* models the required compressor unit to account for the additional energy consumption of the compression process. With the constraint in Eq. (3.43), we normalise the compressor size to the second input commodity, namely hydrogen. Furthermore, with the defined constraint in Eq. (3.44), we assume that the hydrogen input equals the hydrogen output, so no hydrogen losses occur. Finally, the constraint in Eq. (3.45) introduces a factor for electric power consumption in kW_{el} per compressed kWh_{H2} of hydrogen.

$$P_{in2,t}^{H2} \leq P_{N}^{H2} \quad \forall t \in T \tag{3.43}$$

$$P_{out1,t}^{H2} = P_{in2,t}^{H2} \quad \forall t \in T \tag{3.44}$$

$$P_{in1,t}^{el} = P_{in2,t}^{H2} * c_{cons}^{el} \quad \forall t \in T \tag{3.45}$$

Melting and MeltingH2 (BaseComponent)

The central component with the highest energy consumption of the glassworks use case in this dissertation is the melting furnace. We model this component with the *Melting* and *MeltingH2* classes. These very simplified representations do not consider thermodynamic

processes, as this is not the focus of this work. Instead, we connect the two input variables of the classes solely to two exogenous demands, as shown in Eq. (3.46). While the *Melting* class represents the fossil furnace with NG demand, *MeltingH2* receives a hydrogen demand instead.

$$P_{in1,t}^{el} = P_{load,t}^{el} \mid P_{in2,t}^{NG} = P_{load,t}^{NG} \mid P_{in2,t}^{H2} = P_{load,t}^{H2} \quad \forall t \in T \tag{3.46}$$

HeatPump (BaseComponent)

Industrial prosumers often have large waste-heat sources and process-heat demands. Specifically, in use cases involving an electrolysis system, waste heat utilisation can increase overall energy efficiency. The efficient exploitation of waste heat requires high-temperature HPs that convert waste heat at 70-80°C into industrial heat demand at around 100°C (see Subsection 4.1). To model this behaviour, we implement the *HeatPump* class. Eq. (3.47) defines the input and output of the system as connected via a variable efficiency, known as the coefficient of performance (COP). The COP depends on temperature levels, which we calculate outside the optimisation model using Eq. (2.1).

$$P_{out1,t}^{heat} = P_{in1,t}^{el} * COP_t \tag{3.47}$$

DM (BaseGrid)

The component for direct marketing (DM) (German: Direktvermarktung) serves as a sink for RE generation to account for compensation of electric power grid feed-in (see Subsection 2.4.1). The component uses only one input from the *BaseGrid* class and compensates for the energy inflow using a time-varying price defined by the constraint in Eq. (3.48). Moreover, power grid fees, levies, and taxes have to be applied when feeding into the public electric power grid.

$$\kappa_{opex,feed,DM,t} = -P_{in1,t}^{el} * \pi_{DM,t}^{el} * t_{\Delta,t} + \; P_{in1,t}^{el} * \pi_{fee,levy,tax}^{el} \quad \forall t \in T \tag{3.48}$$

3.1.4. Energy management system

Another type of component included in the FOCUS components library is the energy management system (EMS) components. EMS components are fundamentally different from other component types, as they do not fit the typical class-and-inheritance structure. Their purpose is to add the optimisation objective, for instance, minimisation of overall system costs or equivalent CO_2 emissions, or to add additional overall constraints that apply to the prosumer energy system. For this dissertation, we use 6 different EMS components. All EMS components are described in this subsection, except for the services EMS that are covered in detail in Subsection 3.2.4.

Main EMS (EnergyManagementSystem.py)

The purpose of the main EMS is to collect cost and CO_2 emission data from all existing components of the prosumer energy system and use them to formulate the objective function. For costs, we differentiate between capital expenditures (CAPEX) and operational expenditures (OPEX). OPEX mainly consist of energy purchasing costs ($\kappa_{opex,buy,sell}$), emission costs ($\kappa_{opex,em}$), penalty costs ($\kappa_{opex,pen}$), levy and taxes ($\kappa_{opex,levy,tax}$), and revenues from providing grid services ($R_{service}$). We can choose three optimisation strategies, of which we use only the first and second (S1 and S2) in this dissertation. However, the third strategy (S3) is included in the description for the sake of completeness:

- S1: *annuity*: minimisation of annuity
- S2: *annuity_with_peak_power_costs*: minimisation of annuity with consideration of peak power costs
- S3: *co2*: minimisation of equivalent CO_2 emissions

$$\mathrm{Obj}(S1, S2) = \min\left(\sum_{t\epsilon T}\sum_{c\epsilon C}\left[\kappa_{capex,c} + \kappa_{opex,c,t}\right]\right) \quad EUR \tag{3.49}$$

$$\mathrm{Obj}(S3) = \min\left(\sum_{t\epsilon T}\sum_{c\epsilon C} e_{c,t}\right) \quad tCO_2 \tag{3.50}$$

$$\kappa_{\mathrm{opex,c,t}}(S1) = \kappa_{opex,buy,sell,c,t} + \kappa_{opex,em,c,t} + \kappa_{opex,pen,c,t} + \kappa_{opex,levy,tax} + R_{service} \quad EUR \tag{3.51}$$

$$\begin{aligned}\kappa_{\mathrm{opex,c,t}}(S2) &= \kappa_{\mathrm{opex,c,t}}(S1) + \kappa_{opex,PP} \quad EUR \\ &= \kappa_{\mathrm{opex,c,t}}(S1) + \pi^{el}_{PP} * P^{el}_{gcp,max} \quad EUR\end{aligned} \tag{3.52}$$

$$R_{service} = \sum_{t\epsilon T}(R_{FCR,t} + R_{aFRR,t} + R_{arb,t}) \quad EUR \tag{3.53}$$

$$P^{el}_{max} \geq P^{el}_{in1,gcp,t} - P^{el}_{max,sizing} \;\mid\; \text{sizing layer: } P^{el}_{max,sizing} = 0 \tag{3.54}$$

$$\kappa_{opex,levy,tax} = \pi^{el}_{fee,levy,tax} * P^{el}_{in1,gcp} \tag{3.55}$$

where

t = time steps in optimisation interval T
e = equivalent CO_2 emissions
L = lifetime of components
i = interest rate for investment
c = conversion/storage components

P = power
R = revenue
κ = costs
π = price

As the definitions show, the strategies S1 and S2 in Eq. (3.49) are very similar. The only difference from S1 to S2 is that for commodity electricity, we add annual peak power costs as shown in Eq. (3.51) and (3.52). Annual peak power costs (κ_{PP}) are calculated by multiplying the maximum peak load within 15 minutes of one year at the electric power GCP ($P^{el}_{gcp,max}$) with the peak power price (π^{el}_{PP}). The maximum peak power is determined with the constraint in Eq. (3.54). For the operating layer of the model, we subtract the maximum peak power from the sizing layer to factor in only additional peak power. Another part of OPEX is energy-related grid fees, levies, and taxes for electricity. We calculate them for all imported electricity via the GCP in accordance with Eq. (3.55).

Green hydrogen production EMS (EnergyManagementSystemRED.py)

The regulations for green hydrogen production in Europe are defined by the RED II and III [21], as described in detail in Subsection 2.4.2. This requires additional constraints for the developed prosumer model to ensure temporal alignment between RE generation from PPAs and electrolysis system demand. The relevant granularity for the evaluations is hourly and monthly matching. In a first step, we define the sum of all generation from PPAs and RE onsite generation for a potential PV rooftop system available after the GCP, according to Eq. (3.56).

$$P^{el}_{PPA,sum,t} = \sum_{x \in PPA} P^{el}_{x,t} * \eta_{GCP} + P^{el}_{PV,roof,t} \quad \forall t \in T \tag{3.56}$$

Using the available generation from PPAs, we can define constraints on the potential PPA inflow to the battery inverter. This requires the definition of a positively bounded optimisation variable ($P^{el}_{PPA \rightarrow inv,bat,t}$). Eq. (3.57) states that the battery inverter PPA inflow must be less than or equal to the difference between the total available PPA generation and the electrolysis system's total consumption. In addition, we add the battery inverter PPA outflow to avoid infeasibility in the equation when the electrolysis system demand exceeds available generation from PPAs. Furthermore, we need to constrain the battery inverter PPA inflow to the maximum battery charging power and consider other potential inflows from ancillary services, including FCR and aFRR (for definitions see Subsection 3.2.2 and 3.2.3) as defined in Eq. (3.58). We can neglect wholesale energy in the constraints, as generation from PPA has priority, and wholesale power is distributed accordingly on the balance sheet.

$$P^{el}_{PPA \rightarrow inv,bat,t} \leq P^{el}_{PPA,sum,t} - P^{el}_{ely,in1} + P^{el}_{inv,bat \rightarrow PPA,t} \quad \forall t \in T \tag{3.57}$$

$$P^{el}_{PPA \rightarrow inv,bat,t} \leq P^{el}_{in1,inv,bat,t} - \left(P^{el}_{out1,FCR,t} + P^{el}_{out1,aFRR,t}\right) * \eta_{gcp} \quad \forall t \in T \tag{3.58}$$

In the next step, the PPA inflow to the battery inverter can be used to define a virtual energy level ($E_{bat,PPA,t}$) of the battery concerning stored generation from PPAs. This virtual energy level must always be lower than or equal to the actual energy level of the battery storage, as

defined by Eq. (3.59). As for the BaseStorage class in Eq. (3.13), we define an energy conservation constraint on the virtual energy level in Eq. (3.60).

$$E_{bat,PPA,t} \leq E_{bat,t} \quad \forall t \in T \tag{3.59}$$

$$\begin{aligned} E_{bat,PPA,t} = {} & E_{bat,PPA,t-1} * \eta_{self,dch} + P^{el}_{PPA\rightarrow inv,bat,t} * \eta_{inv,bat} * \eta_{in,bat} * t_{\Delta,t} \\ & - P^{el}_{inv,bat\rightarrow PPA,t} * \frac{1}{\eta_{inv,bat} * \eta_{out,bat}} * t_{\Delta,t} \quad \forall t \in T \end{aligned} \tag{3.60}$$

Similar to the inflow of generation from PPAs to the battery inverter, the outflow requires additional constraints. On the one side, we limit the PPA outflow to the available stored generation from PPAs by using the virtual storage level as defined in Eq. (3.61). On the other hand, the PPA outflow is limited by Eq. (3.62) to the battery inverter's total output power minus the activated output power for ancillary services, including FCR and aFRR.

$$P^{el}_{inv,bat\rightarrow PPA,t} \leq E_{bat,PPA,t} * \eta_{inv,bat} * \eta_{out,bat} * t_{\Delta,t} \quad \forall t \in T \tag{3.61}$$

$$P^{el}_{inv,bat\rightarrow PPA,t} \leq P^{el}_{out1,inv,bat,t} - \frac{\left(P^{el}_{in1,FCR,t} + P^{el}_{in1,aFRR,t}\right)}{\eta_{gcp}} \quad \forall t \in T \tag{3.62}$$

With knowledge of the PPA flows to the battery storage, we can construct a constraint to ensure RED II compatibility, as indicated in Eq. (3.63). This means we do not allow the electrolyser system's input power to exceed RE generation from PPAs (directly or via battery storage). Depending on the requirements of the RED II, this condition is ensured within the length of the correlation time interval (Δt). For instance, for hourly correlation, the condition is ensured for every hour ($T_{\Delta t}$) within the optimisation interval (T).

$$\sum_{t}^{t+\Delta t} P^{el}_{ely,in1,t} \leq \sum_{t}^{t+\Delta t} \left(P^{el}_{PPA,sum,t} + P^{el}_{inv,bat\rightarrow PPA,t}\right) \quad \forall t \in T, \forall \Delta t \in T_{\Delta t} \tag{3.63}$$

For the operating layer of the prosumer model, in the case of monthly correlation, another approach must be chosen, as the applied rolling horizon (see Subsection 3.1.5) is limited to a window of 24 hours. Therefore, we use the results of the sizing layer to define an upper threshold, as indicated in Eq. (3.64), that accounts for possible flexibility.

$$\sum_{t}^{t+\Delta t} P^{el}_{ely,in1,t} \leq \max\left(\sum_{t}^{t+\Delta t} P^{el}_{PPA,sum,t}\ , \sum_{t}^{t+\Delta t} P^{el}_{ely,in1,t,sizing}\right) \quad \forall t \in T, \forall \Delta t \in T_{\Delta t} \tag{3.64}$$

Direct marketing EMS (EnergyManagementSystemDM.py)

Direct marketing (DM) (German: Direktvermarktung) refers to a mechanism to regulate compensation for RE generators feeding into the electric power grid in Germany (see Subsection 2.4.1). The EMS for DM is mainly responsible for ensuring that the compensation is applied only to RE generation within the prosumer energy system. Eq. (3.65) ensures the validity of this criterion.

$$P_{in1,DM,t}^{el} \leq \sum_{r}^{R} P_{gen,r,t}^{el} \quad \forall t \in T \mid r \in R\{renewable\ generators\} \tag{3.65}$$

Thermal component sizing EMS (EnergyManagementSystemThermalSizing.py)

The sizing of thermal components can be highly sensitive when aiming to exploit waste heat potential. This is particularly the case when waste heat potential depends on the operation of other components or exhibits seasonal characteristics. Ensuring that the sizing of thermal components in the model's sizing layer is also feasible in the operating layer requires an additional sizing constraint. The critical point for supplying the thermal load is when it reaches the annual maximum. Therefore, in this case, we define that the thermal power rating of all heat-supplying components needs to be equal to the maximum load. For the glassworks use case, thermal conversion components include the electric boiler and industrial HP. Eq. (3.66) ensures that their rating equals the maximum annual thermal load.

$$P_{max}^{th} = P_{N,HP}^{th} + P_{N,e-boiler}^{th} \tag{3.66}$$

Battery sizing EMS (EnergyManagementSystemBatSizing.py)

For sizing the battery storage system, one important characteristic is the energy-to-power ratio (EPR). When considering ancillary services in the operating layer of the model, it is necessary to limit the EPR ratio in the sizing layer to a typical range to improve battery utilisation in the operating layer. As we separately model battery inverter and battery storage units, we formulate an additional constraint in Eq. (3.67) to ensure the EPR stays within the defined lower ($EPR_{bat,min}$) and upper ($EPR_{bat,max}$) bounds.

$$P_{N,inv,bat}^{el} \leq \frac{C_{N,bat}^{el}}{EPR_{bat,min}} \quad \Big| \quad P_{N,inv,bat}^{elec} \geq \frac{C_{N,bat}^{el}}{EPR_{bat,max}} \tag{3.67}$$

3.1.5. Rolling horizon approach

At the operating layer (see Figure 9), we intend to increase the modelling detail for components and the prosumer energy system to obtain results closer to real operation. This results in increased complexity of the optimisation model, pushing it to the limits of solvability. To overcome those computational limitations, we implement a so-called rolling horizon (RH)

approach, commonly used in the literature for MILP problems (see Subsection 2.1.1). The basic principle is to cut the optimisation problem into smaller pieces. Figure 12 shows the basic structure of this approach's implementation for our use case, including the most important variable definitions.

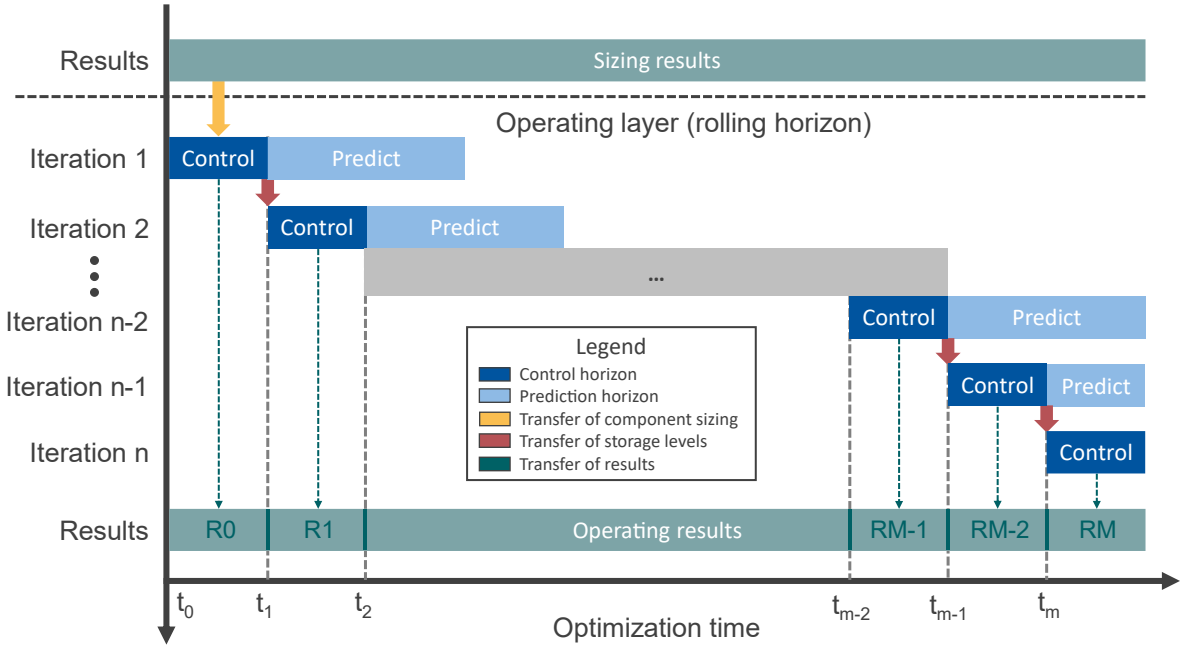

Figure 12: Illustration of the Rolling Horizon (RH) approach for the operating layer in the FOCUS prosumer model. Own illustration based on information in [29].

Usually, the optimisation horizon for the FOCUS prosumer model is one year (8760 time steps). We divide this horizon into smaller sub-problems (scheduling horizon), which consist of a control and a prediction horizon. For the control horizon, as a trade-off between accuracy/predictability and solving time, we choose a length of 24 hours as supported by the literature [29, 57]. The control horizon is the time interval at the beginning of each sub-problem during which we do not modify our inputs, assuming perfect foresight. We set the length of each control horizon to 4 hours to align with the product length in frequency control markets [90]. The prediction horizon is the time range from the end of the control horizon until the last time step of the sub-problem. The resulting length with the above assumptions is 20 hours. Typically, the prediction horizon includes forecasts for all time series of the energy system to achieve a more realistic operational profile. However, for simplicity, we assume perfect foresight as the standard setting in this dissertation. After solving an RH sub-problem, the results for the control horizon are taken as the final results. For the next RH iteration, we shift the sub-problem by the length of the control horizon and transfer the states for continuous variables, such as storage levels. The process is then iteratively repeated until the end of the full optimisation horizon.

To implement the RH approach into the FOCUS prosumer class, some structural adjustments are necessary. Using the method *add_fix_sizing_constraints()*, optimised sizing values can be transferred to the operating layer and between RH sub-problems. For energy storage, we transfer storage levels between RH sub-problems using the *add_fix_storage_constraints()* method. The constraint in Eq. (3.68) defines this transfer.

$$SOE_{t\_start}^{RH,Iteration2} = SOE_{t\_end}^{RH,Iteration1} \tag{3.68}$$

3.2. FOCUS - flexumer model

Flexibility is playing an increasingly important role for industrial companies, especially in view of the fluctuating energy prices during the recent energy crisis [3]. One component that can provide this flexibility is industrial-scale battery storage. Over the past few years, significant technological progress has driven rapid growth in the German market for industrial battery systems (see Figure 2). Moreover, combining battery services in so-called value stacking or multi-use approaches is becoming increasingly popular [12]. Therefore, we develop a value stacking model to complement the FOCUS prosumer model and convert it into a flexumer model. While peak shaving and RE integration are already covered by the implementations in the *BaseStorage* class (see Subsection 3.1.2) and the energy management system (see Subsection 3.1.4), this section adds necessary mathematical formulations for FTM services. This includes a wholesale trading (arbitrage) component in Subsection 3.2.1 and ancillary services components in Subsection 3.2.2 (FCR) and 3.2.3 (aFRR). Moreover, implementing FTM services entails many additional constraints, requiring an energy management component as described further in Subsection 3.2.4.

3.2.1. Wholesale trading (arbitrage)

The arbitrage component inherits from the *BaseGrid* class (see Subsection 3.1.2). In Eq. (3.69), we define the input and output power of the arbitrage component as the sold and bought quantity of a discrete product size ($P_{sell,buy,step}^{el}$) in kW. The current discrete product size (x) for DA and IDC markets is 100 kW ($x_{sell,buy}^{discr} = 100\ kW$). Another important characteristic of trading markets in general is the product length, thus temporal duration. The constraint in Eq. (3.70) ensures that the arbitrage operation complies with the trading product length of the respective market. We apply this constraint to all time steps except for possible start/delivery times for arbitrage (T_{arb}). For instance, in the DA market with a one-hour product length, possible start/delivery times are always at the full hour.

$$P_{in1,t}^{el} = P_{sell,t}^{el,x} * x_{sell}^{discr} \quad \Big| \quad P_{out1,t}^{el} = P_{buy,t}^{el,x} * x_{buy}^{discr} \quad \forall t \in T \tag{3.69}$$

$$P_{sell,t}^{el} = P_{sell,t-1}^{el} \quad \Big| \quad P_{buy,t}^{el} = P_{buy,t-1}^{el} \quad \forall t \notin T_{arb} \tag{3.70}$$

By using the definitions for purchasing and selling power, we can calculate the revenue for the arbitrage component with Eq. (3.71) and (3.72). The revenue mainly depends on the price ($\pi_{arb,sell,buy}$) that is usually time-dependent. However, the implementation also allows the use of fixed prices.

$$\kappa_{arb,sell,t} = P_{in1,t}^{el} * \pi_{arb,sell,t} * t_{\Delta,t} \quad \Big| \quad \kappa_{arb,buy,t} = P_{out1,t}^{el} * \pi_{arb,buy,t} * t_{\Delta,t} \quad \forall t \in T \tag{3.71}$$

$$R_{arb,t} = \kappa_{arb,sell,t} - \kappa_{arb,buy,t} \quad \forall t \in T \tag{3.72}$$

For the sizing layer of the flexumer model, the arbitrage component provides a very flexible energy source, as with perfect foresight, the model can find the optimal trading schedule. However, this might not be a realistic schedule and might overestimate the real arbitrage potential. Therefore, we define a possible trading limit with the constraint in Eq. (3.73).

$$P_{in1,t}^{el} \leq P_{limit,sell}^{el} \quad \Big| \quad P_{out1,t}^{el} \leq P_{limit,buy}^{el} \quad \forall t \in T \tag{3.73}$$

Finally, the arbitrage component needs to account for equivalent CO_2 emissions from the electric power grid. Therefore, with the constraint in Eq. (3.74), we multiply the emission factor (EF) in gCO_2 per kWh by the energy we sell in wholesale markets. The factor can be either a time-dependent variable or a fixed value across all time steps.

$$e_{arb,t} = P_{out1,t}^{el} * EF_{arb,t} * t_{\Delta,t} \quad \forall t \in T \tag{3.74}$$

3.2.2. Frequency containment reserve (FCR)

FCR as an ancillary service is characterised by a simple market design that makes it attractive for battery storage (see definitions in Subsection 2.2.3). It features only one capacity product every four hours, which is symmetrical and thus includes positive and negative provision [90]. To ensure that we fulfil the four-hour product blocks ($T_{len,FCR}$) we apply the identical constraint as for arbitrage in Eq. (3.75) to the FCR capacity product ($P_{cap,FCR}^{el}$). The constraint now is only valid for time steps that are not the delivery times of FCR ($T_{start,FCR}$).

$$P_{cap,FCR,t}^{el} = P_{cap,FCR,t-1}^{el} \quad \forall t \notin T_{start,FCR} = [0h, 4h, 8h, \dots] \tag{3.75}$$

Based on the reserved FCR capacity, we can calculate the activated FCR power. It depends on the frequency deviation of the electric power grid relative to the desired 50 Hz frequency. For frequency deviations, however, data processing is needed. The ancillary services module in the FOCUS Tooling library (see Subsection 3.3.1) converts high-resolution frequency measurement data into activation factors (α) that we can use to formulate constraints. With the net frequency deviation factor ($\alpha_{\Delta f}^{net}$) in Eq. (3.113) and (3.114), we can formulate the potential activated FCR power constraint in Eq. (3.76) for negative and positive activation. The product size for reserved capacity is in megawatt (MW) steps ($x_{FCR}^{discr} = 1000\ kW$). The constraint in Eq. (3.77) defines the maximum of the activation power.

$$\begin{aligned} P_{pot,FCR,t}^{el,+} &= P_{cap,FCR,t}^{el} * x_{FCR}^{discr} * \alpha_{\Delta f,t}^{net,-} \\ P_{pot,FCR,t}^{el,-} &= P_{cap,FCR,t}^{el} * x_{FCR}^{discr} * \alpha_{\Delta f,t}^{net,+} \end{aligned} \tag{3.76}$$

$$P_{act,FCR,t}^{el,max,\pm} = P_{cap,FCR,t}^{el} * 10^3 \tag{3.77}$$

In the following, the potential activation power is limited. Depending on the net frequency deviation ($\Delta f_{net,t}$) we define allowed ranges for the real activated FCR power in accordance with the prequalification (PQ) conditions [94]. The conditions allow exceeding the activated power by 20% at all times. When the net frequency deviation is less than 10 mHz, the operator has the flexibility to choose whether to provide power, a feature referred to as dead band. From 10-200 mHz, the activated power must increase linearly with the frequency deviation. If the deviation exceeds 200 mHz, the operator must fully activate the reserved capacity. The constraint in Eq. (3.81) connects positive activation to the output and negative activation to the input of the FCR component.

$\Delta f_{net,t}$ < 10 mHz: $$0 \leq P_{act,FCR,t}^{el,\pm} \leq P_{pot,FCR,t}^{el,\pm} * 1.2 \qquad \forall t \in T \tag{3.78}$$

10 mHz $\leq \Delta f_{net,t} \leq$ 200 mHz: $$P_{pot,FCR,t}^{el,\pm} \leq P_{act,FCR,t}^{el,\pm} \leq P_{pot,FCR,t}^{el,\pm} * 1.2 \qquad \forall t \in T \tag{3.79}$$

$\Delta f_{net,t}$ > 200 mHz $$P_{act,FCR,t}^{el,\pm} \leq P_{act,FCR,t}^{el,max,\pm} * 1.2 \qquad \forall t \in T \tag{3.80}$$

$$P_{in1,FCR,t}^{el} = P_{act,FCR,t}^{el,+} \;\Big|\; P_{out1,FCR,t}^{el} = P_{act,FCR,t}^{el,-} \quad \forall t \in T \tag{3.81}$$

In a final step, we can calculate the FCR revenue with the constraint in Eq. (3.82). The revenue mainly depends on the reserved power and the market-clearing price for FCR ($\pi_{cap,FCR}$). We normalise the revenue to the product length ($T_{len,FCR}$).

$$R_{FCR,t} = P_{cap,FCR,t}^{el} * x_{FCR}^{discr} * \pi_{cap,FCR,t} * \frac{t_{\Delta,t}}{T_{len,FCR}} \quad \forall t \in T \tag{3.82}$$

3.2.3. Automatic frequency restoration reserve (aFRR)

In contrast to the FCR provision, the aFRR market allows bids for four products (see definitions in Subsection 2.2.3). This includes separate bids for the reserved capacity (aFRR capacity) and activated energy (aFRR energy), as well as separate bids for positive and negative provision [90]. Therefore, it is effectively more complex to integrate the aFRR component in the FOCUS component library. Similar to the FCR implementation in Eq. (3.83) and (3.84), we start by defining constraints that ensure compliance with the aFRR product length. Here, we distinguish between aFRR capacity with a product length of four hours, and aFRR energy with a product length of 15 minutes [90]. At the same time, we consider that when participating in the aFRR capacity market, it makes sense to participate in the aFRR energy market with at least the same capacity to avoid being activated free of compensation.

$$P^{el,\pm}_{cap,aFRR,t} = P^{el,\pm}_{cap,aFRR,t-1} \quad \forall t \notin T_{start,cap,aFRR} = [0h, 4h, 8h, \dots] \tag{3.83}$$

$$P^{el,\pm}_{E,aFRR,t} = P^{el,\pm}_{E,aFRR,t-1} \quad \forall t \notin T_{start,E,aFRR} = [0h, 4h, 8h, \dots] \tag{3.84}$$

$$P^{el,\pm}_{E,aFRR,t} \geq P^{el,\pm}_{cap,aFRR,t} \quad \forall t \in T \tag{3.85}$$

In the next step, a set of constraints is formulated to determine the positive activated aFRR power for the aFRR energy market. This requires using a cumulative activation factor ($\alpha^{cum,\pm}_{act,t}$) as provided in Subsection 3.3.1. The activation of positive and negative power is modelled separately, as it is possible to place individual bids for both directions. Therefore, we implemented the condition that the positive activated aFRR power must not become negative. Eq. (3.86) to (3.87) use a binary variable ($z_{act,1,t}$) in combination with the big M method to ensure that this condition is valid for all time steps. Finally, the constraint in Eq. (3.88) calculates the activated positive aFRR power. It is multiplied by an activation factor $f_{act,aFRR}$ that indicates the average power the asset is called up on. Products for activation are in megawatt steps ($x^{discr}_{aFRR} = 1000\ kW$).

$$P^{*} = P^{el,+}_{E,aFRR,t} * \alpha^{cum,+}_{act,t} - P^{el,-}_{E,aFRR,t} * \alpha^{cum,-}_{act,t} \leq M * z_{act,1,t} \quad \forall t \in T \tag{3.86}$$

$$P^{el,-}_{E,aFRR,t} * \alpha^{cum,-}_{act,t} - P^{el,+}_{E,aFRR,t} * \alpha^{cum,+}_{act,t} \leq M(1 - z_{act,1,t}) \quad \forall t \in T \tag{3.87}$$

$$P^{el}_{in1,aFRR,t} = P^{el,+}_{act,aFRR,t} = P^{*} * x^{discr}_{aFRR} * z_{act,1,t} * f_{act,aFRR} \quad \forall t \in T \tag{3.88}$$

Similarly, the negative activated aFRR power must not become positive. Therefore, we define equivalent constraints for negative activation in Eq. (3.89) to (3.90). Negative power is activated according to the constraint in Eq. (3.91).

$$P^{**} = P^{el,-}_{E,aFRR,t} * \alpha^{cum,-}_{act,t} - P^{el,+}_{E,aFRR,t} * \alpha^{cum,+}_{act,t} \leq M * z_{act,2,t} \quad \forall t \in T \tag{3.89}$$

$$P^{el,+}_{E,aFRR,t} * \alpha^{cum,+}_{act,t} - P^{el,-}_{E,aFRR,t} * \alpha^{cum,-}_{act,t} \leq M(1 - z_{act,1,t}) \quad \forall t \in T \tag{3.90}$$

$$P^{el}_{out1,aFRR,t} = P^{el,-}_{act,aFRR,t} = P^{**} * x^{discr}_{aFRR} * z_{act,2,t} * f_{act,aFRR} \quad \forall t \in T \tag{3.91}$$

With defined factors for aFRR capacity and energy provision, we can calculate the revenue of the component. In contrast to FCR, it depends on reservation power as well as activation energy. Eq. (3.92) calculates revenues for aFRR capacity reservation, and Eq. (3.93) calculates revenues for activated aFRR energy. The total aFRR revenue is the sum of both shares (3.94).

$$R_{cap,aFRR,t} = P^{el,\pm}_{cap,aFRR,t} * x^{discr}_{aFRR} * \pi^{\pm}_{cap,aFRR,t} * t_{\Delta,t} \quad \forall t \in T \tag{3.92}$$

$$R_{act,aFRR,t} = P^{el,\pm}_{act,aFRR,t} * x^{discr}_{aFRR} * \pi^{\pm}_{act,aFRR,t} * t_{\Delta,t} \quad \forall t \in T \tag{3.93}$$

$$R_{aFRR,t} = R_{cap,aFRR,t} + R_{act,aFRR,t} \quad \forall t \in T \tag{3.94}$$

3.2.4. Services Energy Management

In addition to the ancillary services component model, an external energy management model is required. It ensures that FCR and aFRR capacity is reserved at the appropriate components, and that SOE limitations for storage components, such as batteries, are considered.

Capacity provision

For battery storage, capacity needs to be reserved at the battery inverters. We need to differentiate between negative and positive capacity provision. With the constraint in Eq. (3.95), we reserve positive capacity at the inverter output. The battery inverter output must always be less than or equal to the nominal inverter capacity minus the share of unused FCR and aFRR reserve capacity. This unused share results from subtracting reserved capacity from activated energy. For aFRR, reserved capacity refers to the capacity of aFRR energy where we always bid equal to or higher than the aFRR capacity, as defined in Eq. (3.85). Eq. (3.96) provides the equivalent constraint for reserving negative capacity at the inverter input.

$$\begin{aligned} &\sum_{c \in I} P_{out1,c,t} \leq \sum_{c \in I} P^{el}_{N,c} + P'_t \qquad I = \{battery\ inverters\}, \forall t \in T \\ &P'_t = \frac{-P^{el}_{cap,FCR,t} * x^{discr}_{FCR} - P^{el,+}_{E,aFRR,t} * x^{discr}_{aFRR} + P^{el,+}_{act,FCR,t} + P^{el,+}_{act,aFRR,t}}{\eta_{gcp}} \end{aligned} \tag{3.95}$$

$$\sum_{c\in I} P_{in1,c,t} \leq \sum_{c\in I} P_{N,c}^{el} + P_t'' \qquad I = \{battery\ inverters\}, \forall t \in T$$
$$P_t'' = \left(-P_{cap,FCR,t}^{el} * x_{FCR}^{discr} - P_{E,aFRR,t}^{el,-} * x_{aFRR}^{discr} + P_{act,FCR,t}^{el,-} + P_{act,aFRR,t}^{el,-}\right) * \eta_{gcp} \tag{3.96}$$

The activation of FCR results in changes in the battery's storage level. Therefore, the PQ-conditions [94] demand a recharge management for energy storage that can be activated at any time. With the constraints in Eq. (3.97) and Eq. (3.98), we account for a recharge reserve (r) as a percentage of reserved FCR capacity. For aFRR, this limitation does not exist. Depending on the inverters' capacity and the battery's power capacity, one or the other constraint is more restrictive.

$$\sum_{c\in I} P_{N,c}^{el} \geq (1+r) * \left(\frac{P_{cap,FCR,t}^{el} * x_{FCR}^{discr}}{\eta_{gcp}}\right) \quad \forall t \in T \tag{3.97}$$

$$\frac{C_{N,bat}}{EPR_{out,in}} \geq (1+r) * \left(\frac{P_{cap,FCR,t}^{el} * x_{FCR}^{discr}}{\eta_{gcp}}\right) \quad \forall t \in T \tag{3.98}$$

Energy provision

In accordance with the allocated capacity of the respective market, sufficient energy must be available in the battery storage at all times for full activation of FCR and aFRR over the period of the minimum activation times (T_{act}) [94]. Therefore, in a first step, we define the maximum possible charging and discharging energies using Eq. (3.99), based on the current battery storage level. For this, we define a path efficiency (η_{path}) that includes losses at the battery unit and at the inverter.

$$E_{dch,t} = \left(E_{bat,t} - E_{min,bat}\right) * \eta_{path} \ \mid \ E_{ch,t} = \left(E_{max,bat} - E_{bat,t}\right) * \frac{1}{\eta_{path}} \quad \forall t \in T \tag{3.99}$$

$$E_{FCR,max,t} = P_{cap,FCR,t}^{el} * x_{FCR}^{discr} * T_{act,FCR} \quad \forall t \in T \tag{3.100}$$

$$E_{cap,aFRR,max,t}^{\pm} = P_{cap,aFRR,t}^{el,\pm} * x_{aFRR}^{discr} * T_{act,cap,aFRR} \quad \forall t \in T$$
$$E_{E,aFRR,max,t}^{\pm} = P_{cap,aFRR,t}^{el,\pm} * x_{aFRR}^{discr} * T_{act,E,aFRR} \quad \forall t \in T \tag{3.101}$$

Based on the previous definitions, we can formulate the constraints in Eq. (3.102) and Eq. (3.103). They ensure that the service components do not exceed the battery's chargeable and dischargeable energy limits.

$$E_{dch,t} \geq E_{FCR,max,t} + E_{cap,aFRR,max,t}^{+} \quad \forall t \in T$$
$$E_{dch,t} \geq E_{FCR,max,t} + E_{E,aFRR,max,t}^{+} \quad \forall t \in T \tag{3.102}$$

$$E_{ch,t} \geq E_{FCR,max,t} + E^{-}_{cap,aFRR,max,t} \quad \forall t \in T$$
$$E_{ch,t} \geq E_{FCR,max} + E^{-}_{E,aFRR,max,t} \quad \forall t \in T \tag{3.103}$$

Another constraint from the PQ-conditions [94] is the limited permitted operating range for control units with limited storage volume for FCR provision. This ensures that the marketable output can always be provided symmetrically at any point in time. To implement this constraint, we use the maximum frequency deviation factor (see Subsection 3.3.1) to account for the maximum cumulative frequency deviation within one optimisation time step. With this factor in Eq. (3.104) and (3.105), we can formulate constraints on the allowed upper level (UL) and lower level (LL) for the SOE of the battery. In the last step, we use the defined upper and lower levels to constrain the SOE of the battery according to Eq. (3.106).

$$C_{N,bat} * SOE_{UL,t} \geq E_{bat,t-1} * z_{FCR,on} + P^{el}_{cap,FCR,t} * x^{discr}_{FCR} * 1.2 * \alpha^{max}_{\Delta f,t} * t_{\Delta,t} * \frac{1}{\eta_{gcp}} \tag{3.104}$$

$$C_{N,bat} * SOE_{LL,t} * z_{FCR,on} \leq E_{bat,t-1} + P^{el}_{cap,FCR,t} * x^{discr}_{FCR} * 1.2 * \alpha^{min}_{\Delta f,t} * t_{\Delta,t} * \eta_{gcp} \tag{3.105}$$

$$SOE_{LL,t} = 1 - \frac{0.25\ h}{(SOE_{max} - SOE_{min}) * EPR_{min}} \mid SOE_{UL,t} = 1 - SOE_{LL,t} \quad \forall t \in T \tag{3.106}$$

Marketable capacity

The marketable capacity of a battery storage participating in FCR needs to be further limited to ensure that the so-called reserve mode is possible [94]. Therefore, we define the constraint in Eq. (3.107) that limits marketable FCR capacity by a minimum reserve factor ($T_{res,FCR}$) or EPR, depending on which parameter is the limiting one. For aFRR, there is no definition for reserve operation. Therefore, we use minimum activation times (T_{act}) or EPR to limit the marketable capacity for aFRR capacity in Eq. (3.108) and aFRR energy in Eq. (3.109).

$$P^{el}_{cap,FCR,t} * x^{discr}_{FCR} \leq C_{N,bat} * \eta_{path} * min\left(\frac{1}{T_{res,FCR}}, \frac{1}{EPR_{min}}\right) \quad \forall t \in T \tag{3.107}$$

$$P^{el,\pm}_{cap,aFRR,t} * x^{discr}_{aFRR} \leq C_{N,bat} * \eta_{path} * min\left(\frac{1}{T_{act,cap,aFRR}}, \frac{1}{EPR_{min}}\right) \quad \forall t \in T \tag{3.108}$$

$$P^{el,\pm}_{E,aFRR,t} * x^{discr}_{aFRR} \leq C_{N,bat} * \eta_{path} * min\left(\frac{1}{T_{act,E,aFRR}}, \frac{1}{EPR_{min}}\right) \quad \forall t \in T \tag{3.109}$$

Hidden cycling dynamics

The optimisation step length of at least 15 minutes cannot represent the dynamic characteristics of FCR and aFRR provision. Between optimisation intervals, power flows and battery storage cycling can occur within seconds. We refer to this cycling as hidden cycling, as

the optimiser cannot directly see it. In Eq. (3.110) and (3.111), we define optimisation variables (P_{hidden}) to consider hidden cycling. The calculation requires the use of a cumulative frequency deviation and an activation factor, as defined in Subsection 3.3.1. The factor cumulates positive and negative cycling separately. Finally, we incorporate the variables for hidden cycling power into the cycle-limited battery storage constraint in Eq. (3.15) to reduce the usable cycle count accordingly.

$$P^{+}_{hidden,t} = (P^{el}_{cap,FCR,t} * \alpha^{cum,-}_{\Delta f,t} * x^{discr}_{FCR} - P^{el,+}_{act,FCR,t} + P^{el,+}_{E,aFRR,t} * \alpha^{cum,+}_{act,t} * x^{discr}_{aFRR} - P^{el,+}_{act,aFRR,t}) * \frac{1}{\eta_{path}} \quad \forall t \in T \tag{3.110}$$

$$P^{-}_{hidden,t} = (P^{el}_{cap,FCR,t} * \alpha^{cum,+}_{\Delta f,t} * x^{discr}_{FCR} - P^{el,-}_{act,FCR,t} + P^{el,-}_{E,aFRR,t} * \alpha^{cum,-}_{act,t} * x^{discr}_{aFRR} - P^{el,-}_{act,aFRR,t}) * \eta_{path} \quad \forall t \in T \tag{3.111}$$

3.3. FOCUS - tooling library

As part of FOCUS, the tooling library provides additional functionality beyond the core model for energy system optimisation. For instance, this includes packages for processing input and results data or creating scenarios. In the following, we introduce only the two most relevant packages: data preprocessing for ancillary services (see Subsection 3.3.1) and variable-time-step clustering to reduce the optimisation model size (see Subsection 3.3.2). Furthermore, we summarise selected additional calculations relevant to evaluating the optimisation results (see Subsection 3.3.3).

3.3.1. Ancillary services preprocessing module

The provision of ancillary services comes with many side constraints that require additional data processing. This module provides a set of tools to convert required data into a format that we can use to formulate the optimisation constraints for FCR and aFRR. For FCR, this includes frequency deviation factors that convert high-resolution frequency deviations on a second-to-second basis to align with the 15-minute optimisation intervals in FOCUS. For aFRR, activation depends heavily on the bidding strategy, as the market design uses a pay-as-bid approach. This requires preprocessing of the bidding data to generate activation signals.

Frequency containment reserve (FCR)

The activation of FCR directly depends on the frequency and, equally, the stability of the electric power grid. The measure that indicates instability is the frequency deviation from 50 Hz. The frequency deviation ($\Delta f_{n,\tau}$), however, is changing within milliseconds, and

measurements are on a second-by-second basis (τ). Therefore, we have to process the frequency data to align with the 15-minute optimisation intervals in FOCUS. In a first step, we calculate the net frequency deviation by aggregating all single deviations within one optimisation time step ($t_{\Delta,t}$).

$$\Delta f_{n,\tau} = 50\ Hz - f_\tau \quad | \quad \Delta f_{net,t} = \sum_{\tau=t}^{t+t_{\Delta,t}} \Delta f_{n,\tau} * \tau \qquad \forall t \in T \tag{3.112}$$

By using the net frequency deviation, we can calculate a net frequency deviation factor ($\alpha_{\Delta f}^{net}$) according to Eq. (3.113) and (3.114). When the net frequency deviation is 200 mHz, the factor becomes 1.

$$\alpha_{\Delta f,t}^{net,+} = \begin{Bmatrix} \frac{1h}{200\ mHz * 3600s * t_{\Delta,t}} \Delta f_{net,t} & |if\ \Delta f_{net,t} \geq 0 \\ 0 & |else \end{Bmatrix} \quad \forall t \in T \tag{3.113}$$

$$\alpha_{\Delta f,t}^{net,-} = \begin{Bmatrix} \frac{1h}{200\ mHz * 3600s * t_{\Delta,t}} \Delta f_{net,t} & |if\ \Delta f_{net,t} \leq 0 \\ 0 & |else \end{Bmatrix} \quad \forall t \in T \tag{3.114}$$

While the net frequency deviation factor enables the calculation of FCR activation and revenue, it does not provide any information about the storage's true cycling. Therefore, in the following, we define a positive and negative cumulative frequency deviation factor to capture the energy throughput within an optimisation time step. Eq. (3.115) and (3.116) define the calculation of these two factors. We add up all positive or all negative frequency deviations within one optimisation interval ($t_{\Delta,t}$) and normalise the resulting sum to 200 mHz.

$$\alpha_{\Delta f,t}^{cum,+} = \frac{1h}{200\ mHz * 3600s * t_{\Delta,t}} * \overbrace{\sum_{\tau=t}^{\tau+t_{\Delta,t}} \Delta f_{n,\tau}^{+} * \tau}^{\Delta f_{cum,t}^{+}} \qquad \forall t \in T \tag{3.115}$$

$$\alpha_{\Delta f,t}^{cum,-} = \frac{1h}{200\ mHz * 3600s * t_{\Delta,t}} * \overbrace{\sum_{\tau=t}^{\tau+t_{\Delta,t}} \Delta f_{n,\tau}^{-} * \tau}^{\Delta f_{cum,t}^{-}} \qquad \forall t \in T \tag{3.116}$$

Net and cumulative frequency deviation factors indicate a measure at the end of each optimisation interval. However, to estimate the maximum change in storage levels during each interval, we need to determine the maximum and minimum frequency deviation factors. This is an important measure to ensure that for each second, we do not exceed the storage level limits. The calculation of the maximum deviation requires a rolling net frequency

deviation factor over all time steps of one optimisation interval. The function in Eq. (3.117) defines this time-dependent net frequency deviation factor. To detect the maximum and minimum of the net frequency deviation function as indicated in Eq. (3.118), we vary the time (t_{sec}) from beginning of the interval (t) to the end of the interval ($t + t_{\Delta,t}$).

$$\alpha_{\Delta f,t}^{net}(t_{sec}) = \frac{1h}{200\,mHz * 3600s * t_{sec}} * \overbrace{\sum_{\tau=t}^{t+t_{sec}} \Delta f_{n,\tau} * \tau}^{\Delta f_{net,t}^{sec}} \quad \forall t \in T \qquad (3.117)$$

$$\alpha_{\Delta f,t}^{max} = \max_{t_{sec}\epsilon[t:t+t_{\Delta,t}]} \left(\alpha_{\Delta f,t}^{net}(t_{sec})\right) \mid \alpha_{\Delta f,t}^{min} = \min_{t_{sec}\epsilon[t:t+t_{\Delta,t}]} \left(\alpha_{\Delta f,t}^{net}(t_{sec})\right) \quad \forall t \in T \qquad (3.118)$$

As a summary of the definitions, Figure 13 visualises all defined frequency deviation factors for an exemplary optimisation interval.

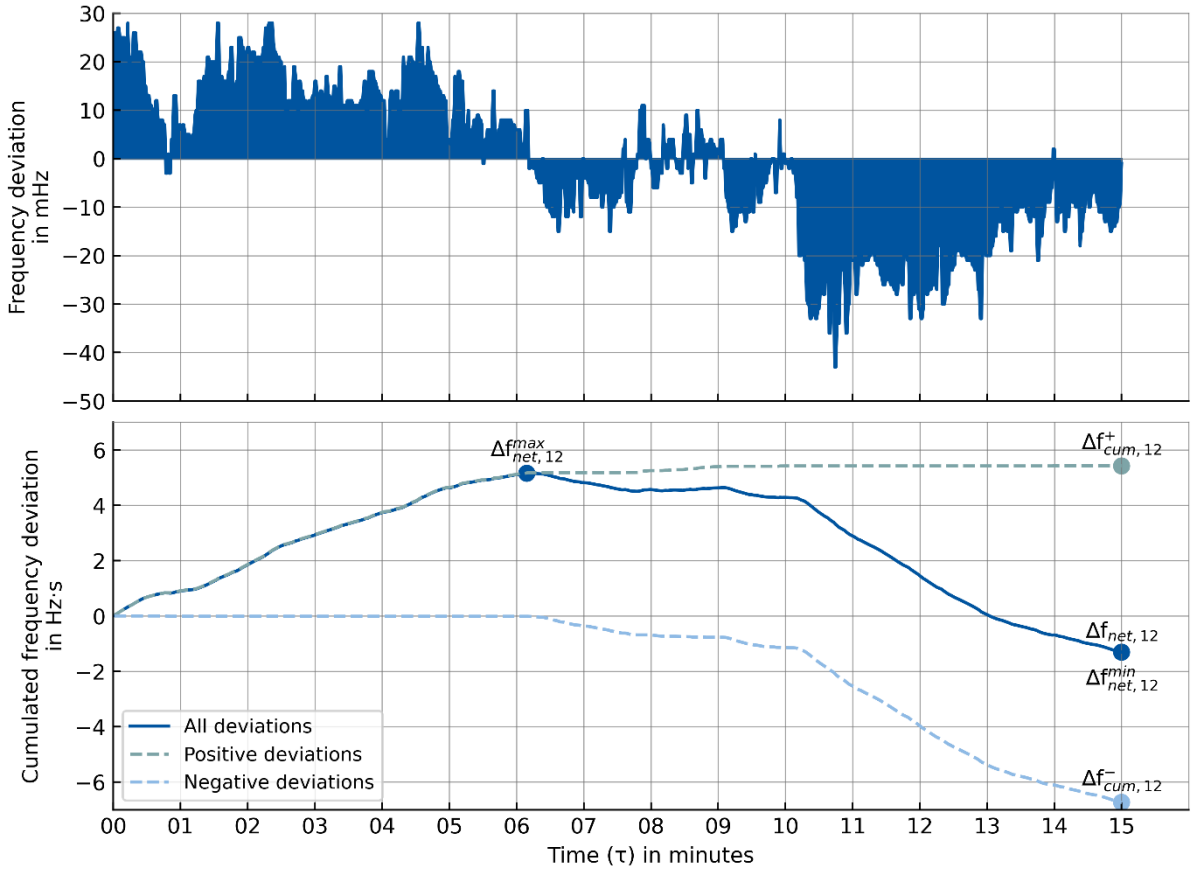

Figure 13: Illustration of calculated frequency deviation factors for an exemplary 15-minute interval on January 1st, 2024, from 3:45-4:00 pm (t=12).

Automatic frequency restoration reserve (aFRR)

Activation for aFRR is fundamentally different from FCR. Instead of the local frequency deviation, it is based on the position on the merit order list of the aFRR energy auction and

the demand for each time step processed by the responsible transmission system operator (TSO) [90]. While for the aFRR capacity market, the responsible TSO publishes average prices of awarded bids, this is not the case for aFRR energy, which requires additional calculations. Therefore, for the aFRR energy market, we sort all bids in ascending order. From that ordered list, we calculate which bids are allocated by summing bids until we reach the market cap published by the TSOs in MW. Using the merit order list of allocated bids, we can determine the correlation between power and energy prices for each bid position. The positioning of our battery asset depends on the bidding strategy. In order to translate the bidding strategy into a measurable value, we define a so-called price position coefficient (x_{pp}). This coefficient is between 0 and 1 and indicates a specific position of the allocated power on the merit order list. A price position of 0.5 corresponds to the power-price-pair where 50% of all allocated power is below, and 50% of all allocated power is above that position. Bidding at a high price position carries the risk of not being allocated. Lower price positions reflect a more conservative bidding strategy. Figure 14 illustrates the definition of the price position coefficient.

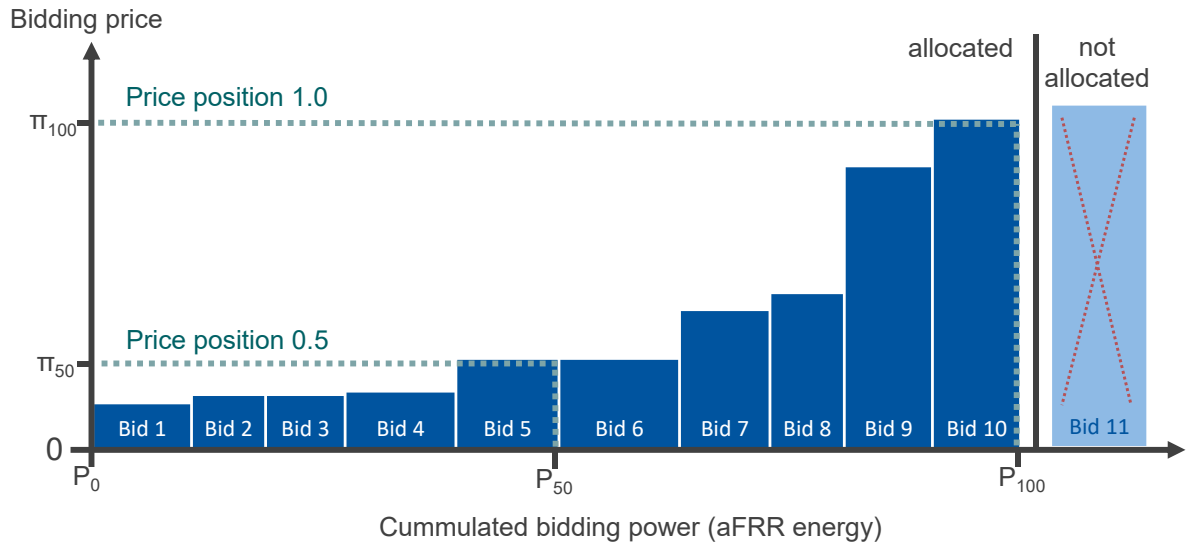

Figure 14: Illustration of the developed price position coefficient (P_x), which indicates the targeted bidding position on the merit order list for the aFRR energy market. The algorithm developed calculates the merit order list for every second and identifies the corresponding price (π_x) based on the selected price position.

In the next step, we use the price position definition to calculate the activated aFRR energy. Eq. (3.119) calculates the power threshold (P_{pp}) for a specific price position (x_{pp}) in dependence on the total allocated power (P_{aloc}). Based on this definition, we define a second-by-second activation signal (A) for both negative and positive aFRR energy in Eq. (3.120). The activation signal equals 1 when the power of the price position is lower than the activation set point by the TSO ($P_{set,\tau}$) for the considered time step. An activation signal of 1 indicates activation of the entire battery power.

$$P_{pp,\tau} = P_{aloc,\tau} * x_{pp,\tau} \qquad x_{pp,\tau} \in [0,1], \forall \tau \in t_{\Delta,t} \tag{3.119}$$

$$A_{\tau}^{\pm} = \begin{cases} 1, & if\ P_{pp,\tau} \leq P_{set,\tau} \\ 0, & else \end{cases} \qquad \forall \tau \in t_{\Delta,t} \tag{3.120}$$

In a last step, we need to convert the second-by-second activation signal (A) to the resolution of the optimisation model ($t_{\Delta,t}$). We use the same approach as for the cumulative FCR activation factors. Eq. (3.121) and (3.122) separately define the calculation of cumulative activation factors for aFRR energy for positive and negative activation.

$$\alpha_{act,t}^{cum,+} = \frac{1h}{3600s * t_{\Delta,t}} \sum_{\tau=t}^{t+t_{\Delta,t}} A_{\tau}^{+} \qquad \forall t \in T \tag{3.121}$$

$$\alpha_{act,t}^{cum,-} = \frac{1h}{3600s * t_{\Delta,t}} \sum_{\tau=t}^{t+t_{\Delta,t}} A_{\tau}^{-} \qquad \forall t \in T \tag{3.122}$$

3.3.2. Variable time step clustering module

For the sizing layer of the FOCUS flexumer model, a reduction in complexity is required to solve the model with available computational resources. In particular, industrial flexumer applications are often highly complex. One possible approach to reduce model size is to reduce the number of optimisation steps through time-step aggregation. The method has been shown by Savvidis et al. [30] for linear programming (LP) market and investment models. Based on this approach, we implement a similar method. In principle, aggregation is possible whenever characteristics of time series for generation and demand are static over a period of time steps. A measure of this is the residual load, the difference between VRE generation and the system's electric load. With Eq. (3.123), we calculate the total power demand of the flexumer energy system by aggregating demands across all energy sectors. Apart from electrical demands, this includes hydrogen and thermal demands that must be converted with the respective conversion efficiencies of the components. For total electric demand, the total system residual load can be calculated using Eq. (3.124). In addition to the total system residual load, we also calculate the electrolysis system residual load in Eq. (3.125). This allows identifying critical times when the electrolysis system supply is in deficit due to RE generation, potentially triggering battery storage operation.

$$P_{load,c,t}^{el} = P_{load,c,t}^{el} + P_{load,c,t}^{H2} * \eta_{H2 \to el} + P_{load,c,t}^{th} * \eta_{th \to el} \qquad \forall t \in T \quad c \in C\{components\} \tag{3.123}$$

$$P_{res,load,t}^{el} = \sum_{r} P_{gen,r,t}^{el} - \sum_{c} P_{load,c,t}^{el} \qquad \forall t \in T \tag{3.124}$$

$$c \in C\{components\} \mid r \in R\{renewable\ generators\}$$

$$P^{el}_{res,load,ely,t} = \sum_{\substack{r \\ r \in R\{renewable\ generators\}}} P^{el}_{gen,r,t} - P^{el}_{load,ely,t} \quad \forall t \in T \tag{3.125}$$

With the calculated residual loads, we can define residual load segments ($x_{seg,res}$) in which conditions are similar and aggregation is possible. However, to account for the flexibility in the operation of sector-coupling components, such as the electrolysis system, we define a power band around the zero point of the residual load. A power threshold (P_{RES}) in MW, that applies both in positive and negative directions, defines the width of this power band. Within this band, we do not allow for any aggregation. To implement this power band, we construct residual power segments for the total residual load ($x_{seg,res,t}$) and electrolysis system residual load segments ($x_{seg,res,ely,t}$). Depending on whether the load is above or below the defined power band, a value of 1 or -1 is applied. For time steps where the residual load is within the defined power band around the zero point of the residual load, the residual segments vector equals 0 as shown in Eq. (3.128). By calculating the derivative of the residual segments vector ($x'_{seg,res,t}$), we can calculate a list of time stamps ($T_{lim,res}$) with Eq. (3.129) indicating when there is a change between the three defined states for the residual load. During these changes, no aggregation is allowed.

$$\begin{aligned} x_{seg,res,t}\left(P^{el}_{res,load,t} \geq P_{RES}\right) = 1 \quad \forall t \in T \\ x_{seg,res,ely,t}\left(P^{el}_{res,load,ely,t} \geq P_{RES}\right) = 1 \quad \forall t \in T \end{aligned} \tag{3.126}$$

$$\begin{aligned} x_{seg,res,t}\left(P^{el}_{res,load,t} \leq -P_{RES}\right) = -1 \quad \forall t \in T \\ x_{seg,res,ely,t}\left(P^{el}_{res,load,t} \leq -P_{RES}\right) = -1 \quad \forall t \in T \end{aligned} \tag{3.127}$$

$$\begin{aligned} x_{seg,res,t}\left(P^{el}_{res,load,t} < P_{RES} \cap P^{el}_{res,load,t} > -P_{RES}\right) = 0 \quad \forall t \in T \\ x_{seg,res,ely,t}\left(P^{el}_{res,load,t} < P_{RES} \cap P^{el}_{res,load,t} > -P_{RES}\right) = 0 \quad \forall t \in T \end{aligned} \tag{3.128}$$

$$T_{lim,res} = T\left[x'_{seg,res,t} \neq 0\right] + T\left[x'_{seg,res,ely,t} \neq 0\right] \quad \forall t \in T \tag{3.129}$$

Another equally important characteristic to account for is peak demand. This can particularly affect component sizing. Therefore, we set an upper demand threshold (p_{peak}) for each demand component above which aggregation is limited. The threshold is defined as a percentile (p_x) of the annual demand of each component. Moreover, we apply the method to the total demand in Eq. (3.123) to properly account for peak power costs that depend on the highest 15-minute peak of an industrial site during one year [82]. As with residual demand, we can define segments based on the peak power threshold. Segments with demand values below the peak power threshold are assigned a value of 0. On the contrary, segments for

demand values above the peak power threshold are allocated to the actual demand values, as indicated by Eq. (3.132). Finally, with the derivative of the residual segments vector ($x'_{seg,peak,t}$), a list of timestamps can be created, indicating changes in peak power demand. A minimum threshold of 100 kW is set to account only for relevant changes in peak demand. However, this excludes cases where peak demand occurs more than once in consecutive time steps. For the glassworks use case in this dissertation, this mainly concerns the hydrogen demand of the furnace with over 1000 hours at maximum load (see Figure 18). In particular, long durations at maximum load can influence the sizing of storage components. Therefore, in Eq. (3.134), we define that whenever peak demand for the hydrogen furnace occurs, no aggregation is possible.

$$P_{peak} = p_x\left(P_{load,c,t}\right) \quad \forall t \in T \tag{3.130}$$

$$x_{seg,peak,t}\left(P_{load,c,t} \leq P_{peak}\right) = 0 \quad \forall t \in T \tag{3.131}$$

$$x_{seg,peak,t}\left(P_{load,c,t} > P_{peak}\right) = P_{load,c,t} \quad \forall t \in T \tag{3.132}$$

$$T_{lim,peak} = T\left[x'_{seg,peak,t} > 100kW\right] \quad \forall t \in T \tag{3.133}$$

$$T_{lim,peak,H2} = T\left[P_{load,H2,t} == \max_{t \in T}\left(P_{load,H2,t}\right)\right] \quad \forall t \in T \tag{3.134}$$

In addition to residual and peak load conditions, component availability can influence optimisation and the desired clustering of time steps. In particular, when central components such as the electrolyser system require maintenance and are unavailable, the energy supply to loads temporarily changes. This can lead to substantially different component operation and higher energy storage utilisation. Therefore, as defined in Eq. (3.135), we ensure that no aggregation is possible when the availability of the electrolyser system ($A_{ely,t}$) equals 0 to capture all operation dynamics. Moreover, the quality of the results is expected to decrease with increasing temporal length of the aggregation window. Eq. (3.136) ensures that a maximum aggregation length (T_{WIN}) is not exceeded.

$$T_{lim,off} = T\left[A_{ely,t} == 0\right] \quad \forall t \in T \tag{3.135}$$

$$T_{lim,win} = T[t\%T_{WIN} == 0] \quad \forall t \in T \tag{3.136}$$

In the final step, the algorithm applies timestep aggregation to all input time series of the FOCUS flexumer model. To achieve this, we first collect unique timestamps that limit aggregation and sort them in ascending order, as indicated in Eq. (3.137). Second, for all input time series (S) of the model mean values are calculated between two consecutive aggregation limits ($T_{lim,aggr}$) according to Eq. (3.138). Figure 15 exemplifies the aggregation procedure.

$$T_{lim,aggr} = UNIQUE_{\Uparrow}\left(T_{lim,res} + T_{lim,peak} + T_{lim,peak,H2} + T_{lim,off} + T_{lim,win}\right) \quad (3.137)$$

$$S_\tau = \overline{\left(S\left[t \geq T_{lim,aggr,\tau} \cap t < T_{lim,aggr,\tau+1}\right]\right)} \quad \forall t \in T, \forall \tau \in T_{lim,aggr} \quad (3.138)$$

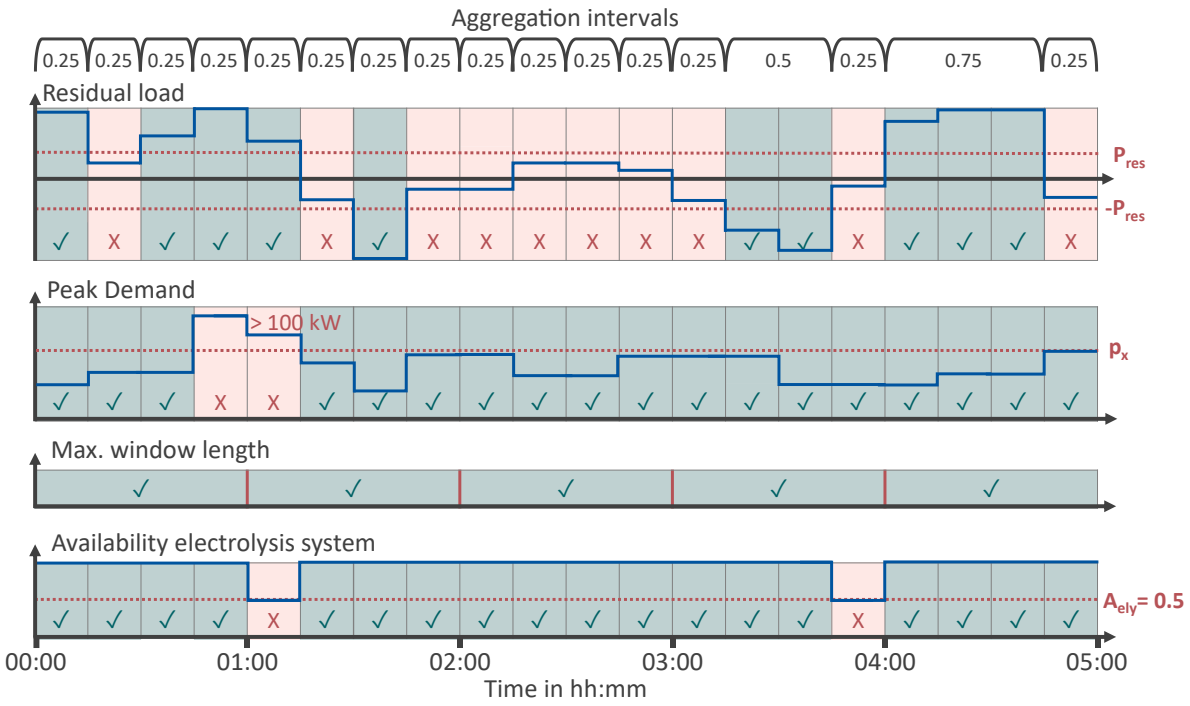

Figure 15: Illustration of clustering of time steps for the sizing layer of the FOCUS flexumer model. Clustering is only possible when there is no violation of the rules for all defined categories (residual load, peak demand, maximum window length, and availability of the electrolysis system)

3.3.3. Additional calculations

The evaluation of optimisation results requires additional calculations to determine correlations and cost factors that are not directly shown by the model output. This includes the calculation of the levelised cost of hydrogen (LCOH) as a relevant key performance indicator (KPI) commonly used in the literature (see Subsection 2.3.3). For the calculation of LCOH, we add up all relevant cost shares and divide them by the produced amount of hydrogen ($m^{H2}_{ely,total}$) as indicated by Eq. (3.139). Relevant cost shares are separated into CAPEX and OPEX. For CAPEX, we consider annualised costs for all components of the hydrogen supply system. For the use case in this dissertation, this includes the electrolyser system, compressor, hydrogen storage, battery inverter, and battery storage. For OPEX, we include all costs associated with operating the hydrogen supply system. This includes costs for peak power, purchasing generation with PPAs, purchasing power from wholesale markets, and levies and taxes.

$$LCOH = \frac{\kappa_{capex,H2} + \kappa_{opex,H2}}{m_{ely,total}^{H2}} \tag{3.139}$$

$$\kappa_{capex,H2} = \kappa_{capex,ely} + \kappa_{capex,comp} + \kappa_{capex,H2sto} + \kappa_{capex,bat} + \kappa_{capex,inv,bat} \tag{3.140}$$

$$\kappa_{opex,H2} = \sum_{t \in T} \left(\kappa_{opex,H2,PP,t} + \kappa_{opex,H2,PPA,t} + \kappa_{opex,H2,ws,t} + \kappa_{opex,H2,tax,levy,t} \right) \tag{3.141}$$

For scenarios that should not include a reduction of peak power, we need to calculate total peak power costs ($\kappa_{opex,PP}$) after the optimisation. We simply calculate them by multiplying the annual 15-minute maximum electric power drawn at the GCP by the peak power price as indicated by Eq. (3.52). However, depending on regulations, in some scenarios, we may need to consider reimbursing peak power costs associated with the electrolysis system. This requires separately calculating the additional share of peak power attributable to the electrolyser supply system. To achieve this, with Eq. (3.142), we first calculate the peak power that is caused by the basic consumption of the industrial site ($P_{PP,base}^{el}$). This benchmark includes all fixed electric consumption, as well as thermal consumption converted using a simple efficiency factor.

$$P_{PP,base}^{el} = \max_{t \epsilon T} \left(P_{demand,t}^{el} + P_{demand,t}^{th} * \eta_{th \to el} \right) \tag{3.142}$$

In a second step, we can calculate the additional peak power ($P_{PP+,H2}^{el}$) that is caused by the restructuring of the energy system to produce green hydrogen. For this, we include energy flows from the GCP to all components (C) that are part of, or connected to, the hydrogen supply system. For the use case of this dissertation, this includes the electrolyser system, compressor, hydrogen storage, battery inverter, and electric boiler.

$$P_{PP+,H2}^{el} = \max_{t \epsilon T} \left(P_{demand,t}^{el} + P_{demand,t}^{th} * \eta_{th \to el} + \sum_{c \epsilon C} P_{gcp \to c,t}^{el} \right) - P_{PP,base}^{el} \tag{3.143}$$

In some scenarios, regulations allow reimbursement of peak power costs associated with the operation of the electrolysis system (see the regulations in Table 10). We calculate the peak power of the electrolysis system by adding up all the supplying energy flows drawn at the GCP. For reimbursement, we consider only the additional peak power of the electrolysis system by subtracting the industrial site's base peak load from the electrolysis system's peak load.

$$R_{reimburse} = \begin{cases} \pi_{PP}^{el} * \overbrace{\left(\max_{t \epsilon T} \left(P_{gcp \to ely,t}^{el} \right) - P_{PP,base}^{el} \right)}^{\Delta PP} & if \quad \Delta PP \geq 0 \\ 0 & if \quad \Delta PP < 0 \end{cases} \tag{3.144}$$

4. Scenario parameterisation

This dissertation focuses on evaluating future energy supply options for an existing glassworks in Herzogenrath, Germany. Subsection 4.1 provides a detailed description of the use case. To evaluate decarbonisation options for this use case, Subsection 4.2 defines a detailed scenario setup. The scenario setup is complemented by descriptions of model input data preparation (Subsection 4.3) and model component parameterisation (Subsection 4.4).

4.1. Use case description

The glassworks in Herzogenrath operated by Saint-Gobain is one of the largest manufacturing sites for car glazing in Germany. The plant has an annual energy demand of over 400 GWh and equivalent CO_2 emissions of over 90 Mt per year, including process-related emissions from the melting of glass raw materials [102]. The plant consists of two separate sections, including Saint-Gobain Glass (SGG) and Saint-Gobain Sekurit (SGS).

The SGG section primarily consists of the melting furnace (see Figure 16), which produces raw glass via the so-called float glass process. This general process is described in detail in Zier et al. [18], which is used as a reference throughout the following description. The site operator provides additional specific information about the Herzogenrath site [102]. At the beginning of the float glass process, the raw glass materials are mixed in the batch preparation. For float glass production, mainly quartz sand (silicon dioxide, SiO_2) with a 70-73% weight share, fluxing agents such as soda ash, and stabilisers such as alkaline earth oxides are used. Other additives include colourants and fining agents. After batch preparation, the preheated raw material mixture is added to the melting furnace, where it is melted at 1200-1600°C. SGG uses a conventional melting furnace that is supplied with fossil NG and electricity [102]. NG burners fire horizontally above the melted glass mass, while electrical heating rods at the bottom of the tank boost the melting process. However, in the current furnace in Herzogenrath, heating rods provide only a small share of the energy required for melting [102]. After melting, in the main forming step of the float process, the molten glass mass flows into a tin bath, where it floats on the surface due to its lower density and different surface tension. To adjust the thickness of the glass, lances are manually inserted into the glass from the outside to draw it apart and adjust the speed of the glass flow [102]. While the glass mass travels through the float bath, the temperature is adjusted from the top by electrical heating elements or radiant burner systems. Above the tin bath, an inert atmosphere consisting of nitrogen (90%) and hydrogen (10%) prevents oxidation. For the Herzogenrath site, the gases are extracted from the atmosphere with an air separation unit [102]. When the glass leaves the float bath, it has a temperature of around 600°C and must be further cooled down. In the final step, the continuous glass strand is cut into uniform pieces, and a quality check is conducted, sorting out glass blanks with defects such as gas bubbles [102]. [18, 102]

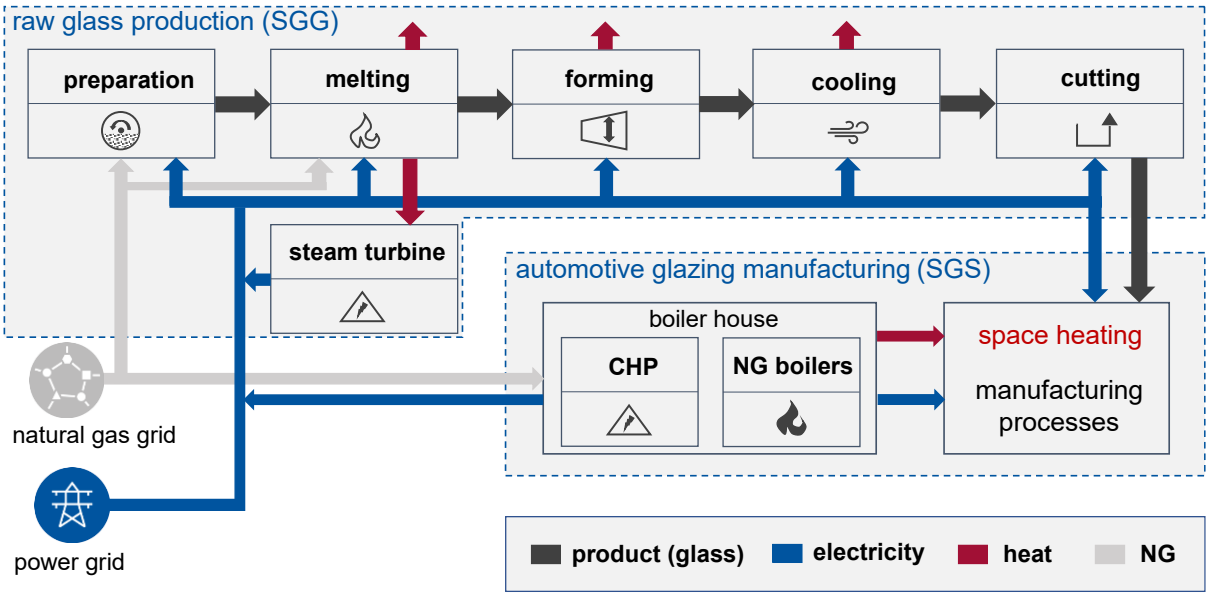

Figure 16: Schematic representation of the status quo energy system of the glassworks use case in Herzogenrath that serves as a use case for the evaluation. The representation is based on information from the site operator [102] and the illustration in [136]. Abbreviations: SGG: Saint-Gobain Glass, SGS: Saint-Gobain Sekurit, NG: natural gas, CHP: combined heat and power.

For the next steps, the glassworks operator provides further information [102]. The glass blanks produced at SGG are first stored in a warehouse before being transported to SGS for further processing. There are four production lines at SGS for different types of car windows, including roof, front, back, and side windows. The production lines run entirely on electricity and are independent of each other, serving different production campaigns that depend on the order situation. For heating the production halls, SGS features its own heating system that includes a combined heat and power plant (CHP) with a rated electric power output of 1.99 MW_{el} and two gas boilers, each with a rated thermal output of 1.05 MW_{th}. The CHP is operated in heat-led mode, and the electricity generated as a by-product is directly consumed by SGS to serve the manufacturing load. Figure 16 illustrates the glassworks energy system and visualises all important demand and component characteristics of the status quo [136]. The electrical power rating of the GCP is 120 MVA, consisting of two medium-voltage transformers, with one usually in standby mode. [102]

4.2. Specification of scenarios

To decarbonise the glassworks, several measures can be implemented, as proposed by Zier et al. [18]. They state that a full decarbonisation requires a fuel switch from fossil to RE sources. From a construction point of view, the simplest solution is to substitute NG with methane from other sources, as the structure of the melting furnace remains the same. Possible alternative sources include biogas or gasification of solid biomass, such as wood. However, both approaches involve uncertainty about the influence of impurities and additional gas components on glass quality. Moreover, the availability of both sources is limited, making

them unsuitable as substitutes for energy-intensive industry. Synthetic methane could overcome the impurity issue. However, the production process has a high energy demand, and there are only a few concentrated CO_2 sources, making this option economically challenging. The most promising solution is to switch from NG to renewable hydrogen, and at the same time, increase the efficiency of the melting furnace through higher electrification [7]. Other possible measures include waste heat recovery (WHR), preheating of combustion gases, and batch cullet- or oxy-fuel combustion. [18]

For the glassworks in Herzogenrath, decarbonising the energy system requires the construction of a novel hydrogen-based furnace. The current NG-based furnace design has a rating of 30 MW_{NG} for the NG burners and an electric power rating of 3 MW_{el}. In collaboration with the site operator [102] and calculations based on the thermodynamic modelling in [137], we choose two different hydrogen furnace designs (F1 and F2) to be considered for decarbonisation of the energy supply, with technical characteristics summarised in Table 9.

Table 9: Glass melting furnaces considered for the decarbonised energy supply of the glassworks use case in Herzogenrath. The values are derived from collaboration with the site operator [102] and calculations based on the thermodynamic model developed in [137].

	Status quo with NG	**Potential future hydrogen furnaces**	
Characteristic	**F0**	**F1 (Low electrification)**	**F2 (High electrification)**
Financials			
Normalised invest (Assumption by site operator)	1	1.5	2.5
Power rating			
Rated electric power in MW	3.0	8.0	20.0
Rated power NG in MW	30.0	0.0	0.0
Rated power hydrogen in MW	0.0	22.4	7.7
Features			
Oxidiser	Air		

The two variations for a future furnace are designed to meet the same annual glass production as the status quo furnace with NG (F0). However, they differ in the degree of electrification. For furnace F1, we consider an electric power rating of 8 $MW_{el,}$ whereas furnace F2 has a considerably higher rating of 20 MW_{el}. It can be observed that, due to efficiency gains, hydrogen furnaces with higher electrification have a lower total power rating. For simplification and better comparability, we consider air as the oxidiser for all three considered furnaces. However, it must be noted that substantial additional energy savings are possible when switching to oxy-fuel combustion, as indicated in [137]. At the same time, this would require additional investments in air separation units [18]. Furthermore, for better comparability with other studies, we also do not model the steam turbine for WHR that exists in the status quo setup (see Figure 16).

4.2.1. Flexumer model configuration

The described use case for the glassworks in Section 4.1 must be transferred to the layout of the FOCUS flexumer model. This requires identifying relevant components and aggregating where possible to reduce complexity. For this, we separate the modelling into a setup for rebuilding the NG-based furnace and one for constructing a novel hydrogen furnace. For hydrogen furnaces, it is further distinguished between access to a future hydrogen pipeline and hydrogen production via an on-site electrolyser system. Figure 17 illustrates the model set-up for all three cases.

The most relevant components for the reference setup for rebuilding the NG furnace (A) are the furnace and an electric boiler to meet the SGS space-heating thermal demand. The central busbar connects all electrical flows within the flexumer model. Before the GCP, we model a balancing group that the glassworks operator manages. However, in the status quo case, there is only one connection to it that allows buying energy from wholesale. Instead of the existing CHP and NG boilers, we model an electric boiler to meet SGS's space heating demand, enabling better comparability among scenarios.
The first model for energy system decarbonisation focuses on accessing green hydrogen via pipeline connection (B). The setup is similar to the reference case with the NG furnace, with the NG pipeline replaced by a hydrogen pipeline that we assume is available at the site at no additional cost. However, we also consider adding an optional PV rooftop and battery storage system. Furthermore, the generation from the PV rooftop system can be sold via the DM component that is connected to the balancing group of the industrial site. Depending on the scenario setup, PV and battery storage are not included as described in more detail in Subsection 4.2.2.
The second model for energy system decarbonisation features on-site hydrogen production via electrolysis (C). Therefore, we add the necessary components for hydrogen production, including an electrolyser system, a compressor, and hydrogen storage, with the latter connecting to the furnace. The waste heat from the electrolyser system is utilised in an industrial HP to meet SGS's space heating demand. In addition, we include a thermal storage to increase the flexibility of the thermal supply. To avoid infeasibilities, we model a slack component for both hydrogen and heat commodities that provides infinite supply. However, slack components are parameterised with very high operational costs and are thus used only as the last possible option by the optimiser. Furthermore, to enable green hydrogen production, RE generation from PPAs and battery storage is required. We connect the PPAs directly to the site's balancing group, applying a loss factor for electric power grid transmission. In addition, as setup (C) by definition features a large battery storage system for PPA buffering (see Figure 19), we connect electric power grid services to the balancing group, effectively enabling the glassworks to become a flexumer. This includes the frequency control markets FCR and aFRR for both negative and positive directions. However, depending on the

scenarios, available flexibility options differ as described in Subsection 4.2.2. The PV rooftop system is optional, equivalent to setup (B).

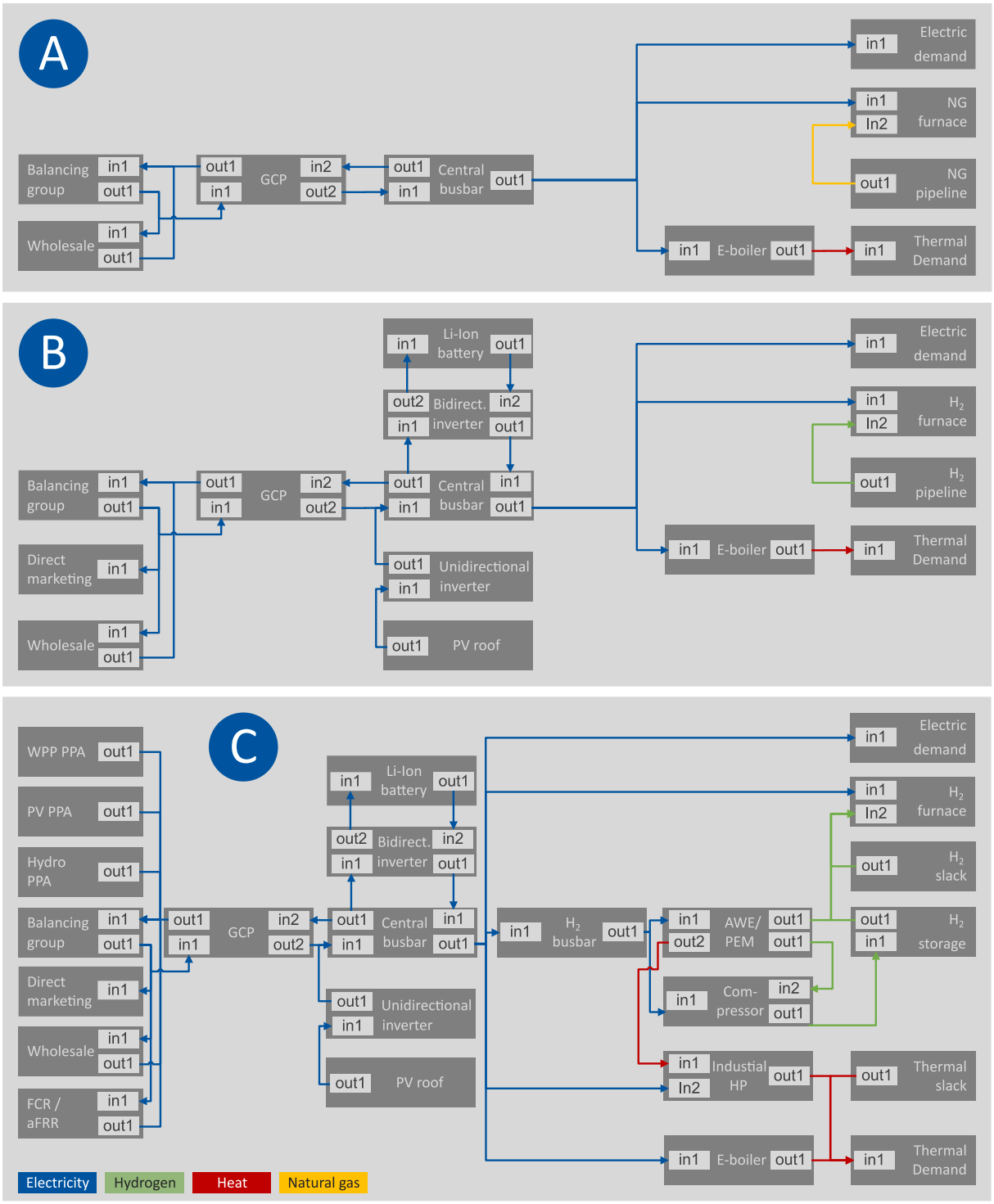

Figure 17: Model structure of the different scenario setups in the FOCUS flexumer model. Setups include a reference case for rebuilding the NG furnace (A), a hydrogen furnace with connection to a future hydrogen pipeline (B), and a hydrogen furnace with electrolysis system on site (C). Abbreviations: GCP: grid connection point, FCR: frequency containment reserve, aFRR: automatic frequency restoration reserve, PV: photovoltaic, WPP: wind power plant, PPA: power purchase agreement, AWE: alkaline water electrolysis, PEM: proton exchange membrane, HP: heat pump

4.2.2. Basic scenario framework

The definition of a basic scenario setup for decarbonising the energy system of the glassworks use case depends heavily on future developments in the German energy system, political decisions, and data availability. For the transformation of the glassworks energy system, the phase out of fossil NG and a higher level of electrification are key aspects. This means that, for the site's future energy supply, the electricity sector plays a particularly important role. Detailed studies are available that analyse pathways for the future German electric power system. For the near future in 2030, a study by Fraunhofer ISE provides four different scenarios on the development of power plant capacities, considering rising electricity demand through the electrification of sectors [138]. For the more distant future, the network development plan (NDP) by the German Federal Network Agency (BNetzA) considers three different scenario pathways for 2037 [139]. The scenarios from both studies serve as a base for the developed scenario framework for the glassworks use case. We define three supporting years that meet data availability requirements and cover different stages of the regulatory framework for hydrogen production (see Subsection 2.4.2). The supporting years include the present year, based on 2024 price data, and two future years that aim to represent conditions in 2030 and 2037. Table 10 summarises the basic scenario framework used to evaluate the decarbonised energy supply for the glassworks use case in this dissertation.

Table 10: Setup of the basic scenario framework to evaluate a decarbonised energy supply of the glassworks use case. The framework consists of three support years that aim at covering relevant projections for political targets and regulations.

<table>
<tr><th></th><th colspan="3">Support years for scenario definition</th><th>Respective Law</th><th>Reference</th></tr>
<tr><th></th><th>Present (2024)</th><th>Future I (2030)</th><th>Future II (2037)</th><th></th><th></th></tr>
<tr><td></td><td colspan="5">General assumptions / regulations</td></tr>
<tr><td>Green hydrogen - availability</td><td>Electrolysis system on site</td><td colspan="2">Electrolysis system on site
Hydrogen pipeline</td><td>-</td><td>[20]</td></tr>
<tr><td rowspan="4">Green hydrogen - production</td><td>PPA: monthly temporal correlation</td><td>PPA: hourly temporal correlation</td><td>PPA: no temporal correlation</td><td>RED II
RED III</td><td>[21, 22]</td></tr>
<tr><td>Exemption from electric power grid fees for 20 years</td><td colspan="2" rowspan="3">Uncertain, no exemptions assumed</td><td>EnWG, §118
StromNEV §19</td><td>[81, 126, 140]</td></tr>
<tr><td>Exemption from offshore and KWKG levies</td><td>EnFG §36</td><td>[141]</td></tr>
<tr><td>Exemption from electricity taxes</td><td>StromStG §9a</td><td>[142]</td></tr>
<tr><td>Battery storage</td><td colspan="3">Exemption of double electric power grid fees and electricity taxes (planned for the beginning of 2025)</td><td>Draft</td><td>[143]</td></tr>
</table>

In the present scenario, historical prices for energy commodities are used, and hydrogen production requires only a monthly temporal correlation. In 2030, the assumed decarbonisation of the electric power grid is at 80% [138] and hydrogen production on site requires hourly temporal correlation of electrolysis system demand and generation from PPAs. In 2037, we assume high decarbonisation of the German electric power grid in

accordance with future scenarios of the (BNetzA) [139]. This leads to the assumption that local electric power grid emission factors at the glassworks fall below the threshold of 18 gCO_2e/MJ (40 gCO_2e/kWh) in 2037, and green hydrogen production from grid electricity is allowed [21]. To simplify the modelling and as future spot market prices are difficult to predict, we do not consider the specific regulation that electricity for the electrolysis system can be drawn from the electric power grid at wholesale prices below 20 EUR/MWh [21]. Furthermore, in 2030 and 2037, we assume that access to a hydrogen pipeline is possible, which is not available in the present scenario. For hydrogen production via an electrolysis system in Germany, electric power grid fees are exempted for plants that start operation before 2029, according to §118 of the EnWG [144]. In addition, according to §9a of the StromStG, the electricity tax is exempted for the electrolysis system consumption if the company is part of the manufacturing industry [145] including glassworks.

In the next step, we collect the necessary parameter data for the basic scenario framework. This includes assumptions about energy prices, levies and taxes, emissions, and financial constraints. Table 11 summarises all relevant parameters for the considered support years. To adjust energy prices from public sources to 2024 price levels, taking inflation into account, we use the Harmonised Index of Consumer Prices (HICP) for industrial goods published by the European Central Bank (ECB) [146] (see Appendix C, Table 24). For currency conversion from US Dollar to Euro, the ECB also provides annual average values [147] (see Appendix D, Table 25). The green colour in the table indicates the default values used for all scenarios. On the contrary, orange and blue indicate that the parameters are solely considered for the sensitivity analysis.

There are only a few sophisticated studies that analyse the development of energy prices in Germany. One study of the EWI from 2022 considers price developments until 2030 for relevant energy carriers, including electricity and NG [151]. The study distinguishes between low availability and unavailability of Russian NG imports. For 2030, this results in NG prices in the range of 18-59 EUR_{2022}/MWh. For electricity, the EWI study considers the development of NG prices alongside moderate or high RE expansion and high or moderate electrification. This leads to a range for wholesale electricity prices of 52-135 EUR_{2022}/MWh.

Another study conducted by Prognos in 2024 focuses on energy price developments for the German industry until 2045 [150]. It contains three pathways for upper-, middle-, and lower-level price developments. The study states NG prices in the range of 14-35 EUR_{2022}/MWh for 2030, which is slightly lower than the EWI study's values. However, 2030 electricity wholesale prices are forecast to be similar, between 54-120 EUR_{2022}/MWh. For 2037, the projection shows declining NG prices between 14-24 EUR_{2022}/MWh and wholesale electricity prices at 57-126 EUR_{2022}/MWh. We combine the results of both studies to specify price ranges for the basic scenario setup shown in Table 11.

Table 11: Parameterisation of the basic scenario framework to evaluate a decarbonised energy supply of the glassworks use case. The data is separated into energy supply, levies and taxes, emissions, financials, and the three support years.

	Unit	Scenarios									Ref.
		Present (2024)			Future I (2030)			Future II (2037)			
		low	high	mid	low	high	mid	low	high	mid	
Energy supply											
Hydro power future (EU27)	EUR_{2024}/MWh	82	88	85	48	115	77	51	113	61	[102, 148, 149]
NG futures (pipeline)	EUR_{2024}/MWh	35			15	62	50	15	25	22	[150, 151]
H_2 (pipeline)	EUR_{2024}/MWh_{LHV}	Not available			148	210	179	140	174	157	[152, 153]
PPA utility-scale PV (GER)	EUR_{2024}/MWh	45	60	53	42			38			[8, 9]
PPA wind on-/offshore (GER)	EUR_{2024}/MWh	45	69	57	52			48			[8, 9]
PPA hydro power (GER) (base load)	EUR_{2024}/MWh	76	208	100				Not used			[148, 149]
Levies and taxes											
Electric power grid fees	EUR_{2024}/MWh	6.5	14.9	10.7	10.7						[102, 154, 155]
Electricity tax	EUR_{2024}/MWh	0.5									[154]
Electricity peak power price	EUR_{2024}/MWh	175.53									[80]
NG grid fees	EUR_{2024}/MWh	8.8	4.8	5.4	5.4			9.4			[156]
Emissions											
Scope 1											
Process-related emissions	tCO_2/a	30,000			21,000						[102]
NG emission factor	$kgCO_2/MWh_{NG}$	202									[157]
CO_2 emission certificate costs	EUR_{2024}/t	68			68	161	125	95	266	200	[102, 150]
Scope 2											
Emissions for NG provision	$kgCO_2/MWh_{NG}$	16			55						[123]
Emissions electric power grid	$kgCO_2/MWh_{el}$	Assumption: zero as only certified green electricity is considered									-
Financials											
Investment horizon	a	20									[102]
WACC	%	8.1	9.0	8.5	8.5						[158]
Inflation rate (10-year avg.)	%	1.354									[146]

Legend:

Default scenario parameters (■) | scenario sensitivity “high energy prices” (■) | scenario sensitivity “low energy prices” (■)

For future hydrogen prices, studies are less detailed. While no hydrogen pipelines are currently geographically relevant for the glassworks use case in Herzogenrath, development plans for a hydrogen core network in Germany indicate potential future availability. However, for the location of Herzogenrath, there is high uncertainty, as the development plan in Germany, approved by the Federal Network Agency in October 2024, does not specifically include a connection near the glassworks site [20]. However, at the European level, an association of mostly NG-associated companies revealed plans that include connections in the Netherlands in close proximity [159]. Despite the planned construction of the Dutch hydrogen network until 2030, a possible date of connection to the glassworks site in Herzogenrath remains speculative. Once a hydrogen pipeline connection is available, another uncertainty is hydrogen pricing. A study by Fraunhofer ISE estimates the hydrogen provision costs via

pipeline from Spain in 2030 to be between 137-145 EUR/MWh [152]. At the same time, the study provides assumptions for the price of liquefied hydrogen from Brazil to Germany via ship, with approximated costs of 171-207 EUR/MWh. To account for the higher uncertainty for the near future, we apply the respective higher values to the 2030 scenario and the lower values to the 2037 scenario. For average price prediction, the simplified assumption is made that half of the hydrogen is imported from Spain and the other half from Brazil. Furthermore, for pipeline transmission values between 2.5-4.5 EUR/MWh per 1000 km are reported in the literature [152, 153]. Therefore, in a simplified approach, we assume that additional transmission costs to the Herzogenrath location within Germany are 2 EUR/MWh for worst-case distances up to 500 km.

The production of green hydrogen faces significant regulatory constraints regarding the origin of green electricity, which can be addressed through PPA contracting. PPA pricing is usually not disclosed, as contracts are individually negotiated between the consumer and the producer. However, we use average values per technology that are reported in [9] for 2024. Even if current PPA price levels are below compensation schemes from the EEG [120], their long-term perspective can be attractive [10]. For future years, we calculate the PPA contracting price by assuming a price decline equal to reductions in the lower-reported LCOEs of the technologies (see Appendix B, Table 23). Hydropower PPAs that can function as a baseload PPA are an exception in this regard. As there is no public data available, the price for this type of PPA contract is estimated at 100 EUR_{2024}/MWh based on LCOE data in [148, 149]. This considers that available capacity is limited, especially as the hydropower plants geographically have to be located in Germany to comply with RED II [21]. On the contrary, for hydropower futures in the EU, we assume that due to the larger available capacity in the Alps and northern Europe, prices at 85 EUR_{2024}/MWh are realistic for 2024, which is 85% of the average wholesale price in Germany [151]. However, as they do not meet the requirements for green hydrogen production, we only use green hydropower futures to meet the remaining electricity demand of the glassworks site. For the future scenarios in 2030 and 2037, we assume that the 85% ratio between EU hydropower futures and wholesale prices in Germany remains the same. Based on this assumption, prices for EU hydropower futures can be calculated from wholesale price predictions in [150, 151].

Other significant assumptions for the base scenario setup include emissions, regulatory constraints such as taxes and levies, and financial parameters. For electric power network charges, there is a wide price range that depends on the industry type and energy consumption. With the abolition of the EEG levy in mid-2022, industrial electricity network charges in Germany significantly decreased to an average of 14.9 EUR/MWh in 2024 [154]. However, for the energy-intensive industry, further reductions of up to 90% of usual charges are possible [155]. Therefore, in collaboration with the glassworks site operator, we choose 6.5 EUR/MWh as a realistic lower bound [102]. In addition to levies, the German industry has

to pay a reduced electricity tax of 0.5 EUR/MWh [154]. Similar to electricity network charges, NG network charges apply to industrial consumers. Based on data from the German Federal Statistical Office, we select an average value of 5.4 EUR/MWh [156]. Furthermore, Then et al. [160] assume that towards 2037, network charges for NG infrastructure will increase by 75% to 9.4 EUR/MWh, with a decreasing number of NG customers. With regard to equivalent CO_2 emissions, we consider scope 1 and scope 2 emissions. Scope 1 emissions mainly include NG combustion in the melting furnace and process-related emissions from melting raw materials for glass production. The process-related emissions account for about 30,000 tonnes per year and are expected to be reduced at least by 30% towards 2030 with improved raw material composition [102]. On the contrary, scope 2 emissions are related to the provision of energy carriers, including NG and electricity. In this regard, we consider upstream emissions for NG provision, which depend heavily on the share of Russian NG and liquefied natural gas (LNG) [123]. For the weighted average cost of capital (WACC), we assume an average value of 8.5% for the industrial manufacturing sector [158].

4.2.3. Scenario variations for flexibility

To benchmark the value of flexibility for the glassworks use case, we define additional scenario variations that derive from the basic scenario framework in Subsection 4.2.2. By default, the basic scenario framework is implemented with fixed energy prices and features no additional flexibility (flexibility level A). Table 12 provides an overview of scenario variations and indicates available flexibilities.

For flexibility levels B and C, we analyse the potential for flexibility through behind-the-meter (BTM) services. This includes peak shaving (PS) (peak power aware operation) and direct marketing (DM) of on-site RE generation. Peak power aware operation is applied to all flexibility levels B-H. Moreover, for BTM, we assume a fixed power price based on long-term green hydropower futures (EU27).
On the contrary, flexibility levels D-F focus on single revenue streams of front-of-the-meter (FTM) services. This includes spot market trading (ST) and frequency control markets. In frequency control markets, we consider the frequency containment reserve (FCR) and the automatic frequency restoration reserve (aFRR). The first value stacking approach (flexibility level G) combines all single FTM services, excluding DM. The second value stacking approach (flexibility level H) combines all FTM and BTM services of the battery storage system.
For the NG furnace, we consider only flexibility level A, with no additional flexibility. On the contrary, flexibility options B and C are applied across all decarbonisation scenarios, with either on-site hydrogen production via an electrolyser system or connection to an external hydrogen pipeline. Flexibility levels with FTM services (D-H) are applied only to scenarios with an electrolyser system, as these already feature a large battery storage system to increase

self-consumption of RE generation from PPAs. For those cases, the EPR of the battery storage system is set to 4 hours, which is a typical upper ratio for large-scale BESS applications providing FTM services [11, 12].

Table 12: Overview of all scenario variations to evaluate flexibility potentials for the glassworks use case. For flexibility levels D-H, the EPR of the battery is constrained to 4 hours. In addition, the sizing of the battery storage system does not account for any FTM services, as the main purpose is to buffer RE generation from PPAs. FTM use cases are applied only to the operating layer of the optimisation model to leverage additional flexibility with the given assets.

Flex Level	**Asset sizing**	**Power supply**	**Flexibilities**					**Scenario overview**		
								Furnace F0	Furnace F1 (low electrification) Furnace F2 (High electrification)	
			BTM		FTM					
			PS	DM	ST	FCR	aFRR	**Pipeline (NG)**	**Electrolysis system (H_2)**	**Pipeline (H_2)**
Present (2024)										
A	Full model	Hydropower future EU27 (fixed price)	Default (no flexibility)					No battery	Optimised battery + PPA + AWE or PEM	No battery
B			✓					Not considered		Optimised battery
C			✓	✓						
D	Without FTM Services	Wholesale: Intraday continuous (IDC)	✓		✓				Optimised battery (EPR = 4 hours) + PPA + AWE or PEM	Not considered
E			✓			✓				
F			✓				✓			
G			✓		✓	✓	✓			
H			✓	✓	✓	✓	✓			
Future I (2030)										
A	Full model	Hydropower future EU27 (fixed price)	Default (no flexibility)					No battery	Optimised battery + PPA + AWE or PEM	No battery
B			✓					Not considered		Optimised battery
C			✓	✓						
Future II (2037)										
A	Full model	Hydropower future EU27 (fixed price)	Default (no flexibility)					No battery	Optimised battery + PPA + AWE or PEM	No battery
B			✓					Not considered		Optimised battery
C			✓	✓						

Legend: applied for scenarios (✓)

Behind-the-meter (BTM)	Front-of-the-meter (FTM)
Peak shaving (PS)	Spot market trading (ST)
Direct marketing (DM) of the rooftop PV system	Frequency containment reserve (FCR)
	Automatic frequency restoration reserve (aFRR)

4.3. Model input data preparation

For modelling the scenarios described in Section 4.2, accurate collection and generation of input data are essential. While historical data is available for the present year scenarios (2024), data for future scenarios often requires preparation. Table 13 provides an overview of all input data used to parameterise the scenarios, grouped into energy demand, power generation, market prices, and market characteristics. Before being applied to the optimisation model, time series that do not comply with a 15-minute resolution are resampled. In the model's operating layer, a rolling horizon is used, with perfect foresight for the prediction horizon across all time series.

For energy demand data for the industrial glassworks site, we use the measured 2019 data and apply it to all NG base-furnace scenarios, including furnace demands. Based on furnace consumption data from 2019, the demand for the hydrogen furnaces (G2, P2) is calculated using the thermodynamic model developed by Jost et al. [137]. Furthermore, we assume a constant space-heating demand for SGS (H1) across all years. Moreover, the capacity factors for PPAs and PV rooftop generation are calculated based on solar radiation and wind speed measurements of the German weather service (DWD) [24, 161] and remain constant for all years.

Table 13: Overview of input data used for the scenario evaluation. For all time series data, we exclude the 29th of February in leap years and harmonise the data to daylight saving time.

ID	Description of dataset	Temp. Res.	Year	Type	Source	Applied scenarios					
						2024		2030		2037	
						NG	H2	NG	H2	NG	H2
Energy demands											
G1	NG demand for NG furnace	60 min	2019	Measurement	[102]	✓	X	✓	X	✓	X
G2	H_2 demand for H_2 furnace	60 min	All	Simulation	[137]	X	✓	X	✓	X	✓
P1	Electricity demand for NG furnace	60 min	2019	Measurement	[102]	✓	X	✓	X	✓	X
P2	Electricity demand for H_2 furnace	60 min	All	Simulation	[137]	X	✓	X	✓	X	✓
P3	Other electricity demand SGG/SGS	60 min	2019	Measurement	[102]	✓	✓	✓	✓	✓	✓
H1	Thermal demand SGS	60 min	2019	Measurement	[102]	✓	✓	✓	✓	✓	✓
Power generation											
A1	Availability electrolyser	15 min	2024	Definition*	[162]	X	✓	X	✓	X	✓
S1	Solar radiation (at glassworks)	15 min	2023	Measurement	[161]	X	✓	X	✓	X	✓
W1	Wind speeds (at glassworks)	15 min	2023	Measurement	[161]	✓	✓	✓	✓	✓	✓
C1	PPA/RE CF based on S1/W1	15 min	2023	Calculation	[24]	✓	✓	✓	✓	✓	✓
Market prices/costs											
K1	Direct marketing (DM) compensation	60 min	2024	Calculation°	[122]	✓	✓	✓	✓	✓	✓
K2	IDC spot market prices (ID1)	15 min	2024	Report	[163, 164]	✓	✓	Not applied			
K3	FCR capacity clearing prices	4 hours	2024	Report	[90]	✓	✓				
K4	Avg. aFRR capacity prices (pos/neg)	4 hours	2024	Report	[90]	✓	✓				
K5	Avg. aFRR energy prices (pos/neg)	15 min	2024	Report	[90]	✓	✓				
Market-related characteristics											
F1	Electric power grid frequency for FCR	1 sec	2024	Measurement	[122]	✓	✓	Not applied			
M1	Tender and market results FCR/aFRR	-	2024	Report	[90]	✓	✓				
M2	Setpoints aFRR	1 sec	2024	Report	[122]	✓	✓				

Legend:
applied without changes for all scenarios (✓)
not applied for scenarios (X)

*Defined according to assumptions in Subsection 4.4.1
°Calculated based on Subsection 2.4.1

4.3.1. Characteristics of input time series

The model's multiple input time series have individual features that substantially influence the optimisation results. This particularly concerns demand series, as their time-specific patterns determine how much energy needs to be imported from which RE sources. Figure 18 illustrates the characteristics of all demand time series, separated into three groups by furnace type.

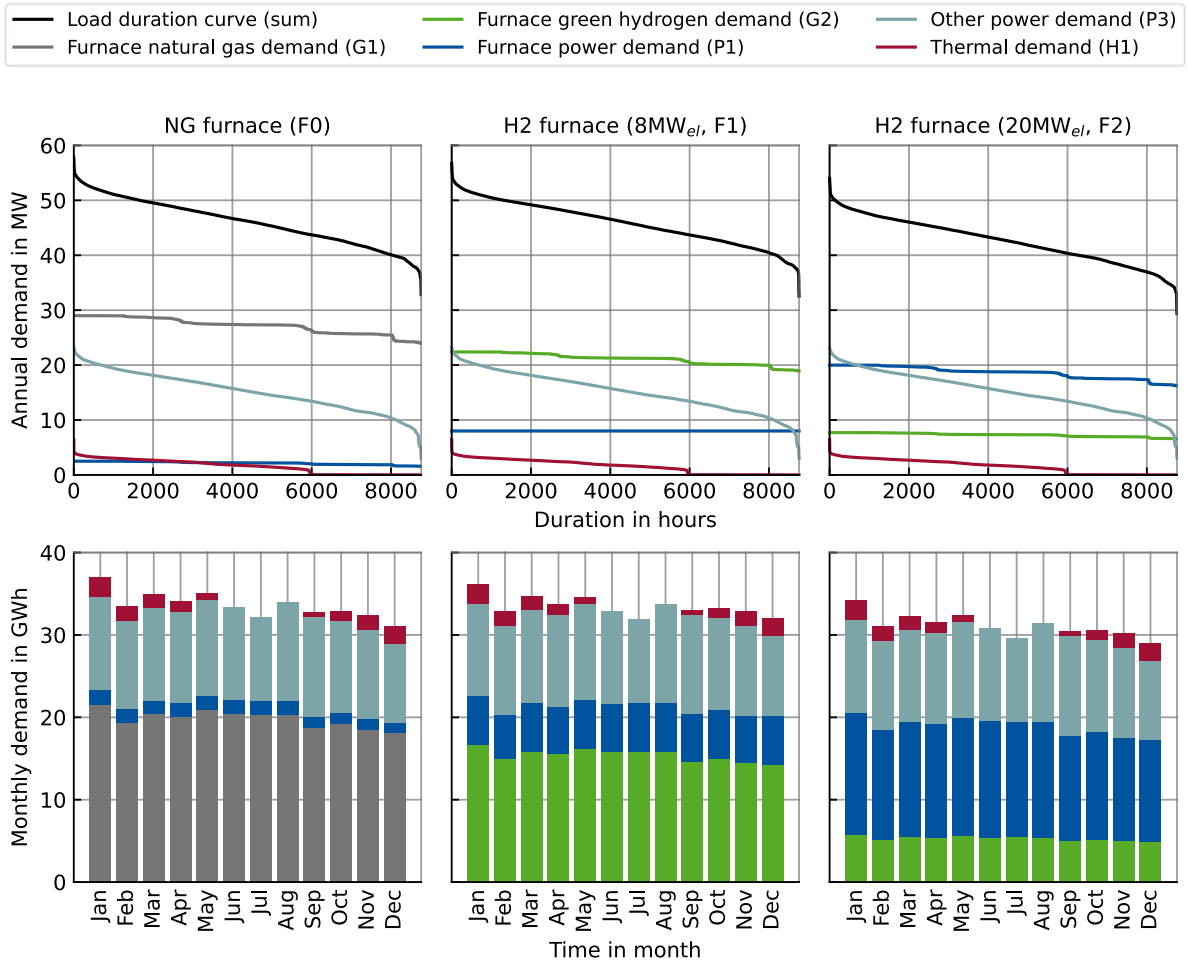

Figure 18: Characteristics of the demand input profiles, classified by type of furnace used for the scenarios. The upper plots show the annual load duration curves, while the lower plots show aggregated monthly energy demands.

Overall, the aggregated load duration curves indicate that the glassworks site's energy demand ranges from 29-58 MW. Moreover, from left to right, demand decreases as electrification and, subsequently, furnace efficiency increase with higher levels of electrification. At the same time, the remaining site's electric and thermal demands are the same across all scenarios. The monthly energy demands complement the picture. The measured data show that energy demand is highest in January and gradually decreases throughout the year. Moreover, thermal demand is comparatively low and shows a seasonal pattern with no demand from June to August. The reason for this pattern is that thermal

demand mainly comes from space heating of the manufacturing halls [102]. Another takeaway from monthly energy demand data is declining hydrogen demand as furnace electrification increases. This is a key characteristic that has a major impact on the model outcome.

4.3.2. Optimised portfolios for power purchase agreements

One of the main inputs for the developed industry flexumer framework is pre-optimised PPA portfolios. To obtain optimised PPA portfolios for the different scenarios, the methodology by Brucksch et al. [24] is used. By applying stochastic optimisation, it is possible to account for uncertainties in RE generation and demand variation. The considered geographical scope for PPA assets is Germany, as it counts as one bidding zone, which complies with the requirement from the EU RED II for green hydrogen production [21]. Moreover, the method employs geographical clustering of Germany, with each cluster representing distinct local PV and WPP generation characteristics. The optimiser can choose from all clusters to put together the best PPA portfolio. In addition to PV and WPP, the optimiser can choose hydropower PPAs that are modelled with 100% availability for the whole year in a simplified approach. However, hydropower capacity in Germany is limited to only 6.44 GW [163]. Therefore, a conservative pricing assumption of 200 EUR/MWh (see Table 11) is chosen to minimise the contracting of hydropower PPAs.

The methodology is applied to the glassworks use case. A simplified representation of the energy system with electrolysis and battery storage system is implemented. Other inputs include the two historical weather years of 2020 and 2023, as well as variations of the load. Finally, the PPA portfolio optimisation is applied to the basic scenario framework as defined in Table 11 for the support years of 2024, 2030, and 2037. In addition, it distinguishes between low (F1) and high (F2) electrification of the hydrogen furnace, as defined in Table 9. Another variation arises from the choice of AWE or PEM technology for the electrolyser system (see Table 16). Moreover, under a conservative assumption, we assume lower efficiencies at full load for the electrolyser system in individual support years, including a maintenance rate of 5% per year (see Table 16). In addition, for the battery storage and the electrolysis system, we assume decreasing specific investment costs (see Table 15 and Table 16). Furthermore, in all scenarios, hourly temporal correlation between generation from PPAs and electrolysis system demand is applied in a conservative manner to account for the highest requirements of the RED II [21]. Overall, this leads to 12 optimised PPA portfolios comprising different PV, WPP, and hydropower generation assets, as summarised in Table 14. We observe that across all portfolios with low furnace electrification, substantial amounts of energy are contracted through hydropower PPAs. In addition, large minimum battery capacities between 115-471 MWh are required to buffer the generation from contracted PV and WPP PPAs. Overall, the contracted capacity of PPAs decreases from 2024 to 2037 as the electrolysis system's efficiency increases. For portfolios with high furnace electrification, the picture changes.

Lower furnace hydrogen demand leads to less PPA contracting. Moreover, the contracted capacity spans across a larger number of assets and a wider variety of PV PPAs orientations.

Understanding the underlying characteristics of the optimised PPA portfolios requires a closer look at the temporal level. Figure 19 illustrates the load duration curves for all portfolios and contracted RE assets, as well as aggregated load duration curves for each portfolio. In addition, the demand for the electrolysis system is approximated by dividing the furnace's hydrogen demand by the assumed electrolyser system efficiencies.

Table 14: Summary of contracted PPAs for the different portfolios, which serve as input data for the decarbonised energy system model of the glassworks use case. The portfolios are optimised with the model developed in [24]. The weather station's data is provided by the German weather service [161].

Furnace type	PPA type	Orientation (if any)	Weather station ID (DWD)	Location of weather station (Distance to site in km)	Contracted capacity in MW					
Type of electrolysis system →					AWE			PEM		
Year of consideration →					2024	2030	2037	2024	2030	2037
Portfolio ID →					1	2	3	7	8	9
Low electrification (F1)	PV	South	1001	51.6451°N, 13.5747°E (526)	16.426	-	-	11.534	-	-
	PV	South	2925	51.3932°N, 10.3123°E (299)	1.134	12.545	9.119	1.460	12.724	13.190
	PV	South	3098	51.2452°N, 7.6425°E (114)	15.609	59.145	59.051	14.354	57.200	67.214
	PV	East	3098	51.2452°N, 7.6425°E (114)	25.053	2.396	3.941	27.882	6.948	-
	PV	South	5100	49.7479°N, 6.6583°E (132)	18.460	59.312	66.414	22.218	59.956	68.275
	WPP	-	197	51.3219°N, 9.0558°E (211)	48.763	63.815	65.496	53.358	68.172	72.930
	WPP	-	691	53.0451°N, 8.7981°E (303)	5.263	6.131	5.893	-	-	-
	WPP	-	1001	51.6451°N, 13.5747°E (526)	40.853	16.218	-	40.030	11.084	3.570
	WPP	-	1200	54.0691°N, 9.0105°E (405)	-	-	-	6.392	6.355	5.996
	WPP	-	2023	48.7918°N, 10.7062°E (403)	49.966	44.971	39.853	55.553	48.845	43.973
	WPP	-	5349	53.5196°N, 12.6654°E (534)	33.528	53.980	54.570	40.754	58.077	62.026
	Hydro	-	-	-	26.383	20.570	16.793	34.374	26.619	22.682
	Minimum battery storage capacity at industrial site in MWh →				115.107	396.449	449.173	115.386	386.287	470.074
Portfolio ID →					4	5	6	10	11	12
High electrification (F2)	PV	South	891	53.8713°N, 8.706°E (376)	-	3.282	-	-	1.862	2.054
	PV	East	1001	51.6451°N, 13.5747°E (526)	-	-	3.724	-	-	-
	PV	South	1001	51.6451°N, 13.5747°E (526)	37.166	35.242	22.685	36.152	31.650	34.752
	PV	East	2925	51.3932°N, 10.3123°E (299)	2.581	8.759	12.620	-	2.678	10.477
	PV	South	2925	51.3932°N, 10.3123°E (299)	-	-	-	-	13.537	0.463
	PV	South	3098	51.2452°N, 7.6425°E (114)	28.571	8.142	-	32.767	12.888	12.359
	PV	East	3098	51.2452°N, 7.6425°E (114)	15.143	35.939	39.765	10.185	23.132	29.231
	PV	East	5100	49.7479°N, 6.6583°E (132)	10.166	20.516	30.842	16.561	7.547	15.261
	PV	South	5100	49.7479°N, 6.6583°E (132)	-	3.126	-	0.227	26.970	15.460
	PV	East	5109	53.5998°N, 13.3039°E (575)	-	-	6.075	-	-	-
	WPP	-	197	51.3219°N, 9.0558°E (211)	41.434	46.052	37.536	49.244	61.247	53.546
	WPP	-	691	53.0451°N, 8.7981°E (303)	4.281	3.954	4.000	-	-	35.687
	WPP	-	1001	51.6451°N, 13.5747°E (526)	40.583	37.336	32.751	41.349	40.352	-
	WPP	-	1200	54.0691°N, 9.0105°E (405)	-	-	-	4.863	4.202	4.031
	WPP	-	2023	48.7918°N, 10.7062°E (403)	43.089	35.415	30.107	41.890	36.725	36.337
	WPP	-	3660	50.3602°N, 6.8697°E (79)	14.917	1.200	6.422	9.060	-	2.446
	WPP	-	5349	53.5196°N, 12.6654°E (534)	32.775	32.925	31.016	39.947	35.607	34.305
	Hydro	-	-	-	0.174	-	-	2.278	-	-
	Minimum battery storage capacity at industrial site in MWh →				80.205	97.007	80.608	73.303	153.000	128.723

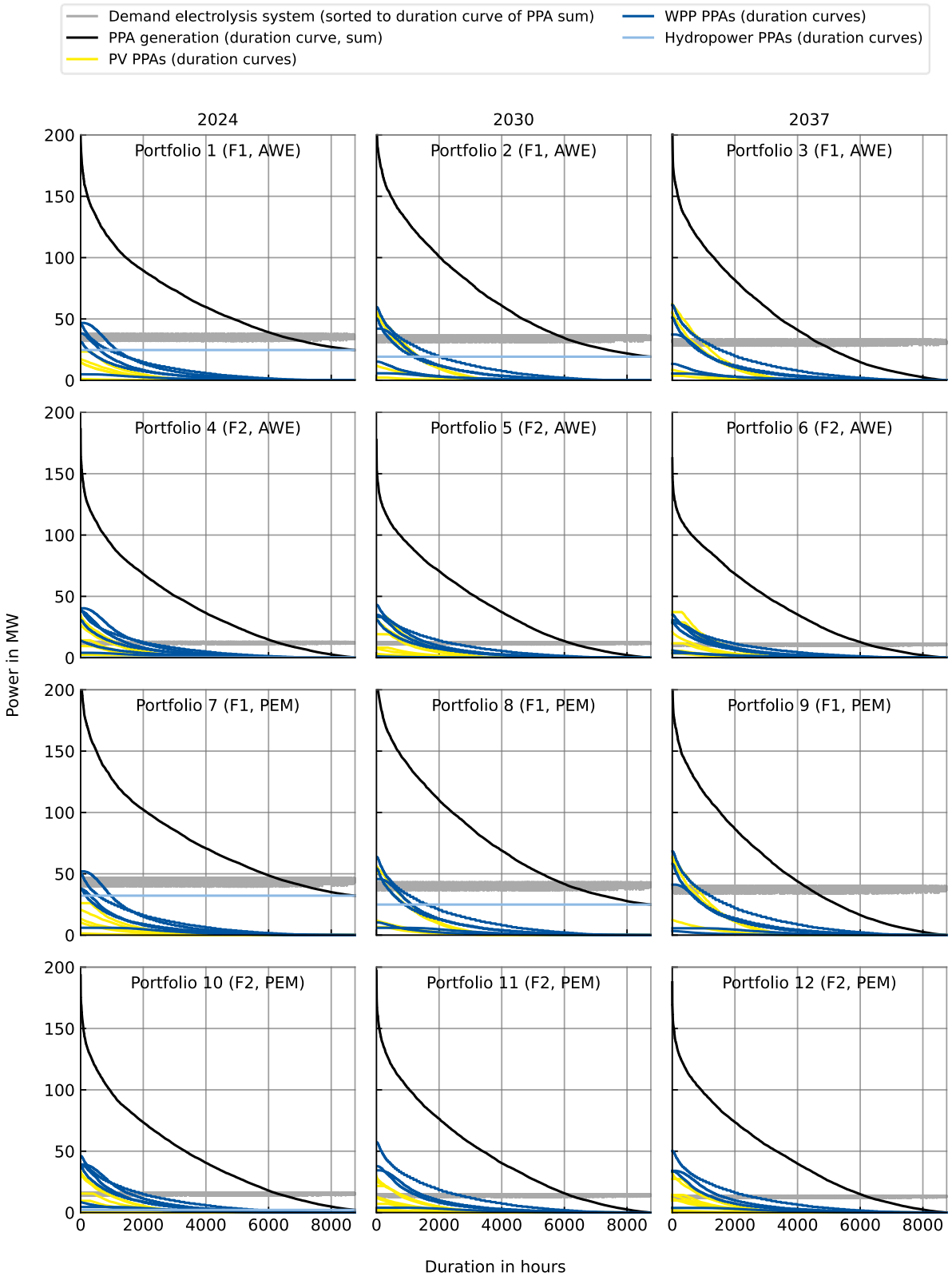

Figure 19: Characteristics of renewable generation from PPA portfolios. It distinguishes between AWE and PEM electrolysis systems, as well as between low (F1) and high (F2) furnace electrification. The electrolysis system demand is approximated based on the furnace's invariable hydrogen consumption, with a fixed electrolysis system efficiency loss.

From the load duration curves in Figure 19, we can observe that hydropower PPAs (light blue) act as a baseload, shifting the portfolio's aggregated load duration curve upward. The area under the electrolysis system demand curve and above the aggregated load duration curve corresponds to the total storage demand that is required. From this correlation, we find that storage demand is reduced with hydropower PPAs. Moreover, the optimisation achieves the highest required storage capacity for low electrification of the furnace when the electrolysis system demand is highest. In particular, in 2037, with low specific investment costs for the battery, this leads to high optimal storage capacities (see Table 14), which is more cost-competitive than a solution with hydropower.

4.4. Component parameterisation

The energy system model for the present and future glassworks site includes a variety of electric, thermal, and hydrogen components. Accurate parameterisation of those component models for defined scenarios is essential to achieving high-quality results. This section summarises the parameterisation for all required components. This concerns all energy conversion and storage components, including the electrolyser system, battery storage system, and other smaller components (see Subsection 4.4.1). In addition, Subsection 4.4.2 highlights the parameterisation of all market components. Furthermore, the time step clustering algorithm for the sizing layer of the FOCUS flexumer model requires adequate parameterisation (see Subsection 4.4.3).

4.4.1. Parameterisation of energy conversion and storage components

For all new component models required for decarbonisation, we provide a sizing range rather than fixed sizes. Within these ranges, the optimiser finds the best sizing of each component based on the chosen objective function. One parameter that primarily influences the sizing layer's results is component investment costs. In particular, components with higher investment costs, such as battery storage or electrolyser systems, have a substantial impact on investment decisions in the modelling.

To adjust investment costs from literature to 2024 price levels, we use the Harmonised Index of Consumer Prices (HICP) for industrial goods published by the European Central Bank (ECB) [146] (see Appendix C, Table 24). For currency conversion from US Dollar to Euro, the ECB provides annual average values [147] (see Appendix D, Table 25). Other parameters include maintenance costs, service life, and efficiencies. Table 15 summarises the parameterisation for all electrical component models in dependence on the scenario years (Subsection 4.2.2).

Table 15: Parameterisation of electrical components for the energy system model of the glassworks use case. Components include a large-scale rooftop PV system, a PV inverter, a battery storage system, an inverter, and a transformer.

Parameter	Unit	Symbol	2024			2030			2037			Ref.
			low	high	mid	low	high	mid	low	high	mid	
Large-scale rooftop PV												
Power capacity	MW_p	$P_{N,PV}$	Optimised: 0 - 12.315									
Spec. investment costs	EUR_{2024}/kW_p	κ_{inv}	831	1531	1181	784	1470	1127	724	1395	1060	[8]
Fixed operational costs	%/Inv.	$f_{fix,op}$	2.39	1.34	1.72	2.59	1.42	1.83	2.88	1.52	1.99	[8]
Service life	a	$L_{calendar}$	30									[8]
PV inverter												
Power capacity	MW	$P_{N,PV,inv}$	Optimised: 0 - 12.315									
Spec. investment costs	EUR_{2024}/kW	κ_{inv}	69			46			23			[165]
Fixed operational costs	%/Inv.	$f_{fix,op}$	0.5	1.5	1.0	0.5	1.5	1.0	0.5	1.5	1.0	[166]
Service life	a	$L_{calendar}$	10	20	15	10	20	15	10	20	15	[166–168]
Efficiency (one-way)	%	η_{inv}	97									[79, 169]
Battery storage system (LFP) – without inverter – MW range												
Energy capacity	MWh	$P_{N,bat}$	Optimised: 0 – inf. / fixed for flexibility scenarios D-H									-
Spec. investment costs	EUR_{2024}/kWh	κ_{inv}	156	330	243	83	217	151	81	199	141	[12, 166]
Fixed operational costs	%/Inv.	$f_{fix,op}$	0.5	1.5	1.0	0.5	1.5	1.0	0.5	1.5	1.0	[166]
Service life	a	$L_{calendar}$	13	21	17	13	23	18	13	26	20	[166]
Cycle lifetime (EFC)	#	L_{cycle}	7200			8300			9600			[166]
Input/output efficiency	%	$\eta_{in} \mid \eta_{out}$	98									[169]
Min. SOE	%	SOE_{min}	10									Assump.
Max. SOE	%	SOE_{max}	90									Assump.
Initial SOE at t_0	%	SOE_{init}	30									Assump.
Efficiency to grid (path)	%	η_{path}	89.4									[166, 169]
Self-discharge	%/month	η_{self_dch}	0.1									[170]
Battery inverter												
Power capacity	MW	$P_{N,bat,inv}$	Optimised: 0 – inf. / fixed for flexibility scenarios D-H									-
Spec. investment costs	EUR_{2024}/kW	κ_{inv}	62	102	82	56	94	76	48	85	66	[166]
Fixed operational costs	%/Inv.	$f_{fix,op}$	0.5	1.5	1.0	0.5	1.5	1.0	0.5	1.5	1.0	[166]
Service life	a	$L_{calendar}$	20	34	27	20	36	28	20	37	29	[166]
Efficiency (one-way)	%	η_{inv}	97									[79, 169]
Battery transformer												
Power capacity	MW	$P_{N,bat,inv}$	Assumption: same as battery inverter									-
Spec. investment costs	EUR_{2024}/kVA	κ_{inv}	16									[171]
Fixed operational costs	%/Inv.	$f_{fix,op}$	Assumption: same as battery inverter									[171]
Service life	a	$L_{calendar}$										
Efficiency (one-way)	%	η_{inv}	97									[169]

Legend: Parameters used for the evaluation (■)

For utility rooftop PV, we assume that the lowest possible investment costs reported in the literature can be achieved, as industrial-scale companies can potentially benefit from purchasing large quantities. By using the tool “Energie Atlas” (Eng.: Energy Atlas) [172] of the federal state of North Rhine-Westphalia (NRW), the maximum size of the PV rooftop system calculates to 12.315 MWp [136], with the simplifying assumption that all panels face south and rooftops can be fully covered. Concerning the efficiency of BESS, we take into account the losses for all relevant components, including the battery inverter and transformer, with typical values reported in [169]. We model the battery inverter and transformer as a single component. At the same time, we assume that transformers at the GCP have the same one-

way efficiency of 97%, resulting in a path efficiency from the BESS to the electric power grid of 89.4%. Furthermore, the assumption is that the transformer capacity at the GCP with 120 MVA [102] is large enough to be able to cover the additional demand of the electrolysis system and other components for decarbonisation.

Similar to the parameterisation of electrical components, we collect parameters for AWE and PEM electrolyser systems in Table 16. One critical parameter is electrical efficiency. However, differentiation of various efficiencies is important. While often voltage efficiencies are stated, the relevant parameter for conversion from electricity to hydrogen is the electrical efficiency [107]. Moreover, the efficiency applies to hydrogen's lower heating value (LHV), as we combust it to exploit its thermal energy in the furnace. To convert from HHV to LHV-based efficiencies, we use a factor of 0.85 [107]. To account for the part-load efficiency of the electrolysis system, the efficiency curves approximated in Subsection 2.3.2 for AWE and PEM are used for the operating layer of the model. We use two support points for the highest efficiency at 47% and 30% for AWE and PEM, respectively, lower efficiencies at 100% nominal load, and lower turn-on powers to model two linearised efficiency curves. For the sizing layer, the average efficiency at 75% load is modelled to account for non-optimal operation. For WHR modelling, the overall electrolyser system efficiency is required. This can be obtained by estimating the irreversible heat loss that cannot be further utilised for waste heat utilisation. We calculate this energy loss by using the energy balance in [173] for a PEM electrolyser and normalising it to the electrical efficiencies that we use for each year. For the AWE electrolysis system, irreversible heat loss is assumed to be at only 2.6% [174]. Another important parameter for the electrolysis system is ageing. To estimate the ageing reserve required in the model, we multiply the ageing rate by the stack lifetime. For the AWE system, this leads to reserves of 8.25%, 9.5%, and 12.5% for 2024, 2030, and 2037, respectively. For the PEM electrolyser system, the reserve needs to be 9.0%, 7.2%, and 15.0% for 2024, 2030 and 2037, respectively. The capacity reserve is incorporated into the model, leading to system oversizing at the beginning of life.

Another characteristic of PEM electrolysers is that the operating range can be up to 120% of the nominal power [180]. However, we limit the operation to 100% of the nominal load to reduce ageing and to avoid inefficient operation. As the electrolyser will be the most critical component of the new energy system, careful consideration of downtime is essential. Downtimes will substantially affect the sizing of other hydrogen components, including storage and compressors. On average, annual downtime is reported to be about 5% across the whole hydrogen production plant, including the electrolyser system, compressors, and pressure storage [162]. Given the large modularity of the hydrogen system, we assume that downtimes are evenly distributed across all 15-minute intervals in each year. Moreover, as a worst-case assumption, we expect a downtime of the hydrogen supply of 2 hours [162] until a hydrogen replacement, for instance, by a trailer, is available.

Table 16: Parameterisation of electrolysis systems to produce green hydrogen for the decarbonisation of the glassworks use case. It is differentiated between AWE and PEM electrolysis systems.

Parameter	Unit	Symbol	2024			2030			2037			Ref.
			low	high	mid	low	high	mid	low	high	mid	
Electrolyser (AWE)												
Power capacity	MW_{el}	$P_{N,el}$	Optimised: 0 – inf.									[102]
Spec. investment costs (incl. stack)	EUR_{2024}/kW_{el}	κ_{inv}	502	1406	954	402	854	628	201	703	452	[108, 112, 175, 176]
Stack costs	EUR_{2024}/kW_{el}	$\kappa_{inv,stack}$	242	429	336	52	257	155	112			[113, 177]
Fixed operational costs	%/Inv.	$f_{fix,op}$	1.3	3.5	2.4	2.5	4.9	3.7	3.9	8.0	6.0	[113, 178]
Service life	a	$L_{calendar}$	22.5	31	26	20	35	27	20	40	30	[113]
Electr. Effic. to H_2 (LHV)	$\eta_{on,N}$	%	63	70	66	65	71	68	70	80	75	[112]
Heat loss (no use)	%	$\eta_{heat,loss}$	2.6									[174]
Maintenance time (off)	% of time	$p_{off,min}$	5.0									[162]
Cold start (ramp up)	%/15min	$p_{ramp,cold}$	20	50	30	30	100	65	100			[113]
Standby power	% of P_N	$p_{standby}$	1	5	3	1	5	3	1	5	3	[113, 135]
Effic. factor at P_N	% of $\eta_{on,N}$	$\eta_{on,upper}$	90									[114]
Effic. factor at 0.47*P_N	% of $\eta_{on,N}$	$\eta_{on,lower}$	100									[114]
Effic. factor at 0.2*P_N	% of $\eta_{on,N}$	$\eta_{on,startup}$	74									[114]
Stack lifetime	1000 h	$T_{stack,life}$	60	90	75	90	100	95	100	150	125	[108, 112]
Aging rate	%/1000 h	$r_{el,aging}$	0.11			0.1						[179]
Capacity reserve	%/100	$r_{cap,res}$	0.0825			0.095			0.125			[108, 112, 179]
Electrolyser (PEM)												
Power capacity	MW_{el}	$P_{N,el}$	Optimised: 0 – inf.									[102]
Spec. investment costs (incl. stack)	EUR_{2024}/kW_{el}	κ_{inv}	1105	2180	1643	653	1873	1263	201	904	553	[108, 112, 176]
Stack costs	EUR_{2024}/kW_{el}	$\kappa_{inv,stack}$	384	1071	728	63	580	322	141	221	181	[113, 177]
Fixed operational costs	%/Inv.	$f_{fix,op}$	0.7	0.9	0.8	0.6	0.8	0.7	0.9	1.6	1.3	[113]
Service life	a	$L_{calendar}$	19	21	20	19	26	22	20	35	27	[113]
Electr. Effic. to H_2 (LHV)	$\eta_{on,N}$	%	56	64	60	63	68	65	67	74	70	[112, 173]
Heat loss (no use)	%	$\eta_{heat,loss}$	8			7			6			[173]
Maintenance time (off)	% of time	$p_{off,min}$	5.0									[162]
Cold start (ramp up)	%/15min	$p_{ramp,cold}$	63	94	78	83	100	91	100			[113]
Standby power	% of P_N	$p_{standby}$	1	5	3	1	5	3	1	5	3	[113, 135]
Effic. factor at P_N	% of $\eta_{on,N}$	$\eta_{on,upper}$	80									[115]
Effic. factor at 0.3*P_N	% of $\eta_{on,N}$	$\eta_{on,lower}$	100									[115]
Effic. factor at 0.05*P_N	% of $\eta_{on,N}$	$\eta_{on,startup}$	93									[115]
Stack lifetime	h	$T_{stack,life}$	30	90	60	20	90	60	100	150	125	[108, 112]
Aging rate	%/1000 h	$r_{el,aging}$	0.15			0.12						[179]
Capacity reserve	%/100	$r_{cap,res}$	0.09			0.072			0.15			[108, 112, 179]
Legend: Parameters used for the evaluation (■)												

Apart from the electrolyser system, the model includes other hydrogen and thermal components. This includes a hydrogen compressor system and a pressurised tank to buffer the produced hydrogen before it is combusted in the furnace. The size of the compressor is limited to 4.5 MW_{el}, which translates to 50 MW_{H2} considering the conversion efficiency. For hydrogen pressure storage, we assume a maximum capacity of 167 MWh_{H2}, corresponding to 5 tonnes of hydrogen. This is a regulatory threshold that, when exceeded, comes with higher requirements for safety measures, as hydrogen is defined as a dangerous substance according to BimSchV [181]. Therefore, the site operator has decided to stay below this threshold [102].

In the thermal sector, an industrial HP unit (including a heat exchanger) and an electric boiler are used to decarbonise SGS's heat supply. As the maximum heat demand is 6.408 MW_{th}, the upper power limits for optimising the industrial HP and the electric boiler are set to 1.8 MW_{el} and 6.5 MW_{el}, respectively, based on the industrial HP's lowest COP of 4. To increase the flexibility of heat supply, we also model the option to include thermal storage that can buffer heat for up to 24 hours, enabling the utilisation of daily wholesale electricity price spreads. With a 6 MW peak load, this yields a theoretical upper limit of 144 MWh_{th}. Table 17 summarises the parameters of all hydrogen and thermal component models.

Table 17: Parameterisation of additional hydrogen and thermal components required for the decarbonised energy system of the glassworks use case. This includes a hydrogen compressor unit, a pressurised hydrogen storage tank, an industrial HP, an electric boiler, and a thermal storage.

Parameter	**Unit**	**Symbol**	**2024**			**2030**			**2037**			**Ref.**
			low	high	mid	low	high	mid	low	high	mid	
H_2 compressor (low pressure)												
Power capacity	MW_{el}	$P_{N,comp}$	Optimised: 0 – inf.									[102]
Spec. investment costs	EUR_{2024}/kW_{H2}	κ_{inv}	52	83	67							[184–186]
Fixed operational costs	%/Inv.	$f_{fix,op}$	2	5	3.5							[183, 185]
Service life	a	$L_{calendar}$	12									[182]
Efficiency	%	$\eta_{H2,comp}$	91									[116, 187]
H_2 storage (pressurised tank type I, 20-30 MPa)												
Max. energy capacity	MWh_{H2}	$P_{N,H2,tank}^{max}$	166.65 (5 tonnes)									[102]
Spec. investment costs	EUR_{2024}/kWh	κ_{inv}	17	30	24							[183, 184, 186, 188]
Fixed operational costs	%/Inv.	$f_{fix,op}$	0.0									Assumption
Service life	a	$L_{calendar}$	40									[189]
Efficiency	%	$\eta_{H2,stor}$	100									Assumption
Initial SOE at t_0	%	SOE_{init}	50									Assumption
Self-discharge	%/day	η_{self_dch}	0.12									[190]
Industrial HP (T_{source}: 60-80°C, T_{sink}: 100-150°C)												
Power capacity	MW_{el}	$P_{N,HP}$	Optimised: 0 – 1.8									[102]
Spec. investment costs	EUR_{2024}/kW_{el}	κ_{inv}	300	1000	600	350	600	475	350	560	455	[101, 173, 191]
Fixed operational costs	%/Inv.	$f_{fix,op}$	2.5			3.2			3.3			[104, 173]
Service life	a	$L_{calendar}$	20			25						[104, 173]
COP	%/100	COP	2	6	4	5						[104, 173]
Heat exchanger												
Spec. investment costs	EUR_{2024}/kW_{th}	κ_{inv}	85									[173]
Electric boiler												
Power capacity	MW_{el}	$P_{N,elec,boil}$	Optimised: 4.2 – 6.5									[102]
Spec. investment costs	EUR_{2024}/kW_{el}	κ_{inv}	136									[191]
Fixed operational costs	%/Inv.	$f_{fix,op}$	0.4									[191]
Service life	a	$L_{calendar}$	20									[191]
Efficiency	%	$\eta_{elec,boiler}$	99									[191]
Thermal storage system (sensible, water)												
Energy capacity	MWh_{th}	$P_{N,stor,th}$	Optimised: 6 - 144									Assumption
Spec. investment costs	EUR_{2024}/kWh	κ_{inv}	40	100	70	36	100	68	34	100	67	[191]
Fixed operational costs	%/Inv.	$f_{fix,op}$	0.5									[191]
Service life	a	$L_{calendar}$	25									[191]
Input/output efficiency	%	$\eta_{storage,th}$	98									[191]
Self-discharge	%/week	η_{self_dch}	0.35	7	3.7							[192]
Legend: Parameters used for the evaluation (■)												

For efficiency considerations in industrial HPs, we assume the sink and source temperatures are constant. Therefore, the COP is constant at an average value of 4, as reported in literature [104] for the current technology development stage. For future years, we assume an improved constant value of 5. In addition to an industrial HP, a heat exchanger is required to utilise waste heat from the electrolyser system. The specific investment costs for the heat exchanger are assumed to be 85 EUR/kW_{th} [173]. Those costs are added to the investment costs for the industrial HP by multiplying them by the COP. Regarding cost and performance data for hydrogen compressors and storage vessels, there is significant uncertainty in the literature. Assumptions include that the storage vessel is lossless and that all losses in the compressed hydrogen storage system are accounted for in the compressor component. Furthermore, we assume that the service life of the low-pressure hydrogen storage is at least as high as the estimations for hydrogen pipelines. In addition, it is expected that fixed operational costs primarily apply to the compressor unit and can be neglected for the pressurised tank. For the compression unit, we assume a conservative service life of 12 years, as stated in [182], given its high technological maturity. However, new approaches to compression might emerge in the coming years, enabling more reliable and cheaper systems [183].

4.4.2. Parameterisation of market components

In addition to physical components, the energy system model of the decarbonised glassworks site also features market components that require parameterisation. The design of the wholesale and ancillary markets varies in terms of pricing, product length, and specific requirements for battery storage systems. Table 18 provides an overview of the parameterisation of the market components considered.

Regarding PPA contracting, we must account for transmission losses between generation and consumption. We assume an average distance of 373 km for PPA portfolios in Table 11 [24], resulting in transmission losses of 2.42% [193]. In addition, we assume that transformer and inverter losses at the generation plant accumulate to 4% [169]. Therefore, in total, we account for PPA transmission and distribution energy losses of 6.42%. For the fair value of DM with regard to the PV rooftop system, historic values are taken from publications of the Federal Network Agency for auctions in mid-2024 to calculate time-variant price signals [194]. For 2030 and 2037, we assume fair values will reduce proportionally to the reported average LCOEs for utility-scale PV (see Appendix B, Table 23). Further, we use fixed values, as we lack future wholesale price forecasts. The market design of the frequency control markets FCR and aFRR is mainly described in [90, 94]. For future frequency control market design, the simplified assumption is that conditions remain as is. For FCR, marketable power may be reduced by requirements for a so-called reserve operation [94]. Therefore, we calculate a minimum reserve factor in accordance with the PQ-conditions in Eq. (4.1), assuming an EPR of 1 and that half of the power can be potentially marked for FCR.

$$T_{res,FCR} = 1h - 2h * \frac{0.5\ MWh}{1\ MWh} * \frac{5\ min}{60\ min} = 0.916\ h \tag{4.1}$$

Table 18: Parameterisation of service/market components. This includes parameters for PPA contracts, DM, and spot markets, as well as for the ancillary services FCR and aFRR.

Parameter	Unit	Symbol	2024			2030			2037			Ref.
			low	high	mid	low	high	mid	low	high	mid	
Power purchase agreements (PPA)												
Efficiency (transm., distrib.)	%	$\eta_{tr,distr}$	93.58									[193]
Direct marketing (DM) (compensation scheme for RE generation)												
Fair value large PV rooftop*	EUR_{2024}ct/kWh	π_{FV}	7.950	10.19	8.940	8.130			6.990			[8, 194]
Intraday continuous (IDC) spot market												
Product length	h	$T_{len,IDC}$	0.25									[85]
Trade limit	kWh	$P^{el}_{limit,sell,buy}$	No limit set									-
Frequency containment reserve (FCR)												
Product length	h	$T_{len,FCR}$	4.0									[90, 94]
Minimum activation time	h	$T_{act,aFRR}$	0.25									[90, 94]
Recharge reserve	% SOE	r	25									[90, 94]
Minimum reserve factor	h	$T_{res,FCR}$	0.916									[90, 94]
Automatic frequency restoration reserve (aFRR) – capacity and energy market												
Product length (capacity)	h	$T_{len,cap,aFRR}$	4.0									[90, 94]
Product length (energy)	h	$T_{len,E,aFRR}$	0.25									[90, 94]
Minimum activation (capacity)	h	$T_{act,cap,aFRR}$	1	4	1.2							[90, 94]
Minimum activation (energy)	h	$T_{act,E,aFRR}$	0.25									[90, 94]
Recharge reserve	% SOE	r	0									[90, 94]
Price position (energy)	%/100	$p_{afrr,pos}$	0.2									Assumpt.
Average activation power	%/reserve	$f_{act,aFRR}$	100									Assumpt.
Legend: Parameters used for the evaluation (■)			*see direct marketing (DM) concept in Subsection 2.4.1									

Another parameter with higher uncertainty is the minimum activation time of aFRR energy for assets with reduced energy storage capability, which includes battery storage. According to the prequalification conditions, a minimum activation of 60 minutes is sufficient in theory; in practice, the storage system operator must ensure that, worst case, the activation lasts the full duration of the 4-hour product window [94]. Therefore, battery storage operators usually need to implement additional storage management measures that account for this worst-case scenario. These measures include recharge management and/or combined control groups of battery storage and assets with unlimited energy storage capability, such as conventional generators [94]. For the glassworks use case, recharge management via intraday trading is the optimal approach, as no other large conventional generation is available. The worst case for recharge management on the intraday is that 20 minutes remain until the next possible delivery, as the product duration is 15 minutes and the gate closure is 5 minutes before delivery [85]. The basic concept of this recharge limitation is explained in more detail by Thien et al. [195]. Therefore, for aFRR, we assume a minimum activation time of 1.2 hours. The actual activation of aFRR is enabled via a set point from the TSO [90]. The extent to which the

reserved power is activated depends on the single asset's geographical location and the electric power grid's characteristics [90, 93]. However, for simplification, we assume that if the battery storage is activated, it must activate its entire marketed power.

4.4.3. Parameterisation of time step clustering algorithm

The algorithm for clustering time steps (see Subsection 3.3.2) requires adequate parameterisation to fit the glassworks use case. For validation, we use the defined scenario with high furnace electrification and AWE electrolysis system, which proves to be the most promising decarbonisation setup during the analysis section. The scenario with no time-step aggregation, using 0.25-hour intervals, serves as a reference. Due to the high computational complexity of this reference, validation of the aggregation results is conducted only for the first half of the year, from January to July. This is expected to be sufficient to cover different seasonal and demand characteristics.
To find the optimal time-step clustering settings, we conduct a sensitivity analysis of the most relevant algorithm parameters (see Figure 20). This first concerns the threshold for the residual load (P_{RES}). It defines a band around the zero crossing of the residual load, where no clustering is allowed, to clearly separate times with deficits and surpluses in RE generation from PPAs. We analyse this parameter between 0.2-0.7 MW, in incremental steps of 0.1 MW. Moreover, we vary the percentile threshold (p_x) that filters time steps with peak power operation between 80-85%, in steps of 1%. In addition, the maximum length of aggregation intervals needs to be defined. For this parameter, we evaluate time intervals from 0.75 to 2.0 hours, with a step size of 0.25 hours.

Overall, the results of the sensitivity analysis indicate that adequate parameterisation is essential to avoid substantial deviations in component sizing of over 10%. Nevertheless, the influence of time step clustering on the overall annual costs is only minor, as the error is always <0.8%, which is less than the 2% error margin (MIP Gap) of the optimiser. In addition, the cost breakdown shows that the error in time-step clustering mostly arises from capital costs, while it does not substantially affect operating or emission costs.
The variation in maximum cluster size (T_{WIN}) indicates that, with increasing window size, the quality of the results generally decreases. In particular, with a maximum cluster size of 2 hours, substantial deviations in the sizing of the battery inverter exceed 20%. In general, for smaller components like the thermal storage (<1 MWh), sizing is more sensitive, as its influence on total costs is negligible. Moreover, for smaller components, such as the compressor, sizing depends heavily on the electrolysis system. Only small changes in the electrolysis system size can lead to substantial deviations for the compressor. A less obvious result can be observed when the maximum cluster size (T_{WIN}) is set to the lowest value of 0.75 hours. The deviation for the sizing of most components is substantially higher than for the 1-hour window. This can

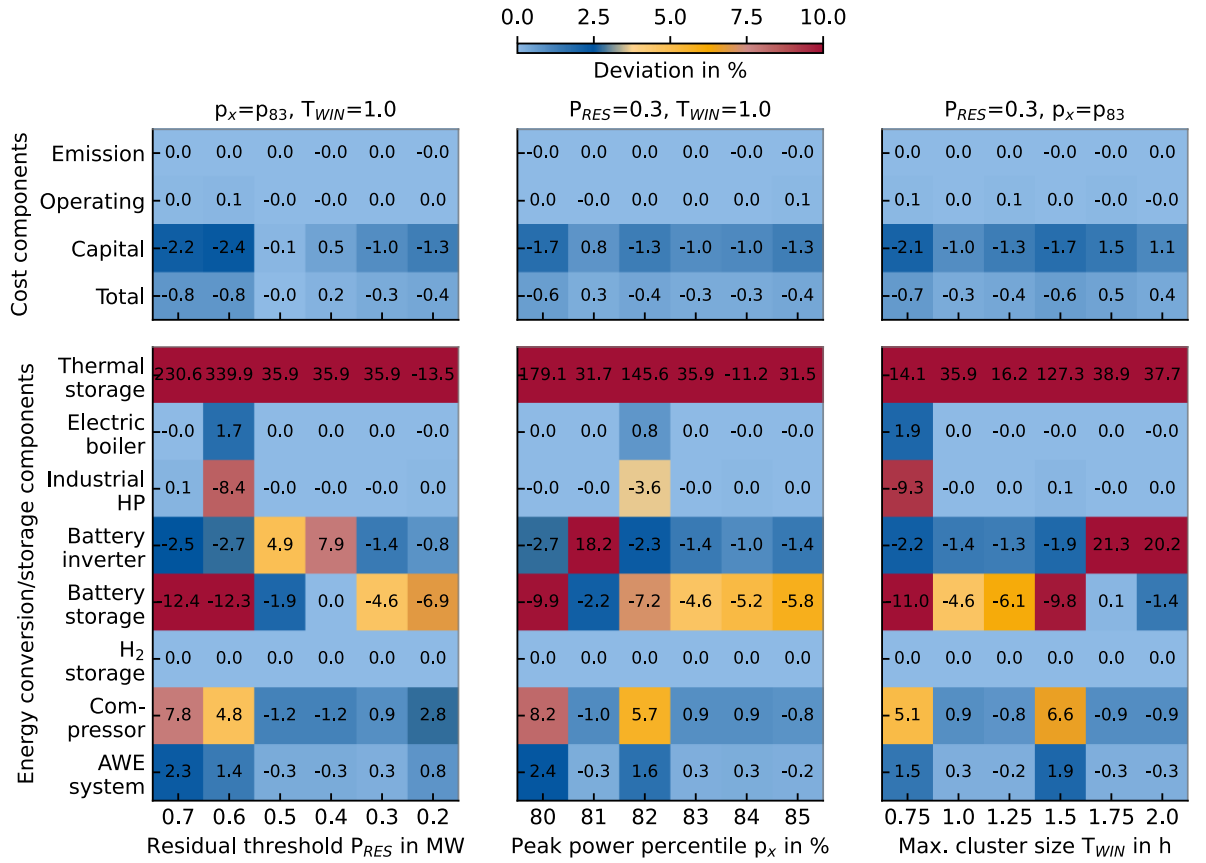

Figure 20: Sensitivity analysis of relevant parameters for the time step clustering algorithm, for the scenario with an AWE electrolysis system and high furnace electrification in 2024. The colours of the heat map indicate the deviation in cost components and component sizing relative to no aggregation, with time steps of 0.25 hours. The results are calculated over half a year, from January to July. For each parameter variation, the other two parameters are kept constant, as indicated above the heat maps.

be explained by the hourly granularity of RE generation from PPAs (see Table 13). The 0.75-hour aggregation intervals are not compatible with this granularity, leading to a RE generation pattern with a different dynamic. Therefore, we set the maximum time step duration to one hour.

Focusing on the threshold for the residual load (P_{RES}) we can observe that deviations are below 15% for most components. An exception is again the sizing of the thermal storage, given its small size (<1 MWh). To keep a safe margin to the higher deviations, we consider a threshold of 0.3 MW for (P_{RES}) to be optimal. The last parameter concerns the peak power threshold. The highest deviations occur when the percentile (p_x) is set to 80% (p_{80}). As the electrolysis and battery storage systems are the most important components of the energy system, we consider a percentile of 83% optimal. With this choice, the deviation in sizing for the electrolysis system is 0.3%, and for the battery storage system, -4.6%. The overall annual system costs, however, only deviate by -0.3%. We apply the identified optimal parameters to the time step clustering algorithm across all evaluation scenarios.

5. Case study: decarbonised energy supply for a glassworks

This section includes a comprehensive analysis of the glassworks use case, as described in detail in Subsection 4.1. The primary target for the future energy system of the glassworks site is to maximise GHG emission reductions at the lowest possible system cost. For the evaluation in this dissertation, we consider different design choices for the energy supply of the glassworks site. This includes variations in furnace design and the source of green hydrogen. For hydrogen furnace design, we differentiate between low electrification (F1) and high electrification (F2) with power ratings of 8 MW_{el} and 20 MW_{el}, respectively. The choices for obtaining green hydrogen break down into on-site electrolyser production and connection to a future hydrogen pipeline network. Specifically, regarding the electrolysis system, we further distinguish between alkaline water (AWE) and proton exchange membrane (PEM) technologies. While the design choices target the decarbonisation of the glassworks' energy supply, additional process-related GHG emissions occur during the melting of the glass raw materials. Solutions to reduce those additional emissions are excluded from the analysis as they are covered in detail by Jost et al. [17].

The analysis section is divided into three subsections. The first subsection (5.1) provides a high-level comparison of the different decarbonisation choices. Based on the insights from the first subsection, the second subsection (5.2) includes an in-depth analysis of the selected most promising decarbonisation setups. For the first and second subsections, we do not include peak power costs in the objective. Finally, Subsection 5.3 evaluates additional cost-reduction potential by leveraging battery storage flexibility, including peak-power-aware operation, wholesale trading, and ancillary services.

5.1. Comparison of decarbonisation options

Evaluating the best possible setup for the future energy system of the glassworks primarily requires comparing total annual system costs. They consist of annualised capital costs and annual operating costs. Figure 21 shows a high-level comparison of all possible decarbonisation scenarios by annual total system costs and share of capital costs. For energy prices, we consider the medium price projections for NG and electricity (see 'mid'-columns in Table 11). Rebuilding the existing NG furnace acts as a benchmark for all decarbonisation scenarios (grey colour). The results for the NG furnace show that, for future scenarios 2030 and 2037, total annual costs increase compared to the present 2024 scenario. In particular, for 2030, the increase is substantially higher, at about 18.9%, compared to 13.2% in 2037. At the same time, the comparably low share of investment costs is further decreasing from 10.7% in 2024 to below 10% in 2030 and 2037. As capital costs remain the same, this indicates that operating costs are increasing, mainly due to higher energy and emission-related costs (see Figure 25).

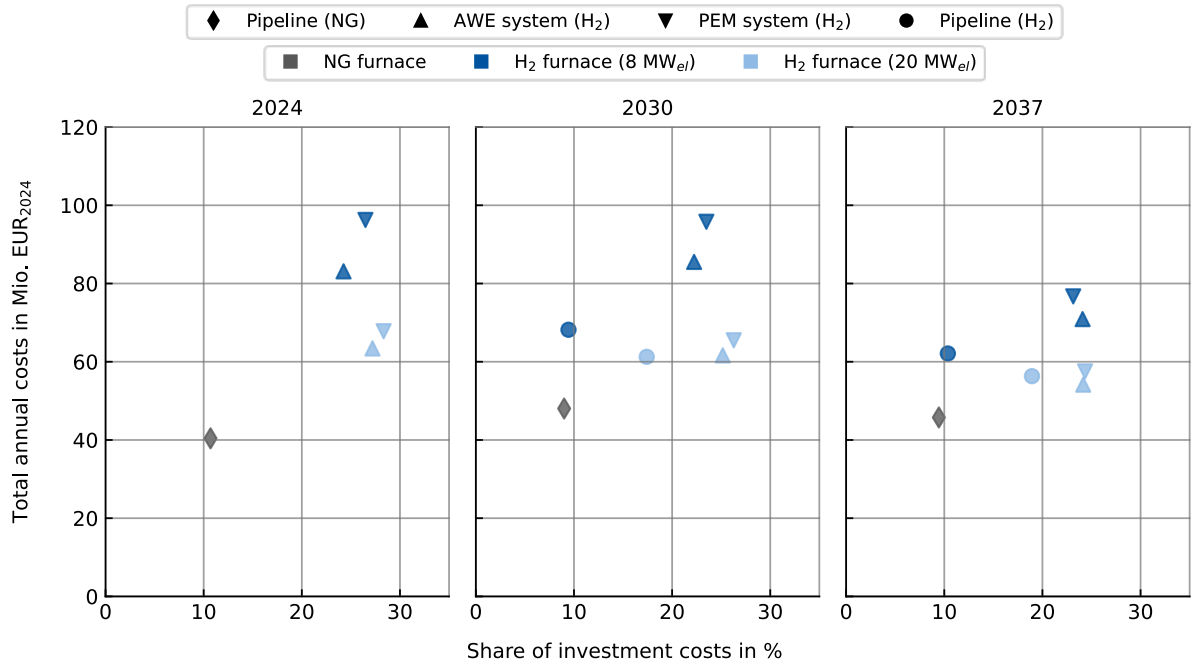

Figure 21: Comparison of all considered decarbonisation scenarios for the future energy system of the glassworks use case, for different years of installation. Rebuilding the existing NG furnace serves as a reference. For future energy prices, medium energy price projections are considered. While the symbol in the upper legend indicates the fuel source, the colour in the lower legend represents the furnace design. Table 19 summarises all source data.

For decarbonisation scenarios (blue colour), the results show that the total annual costs for installing a hydrogen-based solution in 2024 are consistently higher than those of the NG-furnace-based scenario. At the same time, the share of investment costs is substantially higher, with shares between 24-29%. Depending on the decarbonisation scenario, the increase in total annual costs in 2024 is between 56-139% compared to the NG furnace. A hydrogen furnace with high electrification and an AWE electrolysis system achieves the most cost-competitive decarbonisation in 2024 with total annual costs of 63.4 Mio. EUR_{2024}. On the contrary, in the worst case, a low level of furnace electrification combined with a PEM electrolyser system leads to substantially higher total annual costs of 96.2 Mio. EUR_{2024}. This mainly comes from higher capital costs and lower efficiencies for the PEM technology in 2024, compared to the AWE technology.

The picture only marginally changes towards 2030, with most decarbonisation scenarios with electrolysis systems showing total annual costs similar to 2024. In line with the 2024 scenarios, the most economical decarbonisation is achieved with the AWE electrolysis system and high furnace electrification, with total annual costs of 61.6 Mio. EUR_{2024}. The main driver for cost decreases from 2024 to 2030 is lower capital costs for electrolyser and battery systems. However, for scenarios with an electrolysis system and low furnace electrification, the costs are even slightly higher in 2030, particularly due to increased peak power costs, levies, and taxes (see Subsection 5.2.1, Figure 30). In 2030, in addition to the scenarios with the electrolysis system, we consider connecting to a hydrogen pipeline network when available.

The results indicate that, for high furnace electrification, this decarbonisation choice is at similar costs to the solution with AWE electrolysis. With total annual costs of 61.3 Mio. EUR_{2024}, the difference is less than 1%. However, focusing on the low electrification cases reveals the downside of the approach with pipeline connection. The comparatively high hydrogen energy prices in the pipeline case become disadvantageous as the required amount of hydrogen increases.

Table 19: Summary of total annual system costs for all regular scenarios of the future energy system of the glassworks use case. See the data visualisation in Figure 21. For future energy prices, medium energy price projections are considered.

Technology type	**Pipeline (NG)**	**AWE system (H_2)**		**PEM system (H_2)**		**Pipeline (H_2)**	
Furnace type	**NG-F0**	**H2–F1**	**H2-F2**	**H2–F1**	**H2-F2**	**H2–F1**	**H2-F2**
2024							
Share invest costs in %	10.698	24.253	27.200	26.481	28.336		
Total annual costs in Mio. EUR_{2024}	40.414	83.118	63.411	96.246	67.785		
2030							
Share invest costs in %	9.000	22.239	25.160	23.488	26.283	9.441	17.410
Total annual costs in Mio. EUR_{2024}	48.036	85.530	61.639	95.772	65.472	68.179	61.251
2037							
Share invest costs in %	9.448	24.095	24.155	23.138	24.345	10.364	18.936
Total annual costs in Mio. EUR_{2024}	45.758	70.915	54.147	76.703	57.518	62.109	56.315

The picture changes towards 2037, with substantial cost-reduction potential for decarbonisation choices compared to 2024 and 2030. Although rebuilding the NG furnace remains the most economical solution, the gap to the decarbonisation options is narrowing. With 54.1 Mio. $EUR_{2024,}$ the scenario with AWE electrolysis and high furnace electrification has 18.3% higher total annual costs than the NG furnace. The scenario with a hydrogen pipeline and high furnace electrification closely follows this solution.

Overall, the results emphasise that, independent of the decarbonisation choice, a moderate cost increase in glass production in the future can be expected. However, there is significant uncertainty about future developments in energy prices for NG, electricity, and green hydrogen. In particular, recent geopolitical tensions with the Russian invasion of Ukraine have caused unprecedented turbulence in the global energy markets [3] and proven the fragility of such. In addition, there is a high uncertainty regarding the development of CO_2 emission certificates.

While the previous results in Figure 21 hold under the assumption of medium energy price developments, further evaluations are required to account for price uncertainties. Therefore, we analyse the effect of two additional price sensitivities, including a scenario with low and high energy prices (see Table 11). Figure 22 and Figure 23 show the results of the sensitivity analysis. For the scenario of rebuilding the NG furnace, the total annual costs in 2030 and 2037 are similar to or even lower than those in 2024. This is mainly influenced by substantially lower NG prices that overcompensate for the assumed moderate increase in CO_2 emission costs. This leads to reductions of total annual costs for the NG-furnace-based scenario of over 12% in 2037, compared to 2024.

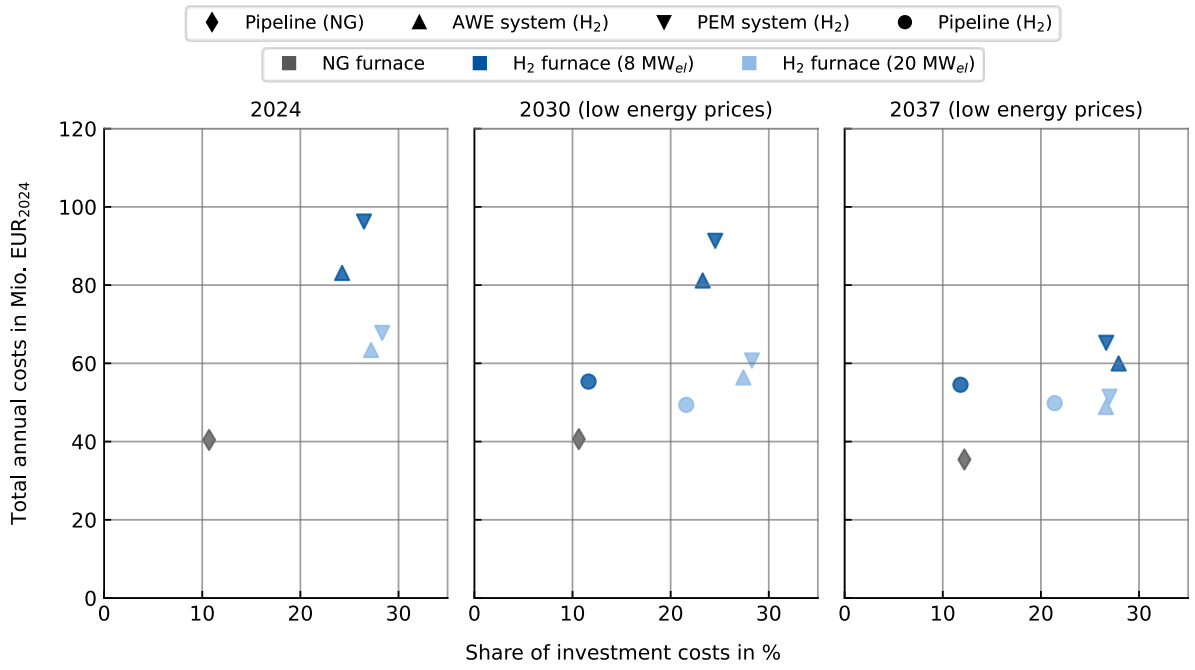

Figure 22: Comparison of all considered decarbonisation scenarios for the future energy system of the glassworks use case, distinguished by their share of investment costs. The status quo case with the NG furnace serves as a reference. For future energy prices, low energy price projections are considered. While the symbol in the upper legend indicates the fuel source, the colour in the lower legend represents the furnace design. Appendix H summarises all relevant source data.

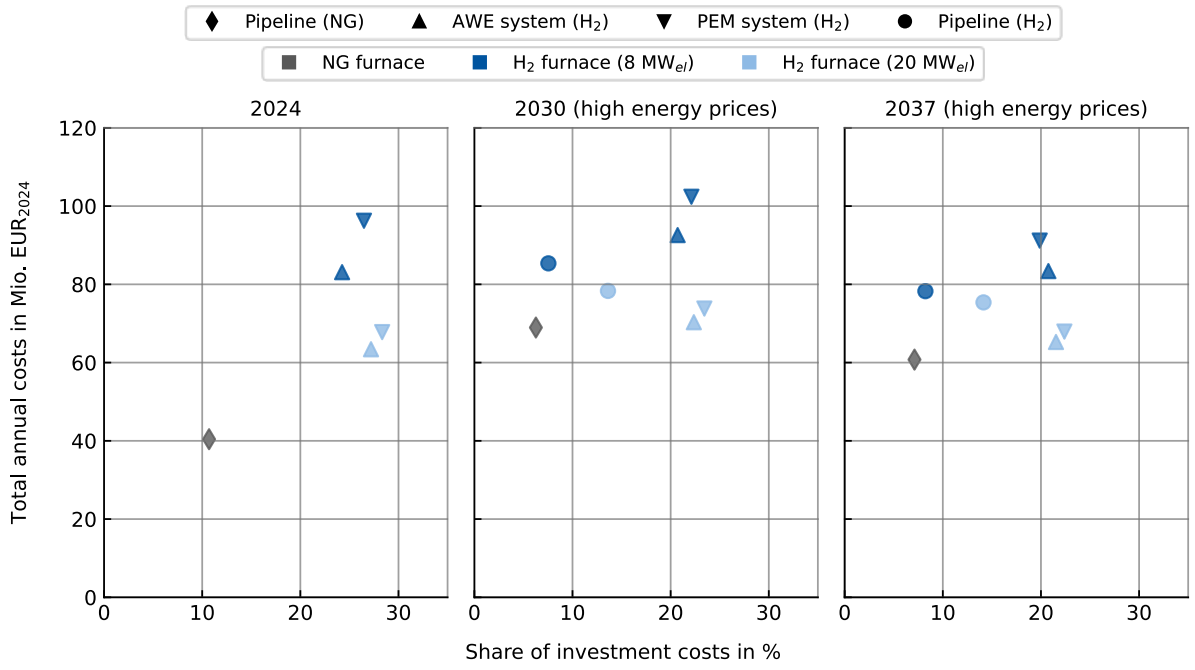

Figure 23: Comparison of all considered decarbonisation scenarios for the future energy system of the glassworks use case, distinguished by their share of investment costs. The status quo case with the NG furnace serves as a reference. For future energy prices, high energy price projections are considered. While the symbol in the upper legend indicates the fuel source, the colour in the lower legend represents the furnace design. Appendix H summarises all relevant source data.

Decarbonisation scenarios show an even greater potential for cost reductions in future years than the fossil setup. For 2037, the setup consisting of a furnace with high electrification and an AWE electrolysis system achieves total annual costs as low as 48.8 Mio. EUR_{2024}. This is 20.9% higher than for the NG furnace in the present 2024 scenario. Furthermore, the competitiveness of the hydrogen pipeline option in 2030 and 2037 substantially increases under the assumption of lower green hydrogen prices from the pipeline. In 2030, total annual costs are over 12% lower than in the best-case electrolysis system scenario for high-furnace electrification. In 2037, the gap closes again, with the hydrogen pipeline scenario costing only about 2% more. Overall, low energy prices are particularly beneficial for rebuilding the NG furnace or connecting to a hydrogen pipeline. However, the competitiveness of scenarios with an electrolysis system also slightly increases.

In contrast to previous conclusions, the results for high energy prices show a smaller gap between decarbonisation scenarios and rebuilding the NG furnace. The high energy prices disproportionately affect the total annual costs of the scenario for rebuilding the NG furnace. High NG and CO_2 emission certificate prices lead to a surge in total annual costs compared to medium energy price assumptions, with 43.6% in 2030 and 32.8% in 2037. On the contrary, the best-case decarbonisation scenario with an AWE electrolysis system and high furnace electrification only increases by 14.1% and 20.5% for 2030 and 2037, respectively, compared with the medium price assumptions. For 2030, this scenario even achieves only a 2% increase in total annual costs compared to the NG furnace. This emphasises the greater robustness of the scenarios with an electrolysis system due to greater independence from global energy prices. On the contrary, in scenarios with a hydrogen pipeline connection, higher energy prices negatively affect competitiveness relative to other decarbonisation choices. Similar to the NG furnace scenario, total annual costs increase disproportionately by 27.8% in 2030 and 33.9% in 2037 compared with the medium energy price scenarios, for high furnace electrification. This reflects the high dependence of this solution on cheap global hydrogen prices. At the same time, the results emphasise the risk of connecting to a hydrogen pipeline as a global market currently does not exist.

5.1.1. Levelised costs of hydrogen

Another key measure for comparing different decarbonisation choices for the glassworks use case is the levelised costs of hydrogen (LCOH). In the case of electrolysis-system-based setups, LCOHs are calculated by summing all required annualised investment and operating costs for hydrogen production and dividing them by the total amount of hydrogen produced. Subsection 3.3.3 provides the detailed mathematical formulations for the calculation of LCOH. For annualised investments, we consider the electrolyser system, compressor, hydrogen pressure storage, battery storage, and battery inverter. Even if the battery is not directly

connected to the hydrogen sector, it is required to power the electrolysis system with green power from PPAs while meeting the conditions for hydrogen production under RED II and RED III (see Subsection 2.4.2). For operating costs, we consider electricity costs for powering the electrolyser system and the compressor. For this, we neglect any revenues from selling PPA or supplying load with energy from PPAs. Moreover, regarding electric power grid fees, we only consider additional peak power costs incurred by hydrogen production. For 2024, some of the peak power costs can be reimbursed under current regulations. A detailed analysis in Subsection 5.2.1 (Figure 30) provides an overview of the cost breakdown. For the decarbonisation case where the site is connected to a future hydrogen pipeline, LCOH are predefined based on the assumption of global hydrogen energy carrier costs (see Table 11). Figure 24 illustrates the LCOH for all decarbonisation choices and years under consideration.

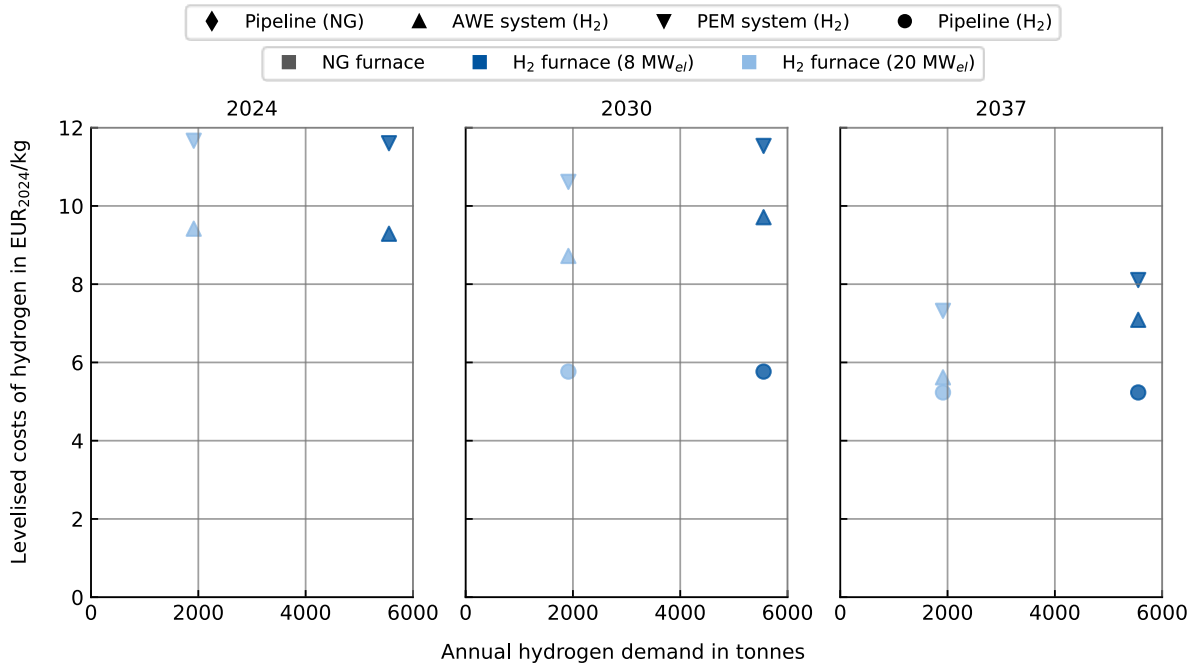

Figure 24: Levelised costs of hydrogen depending on the decarbonisation choice and year. For future energy prices, medium price projections are considered. While the symbol in the upper legend indicates the fuel source, the colour in the lower legend represents the furnace design. Appendix H summarises all relevant source data.

The results show that overall LCOH are decreasing towards 2037. While the LCOH is between 9.3-11.7 EUR_{2024}/kg in 2024, it reduces to between 5.2-8.1 EUR_{2024}/kg in 2037. The increase in LCOH in 2030 for scenarios with an electrolysis system and low furnace electrification mainly stems from higher peak power costs. Furthermore, the electrolysis-system-based scenarios show substantially lower LCOH for the furnace with high electrification. Higher furnace electrification reduces hydrogen production demand and, in turn, additional peak power. Regarding the type of electrolyser system, AWE technology has lower LCOH than PEM technology due to lower specific investment costs and higher efficiencies. This advantage remains similar across the considered years, with the AWE's LCOH 12.5-23.2% lower than the

PEM technology's in 2037. The decarbonisation choice with a connection to a future hydrogen pipeline shows competitive LCOHs of 5.8 EUR_{2024}/kg in 2030 and 5.2 EUR_{2024}/kg in 2037. Moreover, this solution always lies below the scenarios with an electrolysis system.
Reflecting on the total annual system costs (see Figure 21) confirms that the basic trends from the LCOH assessment are consistent. However, hydrogen costs are only one part of the equation. There are additional factors not reflected in the LCOH that improve the competitiveness of electrolysis-system-based scenarios. This includes utilising cheap generation from PPAs to meet the remaining power demand at the glassworks site and generating revenue by selling excess PPA generation to wholesale markets (see Figure 30).

5.1.2. Optimal sizing of components

Understanding the underlying effects and dependencies behind the observed variations in total annual costs requires a closer look at individual cost components and CO_2 emission results. Therefore, Figure 25 provides a comprehensive breakdown of costs and CO_2 emissions for all considered scenarios for the evaluation of the glassworks use case. The breakdown reveals that, for rebuilding the NG furnace in 2024, operating costs account for the largest share at 75.5%. Emission costs solely account for 13.8%. However, we observe substantial changes in this relationship in future-year scenarios. Operating costs for the scenario with an NG furnace increase in 2030, considering the projected increase in NG prices. This is mainly due to short-term scarcity and is expected to change again towards 2037, when NG prices are projected to return to levels before the 2022 energy crisis, assuming decreasing global demand [151]. On the contrary, CO_2 emission certificate costs are projected to increase in future-year scenarios to 125 EUR/t in 2030 and 200 EUR/t in 2037 (see Table 11). This leads to an increasing share of emission costs of 21.4% and 35.9% for 2030 and 2037, respectively. The amount of CO_2 emission is similar for all considered years, with 81.9 Mt in 2024 and 82.2 Mt in 2030 and 2037. The majority of CO_2 emissions come from the combustion of NG. For process-related emissions, we assume that, through advances in raw material composition, a 30% reduction is possible in future years [102]. At the same time, we observe 17.9% higher CO_2 emissions from the combustion of NG in 2030 and 2037, as we assume an increase in the NG provision's emission factor (see Table 11).

When focusing on decarbonisation choices, the factor with the greatest influence on operating costs is the furnace setup. In scenarios with low furnace electrification, operating costs are always higher than in high-furnace electrification scenarios. This mainly stems from the furnace's lower hydrogen consumption with higher electrification, leading to lower electric power demand in scenarios with an electrolyser system (see Section 5.2). For the hydrogen pipeline scenarios, the dominating cost component is operating costs. For 2030, they account for 9.4% and 10.4% of total annual costs under high and low furnace

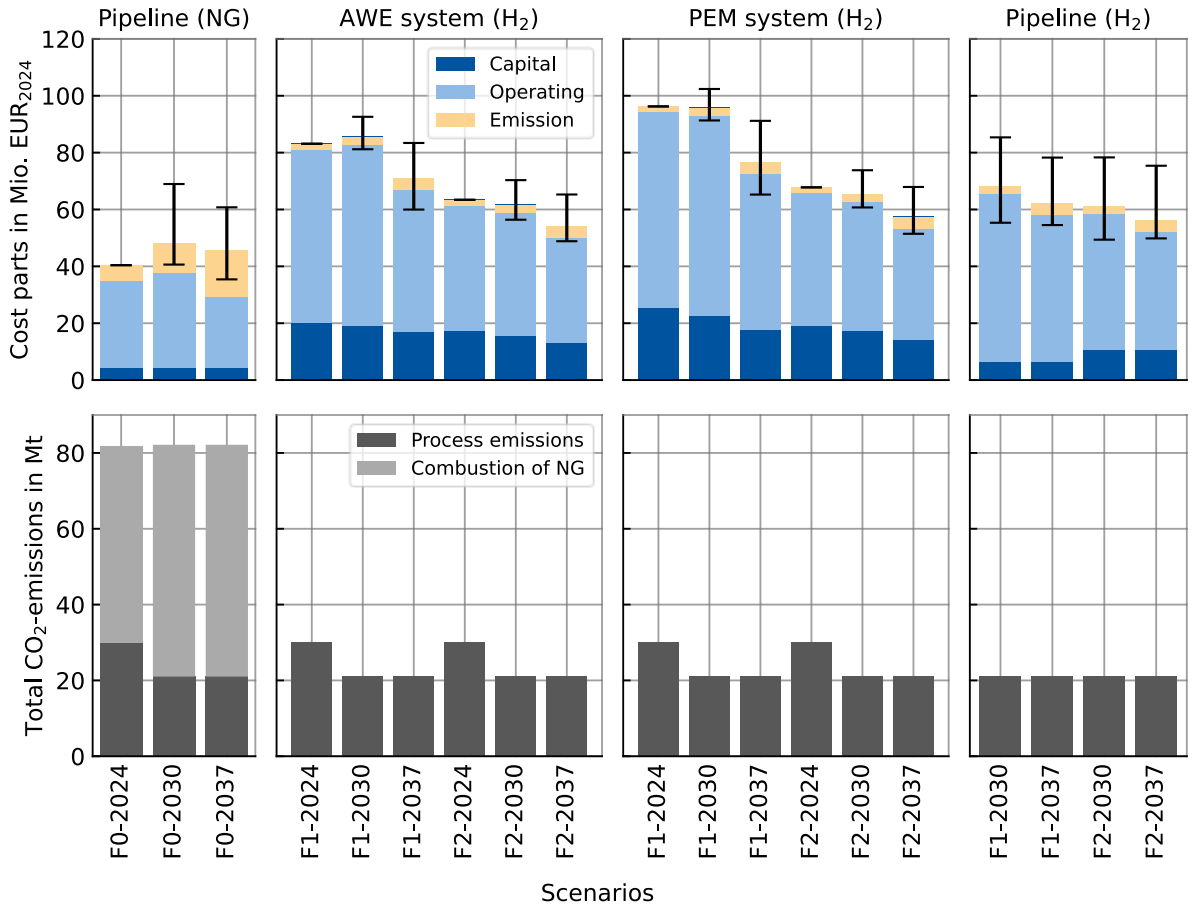

Figure 25: Breakdown of annual costs and CO_2 emissions for all considered scenarios for the glassworks use case evaluation. For future energy prices, medium price projections are considered the default. The error bars indicate the variation in total annual system costs across high and low energy price scenarios. Abbreviations: FO: NG furnace, F1: hydrogen furnace with low electrification, F2: hydrogen furnace with high electrification. Appendix H summarises all relevant source data.

electrification, respectively. This underscores the high dependence of this scenario on low import prices for green hydrogen. The comparatively large error bar representing price uncertainty leads to the same conclusion. Furthermore, we observe that, in scenarios with an electrolysis system, the main cost component remains operating costs. However, capital costs make up a substantially larger share than for the scenarios with an NG furnace and hydrogen pipeline. A clear trend can be observed that for all electrolysis-system-based setups, the operating and capital costs are decreasing towards 2037. For the AWE electrolysis system with high furnace electrification, operating costs decrease from 44.1 Mio. EUR_{2024} in 2024 to 36.9 Mio. EUR_{2024} in 2037. In general, the main driver of this trend is declining electricity and capital costs for electrolyser and battery storage systems (see the assumptions in Section 5.2). However, for 2030, the electrolysis-system-based scenarios show mostly similar or increasing operating costs. This particular comes from increased peak power costs and electric power grid levies (see Subsection 5.2.1, Figure 30). For the PEM electrolysis system, operating costs are substantially higher than for the AWE electrolysis system due to lower efficiencies.

For capital costs, several factors must be taken into account. On the one hand, capital costs for the furnace are assumed to be the same across all years, with substantially higher capital costs for higher furnace electrification. This difference is shown specifically for the hydrogen pipeline scenarios. On the other hand, capital costs for electrolysis and battery storage systems decrease over time. Therefore, overall capital costs for the scenarios with an AWE electrolysis system decrease by 15.2% and 24.2% from 2024 to 2037 for low and high furnace electrification, respectively. Compared with the AWE electrolysis system, the PEM electrolysis system has substantially higher capital costs due to higher specific investment costs.

The remaining cost position for emissions depends directly on the amount of CO_2 emitted. In the decarbonised energy system, we substitute NG combustion, leading to reductions in CO_2 emissions of 52.9% in 2024 and 74.4% in both 2030 and 2037. Consequently, the emission costs are substantially lower than in the scenario with an NG furnace. For all decarbonisation choices, this leads to emission costs of 2.0 Mio. EUR_{2024}, 2.6 Mio. EUR_{2024}, and 4.2 Mio. EUR_{2024} for 2024, 2030, and 2037, respectively. In particular, the impact of increasing CO_2 emission certificate costs for future years is substantially reduced. However, a share of process-related emissions of 21 Mt remains in 2030 and 2037, which can only be decreased further with additional measures, including CCS technologies. However, this is not within the scope of this dissertation and has been analysed in detail by Jost et al. [17].

Although operating costs account for the largest share of total annual costs across all scenarios, adequate component sizing, particularly in the electrolysis-system-based scenarios, is essential to remain within the range of competitiveness. Figure 26 shows the sizing of the relevant components to meet the hydrogen furnace's energy demand. This includes the electrolyser system, compressor, and hydrogen pressure storage. For reference, we include the furnace's predefined electrical power ratings (see Table 9). In addition, Table 20 summarises the optimal component sizes for all scenarios.
The optimal sizing results of components to supply the energy demand of the hydrogen furnace primarily show that the electric power rating of the electrolyser system is highly dependent on the level of electrification of the furnace. For the scenarios with AWE technology, the optimal electric power rating of the electrolyser system is between 39-44 MW_{el} and 13-19 MW_{el} for low and high furnace electrification, respectively. The decreasing trend from 2024 to 2037 is due to increasing efficiencies and declining capital costs over time. As the capital costs of the electrolysis system are a major cost driver for the new energy system (see Figure 29), scenarios with higher electrification are generally more beneficial. For the PEM technology, the lower efficiency compared to the AWE technology even leads to higher electrical power ratings of up to 55.4 MW_{el} in the case of low furnace electrification in 2024. Furthermore, we can observe that the reduction of electrolyser system size from 2024 to 2030 for AWE technology is only minor or even slightly increases. One factor

that leads to this outcome is the higher requirements for temporal matching of RE generation from PPAs and electrolysis consumption for 2030, according to the RED II [21]. While only monthly matching is required in 2024, hourly matching must be ensured in 2030. This requires increasing the size of the electrolysis system to allow greater flexibility during operation. In addition, as hydropower PPAs are increasingly avoided in future years (see Figure 19), generation variability increases. This can be better utilised with a larger electrolyser system.

Table 20: Summary of the optimal sizing of all energy system components, for all regular scenarios of the evaluation. Abbreviations: FO: NG furnace, F1: hydrogen furnace with low electrification, F2: hydrogen furnace with high electrification.

Tech.	Scenario	Energy conversion components (rated electric power in MW)					Energy storage components (rated capacity in MWh)		
		Electrolysis system	Compressor	Industrial HP	E-boiler	Battery inverter	Battery storage	H2 storage	Thermal storage
Pipe. (NG)	F0-2024	0.0	0.0	0.0	6.408	0.0	0.0	0.0	0.0
	F0-2030	0.0	0.0	0.0	6.408	0.0	0.0	0.0	0.0
	F0-2037	0.0	0.0	0.0	6.408	0.0	0.0	0.0	0.0
AWE system (H2)	F1-2024	43.606	3.793	3.792	2.616	29.883	225.668	166.650	0.0
	F1-2030	44.020	4.359	6.408	0.0	42.437	416.926	166.650	0.0
	F1-2037	39.292	2.337	6.408	0.0	37.996	449.173	21.226	0.0
	F2-2024	18.710	3.305	3.776	2.632	16.270	110.440	166.650	0.0
	F2-2030	17.133	2.625	4.266	2.142	19.643	144.483	166.650	0.345
	F2-2037	13.507	0.832	4.512	1.896	8.066	80.608	7.296	1.271
PEM system (H2)	F1-2024	55.361	4.245	3.792	2.616	33.722	145.670	166.650	0.0
	F1-2030	48.684	3.507	6.408	0.0	41.034	386.287	141.808	0.0
	F1-2037	48.414	2.354	6.408	0.0	39.565	470.074	21.226	0.0
	F2-2024	22.965	3.163	3.792	2.616	14.190	73.303	166.650	0.0
	F2-2030	18.253	1.904	4.173	2.235	22.017	155.409	166.650	0.0
	F2-2037	16.642	0.959	4.604	1.804	12.409	128.723	7.296	0.390
Pipeline (H2)	F1-2030	0.0	0.0	0.0	6.408	0.0	0.0	0.0	0.0
	F1-2037	0.0	0.0	0.0	6.408	0.0	0.0	0.0	0.0
	F2-2030	0.0	0.0	0.0	6.408	0.0	0.0	0.0	0.0
	F2-2037	0.0	0.0	0.0	6.408	0.0	0.0	0.0	0.0

The optimal sizing of the electrolysis system interacts with the sizing of the hydrogen pressure storage (see Figure 26) and battery storage capacity (see Figure 27). The optimiser tries to find a balance between increasing/decreasing the power rating of the electrolysis system and sizing the hydrogen and battery storage capacities. Possible factors that particularly influence this trade-off include specific investment costs and efficiencies that improve from 2024 to 2037. On the contrary, for the hydrogen pressure storage, those parameters are constant across all considered years. Another factor to consider is the maximum allowed hydrogen storage size in the modelling, in accordance with current safety regulations that limit storage to 5t (167 $MWh_{H2,LHV}$) without additional safety requirements [181]. Increasing this threshold can lead to substantially higher storage capacities for hydrogen and battery storage systems, as shown in Brucksch et al. [24]. Moreover, individual PPA portfolios across all scenarios may lead to different operational characteristics (see Figure 19). The superposition of all these factors yields less intuitive results regarding the sizing of the storage components.

For the hydrogen pressure storage, we can observe that in 2024 and 2030, the capacity is usually optimised to the maximum threshold of 167.65 $MWh_{H2,LHV}$ (see Figure 26). Another

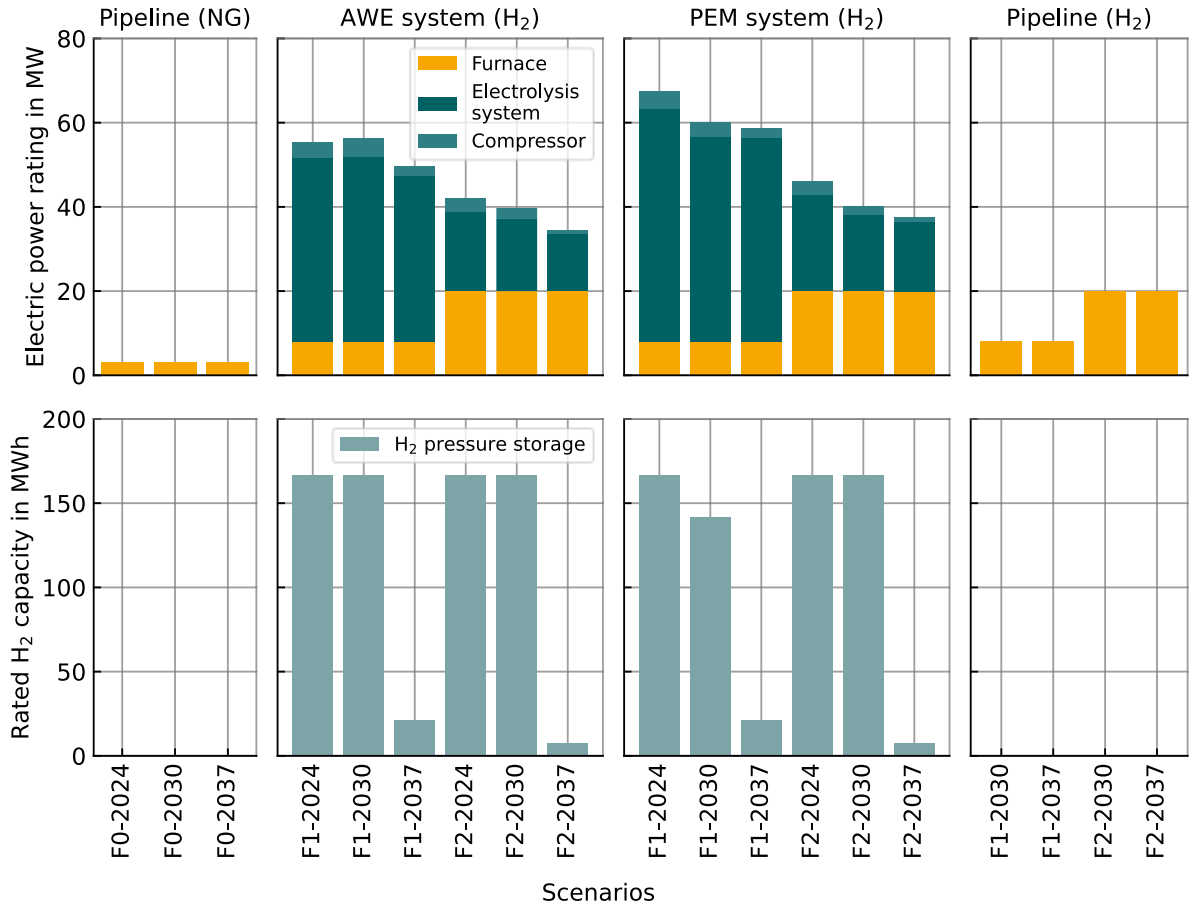

Figure 26: Optimised sizing of components to supply the energy demand of the furnace, including electrolyser system, compressor, and H_2 pressure storage, for all scenarios of the evaluation. For reference, we include the furnace's electric power ratings. Abbreviations: FO: NG furnace, F1: hydrogen furnace with low electrification, F2: hydrogen furnace with low electrification. Source data is provided in Table 20.

overall trend is that optimal capacities are decreasing towards 2037. This trend is mainly driven by improved performance parameters in the electrolysis system, including higher efficiencies. In 2037, the optimal hydrogen storage capacity reaches minimum values of 21.2 $MWh_{H2,LHV}$ for low electrification, and 7.3 $MWh_{H2,LHV}$ for high electrification of the furnace. The fact that those minimum capacities are independently reached for AWE and PEM technology proves that this is a lower threshold of the optimisation space. The threshold occurs when we model maintenance times of 5% per year for the electrolysis system, with only 50% of the system's capacity available in the worst case. During standby and off times when half of the electrolysis system's capacity is idle, the hydrogen storage needs to act as a buffer to meet the mostly constant hydrogen demand of the furnace (see Table 16). The electrical power rating of the compressor for pressure storage mainly depends on the size of the electrolyser system and the generation characteristics of the PPA portfolio. The results show sizes between 0.8-4.4 MW_{el}, which corresponds to between 4-18% of the electric power rating of the electrolysis system.

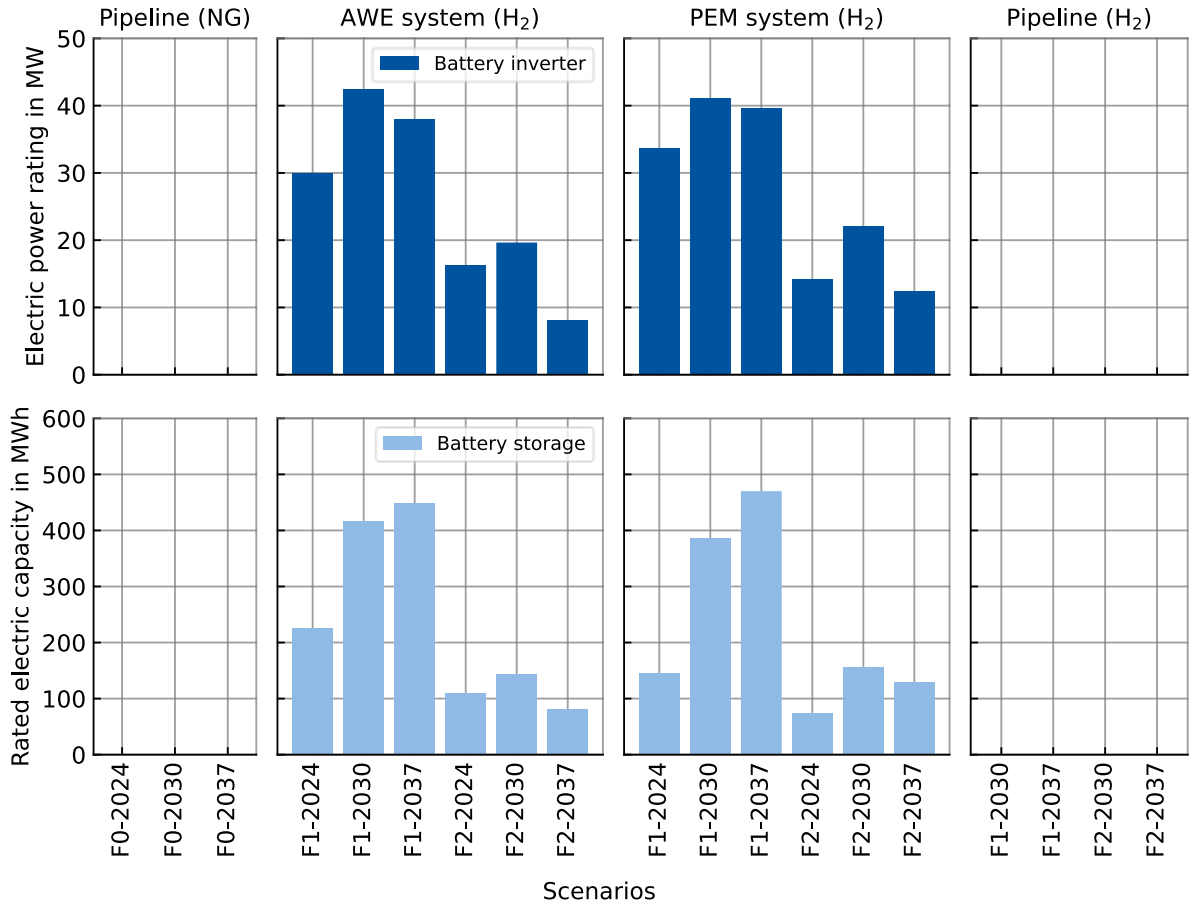

Figure 27: Optimised component sizing for the battery storage system to maximise utilisation of RE generation from PPAs. Abbreviations: FO: NG furnace, F1: hydrogen furnace with low electrification, F2: hydrogen furnace with low electrification. Source data is provided in Table 20.

For battery storage sizing, the results show a partial inverse trend compared to hydrogen storage sizing. By 2030, optimal battery storage capacity is expected to increase (see Figure 27). However, this is particularly pronounced in scenarios with low furnace electrification and less pronounced in those with high furnace electrification. At the same time, the results are very similar for scenarios with an AWE and PEM electrolysis system. The main reason for larger battery capacities with low furnace electrification is the increased hydrogen demand. This results in higher electricity demand for the electrolysis system. Serving the increased electricity demand requires additional contracting of RE generation via PPAs (see Table 14). This leads to an increased need for buffering RE excess generation to serve the electrolysis system and the remaining electricity demand of the glassworks site (see Figure 19). For low electrification of the furnace, battery capacities reach up to 449.2 MWh_{el}. Given that BESSs with a capacity of around 600 MWh are planned in Germany [11], this falls within a realistic range from a technical perspective. Nevertheless, with limited available space at the glassworks site, we consider this an ambitious and rather unlikely setup. On the contrary, for the economically most viable case with high electrification and an AWE electrolyser system, the optimal battery capacity is between 80.6-110.4 MWh_{el}, which we consider a more realistic

setup. Another important takeaway from battery storage sizing results is the comparatively high EPR ratios between 2-14 h. This implies that the battery storage is operated for slow charging with excess generation from the PPAs over a longer period. The optimal electric power rating of the battery inverter depends solely on fluctuations in PPA profiles (see Figure 19). This leads to optimal sizing between 29-43 MW_{el} and 8-23 MW_{el} for low and high electrification of the furnace, respectively.

Another part of the decarbonised energy system is the supply of thermal space heating demand for the SGS department. Figure 28 shows the results of component sizing, including an industrial HP, an electric boiler, and thermal storage. For the scenarios with an NG furnace and hydrogen supply via pipeline, the only option to supply the heat demand is to size the electric boiler to the maximum annual demand of 6.408 MW_{th}. On the contrary, sizing is less intuitive in scenarios with an electrolysis system. Those scenarios are implemented with the option to build an industrial HP WHR from the electrolysis system. In addition, a sizing constraint ensures that the sum of thermal ratings of high-temperature HP and electric boiler equals the maximum thermal load as defined in Eq. (3.66).

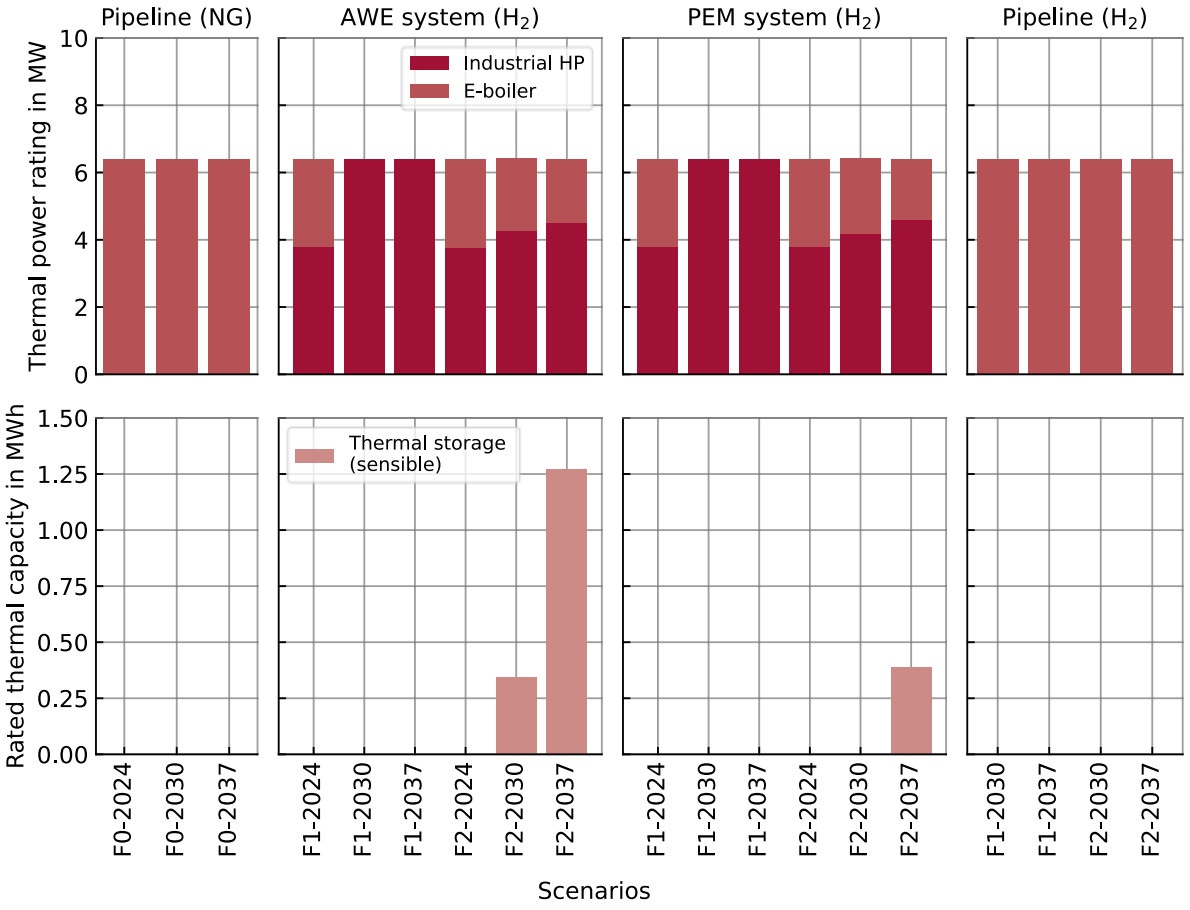

Figure 28: Optimised component sizing for the thermal energy supply of the SGS department, for all scenarios of the evaluation. Abbreviations: FO: NG furnace, F1: hydrogen furnace with low electrification, F2: hydrogen furnace with low electrification. Source data is provided in Table 20.

The results indicate that the sizing of thermal components is very similar across scenarios with an AWE and a PEM electrolysis system. Moreover, for 2024, the sizing results for the electric boiler and the industrial HP are almost identical, at around 3.8 MW_{th} and 2.6 MW_{th}, respectively. At the same time, no thermal storage capacity is required in 2024, as the electrolyser efficiency is comparatively low, resulting in a high waste-heat potential. Overall, the sizing results indicate that in 2024, capital costs for the HP are the dominant factor, and a comparatively large electric boiler is required to cover peak demand. However, this picture changes in 2030 and 2037 with decreasing specific investment costs for the high-temperature HP and an assumed increase of COP from 4 to 5. For scenarios with low furnace electrification, this eliminates the electric boiler across all setups. The higher hydrogen demand in these scenarios and thus larger electrolysers leads to sufficient amounts of waste heat, with no need to install any additional thermal storage. For high furnace electrification, however, the waste heat from the electrolyser is insufficient to meet the entire thermal load. Therefore, electric boilers with an optimal thermal power rating of between 1.804-2.235 MW_{th} are required. They are partly combined with additional thermal storage capacity. As the AWE electrolysis system features higher efficiencies, less waste heat is available, leading to larger thermal storage sizing of up to 1.271 MW_{th}.

5.2. Detailed evaluation of the most promising decarbonisation choices

A detailed understanding of the outcomes of the high-level comparison of decarbonisation choices in Section 5.1 requires an in-depth analysis of single scenarios. In this section, we specifically focus on the two most promising decarbonisation scenarios. On the one hand, this includes the scenario with an AWE electrolysis system, which offers clear economic advantages over the PEM electrolysis system. On the other side, we further evaluate the scenario with a connection to a future hydrogen pipeline. For both options, we primarily focus on scenarios with high hydrogen furnace electrification, which promise the lowest total annual costs (see Subsection 5.2.2, Figure 21). This is required to stay within a competitive cost range with the NG furnace. Nevertheless, the alternative with low electrification of the hydrogen furnace may offer the benefit of transferability in construction and operation, as it is closer to the current NG-based furnace design. Therefore, additional evaluations for this option are included in Appendix I and referenced during the evaluation.

5.2.1. Solution I: electrolysis system with high furnace electrification

As a first decarbonisation option, we analyse the hydrogen furnace with high electrification (see Table 9, F2) in combination with AWE electrolysis. The furnace has an annual hydrogen demand of 5553 tonnes, which must be produced by the electrolysis system using green electricity from PPAs. From the sizing results summarised in Table 20, we can obtain the

optimal sizes for all single components. For the AWE systems, optimal electrical power ratings are 18.7 MW_{el}, 17.1 MW_{el}, and 13.5 MW_{el} for 2024, 2030, and 2037, respectively. Another central component of the new energy system is the battery storage system. Its optimal capacity is 110.4 MWh, 144.5 MWh, and 80.6 MWh for 2024, 2030, and 2037, respectively. In a first evaluation, we break down all cost components to identify relevant cost drivers. Figure 29 illustrates a breakdown of the annualised capital costs for all relevant, modelled energy conversion and storage components of the energy system. Similarly, Figure 30 shows a breakdown of annual operating costs, including emission costs.

The distribution of capital costs clearly shows that the melting furnace, the AWE electrolyser system, and the battery storage system make up the largest share. The annualised investment of the furnace is 10.6 Mio. EUR_{2024}, which corresponds to a share of 61.3% of capital costs in 2024. This share increases to 68.1% in 2030 and 80.8% in 2037. On the one hand, this shows that capital costs are a major weakness of a novel furnace with high electrification. It is estimated to be 2.5 times more expensive than an NG-based furnace [102]. The expected high costs of this new type of furnace are highly uncertain, as it must be developed from scratch. On the other hand, this can also be an opportunity for long-term cost reductions if a more cost-efficient design is found. On the contrary, for investment costs of other components, detailed future price projections are available. For the AWE and battery storage system, the specific investment costs are expected to substantially decrease towards 2037. At the same time, as efficiency increases, the required capacity of the electrolysis system decreases. While capital costs for the AWE system account for 2.6 Mio. EUR_{2024} in 2024, they decrease to 1.6 Mio. EUR_{2024} in 2030 and 1.0 Mio. EUR_{2024} in 2037. Similarly, the annualised capital costs for the battery storage system (incl. battery inverter) reduce from 3.5 Mio. EUR_{2024} in 2024 to 1.4 Mio. EUR_{2024} in 2037, considering a substantial reduction in required capacity. Overall, the results show that total investment costs have the potential to decrease by 10.1% and 24.2% towards 2030 and 2037, respectively. This leads to greater competitiveness for this solution compared to the NG-based furnace scenario.

Although capital expenditures account for a significant share of costs in the electrolysis-system-based scenarios, the majority of annual costs are operating costs (see Figure 30). The largest share of operating costs comes from purchasing RE generation with PPAs to operate the AWE system. In 2024, this corresponds to 20.3 Mio. EUR_{2024}, which is 44% of all operating costs. However, with decreasing PPA prices for 2030 and 2037, this share substantially decreases to 38% and 37.2%, respectively. Although the PPA portfolios are optimised to follow the furnace's demand, a substantial share of RE generation must be resold on wholesale markets. This leads to revenues between 3-5 Mio. EUR_{2024}, depending on the year of consideration. In addition to the PPA supply, contracting green hydropower futures (EU27) to cover the remaining power demand of the glassworks site accounts for a large share of costs.

In 2024, this is the third-largest cost share at 12.2 Mio. EUR_{2024}. Nevertheless, this position shows a substantial reduction potential towards 2037 when the amount decreases to 9 Mio. EUR_{2024}, with assumed reductions in prices for hydropower futures.

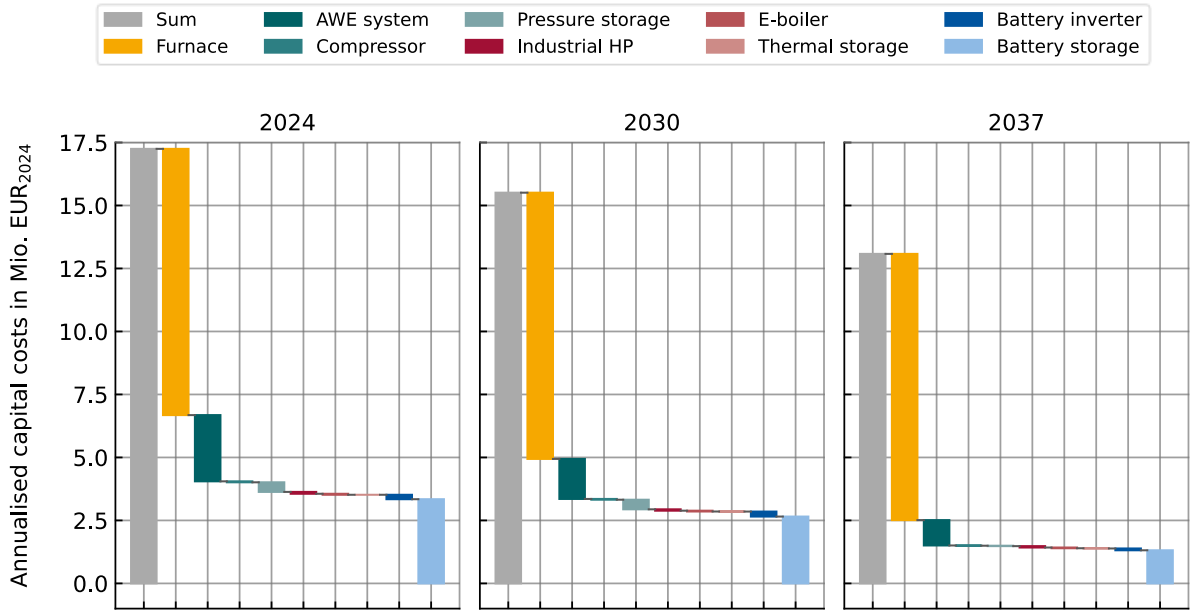

Figure 29: Breakdown of annualised investment costs of all required components for the decarbonised energy system of the glassworks, in case of high electrification (20 MW_{el}) of the melting furnace. The electrolysis system is AWE-based.

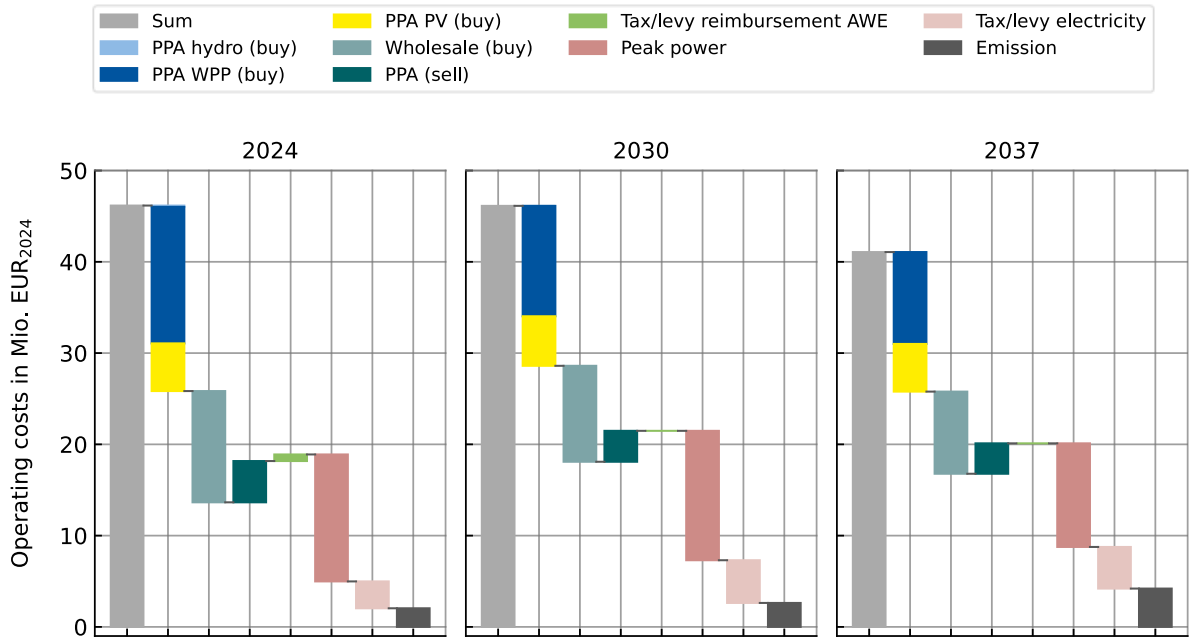

Figure 30: Breakdown of annual operating costs for the decarbonised energy system of the glassworks, in case of high electrification (20 MWel) of the melting furnace. The electrolysis system is AWE-based.

The second-largest cost position in 2024 is peak power costs for electricity drawn from the electric power grid. In 2024, they account for 30.1% of all operating costs. However, with increasing efficiency of the AWE system, they are reducing from 13.9 Mio. EUR_{2024} in 2024 to 11.4 Mio. EUR_{2024} in 2037. It should be considered that there is a high uncertainty concerning peak power tariffs with substantial increases since 2021, introduced by the local distribution system operator (DSO) at the glassworks location [80, 196]. Depending on political decisions, the results could deviate substantially. Nevertheless, the high costs lead to the conclusion that measures to reduce peak power are becoming increasingly relevant. The evaluation of peak-power-aware operation in Subsection 5.3.1 shows that substantial cost reductions are possible. In addition to peak power costs, other electric power grid fees and taxes account for a relevant cost share of 4.8%, 10.1%, and 11.1% for 2024, 2030, and 2037, respectively. Similar to peak power costs, this cost share is considered highly uncertain. Overall, the insights clearly show that, with high electrification of energy-intensive industries, electric power grid fees are a substantial factor in whether decarbonisation is cost-competitive. Therefore, future electric power grid fees should be designed to support industries with rising electric power demand in their decarbonisation efforts. Furthermore, the 2024 reimbursement of electric power grid fees and taxes for the electrolysis system reduces overall costs by only 1.5% for high electrification of the furnace and AWE system. On the contrary, for low furnace electrification, higher savings are possible, as peak power costs can be effectively reduced (see Appendix I, Figure 48). In addition, it can be noted that emission costs for remaining process-related CO_2 emissions are increasingly relevant towards 2037. Therefore, investing in additional measures to reduce those emissions has to be carefully considered [17].

With the relevant cost factors in mind, gaining further insights into the operational behaviour of the decarbonised energy system requires a closer look at individual energy flows. Figure 31 provides an overview of the resulting required annual energy flows between components for an installation in 2024. The visualisation of annual energy flows for the 2024 scenario with an AWE electrolysis system and high furnace electrification shows a total inflow of 362.4 GWh of PPA power generation to the balancing group of the industrial glassworks site. The largest share comes from WPP generation (262.4 GWh), followed by PV (98.6 GWh) and only a small share from hydropower (1.4 GWh). Timely mismatches between PPA power generation and energy consumption at the glassworks site result in 85.3 GWh that must be resold on wholesale markets. Under the constraints of the European RED II directive on green hydrogen production, the demand for the electrolyser system (103.2 GWh) must be fully met by PPA generation (monthly correlation). With 49.4 GWh, WPP covers the majority of the electrolyser system demand. Generation from PV PPAs adds another 39.9 GWh. From the battery storage system, 12.6 GWh of additional PPA power generation covers the electrolysis system demand. Moreover, in 2024, only a small additional amount of energy from wholesale markets of 0.7 GWh is supplied to the electrolysis system, as only monthly matching is required for PPA

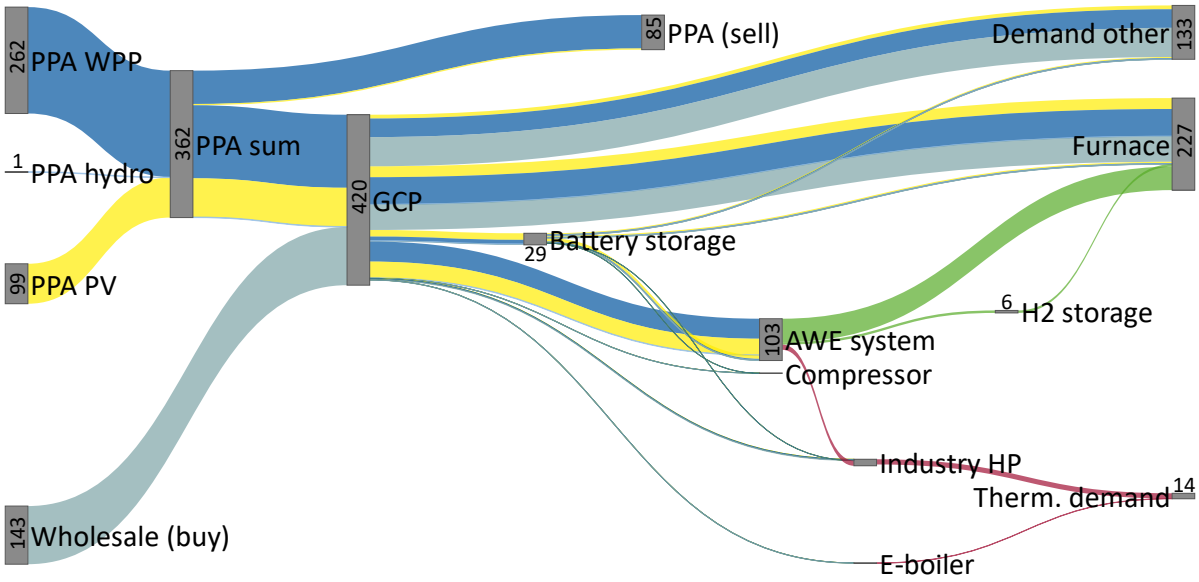

Figure 31: Annual energy flows in GWh for the 2024 decarbonisation scenario with an AWE electrolysis system and high electrification of the furnace (20 MW_{el}). Flows smaller than 1 MWh are not displayed. "Demand other" includes all remaining electricity demand of the sections SGG and SGS.

and the electrolysis system. The electric load of the furnace and other power demands of the glassworks site consume the remaining PPA power generation of 94.1 GWh and 55.3 GWh, respectively. Nevertheless, PPA power generation cannot cover demands at all times. Therefore, 143.4 GWh of additional power generation must be purchased on the wholesale markets, for which we assume green hydropower futures (EU27) as the source. The furnace and other sites' power demands mostly consume this additional energy share. Other smaller, less significant power consumers include the compressor, the industrial HP, and the electric boiler. Focusing on the hydrogen production, the furnace directly consumes 57.8 GWh (90.1%) of the total hydrogen production, while only 6.0 GWh are temporarily stored by the hydrogen pressure storage. In the thermal sector, with 12.8 GWh, the industrial HP supplies most of the thermal demand through WHR from the electrolysis system. Thermal peak demands are only occasionally met by the electric boiler, resulting in an annual supply of only 0.7 GWh.
Another important aspect when analysing the energy flows of the new energy system is losses. The highest annual losses of 26.4 GWh occur for the electrolyser system. This leads to a combined annual efficiency including WHR of 74.4%. However, it must be noted that this efficiency could be increased by utilising higher amounts of waste heat, for instance, in CCS processes [17]. Another substantial source of energy losses is the transformers at the GCP. They are modelled with a single efficiency of 97%, resulting in annual losses of 12.6 GWh in this scenario. Less substantial losses of 4.3 GWh are occurring at the battery storage system.

For the decarbonised energy system scenarios in 2030 and 2037, energy flows change substantially (see Figure 32 and Figure 33). Most importantly, due to the higher efficiency, the electric power demand of the electrolysis system decreases to 100.5 GWh in 2030 and

92.8 GWh in 2037. However, in 2030, a similar amount of RE generation from PPAs compared to 2024 is still required, totalling 361.9 GWh. This mainly stems from the shift from WPP to PV PPAs, driven by lower PV prices. At the same time, PV generation aligns less well with the relatively constant demand for hydrogen, thereby increasing the ratio of PPA generation to electrolyser system demand.

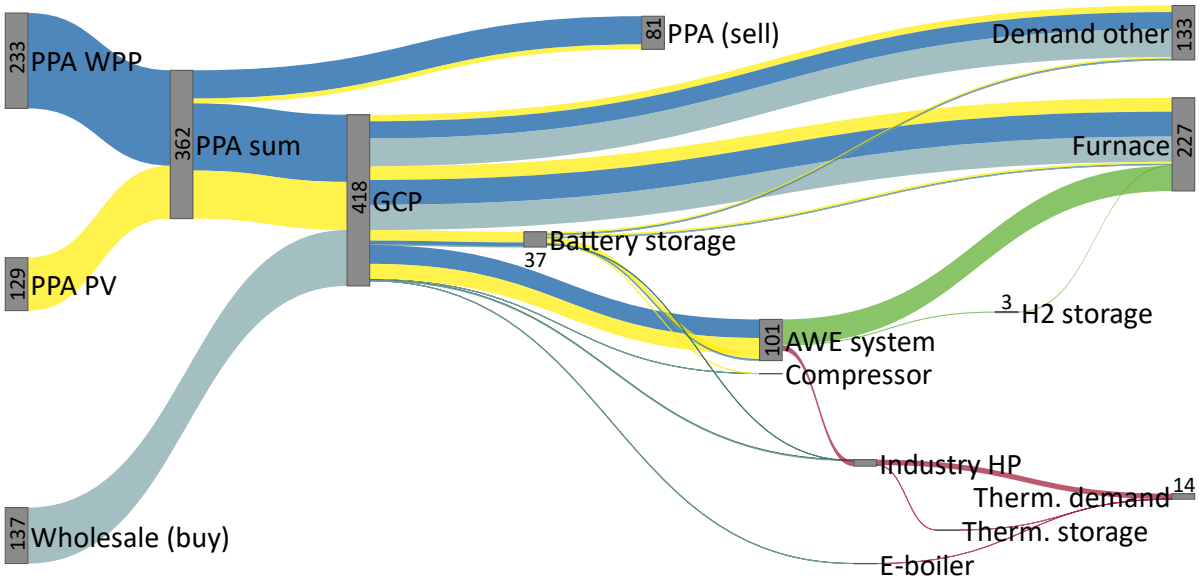

Figure 32: Annual energy flows in GWh for the 2030 decarbonisation scenario with an AWE electrolysis system and high electrification of the furnace (20MW$_{el}$). Flows smaller than 1 MWh are not displayed. “Demand other” includes all remaining electricity demand of the sections SGG and SGS.

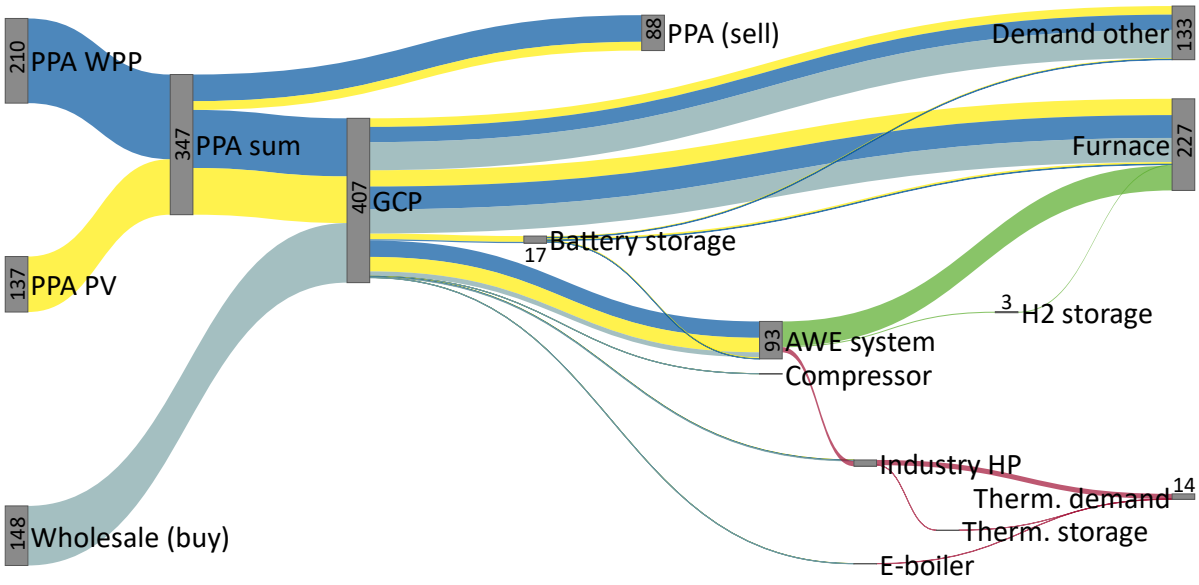

Figure 33: Annual energy flows in GWh for the 2037 decarbonisation scenario with an AWE electrolysis system and high electrification of the furnace (20MW$_{el}$). Flows smaller than 1 MWh are not displayed. “Demand other” includes all remaining electricity demand of the sections SGG and SGS.

In addition, in 2030, hydrogen production is subject to stricter requirements, including hourly temporal matching, as per the RED II (see Subsection 2.4.2). Overall, these factors lead to a higher battery storage throughput of 37.1 GWh in 2030. On the contrary, in 2037, we assume the electric power grid is sufficiently decarbonised and that no temporal matching is required. For this reason, 13.4% (12.2 GWh) of the electrolyser system's electrical power demand originates from wholesale markets. Furthermore, with higher electrolyser system efficiencies in 2037, the total RE generation from optimised PPA portfolios decreases to 347.2 GWh. At the same time, the amount of energy to be purchased via wholesale power futures increases to 147.5 GWh.

Another effect caused by the higher efficiency and lower specific investment costs of the electrolysis system towards 2037 is the reduced energy flow of only 2.6 GWh to the hydrogen pressure storage. Moreover, higher electrolysis system efficiency and greater utilisation of the lower share of waste heat by the industrial HP reduce overall electrolysis system losses to 23.4 GWh in 2030 and 16.1 GWh in 2037. This leads to combined electrolysis system efficiencies of 76.7% and 82.7% in 2030 and 2037, respectively.

For all scenarios that include an electrolysis system and industrial HP, we model the possibility to draw energy from a hydrogen and thermal slack component to avoid infeasibilities. The evaluation of cumulated energy flows from slack components (see Appendix J, Figure 52) shows that the highest uncovered load is 415.3 MWh for hydrogen and 0.2 MWh for thermal demand. The uncovered load occurs because the operating layer uses a rolling-horizon approach with foresight of only 24 hours. This can, in some scenarios, lead to insufficient storage level filling at a single time step. However, in the worst case, the uncovered load is less than 0.3% of hydrogen and 0.002% of thermal demand. This does not affect the overall results outcome. Moreover, no slack flows occur in the most promising scenario with AWE electrolysis and high furnace electrification. Uncovered demand can be avoided in a real operation through the implementation of a sophisticated, prognosis-based energy management system that detects critical future supply situations and applies adequate storage filling or load shifting when possible.

In the next step, the obtained energy flows enable an accurate calculation of LCOH in EUR/kg, as described in Subsection 3.3.3. This allows for a better comparison of decarbonisation with an electrolysis system versus connecting to a future hydrogen pipeline. To better understand the cost components of the calculation, Figure 34 provides a cost breakdown. We calculate the additional peak power according to Eq. (3.143).

The LCOH cost breakdown illustrates that one of the dominating factors is PPA purchasing costs, with a rather constant share for all years. They account for 33.3%, 29.7%, and 33.5% in 2024, 2030, and 2037, respectively. WPP PPAs account for the largest share, representing more than half of the generation from PPAs and being attached to slightly higher prices. The other dominant factor is the increase in peak power costs associated with electrolyser system

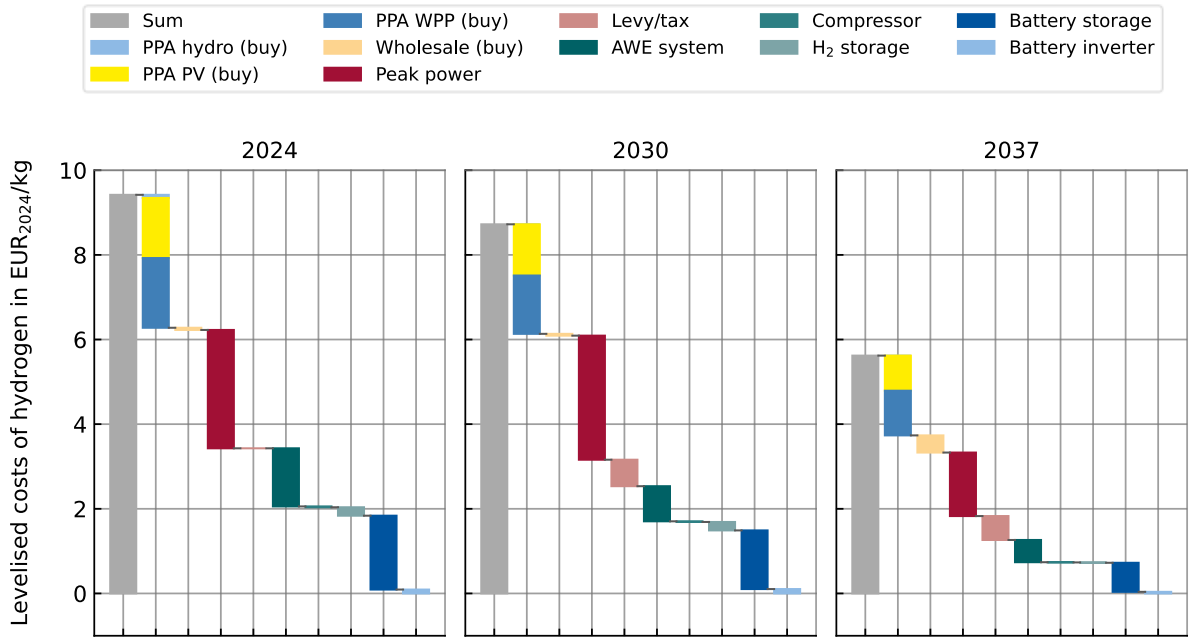

Figure 34: Breakdown of LCOH for a one-year operation of the decarbonised glassworks energy system in the case of high electrification (20 MW_{el}) of the furnace. The electrolysis system is AWE-based.

operation. This increase in peak power leads to cost shares of 29.7%, 33.6%, and 26.7% in 2024, 2030, and 2037, respectively. The high share of peak power costs indicates that peak-power-aware operation of the electrolysis system should be implemented, as further analysed in Subsection 5.3.1. The remaining operating cost shares of the LCOH calculation are less significant. This includes wholesale purchases that cover the remaining electric power demand for the hydrogen production. In 2024 and 2030, this is mostly due to the compressor consumption of the hydrogen pressure storage with small shares of <0.1 EUR_{2024}/kg. In 2037, the wholesale share increases to 0.4 EUR_{2024}/kg, as it covers part of the electrolyser system's demand.

Other major contributors to LCOH are capital costs for the battery storage and electrolysis system. The battery storage system (incl. inverter) accounts for 1.8 EUR_{2024}/kg, 1.5 EUR_{2024}/kg, and 0.7 EUR_{2024}/kg in 2024, 2030, and 2037, respectively. The AWE system shows slightly lower shares of 1.4 EUR_{2024}/kg, 0.8 EUR_{2024}/kg, and 0.5 EUR_{2024}/kg in 2024, 2030, and 2037, respectively. However, as capital costs decline towards 2037, the impact of levies and taxes increases, accounting for 10.1% of LCOH in 2037.

Gaining further insights into the operation of the decarbonised energy system requires a closer look at the behaviour of individual components. This concerns all energy conversion and storage components of the decarbonised energy system. Figure 35 illustrates the distributions of electrical input power for conversion components and of input and output power for storage components. Figure 36 complements the picture by showing the distribution of state-of-energy (SOE) of all storage components.

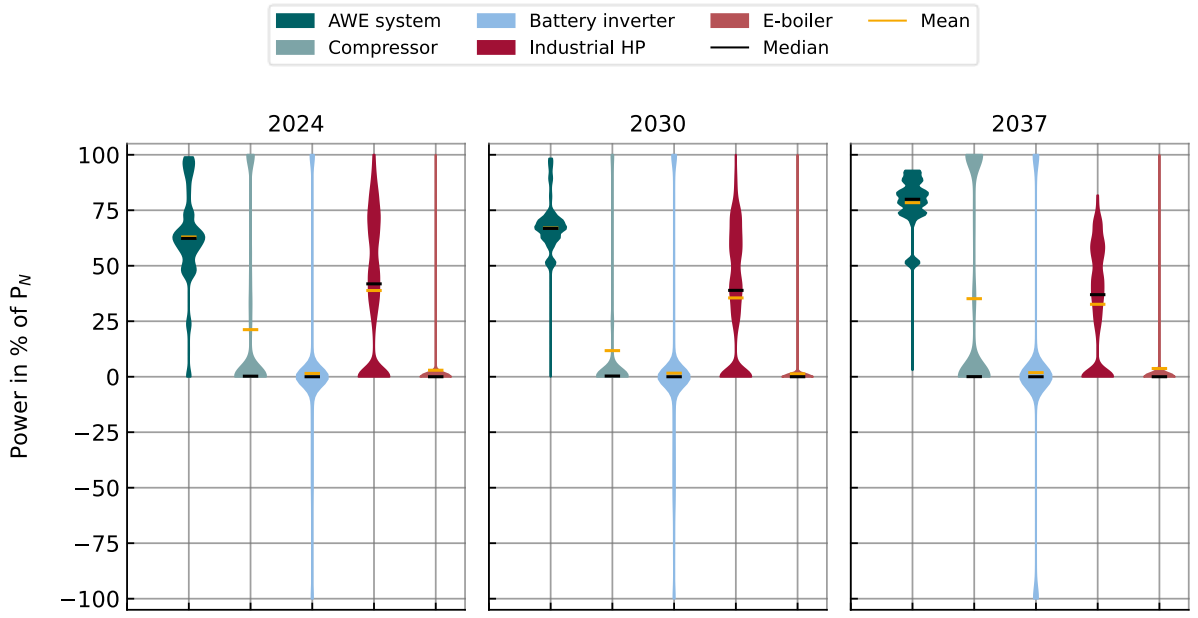

Figure 35: Distribution of electric input power for all conversion components of the decarbonised energy system and input/output power for the storage components of the glassworks use case. The electrolysis system is AWE-based. For H_2 storage, the values are normalised to the maximum H_2 throughput. For all other components, values are normalised to the electric input power rating.

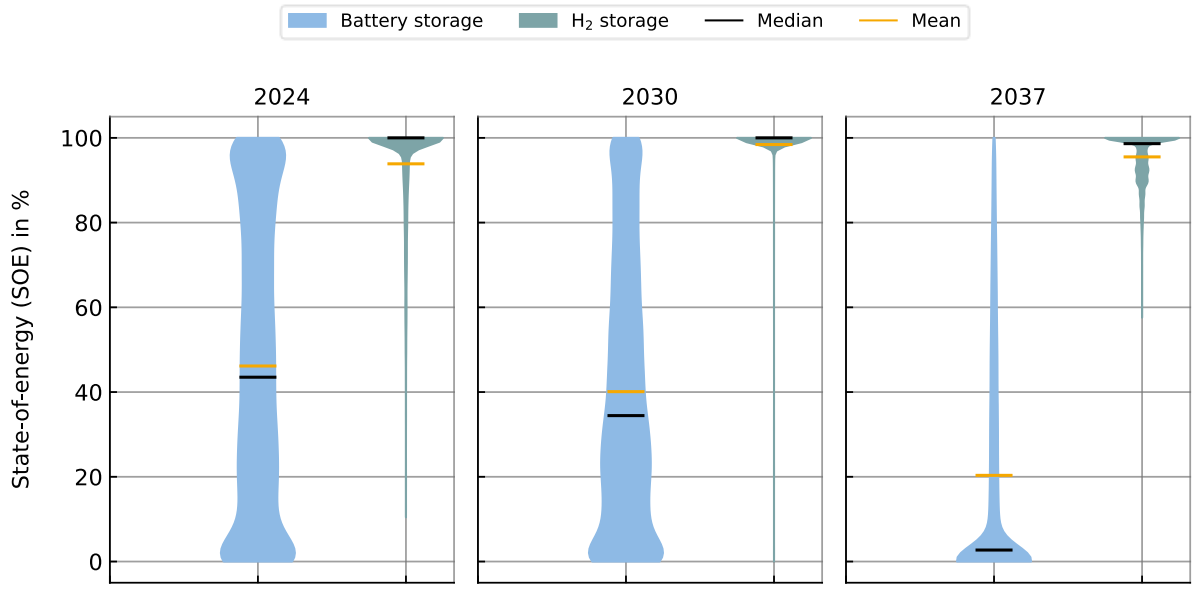

Figure 36: Distribution of the SOE for all relevant storage components of the decarbonised energy system of the glassworks use case. The electrolysis system is AWE-based. All values are normalised to the maximum storage level.

Focusing on the electrolyser system, the distribution shows that the operation is substantially different for the considered years. In 2024, the AWE system is operated across a wide range of different operating points, with an average of 63.0% of rated electric input power. This low average utilisation is due to the modelled efficiency curve for the AWE electrolysis system,

which peaks at 47% of the nominal load and decreases towards full load (see Figure 6). With increasing efficiencies of the electrolysis system in future-year scenarios, the average operating point shifts upwards to 67.0% in 2030 and 78.4% in 2037. The lower utilisation of the system in 2024 and 2030 is due to the optimiser selecting a larger power rating for the AWE system (see Figure 26). On the one hand, this is driven by lower electrolyser system efficiencies. On the other hand, monthly and hourly temporal matching between the electrolyser system's demand and RE generation from PPAs must be ensured to comply with the RED II regulation (see Subsection 2.4.2). For 2037, the distribution is more concentrated, and the maximum power input is even below the rated input power to avoid the most inefficient operating points. In addition, at around 50% of rated electric power, there is another accumulation of operating points when half of the electrolysis system is in the off state or in standby mode during maintenance.
For the compressor, the median of the input power distribution indicates it is switched off at least 50% of the time. When it is switched on, however, there are two main operating points, either close to the minimum or close to the maximum electric power rating. The compressor system operates at part load only on a few occasions. This distribution of power for the compressor represents the implemented operating strategy for the hydrogen pressure storage, as defined by Eq. (3.14).
The strategy implemented for the pressure storage incentivises a rapid replenishment to maintain the highest possible hydrogen backup reserve at all times. When small amounts of hydrogen are drawn from the pressure storage during a time step, they are immediately refilled with mostly low input power at the compressor. When the electrolysis system is in maintenance, however, larger amounts of hydrogen are taken from the pressure storage. Afterwards, it is filled as quickly as possible with maximum compressor power. This operating strategy leads to high average SOEs of 93.9%, 98.4%, and 95.5% for hydrogen pressure storage in 2024, 2030, and 2037, respectively.

For thermal components, the behaviour mainly depends on the waste heat potential of the electrolysis system. This potential decreases towards 2037 as the electrolysis system size decreases and its efficiency increases. At the same time, the COP of the industrial HP is assumed to increase from 4.0 in 2024 to 5.0 in 2030 and 2037. Consequently, the average point of operation concerning electric power rating reduces from 38.9% in 2024 to 35.5% and 32.6% for 2030 and 2037, respectively. The electric boiler covers situations when the waste heat potential is insufficient. This leads to a high distribution of input power at low shares of the rated power, and it occurs only on a few occasions that it is operated at the maximum power rating.

Looking at the battery storage system, we observe that the average SOE declines substantially over the considered years. While in 2024 the average SOE is at 46.2%, it reduces to 40.1% in

2030 and 20.3% in 2037. This shows that less RE generation from PPAs needs to be buffered as the electrolyser efficiency increases. Moreover, the inverter's power distribution shows that, even with high EPRs, it mostly operates near 0% of nominal electric power. Most of the time, the battery storage system is in an idle state. The maximum charging or discharging power is only utilised on very few occasions. In addition, the average SOE shows that the full capacity is only partially used.

To improve understanding of the timely correlation between battery storage operation and daily or seasonal characteristics, Figure 37 illustrates the average SOE categorised by daily 15-minute intervals and month of the year.

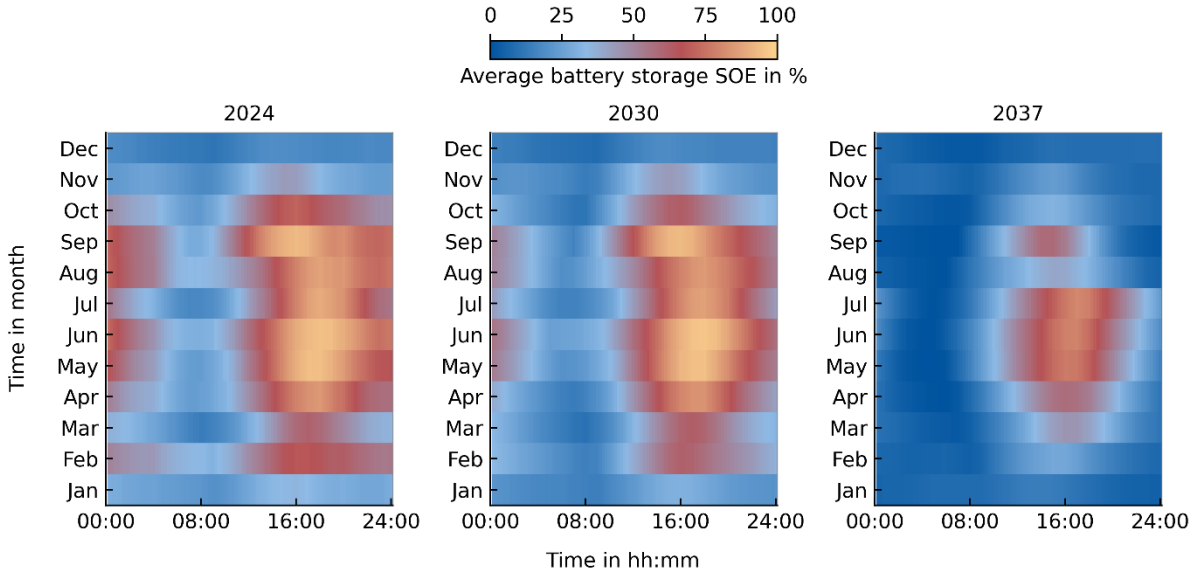

Figure 37: Average annual battery storage SOE categorised for all months and all quarter hours of the day, for the scenario with high electrification of the furnace (20 MW_{el}) and AWE electrolysis system.

In 2024, the timely distribution of SOE for the battery storage shows a pattern similar to that of typical PV battery storage applications [78]. The battery is charged mainly between 10:00-16:00, with mostly PV generation from PPAs (see energy flows in Figure 31), and discharged between 20:00-04:00. This behaviour is more pronounced during the months from May to September, with higher solar radiation. In January, November, and December, the distribution shows substantially lower battery storage usage. Focusing on 2037, the utilisation of battery storage substantially reduces, leaving the asset unused for most of the time. The main factor in this outcome is that the battery's optimal capacity remains similar or even slightly increases due to lower specific investment costs. At the same time, the electrolysis system's efficiency increases. Moreover, in 2037, no temporal matching between generation from PPAs and supply to the electrolysis system is required. Considering the comparatively high capital costs of battery storage (see Figure 29), the results raise the question of how to achieve higher

utilisation of the battery storage. Therefore, in Section 5.3, we evaluate whether the battery storage can provide additional flexibility by combining the main operation of integrating VRE generation from PPAs with additional use cases.

5.2.2. Solution II: hydrogen pipeline with high furnace electrification

The alternative decarbonisation option, compared with the electrolysis-system-based scenario in Subsection 5.2.1, is to connect to a future hydrogen pipeline. We evaluate this option for the more promising setup with high furnace electrification (20 MW_{el}) in 2030 and 2037. It is important to note that for 2030, there is high uncertainty regarding the availability of a hydrogen pipeline connection to the glassworks use case site (see Subsection 4.2.2). For capital costs, no additional components other than the hydrogen furnace are considered. The capital costs for the furnace are equal to those in the electrolysis-system-based scenario, at 6.3 Mio. EUR_{2024} (see Figure 29). For operating costs, Figure 38 provides a detailed cost breakdown. In addition, we illustrate the energy flows for the pipeline scenarios, which are identical for 2030 and 2037 (see Figure 39).

The cost breakdown shows total annual operating costs of 50.6 Mio. EUR_{2024} in 2030 and 45.7 Mio. EUR_{2024} in 2037 for the pipeline scenarios with high furnace electrification. This is considerably above the operating costs of the electrolysis-system-based scenarios (see Figure 30). The decreasing trend towards 2037 can be explained by reductions in the energy costs of hydrogen and electricity, while energy flows remain identical. The largest share of operating costs comes from purchasing 319.2 GWh of green hydropower generation (EU27 futures) on the wholesale markets with 24.6 Mio. EUR_{2024} in 2030 and 19.5 Mio. EUR_{2024} in 2037. They account for 48.6% and 42.7% of total annual operating costs in 2030 and 2037, respectively. This indicates that the largest cost-reduction potential in the scenarios with hydrogen pipeline connection and high furnace electrification is low-cost RE generation. Therefore, in Subsection 5.3.2, we analyse possible cost reductions with PV rooftop installations at the glassworks.
The other cost factors for the pipeline scenario with high furnace electrification are substantially lower. Despite comparatively high prices, hydrogen purchasing costs accounted for only 22.6% of total annual operating costs in 2030 and 22.0% in 2037. However, this corresponds to only 63.8 GWh of imported hydrogen, or 16.7% of aggregated energy imports. This shows the benefit of high furnace electrification, which reduces the demand for expensive green hydrogen imports compared to low furnace electrification. The remaining operating costs are peak power, taxes and levies, and emission costs. In particular, peak power costs account for shares of 16.6% and 18.4% in 2030 and 2037, respectively. However, compared to the scenarios with the electrolysis system, they are substantially lower. Nevertheless, the potential to reduce peak power costs needs to be evaluated (see Subsection 5.3.1).

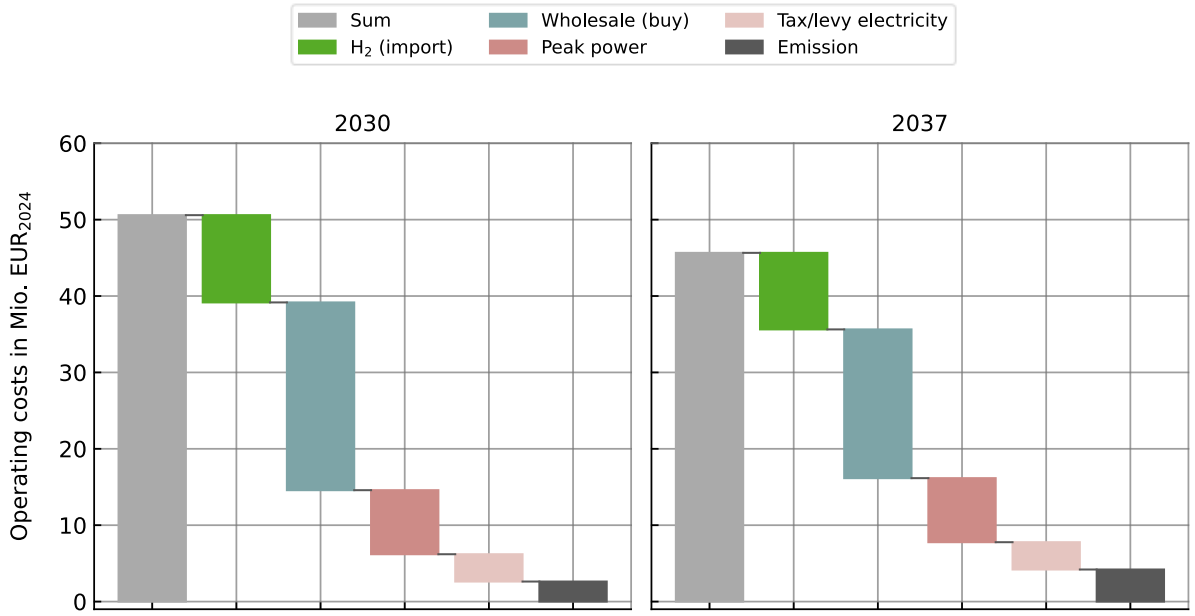

Figure 38: Breakdown of annual operating costs for the decarbonised glassworks energy system in case of high electrification (20 MW_{el}) of the melting furnace and connection to a future hydrogen pipeline.

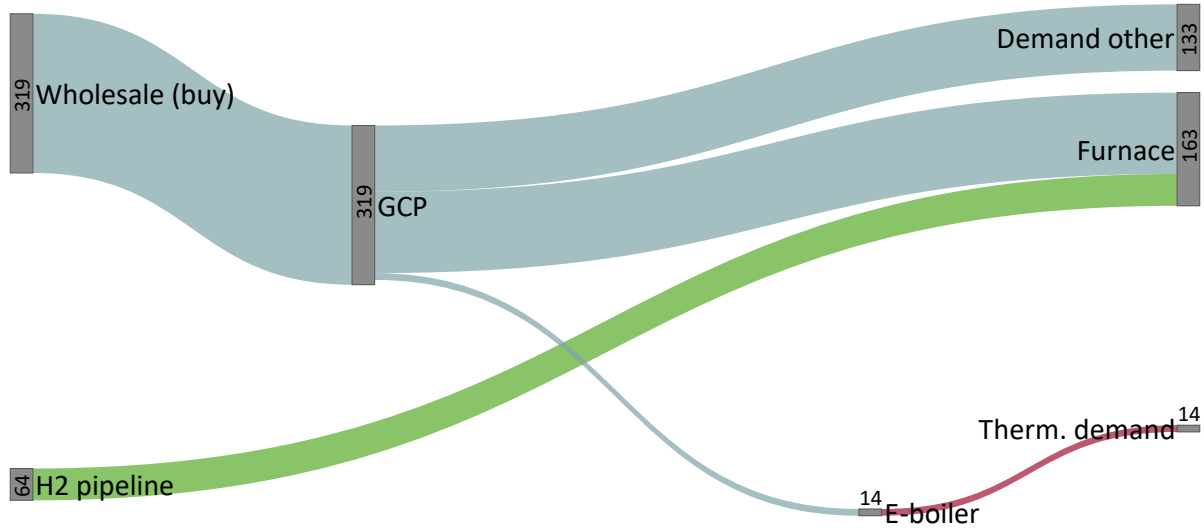

Figure 39: Annual energy flows in GWh for the 2030 and 2037 decarbonisation scenarios with connection to a future hydrogen pipeline and high electrification of the furnace (20MW_{el}).

5.3. Evaluation of flexibility potentials

The electrification of the energy system of the glassworks use case leads to higher annual electric power demands, which comes with the risk of high operational costs. Moreover, large investments in electrolysis and battery storage systems are required to produce on-site green hydrogen (see Figure 29). At the same time, the battery storage system is only partially used to buffer PPA generation. Most of the time, a large share of its capacity remains unused (see Figure 37). Furthermore, sector-coupling components such as electrolyser systems, industrial HP, or electric boilers can shift their operational characteristics. This provides the unique opportunity to leverage additional cost savings through a more flexible operation of the energy system. This includes reducing peak power from the electric power grid, increasing self-consumption of RE generation, trading on the wholesale electricity markets, or providing ancillary services to stabilise the electric power grid. The following subsections provide a detailed analysis of the potential benefits of flexible operating strategies.

5.3.1. Flexibility level B: reduction of peak power

One primary disadvantage of higher electrification of the energy system of the glassworks is increased peak power costs (see Figure 30). The peak power costs linearly scale with the peak power price, which is assumed to be 175.53 EUR_{2024}/kW for the electric power distribution grid that the glassworks is connected to [80]. Applying peak-power-aware operation offers the opportunity for substantial cost reductions. Therefore, in Eq. (3.52), we add peak power costs to the objective function of the optimisation problem. We apply peak-power-aware operation across all scenarios with an AWE electrolyser system and hydrogen pipeline, both for low (F1) and high (F2) electrification of the furnace. Figure 40 shows the peak power reduction per scenario and the resulting cost-saving potentials.

The results for peak-power-aware operation indicate that substantial reductions in peak power are possible. This, in particular, concerns the scenarios with an AWE electrolysis system and low electrification of the furnace that achieves peak power reductions of between 31.0%-40.9%, depending on the year of installation. Those peak power reductions overall correspond to a reduction in total annual costs between 6.6%-10.3%. Overall, with high furnace electrification, peak power is lower because the electrolyser system has a lower energy demand. Therefore, a smaller peak power reduction of 17.0%-18.1% is achieved, leading to reductions in total annual costs of 3.2%-4.2%. The lowest total system costs of 52.4 Mio. EUR_{2024} is achieved with high furnace electrification in 2037. Consequently, peak-power-aware operation reduces the gap relative to the 2037 scenario for rebuilding the NG-based furnace, which features total annual costs of 45.8 Mio. EUR_{2024} (see Table 19).

Another striking feature of the results is that a reduction of peak power does not necessarily lead to a reduction in total annual costs. This can be observed in the 2037 scenario with high

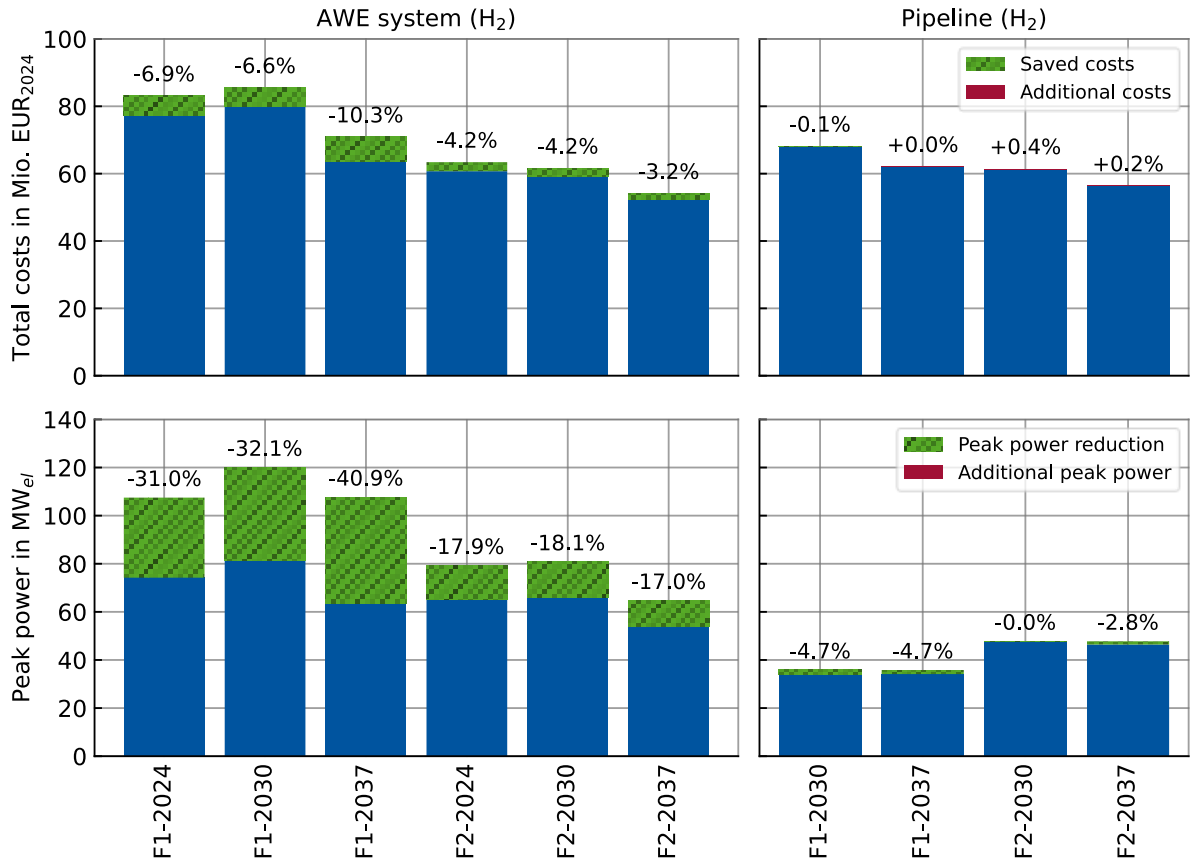

Figure 40: Peak power reduction and cost savings potential with peak power aware operation for scenarios with AWE electrolysis system and hydrogen pipeline connection, both for low (F1) and high (F2) electrification of the furnace. Reductions are calculated in comparison with the basic results in Section 5.1.

furnace electrification and connection to a hydrogen pipeline. Despite a peak power reduction of 2.8%, total annual costs increase by 0.2%. The main reason for this outcome is that peak-power-aware operation results in higher capital costs in the model's sizing layer, which assumes perfect foresight over the entire optimisation horizon. However, at the operating layer, the implemented rolling horizon reduces this foresight to 24 hours, potentially leading to suboptimal operation compared to the sizing layer. Overall, the results indicate that a battery storage system for the hydrogen pipeline scenarios has limited value as no flexibility can be exploited. To better understand increases in capital costs, Figure 41 illustrates changes in optimal capacities for the relevant components, including the battery storage system, electrolyser system, and hydrogen pressure storage.

Overall, peak-power-aware operation clearly affects the sizing of relevant components. In particular, the battery inverter size is reduced while the electric power rating of the electrolysis system is mostly increased. We observe the largest reduction in battery inverter size of 64.0% for low furnace electrification in 2037. For the electrolysis system, the highest increase in electric input power rating of 8.7% occurs with low furnace electrification in 2024. The results overall indicate that, rather than increasing the utilisation of battery storage, it is

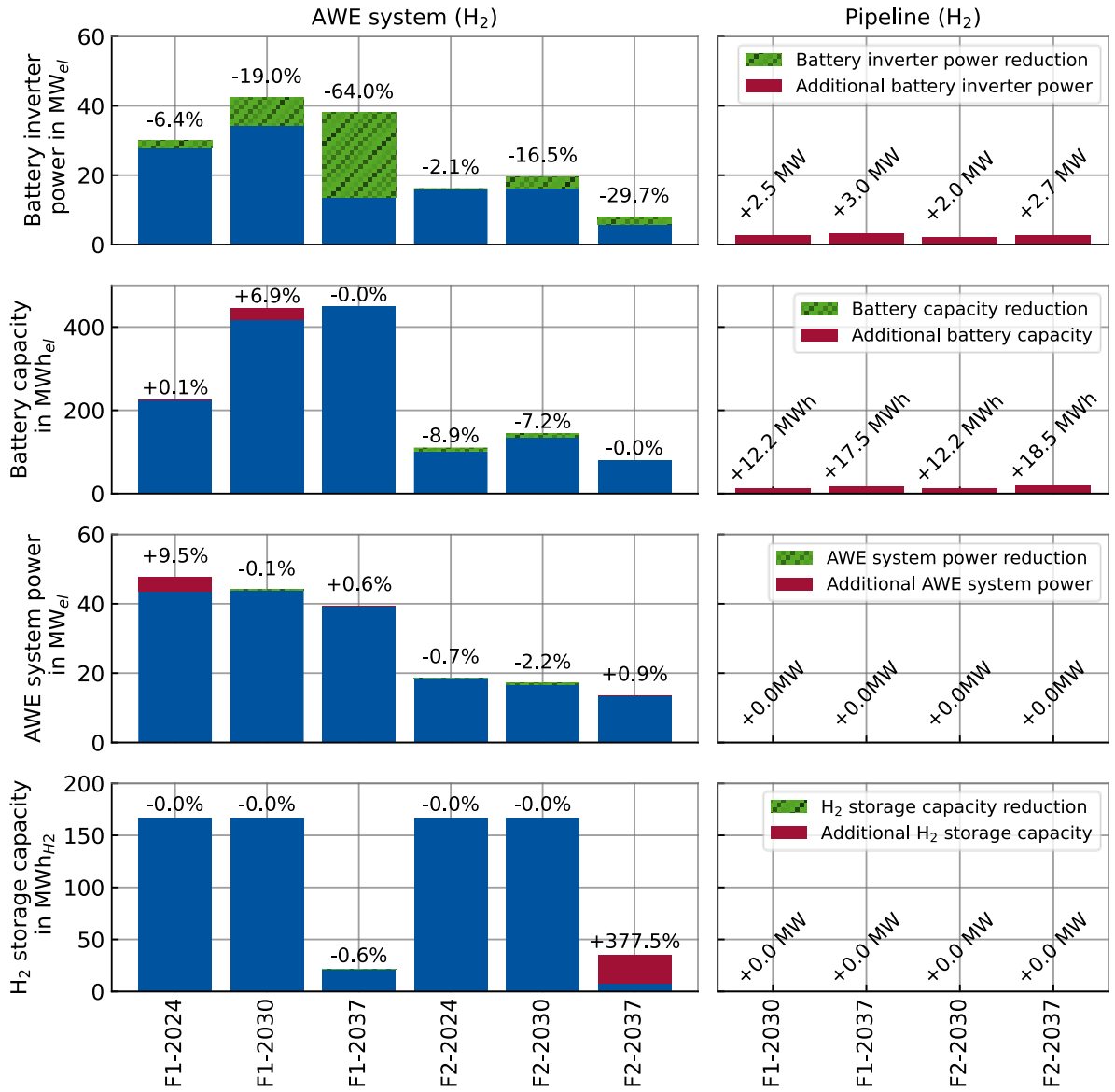

Figure 41: Impact of peak power aware operation on sizing of relevant components including battery storage system, electrolyser system, and hydrogen pressure storage. Results are shown for scenarios with AWE electrolysis system and hydrogen pipeline connection, both for low (F1) and high (F2) electrification of the furnace. Reductions are calculated relative to the basic results in Section 5.1.

often more cost-effective to increase the electrolysis system size to enable more flexible operation. Another option to increase flexibility and reduce the peak power of the hydrogen production is to install a larger hydrogen storage tank. This is indicated by the substantial 377.5% increase in furnace capacity for high electrification in 2037. However, in most scenarios, this is not possible as the maximum allowed size of 167 $MWH_{H2,LHV}$ (see Subsection 4.4.1) is already reached. Furthermore, it must be noted that, in some scenarios, the battery storage capacity remains at the minimum required by the PPA portfolio optimisation and cannot be further reduced (see Table 14). For hydrogen pipeline scenarios, the optimal capacity for a new battery storage is between 12-19 MWh. However, the comparatively small reduction in peak power does not yield substantial cost savings.

Apart from differences in component sizing, the operation of the glassworks energy system changes substantially when peak power costs are included in the objective function. Figure 42 illustrates the changed behaviour of the most relevant components, including electrolysis and battery storage systems, during the highest annual power peak.

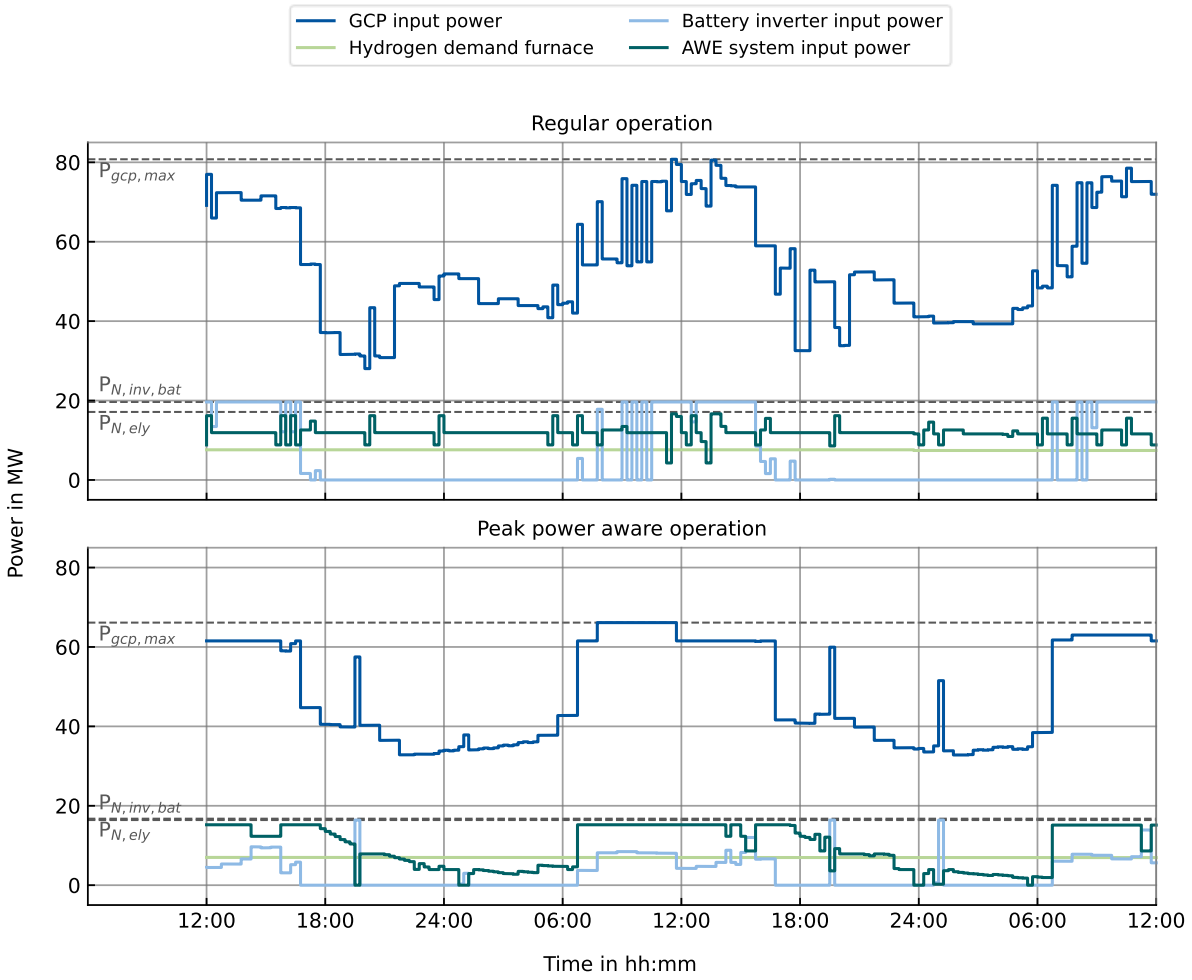

Figure 42: Visualisation of component behaviour during the occurance of the highest 15-minute annual power peak on 21th of May at 11:45, for the 2030 scenario with AWE electrolysis system and high (F2) electrification of the furnace. The upper plot shows the operation without, and the lower plot shows the operation with peak-power-aware operation.

We can observe that, for regular operation without peak power awareness, the electrolysis system operates at a very constant input power that changes only during maintenance, when half of the system is temporarily unavailable. Furthermore, its input power is always above the furnace's hydrogen demand. For battery storage, charging is more volatile, resulting in many single 15-minute power peaks at the GCP. This is especially true during the day, when PV generation from PPAs is at its peak, and the battery often charges. Moreover, at the GCP, the aggregated electric power at the glassworks site shows that the highest demand typically occurs during the day. Consequently, the annual electric peak power of 80.8 MW also occurs at noon at 11:45.

With peak-power-aware operation, however, the components' behaviour changes substantially. The electrolysis system now operates much more flexibly, and the rated capacity slightly decreases by 0.1 MW_{el}. Moreover, charging the battery storage system is more beneficial to the system. This especially occurs when the power at the GCP is below the new annual 15-minute peak power, which has been reduced to 65.1 MW_{el}. However, this reduces the required power rating of the battery inverter (see Figure 41) and potentially leads to less utilisation of RE generation from PPAs.

5.3.2. Flexibility level C: PV generation on-site

Applying a simple strategy for peak-power-aware operation (flexibility level B) is beneficial in most scenarios for total annual system costs (see Subsection 5.3.1). In the next step, we add the option to install a PV rooftop system at the glassworks use case site to achieve further cost savings. The maximum size of the PV rooftop system the optimiser can choose is 12.3 MWp. Table 21 shows the optimal sizing results for the PV rooftop system and inverter for all scenarios with an AWE electrolysis system and hydrogen pipeline connection.

Table 21: Optimal sizing results, self-consumption rates, and DM revenues for a PV rooftop system installed at the site of the glassworks use case. All panels face south.

KPI	AWE system						Hydrogen pipeline			
	Low electrification of furnace (F1)			High electrification of furnace (F2)			Low electrification of furnace (F1)		High electrification of furnace (F2)	
	2024	2030	2037	2024	2030	2037	2030	2037	2030	2037
PV rooftop rated power in MW_p	12.315	12.315	12.315	12.315	12.315	12.315	12.315	12.315	12.315	12.315
PV inverter rated power in MW	11.552	11.928	12.315	11.500	11.862	12.257	11.804	12.257	11.804	12.257
Self-consumtion rate in %	0.624	0.001	0.0	0.271	0.0	0.0	0.0	0.0	0.0	0.0
DM revenue in Mio. EUR_{2024}	1.042	1.058	0.912	1.034	1.059	0.912	1.059	0.912	1.059	0.912

For all scenarios, the PV rooftop system is sized to the maximum possible capacity. This proves that installing a PV system on the glassworks site is a no-regret option. The PV inverter is sized slightly below the capacity of the PV rooftop system and varies between scenarios. Moreover, the self-consumption rate indicates that almost all of the PV rooftop system's generation is sold via DM. Depending on the scenario and year, the revenue is between 0.9-1.1 Mio. EUR_{2024}. The difference can be explained by the modelling assumptions. In 2024, DM has been modelled with variable prices according to the DM model (see Subsection 2.4.1). For a few time steps with low spot market prices, this leads to low compensations that prevent feeding PV generation into the electric power grid. For 2030 and 2037, however, fixed feed-in tariffs based on electricity prices are assumed, as no market data is available. Consequently, all the generation from rooftop PV is fed into the electric power grid. Similar to the evaluation for

flexibility level B with peak-power-aware operation, in Figure 43, we evaluate the reduction of total annual system costs and peak power when installing a PV rooftop system.

The results for reductions in total annual costs show that installing a PV rooftop system is beneficial across all considered scenarios. On the one hand, the PV rooftop system provides low-cost RE generation. On the other hand, it proves valuable by further reducing the site's peak power compared to applying only peak-power-aware operation (see Figure 43). For the considered scenarios with an AWE electrolysis system, the peak power reduction ranges from 18.4%-41.7%, leading to total annual cost reductions of 3.6%-10.6%. Compared with peak-power-aware operation only (see Figure 40), scenarios with low furnace electrification particularly benefit from the PV rooftop system in terms of peak power. The lowest total system costs of 52.2 Mio. EUR_{2024} is achieved through high-furnace electrification in 2037. Despite additional reductions, a substantial gap to the scenario with an NG-based furnace remains (see Table 19).
For the cases with a connection to a future hydrogen pipeline, substantially smaller reductions are achieved. This is the case because the site's peak power and power consumption are lower

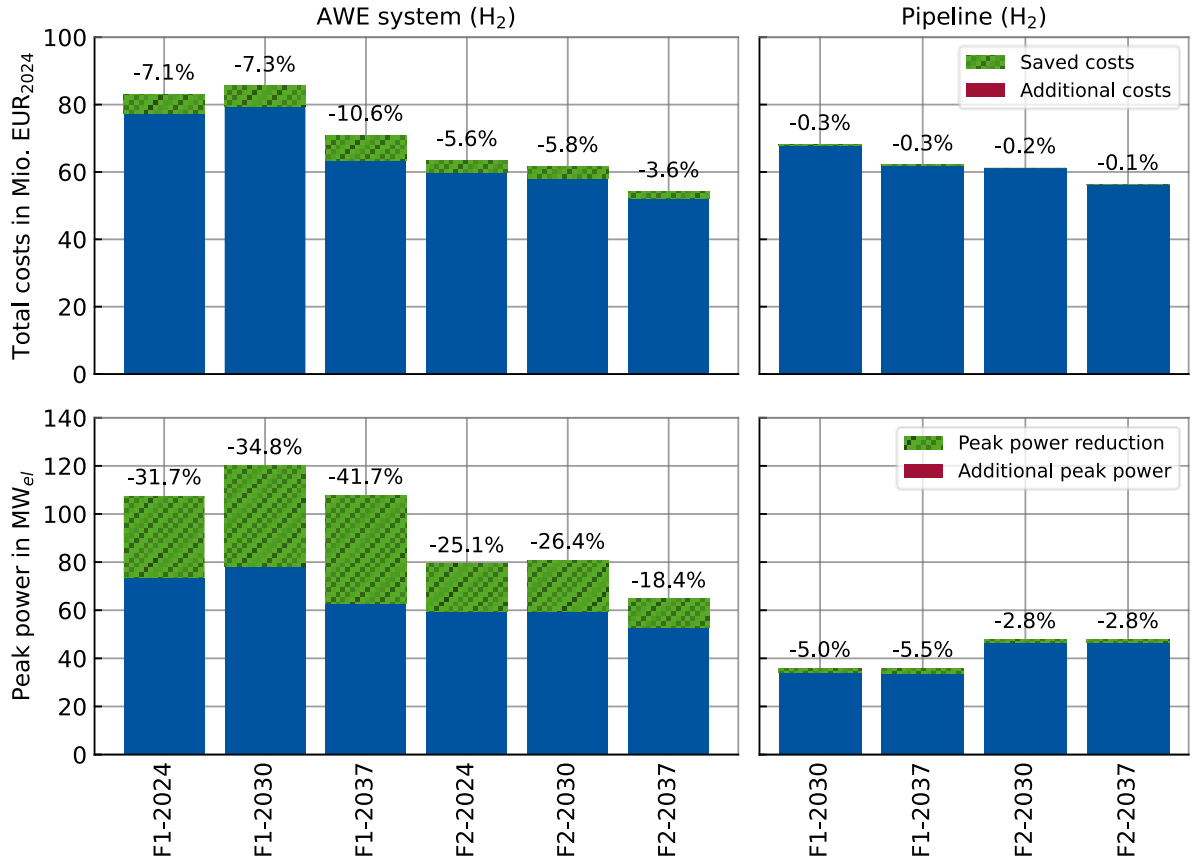

Figure 43: Peak power reduction and cost savings potential with peak power aware operation and installation of a PV rooftop system at the site of the glassworks. Results are calculated for scenarios with an AWE electrolysis system and a hydrogen pipeline connection, for both low (F1) and high (F2) furnace electrification. Reductions are calculated relative to the basic results in Section 5.1.

than those in the electrolysis-system-based scenarios (see Figure 39), thereby reducing overall reduction potentials. Nevertheless, all pipeline scenarios now show small reductions of 0.3% or less compared to peak-power-aware operation only (flexibility level B).

Understanding the benefits of the PV rooftop system requires a closer look at the correlation between peak power and PV rooftop generation. Figure 44 illustrates the 1,000 highest power peaks before and after the installation of the PV rooftop system for the AWE electrolysis system and high-furnace electrification. This enables the identification of the correlation between peak power occurrence and PV rooftop generation. The results show that the PV rooftop system further reduces the peak power by up to 13.5 MW_{el}, compared to flexibility level B, which is slightly above the rated power of 12.3 MW. The highest relative reduction is at 20.8%. However, we observe that the lowest peak power with the PV rooftop system already occurs at the 50th-highest peak, with 63.1 MW_{el}. Nevertheless, with additional flexibility in asset operations, the peak power can be further reduced to 59.4 MW (see Figure 43). Focusing on the 300th highest power peaks and above, we can observe that a limitation is reached as more and more instances occur when the PV system cannot further reduce peak power. It must be noted that the shown results are only valid for the specific use case of the glassworks and might differ substantially for other applications. Nevertheless, for applications where peak power occurs at or near noon, PV systems offer the opportunity to substantially reduce peak power and save costs.

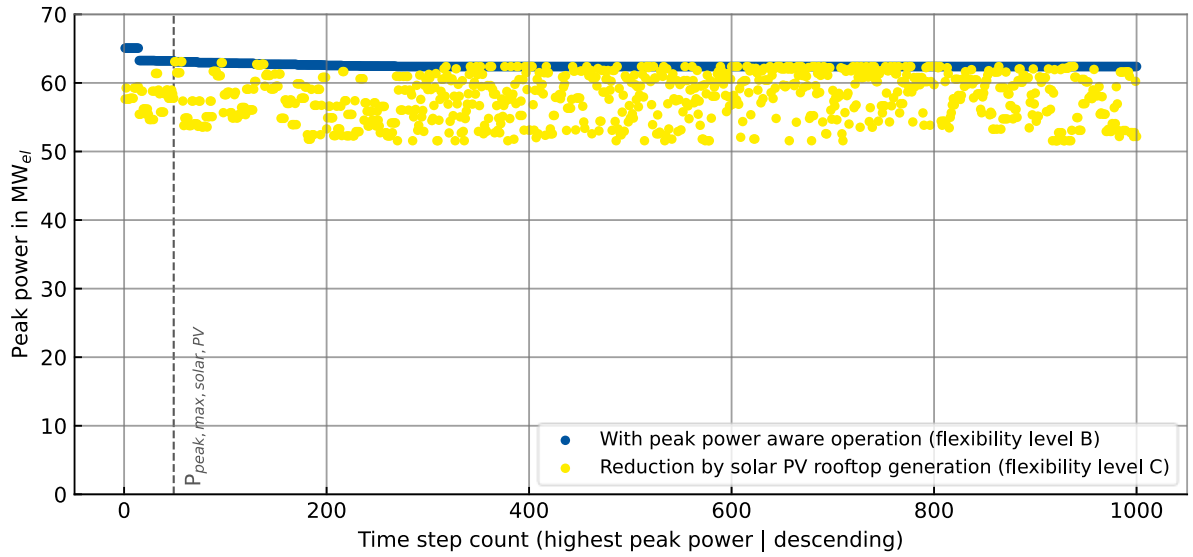

Figure 44: Peak power reduction with the PV rooftop system compared to peak power aware operation only, for the 1000 highest power peaks of the scenario with an AWE electrolysis system and high electrification of the furnace.

5.3.3. Flexibility level D-H: FTM services and value stacking

With peak-power-aware operation and installation of an on-site PV rooftop system, substantial total annual cost savings can be achieved (see Figure 40 and Figure 43). However, as both cases do not substantially increase the utilisation of the battery storage system, we want to evaluate the additional potential for integration of FTM services. This includes spot market trading (ST) and ancillary services. For ancillary services, we consider frequency containment reserve (FCR) and automatic frequency restoration reserve (aFRR). As the evaluation of FTM services requires extensive market data that is difficult to predict for future years, the focus is on the support year 2024, where historical data is available. Moreover, throughout the analysis, we focus exclusively on scenarios with an AWE electrolysis system that yield the most promising economic results (see Figure 21).

In a first step, we want to compare the cost-reduction potential of different single services and value stacking approaches. We stick to the flexibility levels defined in the scenario setup in Table 12. On the one hand, this includes isolated consideration of ST, FCR, and aFRR. On the other hand, we evaluate two value stacking approaches. This includes stacking of only FTM services without considering a PV rooftop system (flexibility level G) and stacking of all available flexibility options (flexibility level H). Figure 45 compares reductions in total annual system costs across the different flexibility choices considered. Flexibility level A (REF) serves as a reference representing the basic results from the decarbonisation analysis of the glassworks use case in Sections 5.1 and 5.2. The reference values are 83.1 Mio. EUR_{2024} and 63.4 Mio. EUR_{2024} for low and high electrification of the furnace, respectively. Moreover, the results for peak-power-aware operation (flexibility level B) and for a PV rooftop system with DM (flexibility level C) are included for comparison. In contrast to BTM services, FTM services are not part of the model's sizing layer and are implemented only in the operating layer. This means that the component sizing for all scenarios with FTM services is very similar to that for flexibility levels B or C, depending on whether a PV rooftop system is included. However, to enable FTM services to be properly used, we set the EPR of the battery storage system to 4 hours. This is a typical upper ratio for a large-scale BESS in Germany, designed to provide FTM services [11, 12].

Overall, substantial reductions in total annual costs are possible by leveraging additional flexibility potential for both low and high furnace electrification (see Figure 45). Combining flexibility services generally leads to higher cost reductions. Moreover, the reductions are higher for the low-electrification case, as a substantially larger battery storage system is installed to buffer RE generation from PPAs (see Figure 27).

One flexibility option with a large cost-reduction potential is ST (flexibility level D). This means that, instead of fixed tariffs for buying and selling wholesale power, time-variant prices are applied in the intraday continuous (IDC) market. This leads to an overall reduction in total annual costs of 15.2% and 9.7% for low and high furnace electrification, respectively. The

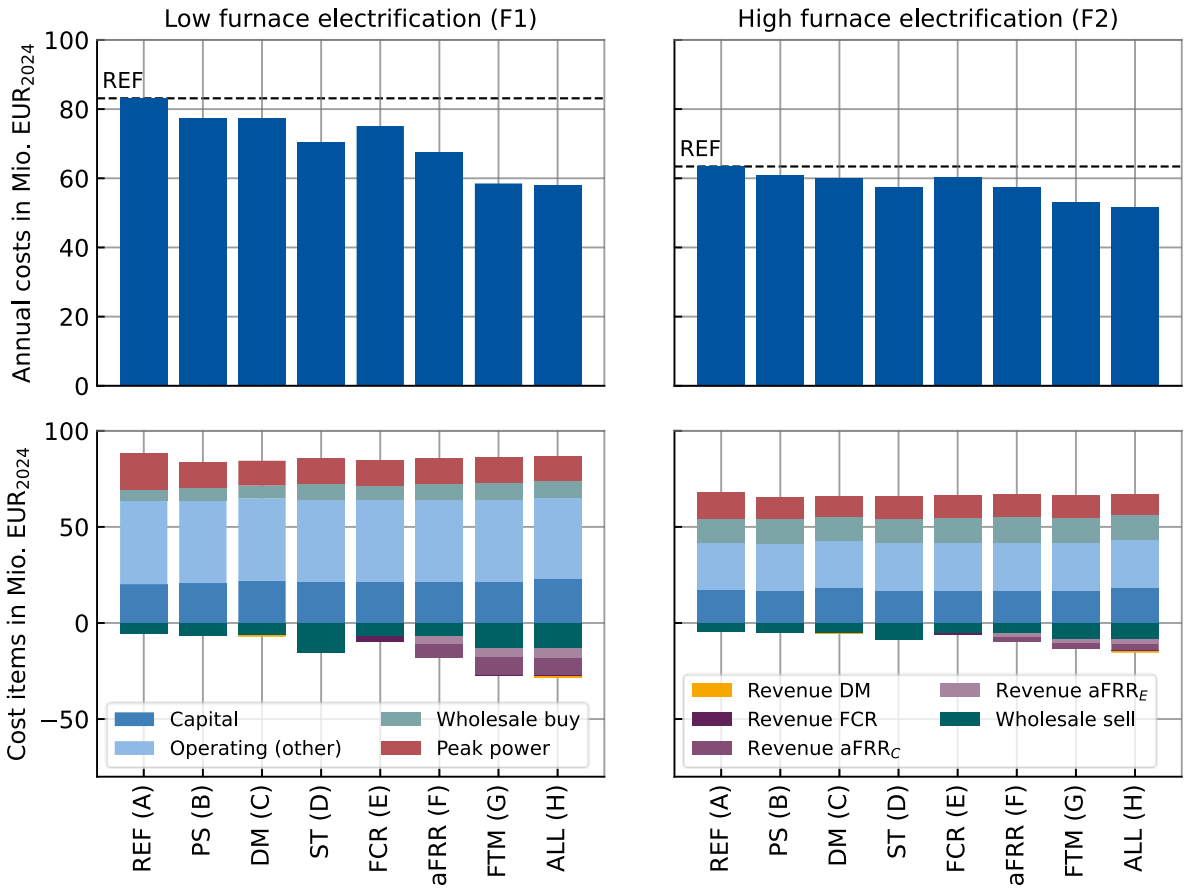

Figure 45: Comparison of reductions in total annual system costs for different flexibility choices. Results are shown for scenarios with an AWE electrolysis system as well as low (F1) and high (F2) electrification of the furnace. Flexibility level A (REF) serves as a reference representing the basic results from the decarbonisation analysis in Sections 5.1 and 5.2. For all scenarios, peak-power-aware operation is implemented. The scenario with flexibility level G features a stacking of all FTM services. The scenario with flexibility level H combines all BTM and FTM services. For the aFRR energy market, a conservative bidding strategy is applied, targeting a price position at 20% of allocated bids.

breakdown of costs shows that this is mostly due to selling more energy on the IDC. On the one hand, excess RE generation from PPAs can be used for this purpose. With the battery storage system, a larger share of this excess generation is stored compared to flexibility level B, and it is sold when prices at the IDC are high (see Figure 46). On the other hand, when prices on the IDC are low, the battery storage can be charged, and the energy used to cover the glassworks demand at a later point in time. However, a potential disadvantage of applying ST is that the glassworks' scope 2 emissions might increase when trading power from a non-renewable source. This needs to be carefully evaluated when implementing this flexibility option. However, electricity is usually bought at low prices when the electric power grid's emissions are lower [163]. In addition, with the ongoing decarbonisation of the electric power system [138], emissions associated with trading are expected to gradually decline.

Compared with ST, participating in the FCR market with the battery storage system yields lower cost savings of 9.6% and 4.7% for low and high furnace electrification, respectively. The

FCR revenue is at 3.0 Mio. EUR_{2024} for low and 1.1 Mio. EUR_{2024} for high furnace electrification. With 52 weeks a year, this leads to weekly average revenues of 973.7 EUR_{2024}/MW/week (F1) and 810.6 EUR_{2024}/MW/week (F2). Compared with the achievable FCR revenues displayed on the Battery Revenue Index [197], this is substantially below the full market potential. This can be explained by the fact that storage is also used to buffer generation from PPAs, leaving less capacity for FCR. Moreover, strict regulations on SOE management under the PQ-conditions for FCR effectively reduce reservable capacity when the battery SOE is out of the required range, as implemented in the model via Eq. (3.106). The results align with the expectation that the FCR market for battery storage will become less attractive in the coming years due to cannibalisation as an increasing number of batteries are prequalified for this market [95].

On the contrary, participation in the aFRR market proves to be the best choice in terms of flexibility when comparing single-service results. Reductions of 18.8% and 9.7% can be achieved for low and high furnace electrification, respectively. The aFRR revenue is split between the capacity ($aFRR_{cap}$) and energy ($aFRR_E$) markets. For the conservative bidding strategy in the aFRR energy market, targeting a price position of 20%, the revenue share from the capacity market is substantially higher than that from the energy market. Overall, a revenue of 11.4 Mio. EUR_{2024} for low and 4.4 Mio. EUR_{2024} for high furnace electrification can be achieved. Similar to FCR results, we can calculate the weekly average aFRR revenues to 3,760.1 EUR_{2024}/MW/week (F1) and 3,380.3 EUR_{2024}/MW/week (F2). This is in the expected range [197] and proves that the aFRR market is well-suited for combining increasing self-consumption of RE generation from PPAs in one battery. However, the complexity of the bidding process on the aFRR market leads to greater uncertainty about the reduction that will be achieved in real operation. In contrast to FCR, a sophisticated bidding strategy is required, as it is possible to place separate bids for capacity and the energy market, as well as for positive and negative direction (see Subsection 2.2.3). Nevertheless, the variation in price positions (Appendix I, Figure 50) shows that revenues remain on a similar level when applying a different bidding strategy on the aFRR energy market. Lower revenues on the energy market are partly compensated by increased bidding and revenues on the capacity market. Another development to consider is that in the long term, the potential for the aFRR market might also decrease when more and more batteries participate [95]. This risk can be reduced by adopting value stacking approaches that leverage multiple market channels.

Focusing on the two scenarios using a value stacking approach (flexibility levels G and H), the results clearly show a benefit over single-market results. The main difference between the two approaches is that for the flexibility level H, the PV rooftop system with DM is considered as an additional option. Overall, flexibility level H leads to the highest reductions of total annual costs of 30.1% and 18.8% for low and high furnace electrification, respectively. For high furnace electrification, this corresponds to 51.5 Mio. EUR_{2024}, which is still 27.4% higher than

rebuilding the NG furnace in 2024. In both value stacking approaches, the role of FCR is minor and does not substantially reduce total annual costs. This is the case because aFRR allows bidding on both positive and negative markets, thereby providing greater flexibility to adjust to battery storage SOE. The PV system for flexibility level H proves advantageous, as it generates additional RE that can be flexibly used. Overall, the results emphasise that, in future years, utilising flexibility could close the competitiveness gap relative to rebuilding the NG furnace.

We can identify further causalities by analysing the operation of the battery storage system in detail. Figure 46 illustrates the sizing and cycling of the battery storage system, separated into the different flexibility services. For sizing results, we find that the scenario design yields very similar results across all flexibility cases. For flexibility levels A-C, the battery storage systems are part of the sizing layer. This leads to slight differences in battery capacity for low furnace electrification, stemming from peak-power-aware operation. For flexibility level B, the battery size is optimised to a lower value as the electrolysis system size increases and less battery capacity is required (see Figure 41). On the contrary, for flexibility level C and low furnace electrification, the optimiser chooses a higher battery capacity, as PV rooftop generation reduces peak power, opening up more flexibility for battery storage (see Figure 43). For FTM services, the EPR of the battery is set to the typical upper value of 4 hours [11, 12]. This additional constraint leads to small differences in battery capacity sizing for the flexibility case H compared with flexibility level C.

Focusing on battery cycling, we observe that for the reference case (A), the cycling is 190.2 EFC/year and 238.9 EFC/year for low and high furnace electrification, respectively. Moreover, the cycling is considerably smaller for the larger battery storage system with low furnace electrification. Adding flexibility does not necessarily lead to higher cycling. In the flexibility cases B and C, peak-power-aware operation results in lower EFCs, as it primarily limits battery charging during peak load periods when RE generation from PPAs is high. The highest cycling is observed for ST (flexibility level D), with 262.1 EFCs (F1) and 455.3 EFCs (F2). For high furnace electrification, the EFCs even exceed the theoretically available 424 EFCs per year, calculated by dividing the cycle lifetime by the calendar lifetime in years. Usually, this threshold should not be exceeded by the model with cycle limitation implemented according to Eq. (3.15). However, at the operating layer of the model, this constraint can lead to divergent behaviour if the cycling in the rolling horizon is unequally distributed between the control and prediction horizons. When focusing on the origin of the increased cycling in the

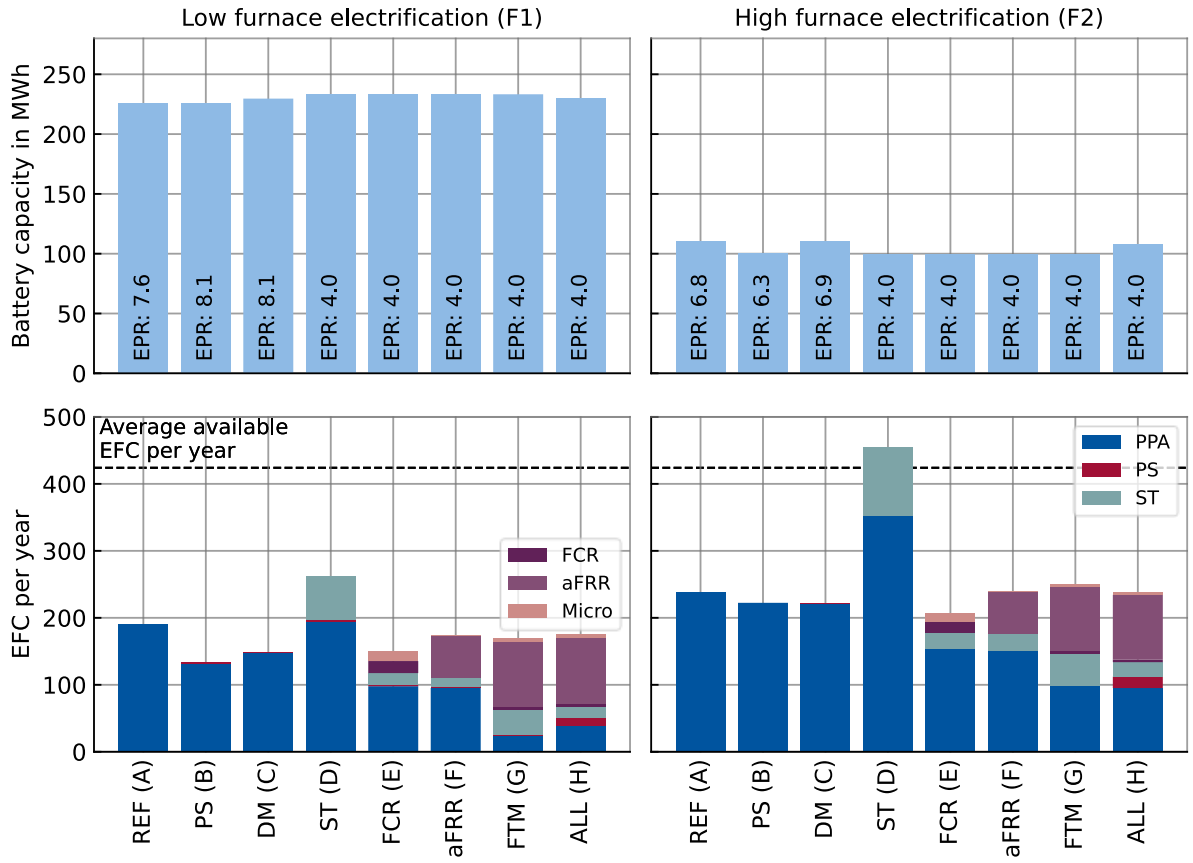

Figure 46: Sizing and cycling of the battery storage system for the considered flexibility scenarios A-H. EFCs are separated into the services provided by the battery storage system. In addition, micro cycling for FCR and aFRR is a separate category. Results are shown for scenarios with an AWE electrolysis system as well as low (F1) and high (F2) electrification of the furnace. For the aFRR energy market, a conservative bidding strategy is applied, targeting a price position at 20% of allocated bids.

flexibility case D, the results indicate that trading itself accounts for only part of the additional cycling. In particular, for low furnace electrification, most of it is due to higher utilisation of RE generation from PPAs. This is beneficial, as low-cost RE generation from PPAs can substitute for power purchases on the spot market during periods of high prices.

In contrast to ST, adding ancillary services in cases E-H leads to substantially reduced additional cycling. In addition, we can observe the displacement of intermediate storage of generation from PPAs, as reserving capacity for ancillary services is more lucrative. In particular, participating in the FCR market (flexibility level E) results in only a minor increase, or even a reduction, in overall cycling. On the one hand, FCR must be reserved for 4-hour blocks and be symmetrical in both directions, which reduces flexibility for other services, for instance, buffering RE generation from PPAs. On the other hand, it also only adds smaller amounts of cycling. Cycling is almost evenly distributed between net cycling for FCR and additional cycling via micro cycling. With the micro-cycling-aware implementation, the model accounts for cycling over the time range of seconds when responding to frequency deviations, even though the overall modelling resolution is 15 minutes. Overall, net and micro cycling

leads to 27-33 additional EFCs for participating in the FCR market. In addition, recharge management via wholesale adds up to another 18 cycles/year. In sum, this is substantially below the expected cycling of this application, around 250 EFCs per year, when applying FCR only as a service for a battery storage system [198].

The picture changes for aFRR that features substantially higher cycling. The amount of aFRR cycling is mainly influenced by the bidding strategy on the energy market. By default, the model uses a conservative bidding strategy that targets a price position of 20% of allocated bids. This results in frequent activation of the battery storage system. For aFRR-only operation (flexibility level F), depending on high or low electrification of the furnace, 61-63 EFC/years are added with up to 25 cycles/year for recharge management. The numbers show negligible micro-cycling for aFRR below 2 EFCs/year. When aiming for higher risk and higher-priced positions in the aFRR energy market, cycling can be substantially reduced (see Appendix I, Figure 51).

For the most profitable case of stacking all services for the battery storage system, the EFCs per year are similar to those for the single markets, despite substantially higher revenues. This is the case because flexibilities supplement each other, and ancillary services that are only attached to moderate cycling reserve large parts of the capacity. A possible supplement to flexibility is that energy charged to the battery from negative aFRR activation can be sold on the spot market when prices are high. Overall, the results highlight that, for the glassworks use case, battery storage value stacking offers substantial economic benefits without negatively impacting its anticipated battery cycle life. For ST only, however, the EFCs should be observed more clearly to prevent faster ageing with more intense cycling.

6. Discussion and outlook

Achieving climate neutrality requires decarbonisation across all sectors. One particularly challenging sector is the industry sector, in particular, when it comes to energy-intensive applications that require high-temperature process heat. In this dissertation, decarbonisation options for a glassworks in Herzogenrath, Germany, are analysed. The process of melting raw materials for glass production in the furnace requires large amounts of energy, currently provided by the combustion of fossil NG and a small share of electric boosting. To decarbonise the energy system of the glassworks, a fuel switch to renewable hydrogen is required in combination with a higher degree of furnace electrification. However, currently, there are only limited sources of renewable hydrogen. A short-term solution to produce on-site green hydrogen is to operate an electrolyser system powered by renewable electricity. The long-term alternative is to import renewable hydrogen via a future pipeline as part of Germany's planned hydrogen core network. Choosing the economically best system design and making the right technology choices requires a comprehensive energy system analysis. To achieve this, the FOCUS flexumer optimisation framework is developed based on MILP programming. It provides a modular structure that can be applied to any industrial sector-coupled energy system. For better performance, its structure is split into a sizing and an operating layer, enabling efficient optimisation. Further speed-up is achieved through time-step aggregation in the sizing layer and a rolling horizon approach in the operating layer of the model.

Overall, the evaluation results show clear options for achieving a decarbonised energy supply for the glassworks. Both the solution with the own production of hydrogen on-site and connecting to a hydrogen pipeline have advantages as well as disadvantages and show similar economic outcomes. The decision on which option to implement mainly depends on the type of risk site owners are willing to accept. With the electrolyser-based solution, the energy system becomes substantially more complex, requiring substantial investments in new components. At the same time, it provides a more robust solution by reducing dependencies on global energy prices, which can be further reduced with on-site RE generation. On the contrary, the solution with a hydrogen pipeline is more similar to the status quo, with a comparatively simple system operation. On the downside, it is a bet on the future, as no hydrogen pipeline network or global hydrogen market currently exists, which entails significant price uncertainty. In addition, regarding the furnace design, most of the R&D effort should be invested in achieving higher levels of electrification. This is the most important lever to enable cost-competitive glass production in the future. In addition to economic considerations, the higher electrification features more realistic components and PPA sizing, avoiding mostly hydropower PPAs with limited capacity available in the German bidding zone. Nevertheless, the evaluations show that even in 2037, there is still a substantial economic gap between rebuilding the NG furnace and the renewable scenarios for the glassworks energy system.

6.1. Technology comparison

For the analysis of decarbonisation choices, we consider three different years for constructing the new furnace. This includes 2024 as a present year, 2030 as a near-future year, and 2037 as a more distant future year. The scenario that rebuilds the NG-based furnace serves as a benchmark for the decarbonised energy system across all years. For the furnace, we consider low (8 MW_{el}) and high (20 MW_{el}) electrification, compared to only 3 MW_{el} for the NG furnace. Another variation involves two different types of electrolyser systems based on AWE or PEM technology. For all scenarios with on-site hydrogen production, we apply optimised PPA portfolios to meet the electrolyser system's demand in accordance with the requirements of the EU RED II regulation. The regulation demands monthly and hourly temporal matching of PPAs and electrolysis system demand for 2024 and 2030, respectively. To achieve better matching, battery storage systems are used.

The results of the evaluation indicate that total annual costs for the scenario of rebuilding the NG-based furnace increase from 2024 to 2037. The main factors are rising NG prices and higher CO_2 emission certificate costs. In particular, emission costs show increasing shares of 21.4% and 35.9% for 2030 and 2037, respectively. For decarbonisation in 2024, setups with an electrolysis system incur higher total annual costs than rebuilding the NG-furnace-based system. This is particularly due to higher operating costs for peak power, levies, and taxes. However, the competitiveness of decarbonisation scenarios improves towards 2037 with substantial decreases in total annual costs. The cost savings are mainly due to reductions in the capital costs of the electrolyser system and battery storage, as well as lower future electricity prices. Capital costs for the scenarios with an AWE electrolysis system show a potential to decrease by up to 24.2% from 2024 to 2037. In the best case, the 2037 scenario with an AWE electrolysis system and high furnace electrification has total annual costs 18.3% higher than the NG-furnace-based setup. The scenario with a hydrogen pipeline connection and high furnace electrification lies only slightly above. In addition, a high level of furnace electrification is substantially more cost-competitive than a low level. This particularly applies to scenarios with a hydrogen pipeline connection, where operating costs are the dominating factor and highly dependent on the amount of imported hydrogen. Another measure to benchmark different decarbonisation choices is the LCOH. While in 2024 the LCOH is between 9.3-11.7 EUR_{2024}/kg, it reduces to between 5.2-8.1 EUR_{2024}/kg in 2037. In particular, electrolyser-system-based scenarios with AWE technology have lower LCOHs than those with PEM technology, due to lower specific investment costs and higher efficiencies. Moreover, scenarios with an electrolysis system can be competitive with the hydrogen pipeline setup by utilising low-cost RE generation from PPAs. Independent of the decarbonisation choice, CO_2 emissions show a reduction potential of 52.9% in 2024, and 74.4% in 2030 and 2037. This substantially reduces the impact of CO_2 certificate costs on total annual costs. The remaining

emissions are process-related and can only be further reduced with new raw material combinations or CCS technology.

Other factors that substantially influence the results are energy price assumptions for future years. While the basic results assume a medium price corridor, a sensitivity analysis accounts for the uncertainty associated with price predictions. To cover extremes in both directions, the sensitivity analysis considers low- and high-priced scenarios. In both cases, the annual costs are increased/decreased simultaneously for NG, electricity, and green hydrogen. The low energy price corridor is particularly beneficial for rebuilding the NG furnace. However, the competitiveness of the scenario with a hydrogen pipeline connection slightly increases. On the contrary, the results for high energy prices show a substantial reduction of the gap between decarbonisation scenarios with an electrolysis system and rebuilding the NG furnace. This emphasises the greater robustness of total annual costs for the electrolysis-system-based scenarios, as they are less dependent on global energy prices. The opposite holds for scenarios with a connection to a future hydrogen pipeline, where higher energy prices for green hydrogen have a clear negative impact. The competitiveness of the hydrogen pipeline case mainly depends on cheap global hydrogen prices, which are highly uncertain because no global market currently exists.

6.2. Design considerations

While the decarbonisation solution with a hydrogen pipeline connection shows high uncertainty regarding total system costs, the energy system setup is fairly simple and comparable to the scenario with an NG-based furnace. On the contrary, the solution with an electrolysis system results in a more complex design that requires several novel components. The central component next to the furnace is the electrolyser system for hydrogen production. Its electric power rating is very much dependent on the level of electrification of the hydrogen furnace. For an AWE electrolyser system, the optimal electrical power rating is 44-39 MW_{el} and 19-13 MW_{el} (2024-2037) for low and high furnace electrification, respectively. The lower efficiency of PEM technology even results in optimal power ratings of up to 55.4 MW_{el}. The electrolysis system is combined with a hydrogen pressure and battery storage system, which provides flexibility to buffer RE generation from PPAs. In addition, the hydrogen storage is used to bypass maintenance periods of the electrolysis system. Overall, optimal sizing results for hydrogen storage range from 7.3 $MWh_{H2,LHV}$ to the regulatory threshold of 167.65 $MWh_{H2,LHV}$ (5 tonnes of hydrogen), showing a decreasing trend towards 2037 as electrolyser efficiencies improve. The fact that the optimiser chooses the largest allowed hydrogen storage size for all scenarios in 2024 and 2030 indicates that the ideal size would be even larger. In Brucksch et al. [24], eliminating this threshold shows that both battery- and

hydrogen-storage capacity would increase substantially, allowing for higher shares of low-cost PV in PPA portfolios.
Overall, for the battery storage system, optimal capacities increase towards 2037 as specific investment costs decrease. One peculiarity of the battery sizing results is comparatively high EPR ratios between 2-14h, indicating a slow charging characteristic and excess generation from PPAs over a longer time. The wide range originates from different PPA portfolio designs. Moreover, low furnace electrification results in comparatively high capacities of up to 449.2 MWh_{el}. Although technically feasible, this solution is considered challenging due to space limitations at the industrial site. On the contrary, a more realistic setup is reached with high furnace electrification in combination with an AWE electrolysis system that shows optimal battery capacity between 80.6-110.4 MWh_{el}. This is a clear argument in favour of a high degree of furnace electrification. Moreover, the results show that applying WHR to the electrolysis system can provide a major share of the thermal demand for space heating, and electric boilers can be effectively downsized.

The comparison of all decarbonisation options shows that the economically most promising scenarios involve high electrification of the hydrogen furnace, either via an AWE electrolyser system or via connection to a future hydrogen pipeline. The main challenge for all decarbonisation choices is the design of a novel hydrogen furnace from scratch. This particularly concerns a high level of furnace electrification, which substantially differs from that of existing NG-based furnaces with low electrification. While the hydrogen furnace with low electrification is estimated to be only 1.5 times more expensive than an NG-based furnace design, high furnace electrification is estimated to be 2.5 times more expensive. Consequently, in scenarios with an AWE electrolysis system, the high-electrified furnace accounts for the majority of total capital costs, ranging from 61.3% to 80.8% (2024-2037). Other relevant shares of capital costs come from the AWE electrolyser and the battery storage system.
Nevertheless, the main share of total annual costs is operating costs. The largest amount is required to purchase RE generation under PPAs to operate the electrolysis system with green electricity. While in 2024 the main share of generation from PPAs is supplied by WPP (49.4 GWh), this shifts towards PV in future years as PPA prices decline. One main advantage of the electrolysis-system-based scenarios is that low-cost excess generation from PPAs can be used to supply the remaining load of the glassworks. Nevertheless, the timely misalignment between PPA power generation and the glassworks' energy consumption results in substantial amounts of renewable electricity that need to be resold to the wholesale market (85.3 GWh in 2024). This mismatch reduces in 2037 under the assumption that the temporal matching of generation from PPAs and electrolysis system demand, as of the EU RED II, no longer applies. As renewable generation from PPAs cannot cover demands at all times, additional power generation from hydropower futures (EU27) has to be purchased on the wholesale market

(143.4 GWh in 2024). Another large contributor to operating costs is peak power costs, as well as taxes and levies, with an increasing cost share towards 2037. The results show that peak power costs are a substantial factor that can determine whether decarbonisation is cost-competitive. With higher electrification, peak power costs increase substantially compared to an NG-based furnace and account for 30.1% of all operating costs in 2024. Therefore, future electric power grid fees should be designed to support industries with rising electric power demand in their decarbonisation efforts.

Furthermore, a main disadvantage of the electrolysis-system-based setup is the high energy losses of the components. This mainly concerns the electrolysis system, which has a combined efficiency of only 74.4% when considering WHR (2024). However, with the anticipated increase in the efficiency of the electrolysis system towards 2030, lower amounts of waste heat will result. This leads to a substantial reduction in losses and a higher utilisation of waste heat with the industrial HP. Another aspect that influences losses is the operational characteristic of the electrolysis system that is modelled with variable efficiency. In 2024 and 2030, the AWE electrolyser system is often operated at a part load of around 50% to exploit maximum efficiency. With increasing electrolysis system efficiency in 2037, however, it is more optimal to reduce the power capacity and approach maximum load points instead. Other, less substantial losses occur at the battery storage system, which has a much lower energy throughput and better efficiency than the electrolysis system. Moreover, the battery storage shows a pattern similar to that of typical PV battery storage, with higher usage in summer months and lower usage in winter months. Considering the comparatively high capital costs of battery storage, better utilisation can be achieved by integrating additional use cases.

Compared with electrolysis-system-based scenarios, setups including a connection to a hydrogen pipeline are characterised by lower capital costs, as only the hydrogen furnace needs to be considered. On the contrary, the operating costs are substantially higher. The main share of operating costs is required to purchase green electricity from hydropower futures (EU27), amounting to 319.2 GWh. This indicates that the largest cost-reduction potential in the scenarios with hydrogen pipeline connection and high furnace electrification is low-cost RE generation. The other major cost contributor is the purchase price of imported green hydrogen from the pipeline. Despite the comparatively low annual energy consumption of 63.8 GWh, they account for over 20% of operating costs. Other cost factors, such as peak power costs, taxes, and levies, are substantially lower than for the electrolysis-system-based scenarios.

6.3. Flexibility potentials

A central approach to further increase the competitiveness of decarbonisation scenarios is to leverage their flexibility potential. By leveraging the flexibility of the battery storage and electrolyser system, the industrial site can be converted from a prosumer to a flexumer application. Applying peak-power-aware operation already shows substantial cost-reduction potential. In scenarios with an AWE system, total annual costs decrease by 3.2-10.3%. This is mainly achieved by increasing the electrolysis system capacity, thus enabling more flexible hydrogen production during off-peak times. Moreover, the results indicate that, for scenarios with a hydrogen pipeline connection, the peak power and cost-reduction potential are limited, as the energy system lacks flexible power-consuming components. In this case, investing in a new battery storage system only shows negligible reductions.

Another solution that effectively reduces peak power is the installation of a 12.3 MW_p PV rooftop system at the industrial site. PV generation shows a strong correlation with the site's peak power consumption, so most of the generation is directly fed into the electric power grid to reduce peak power and save costs. This is advantageous in two ways, as the feed-in is also reimbursed through the DM mechanism. Overall, this simple measure leads to total annual cost savings of 3.6-10.6% in scenarios with an AWE electrolysis system, making the investment in the rooftop PV system a no-regret decision.

In electrolysis-system-based scenarios, further cost reductions can be achieved by applying front-of-the-meter (FTM) services. Switching from fixed wholesale futures prices to variable intraday continuous prices proves beneficial for the power supply. This scenario variation achieves total annual cost reductions of 15.2% and 9.7% for low and high levels of furnace electrification, respectively. However, scope 2 emissions for the glassworks might be increasing when trading power from a non-renewable source. Those additional emissions depend on the electric power grid mix and need to be carefully considered when implementing this flexibility option. Another characteristic of applying ST only is that the cycling of the battery storage system can substantially increase, which potentially leads to higher ageing rates.
Another flexibility option for scenarios with an electrolysis system is to participate in ancillary services for frequency control with the already existing battery storage system. This comes with the advantage that the cycling of the battery storage system is lower than for participating in ST only. For the glassworks, aFRR shows the most promising results, with cost reductions of 18.8% and 9.7% for low and high furnace electrification, respectively. On the contrary, participating in the FCR market proves substantially less beneficial, as the market design is less flexible and thus less compatible with the PPA operation of the battery.

Moreover, as battery installations increase, cannibalisation effects on the FCR market could further reduce revenue in the near future.
The largest economic benefits can be achieved with the so-called value stacking of all single flexibilities. However, this substantially changes the original operation of the storage as ancillary services are partly displacing the buffering of RE generation from PPAs. Nevertheless, in 2024, the full value stacking approach yields the highest total annual cost reductions of 30.1% and 18.8% for low and high furnace electrification, respectively. Nevertheless, for the most promising decarbonisation case with high furnace electrification in 2024, total annual costs are still 27.4% higher than for rebuilding the NG furnace. However, given the closing cost gap towards 2037, utilising flexibilities could help achieve cost parity between the fossil and decarbonised energy systems in the future.

6.4. Research Outlook

Although the evaluation focuses on the specific glassworks use case in Herzogenrath, the results act as a blueprint for decarbonisation concepts for other industrial sites. However, further advances could be achieved when applying the developed industry flexumer modelling framework to other use cases and benchmarking the results. In addition, improving the model's operating layer through sophisticated predictions could yield even higher-quality results. Furthermore, the higher profitability of battery storage can be demonstrated by integrating more sophisticated trading strategies into the value stacking approach.
One of the major disadvantages of the used methodology is that it is on the verge of reaching the limitations of MILP programming. Based on the findings of this dissertation, rule-based approaches could be implemented that allow for greater modelling detail and are closer to real operations. Another improvement could be integrating a pathway approach into the flexumer framework design. This would enable an aggregated cost comparison over the lifetime of a newly installed furnace. Regarding flexibility, the evaluation could also be further extended. While this evaluation assumes constant consumption profiles for all scenarios, load shifting could provide another substantial flexibility lever. In addition, flexible components such as the electrolyser system could participate in frequency control markets to increase marketable power in combination with the battery storage system.

Apendix

Appendix A - List of variables

Table 22: List of optimisation variables and sets for the MILP model of the developed FOCUS flexumer framework. In addition, other relevant modelling variables that are not directly part of the MILP model are summarised.

Optimisation variables and sets					
Programme code ID	**Formula letter**	**Unit**	**Data type**	**Variable Type**	**Description**
input_1	P_{in1}^{m1}	kW	float	unbounded	Input power for commodity m1
output_1	P_{out1}^{m2}	kW	float	unbounded	Output power for commodity m2
capacity	P_N^{m1}	kW	float	bounded	Nominal power capacity based on input commodity m1
capacity (BaseStorage)	C_N^{m1}	kWh	float	bounded	Nominal energy capacity based on input commodity m1
energy	SOE	kWh	float	unbounded	Storage level (state-of-energy)
capacity_discrete_intervall	n_{discr}	none	integer	unbounded	Quantity of discrete sizing capacity
z_input	z_{in1}	none	∈{0,1}	binary	Binary variable to switch on/off component input
z_output	z_{out1}	none	∈{0,1}	binary	Binary variable to switch on/off component output
z_off	z_{off}	none	∈{0,1}	binary	Binary variable for electrolyser off-mode
z_standby	$z_{standby}$	none	∈{0,1}	binary	Binary variable for electrolyser standby-mode
z_2p	z_{on}	none	∈{0,1}	binary	Binary variable for electrolyser on-mode
z_cold	z_{cold}	none	∈{0,1}	binary	Binary variable electrolyser cold start-mode
curtailment_1	$P_{curtail}^{m1}$	kW	float	unbounded	Surplus power for BaseBusBar component
slack_1	$P_{slack,t}^{m1}$	kW	float	unbounded	Deficit power for BaseBusBar component
capital_cost	κ_{capex}	EUR	float	unbounded	Capital costs of components
operating_cost	$\kappa_{opex,buy,sell,fix}$	EUR	float	unbounded	Grid operating costs with fixed price
	$\kappa_{opex,buy,sell,var}$	EUR	float	unbounded	Grid operating costs with variable price
	$\kappa_{opex,pen}$	EUR	float	unbounded	Penalty costs for imbalance of BusBar
	$\kappa_{opex,contr.PPA}$	EUR	float	unbounded	PPA purchasing/contracting costs
contracting_costs	$\kappa_{opex,contr,el}$	EUR	float	unbounded	Electrolyser contracting costs
Modelling variables					
Programme code ID	**Formula letter**	**Unit**	**Data type**	**Description**	
t_step	t_Δ	h	float	Time series with the length of all optimisation time steps	
-	n_T	none	integer	Number of time steps in optimisation horizon	
discrete_sizing_intervall	P_{discr}	kW	integer	Size of one unit / discrete sizing interval	
consumption	P_{load}^{m}	kW	Series (float)	Time series with consumption data for commodity m	
-	P_{gen}^{m}	kW	float	Power generation of commodity m	
efficiency	η	%/100	float	Efficiency for conversion components	
	$\eta_{tr,distr}$	%/100	float	Efficiency for PPA due to transm./distr. losses	
	η_{inv}	%/100	float	Inverter efficiency	
	$\eta_{el,H2}$	%/100	float	Electrolyser efficiency to hydrogen output	
total_efficiency	η_{el}	%/100	float	Total electrolyser efficiency (including heat)	
eta_h2_2p	$\eta_{on,upper}$	%/100	float	Electrolyser efficiency factor for upper power during on-mode	
eta_h2_3p	$\eta_{on,lower}$	%/100	float	Electrolyser efficiency factor for lower power during on-mode	
eta_h2_nominal	$\eta_{on,N}$	%/100	float	Electrolyser nominal efficiency	
input_efficiency	η_{in}	%/100	float	Input efficiency for storage components	

output_efficiency	η_{out}	%/100	float	Output efficiency for storage components
e2p_in	EPR_{in}	h	float	Input EPR for storage components
e2p_out	EPR_{out}	h	float	Output EPR for storage components
min_soe	SOE_{min}	%/100	float	Minimum SOE for storage components
max_soe	SOE_{max}	%/100	float	Maximum SOE for storage components
yearly_interest	i	%/100	float	Interest rate for investments
cycle_life	L_{cycle}	none	integer	Cycle life of storage system
life	$L_{calendar}$	a	integer	Calendar life of storage system
curtailment_price	$\pi_{curtail}$	EUR/kWh	float	Price for curtailing energy in BusBar
slack_price	π_{slack}	EUR/kWh	float	Price for drawing slack energy in BusBar
price	π_{buy}^{m1}	EUR/kWh	float / Series	Price for buying energy from the grid
injection_price	π_{sell}^{m1}	EUR/kWh	float / Series	Compensation for selling energy to the grid
ppa_price	$\pi_{PPA,contr}$	EUR/kWh	float / Series	PPA contracting price
contract	$\pi_{el,contr}$	EUR/kWh$_{H2}$	float	Contracting price for H_2 from electrolyser
cost	κ_{inv}	EUR/kW(h)	float	Investment costs of components
ann	ANF	none	float	Annuity factor for investments
f_w	$f_{fix,op}$	none	float	Factor for fixed operational costs (investment)
-	$f_{replace}$	none	float	Factor for investment costs for replacement
-	$f_{residual}$	none	float	Factor for investment costs for residual value
power_factors	CF	none	Series (float)	Capacity factor for RE generators/PPAs availability
cop	COP	%/100	float	Efficiency of heat pump/coefficient of power
set_t	T_{sink}	°C	float	Temperature of heat pump sink
amb_t	T_{source}	°C	float	Temperature of heat pump source
consum_elec	c_{cons}^{elec}	kW$_{el}$/kW$_{H2}$	float	Electricity consumption hydrogen compression
LB_standby	$p_{standby}$	%/100	float	Electrolyser standby power as share of nom. power
LB_1	$p_{on,lower}$	%/100	float	Electrolyser lower power limit during on-mode as share of nom. power
capacity_reserve	$r_{cap,res}$	%/100	float	Capacity reserve for energy conversion components (only in sizing layer)

Appendix B - Levelised costs of electricity (LCOE)

Table 23: Summary of the levelised costs of electricity (LCOE) that are used for the parametrisation of the scenarios, based on [8]. Values are linearly extrapolated for years that are not included in the study. For PV rooftop and offshore wind, we assume the same relative LCOE decline as utility-scale PV and onshore wind.

Technology	**Unit**	**Year in Study**						**Extrapolation years**			
		2024		2035		2045		2030		2037	
		low	high	low	high	low	high	low	high	low	high
Large-scale PV rooftop	$EURct_{2024}$/kWh	5.65	11.93	4.50	9.50	4.06	8.58	5.02	10.60	4.41	8.98
Utility-scale PV	$EURct_{2024}$/kWh	4.12	6.98	3.28	5.56	2.96	5.02	3.66	6.21	3.22	5.45
Wind onshore	$EURct_{2024}$/kWh	4.26	9.18	3.94	8.42	3.62	7.81	4.09	8.77	3.88	8.30
Wind offshore	$EURct_{2024}$/kWh	5.37	10.37	4.97	9.51	4.57	8.82	5.15	9.90	4.89	9.37
Legend: Calculated/extrapolated values (■)											

Appendix C - Inflation rates

Table 24: Inflation rates for the Euro area as published in the European Central Bank (ECB) data portal [146].

Time range from year (July) → to year (July)	**Harmonised Index of Consumer Prices (HICP)**		**Average inflation rate in % - HICP industrial goods excl. energy**
	Energy	Industrial goods excluding energy	
2010 → 2024	-7.9	1.172	1.140
2011 → 2024	-11.6	1.166	1.188
2012 → 2024	-5.9	1.148	1.157
2013 → 2024	-1.4	1.143	1.222
2014 → 2024	1.2	1.144	1.354
2015 → 2024	5.8	1.139	1.457
2016 → 2024	6.9	1.135	1.596
2017 → 2024	2.4	1.131	1.774
2018 → 2024	9.7	1.128	2.028
2019 → 2024	0.7	1.125	2.384
2020 → 2024	8.6	1.108	2.597
2021 → 2024	-14.1	1.101	3.259
2022 → 2024	-39.4	1.055	2.713
2023 → 2024	-5.9	1.005	0.500

Appendix D - Currency exchange rates

Table 25: Currency exchange rates for the Euro area as published in the European Central Bank (ECB) data portal [147].

Year	**Euro (EUR) per US Dollar (US$)**
2010	0.754
2011	0.718
2012	0.778
2013	0.753
2014	0.753
2015	0.901
2016	0.903
2017	0.885
2018	0.847
2019	0.893
2020	0.876
2021	0.846
2022	0.950
2023	0.925

Appendix E - Financial calculations

The following equations provide the calculation basis for the annualised capital cost of components in the FOCUS framework. All calculations are according to VDI2067 [199].

$$ANF = \frac{(1+i)^L * i}{(1+i)^L - 1} \tag{A.1}$$

$$f_{replace} = ANF * \sum_{i=1}^{n_{replace}} \frac{1}{(i+1)^{i*L}} \tag{A.2}$$

$$f_{residual} = ANF * \frac{(n_{replace}+1) * L - H}{L} * \frac{1}{(i+1)^H} \tag{A.3}$$

Appendix F - Optimiser and server settings

Table 26: Summary of the optimiser settings and server specifications that have been used for optimisation.

Solver settings	
Solver parameter	**Value**
Solver name	Gurobi
MIPGap	0.02
Presolve	2
TimeLimit	900
Threads	5
IntFeasTol	0.001
Server specifications	
Model name	AMD EPYC 7H12 64-Core Processor
CPUs	256
CPU MHz	3277.758
Architecture	X86_64
Threads per core	2
Memory	2.0 TB
Swap	996 GB

Appendix G - Reduction of model size with time step clustering

Table 27: Summary of achieved model reductions with the time step clustering algorithm in the sizing layer of the FOCUS flexumer model. Reduction values are calculated for all scenario variations.

Year (flexibility level)	Model size reduction in %						
	NG furnace – F0	Low furnace electrification (H_2) – F1			High furnace electrification (H_2) – F2		
	Pipeline	AWE	PEM	H_2 pipeline	AWE	PEM	H_2 pipeline
2024 (A)	67.29	49.39	49.38		49.52	49.39	
2030 (A)		49.78	49.80	62.31	49.73	49.69	63.14
2037 (A)		49.81	49.95		49.69	49.77	
2024 (B)		49.39			49.52		
2030 (B)		49.78		62.31	49.73		63.14
2037 (B)		49.81			49.69		
2024 (C)		49.34			49.48		
2030 (C)		49.90		62.31	49.77		63.14
2037 (C)		49.89			49.70		
2024 (D)		49.39			49.52		
2024 (E)		49.39			49.52		
2024 (F)		49.39			49.52		
2024 (G)		49.39			49.52		
2024 (H)		49.34			49.48		
➔ The different energy price levels that are evaluated do not influence the model size reduction							

Appendix H - Figures source data

Figure source data for Subsection 5.1:

Table 28: Source data for Figure 22 - comparison of total annual system costs with low energy price assumptions.

Technology type	Pipeline (NG)	AWE system (H_2)		PEM system (H_2)		Pipeline (H_2)	
Furnace type	NG-F0	H2–F1	H2-F2	H2–F1	H2-F2	H2–F1	H2-F2
2030							
Share invest costs in %	10.642	23.265	27.411	24.543	28.284	11.632	21.593
Annual costs in mio. EUR_{2024}	40.625	81.187	56.401	91.314	60.718	55.335	49.386
2037							
Share invest costs in %	12.204	27.921	26.629	26.655	26.992	11.805	21.399
Annual costs in mio. EUR_{2024}	35.427	59.974	48.841	65.249	51.456	54.524	49.833

Table 29: Source data for Figure 23 - comparison of total annual system costs with high energy price assumptions.

Technology type	Pipeline (NG)	AWE system (H_2)		PEM system (H_2)		Pipeline (H_2)	
Furnace type	NG-F0	H2–F1	H2-F2	H2–F1	H2-F2	H2–F1	H2-F2
2030							
Share invest costs in %	6.270	20.714	22.363	22.114	23.435	7.540	13.615
Annual costs in mio. EUR_{2024}	68.957	92.594	70.326	102.379	73.803	85.364	78.321
2037							
Share invest costs in %	7.115	20.757	21.532	19.873	22.388	8.226	14.146
Annual costs in mio. EUR_{2024}	60.763	83.395	65.270	91.174	67.916	78.254	75.385

Table 30: Source data for Figure 34: levelised costs of hydrogen (LCOH) and hydrogen consumption.

Technology type	AWE system (H_2)		PEM system (H_2)		Pipeline (H_2)	
Furnace type	H2–F1	H2-F2	H2–F1	H2-F2	H2–F1	H2-F2
2024						
Annual H_2 demand in t	5553.200	1914.814	5553.200	1914.814		
Cost of H_2 in EUR_{2024}/kg	9.289	9.419	11.603	11.665		
2030						
Annual H_2 demand in t	5553.200	1914.814	5553.200	1914.814	5553.200	1914.814
Cost of H_2 in EUR_{2024}/kg	9.712	8.722	11.533	10.614	5.766	5.766
2037						
Annual H_2 demand in t	5553.200	1914.814	5553.200	1914.814	5553.200	1914.814
Cost of H_2 in EUR_{2024}/kg	7.089	5.620	8.106	7.319	5.233	5.233

Table 31: Source data for Figure 25 – breakdown of all cost and emission shares for all regular scenarios.

Tech.	Scenario	Cost parts in Mio. EUR_{2024}			Emissions in Mt	
		Capital costs	Operating costs	Emission costs	Process-related emissions	Combustion of NG
Pipe. (NG)	F0-2024	4.324	30.523	5.567	30.000	51.872
	F0-2030	4.323	33.444	10.269	21.000	61.152
	F0-2037	4.323	25.004	16.430	21.000	61.152
AWE system (H_2)	F1-2024	20.159	60.919	2.040	30.000	0.0
	F1-2030	19.021	63.884	2.625	21.000	0.0
	F1-2037	17.087	49.628	4.200	21.000	0.0
	F2-2024	17.248	44.123	2.040	30.000	0.0
	F2-2030	15.508	43.506	2.625	21.000	0.0
	F2-2037	13.079	36.868	4.200	21.000	0.0
PEM system (H_2)	F1-2024	25.487	68.719	2.040	30.000	0.0
	F1-2030	22.495	70.652	2.625	21.000	0.0
	F1-2037	17.747	54.755	4.200	21.000	0.0
	F2-2024	19.207	46.537	2.040	30.000	0.0
	F2-2030	17.208	45.639	2.625	21.000	0.0
	F2-2037	14.003	39.316	4.200	21.000	0.0
Pipeline (H_2)	F1-2030	6.437	59.117	2.625	21.000	0.0
	F1-2037	6.437	51.472	4.200	21.000	0.0
	F2-2030	10.664	47.963	2.625	21.000	0.0
	F2-2037	10.664	41.451	4.200	21.000	0.0

Figure source data for Subsection 5.2.1:

Table 32: Source data for Figure 29 - breakdown of annualised investment costs for the scenario with AWE system and high furnace electrification.

Cost items	Furnace	AWE system	Compressor	Pressure storage	Industrial HP	E-boiler	Thermal storage	Battery storage	Battery inverter
Invest. costs in Mio. EUR_{2024}	2024								
	10.567	2.629	0.038	0.381	0.074	0.040	0.000	0.176	3.342
	2030								
	10.567	1.589	0.031	0.381	0.054	0.032	0.002	0.198	2.654
	2037								
	10.567	1.006	0.010	0.017	0.055	0.029	0.009	0.072	1.315

Table 33: Source data for Figure 30 - breakdown of operating cost components for the scenario with AWE system and high furnace electrification.

Cost items	PPA hydro (buy)	PPA WPP (buy)	PPA PV (buy)	Whole-sale (buy)	PPA (sell)	Tax/levy reimbursement AWE	Peak power	Tax/Levy electricity	Emission
Operating costs in Mio. EUR_{2024}	2024								
	0.143	14.958	5.224	12.190	-4.523	-0.722	13.911	2.943	2.040
	2030								
	0.000	12.097	5.428	10.513	-3.388	0.000	14.177	4.679	2.625
	2037								
	0.000	10.066	5.223	9.000	-3.332	0.000	11.353	4.558	4.200

Appendix I - Additional evaluations

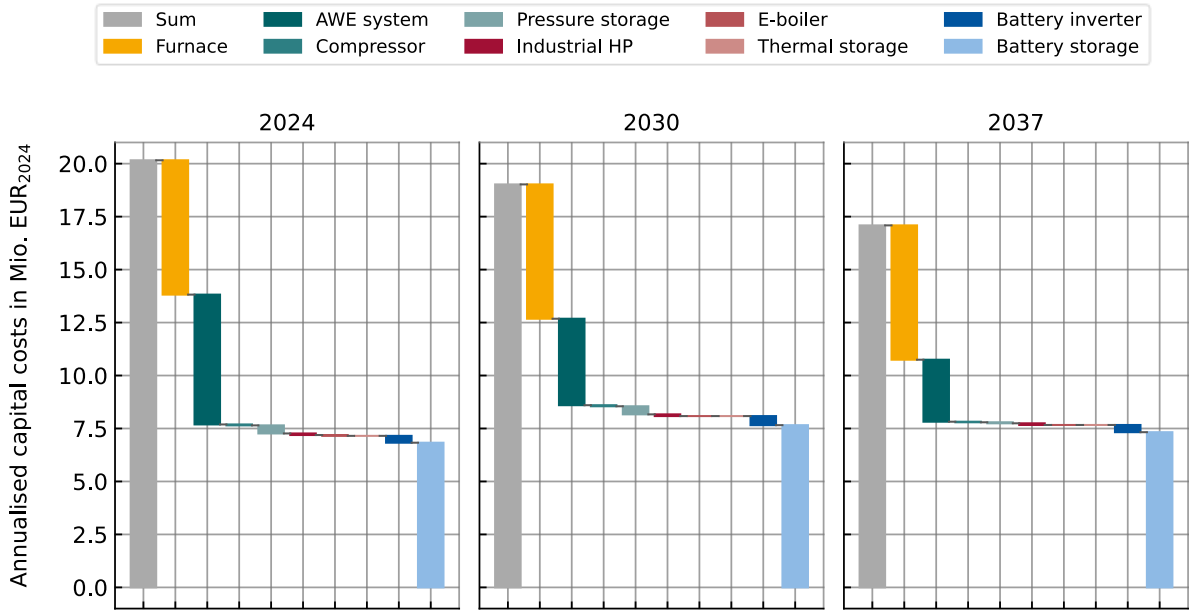

Figure 47: Breakdown of annualised investment costs of all required components for the decarbonised energy system of the glassworks in case of low electrification (8 MW_{el}) of the melting furnace. The electrolysis system is AWE-based.

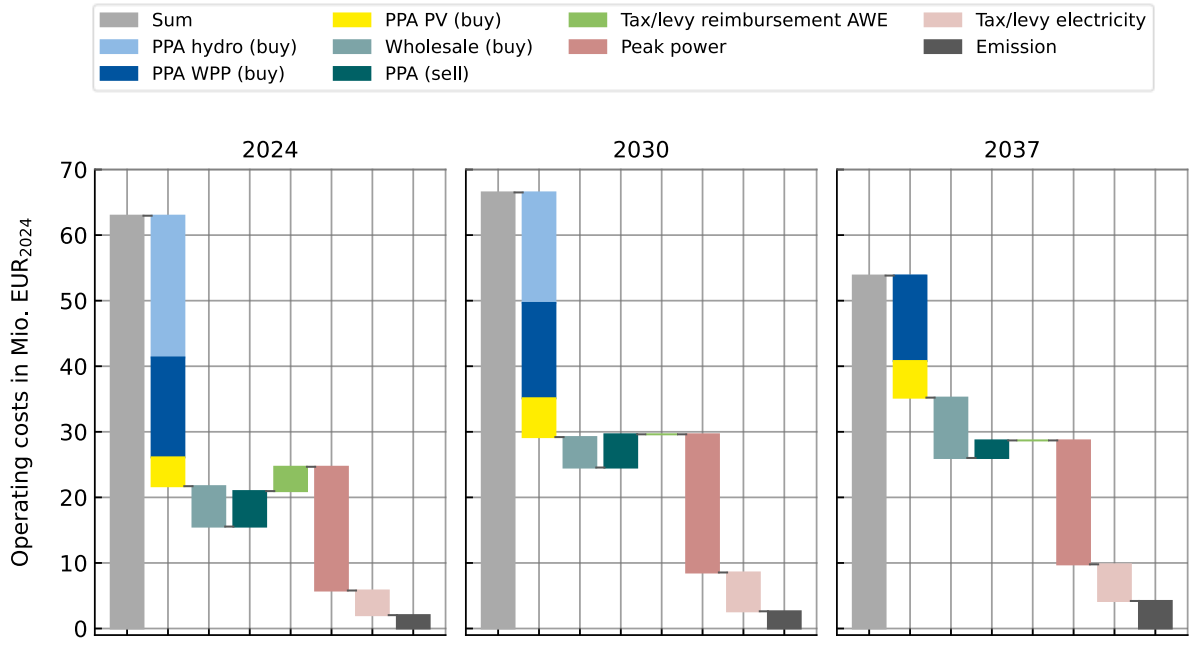

Figure 48: Breakdown of annual operating costs for the decarbonised energy system of the glassworks in case of low electrification (8 MWel) of the melting furnace. The electrolysis system is AWE-based.

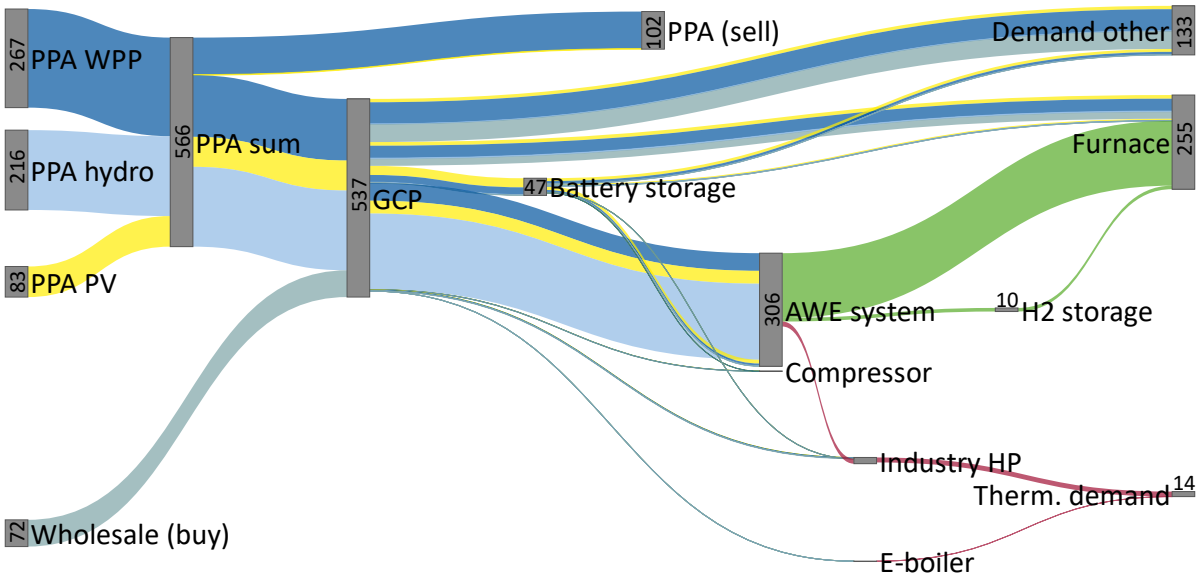

Figure 49: Annual energy flows in GWh for the 2024 decarbonisation scenario with AWE electrolysis system and low electrification of the furnace (8 MW_{el}). Flows smaller than 1 MWh are not displayed. “Demand other” includes all remaining electricity demand of the sections SGG and SGS.

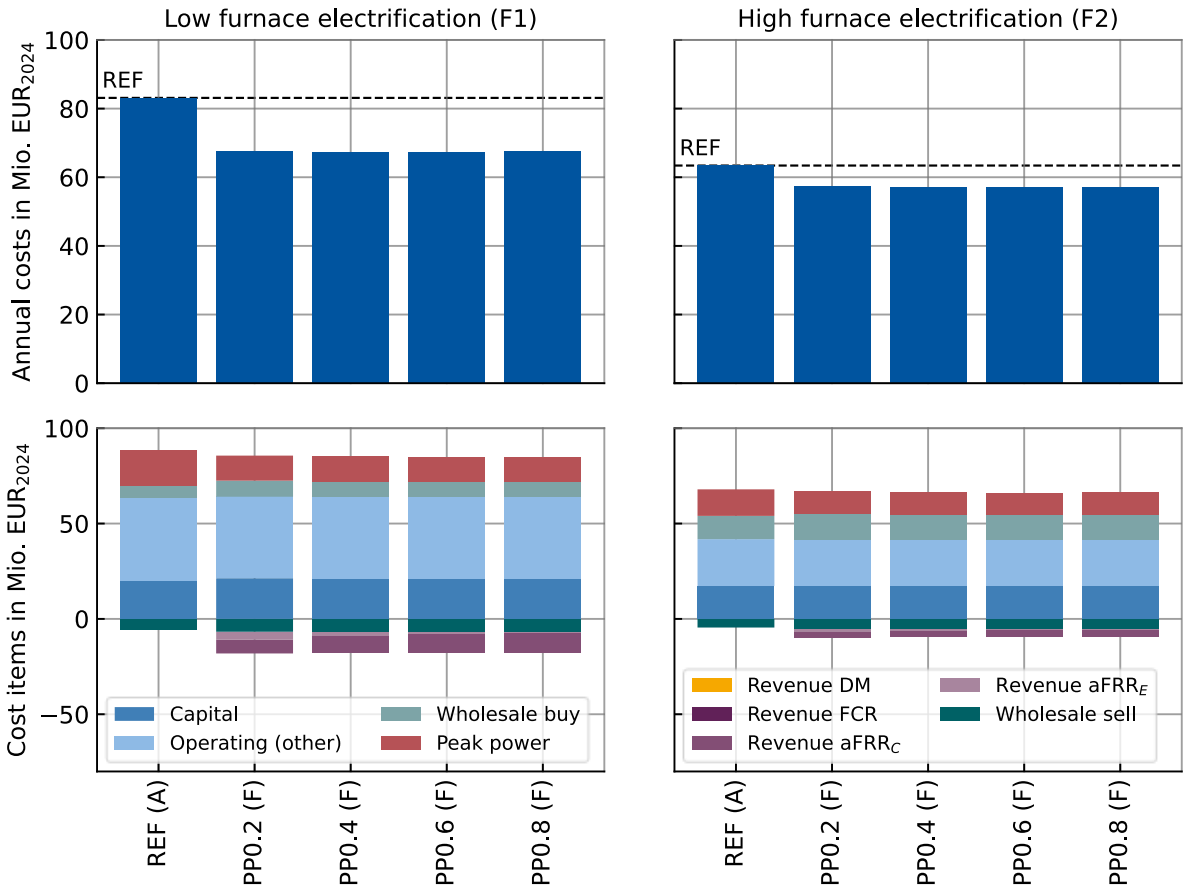

Figure 50: Comparison of reductions in total annual system costs for flexibility level F (aFRR) for different price positions (PP) on the aFRR energy market. Results are shown for scenarios with an AWE electrolysis system as well as low (F1) and high (F2) electrification of the furnace. Flexibility level A (REF) serves as a reference representing the basic results from the glassworks decarbonisation analysis. For all scenarios, peak-power-aware operation is implemented. The default, more conservative setting for modelling the price position in the aFRR energy market is 0.2 (PP0.2), meaning that 20% of all bids are lower than the own position and 80% are higher.

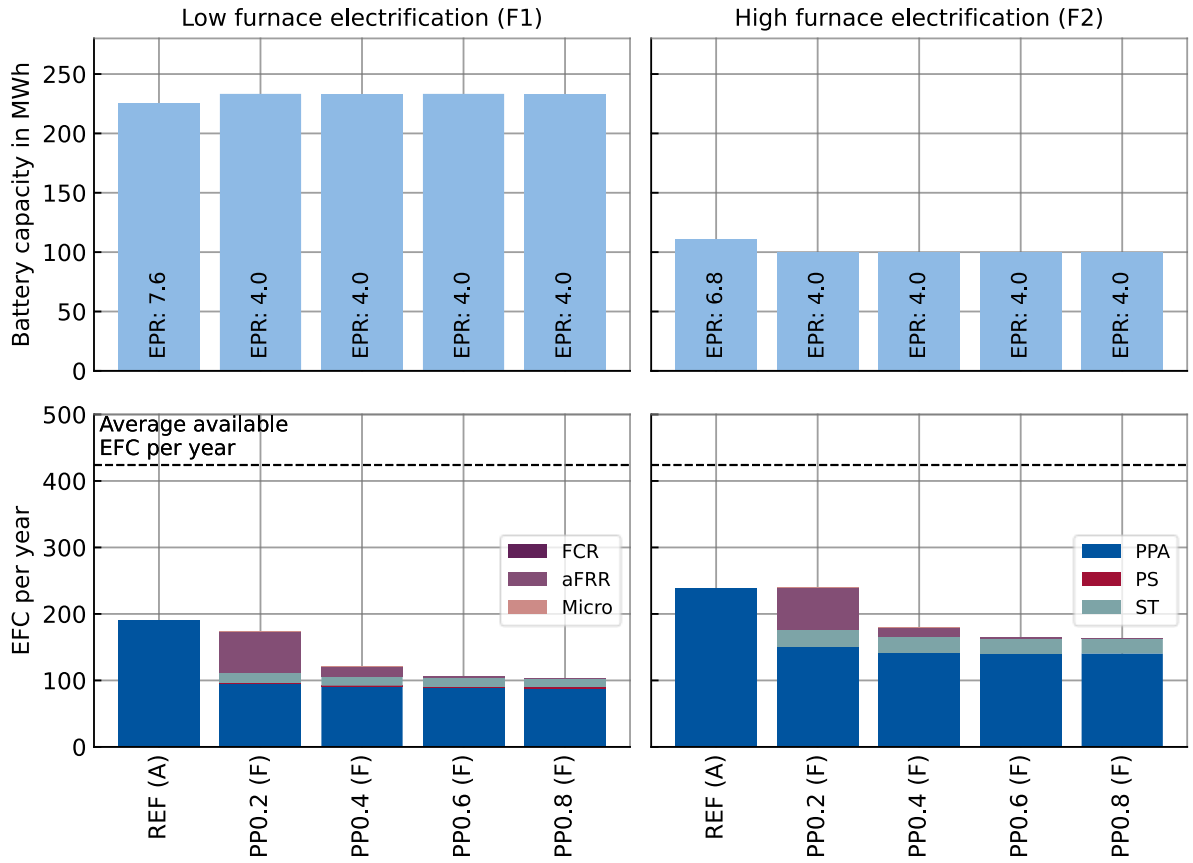

Figure 51: Sizing and cycling of the battery storage system for flexibility level F (aFRR) for different price positions (PP) on the aFRR energy market. EFCs are separated into the services provided by the battery storage system. In addition, micro cycling for aFRR is a separate category. Results are shown for scenarios with an AWE electrolysis system as well as low (F1) and high (F2) electrification of the furnace. The default, more conservative, setting for modelling the price position in the aFRR energy market is 0.2 (PP0.2), meaning that 20% of all bids are lower and 80% are higher than the own position.

Appendix J - Evaluation of uncovered load (slack)

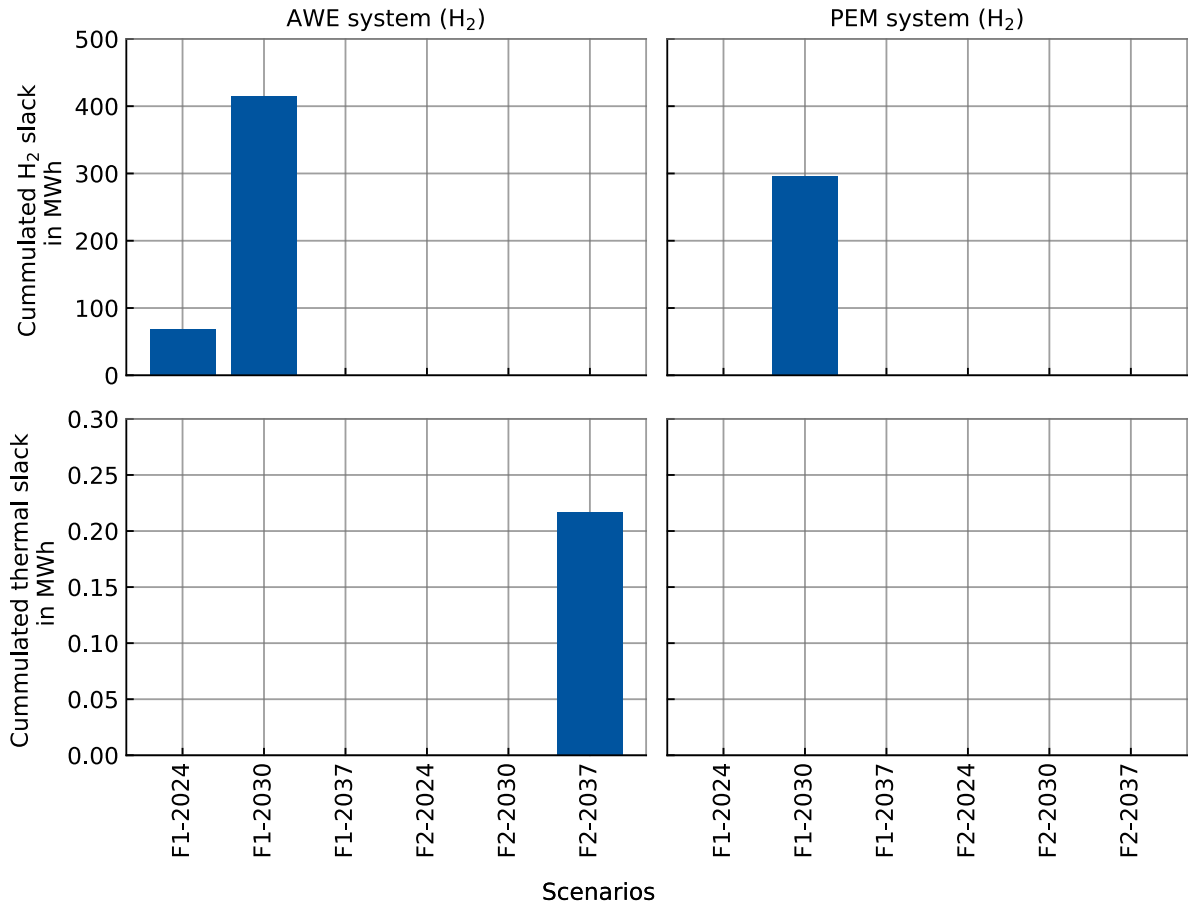

Figure 52: Annual cummulated uncovered load (slack) for all scenarios with electrolysis system and medium price assumptions. The evaluation is separated into hydrogen and thermal slack.

Nomenclature

aFRR	automatic frequency restoration reserve
AC	alternating current
AWE	alkaline water electrolysis
BESS	battery energy storage system
BTM	behind-the-meter
CAPEX	capital expenditures
CCS	carbon capture and storage
CESA	Continental Europe Synchronous Area
CF	capacity factor
COP	coefficient of performance
DC	direct current
DM	direct marketing
DOD	depth-of-discharge
DR	demand response
DSM	demand side management
DSO	distribution system operator
ECB	European Central Bank
EEG	Erneuerbares Energien Gesetz (German Renewable Energy Act)
EF	emission factor
EFC	equivalent full cycles
EMS	energy management system
EPR	energy-to-power ratio
FCR	frequency containment reserve
FTM	front-of-the-meter
GAMS	General Algebraic Modelling System
GCP	grid connection point
HP	heat pump
IDC	intraday continuous
KPI	key performance indicator
LCA	life cycle assessment
LCOH	levelised costs of hydrogen
LFP	lithium iron phosphate
LHV	lower heating value
mFRR	manual Frequency Restoration Reserve
MILP	mixed-integer linear programming
NG	natural gas
NMC	nickel manganese cobalt
NRW	North Rhine-Westphalia

OPEX	operational expenditures
PEM	Proton Exchange Membrane
PQ	prequalification
PS	peak shaving
PV	photovoltaic
RE	renewable energy
REF	reference
RH	rolling horizon
SGG	Saint-Gobain Glass
SGS	Saint-Gobain Sekurit
SOC	state-of-charge
SOE	state-of-energy
ST	spot market trading
TES	thermal energy storage
TSO	transmission system operator
VRE	variable renewable energy

References

[1] European Comission, Joint Research Centre (JRC), "GHG Emissions of all World Countries 2024," 2024. [Online]. Available: https://edgar.jrc.ec.europa.eu/booklet/GHG_emissions_of_all_world_countries_booklet_2024report.pdf

[2] European Comission - Copernicus, "Global Climate Highlights 2024," 2025. [Online]. Available: https://climate.copernicus.eu/sites/default/files/custom-uploads/GCH-2024/GCH2024.pdf

[3] European Comission, Market Observatory for Energy (DG Energy), "Quarterly Report on European Gas Markets," [Online]. Available: https://circabc.europa.eu/ui/group/3ef9355f-1ffe-4c82-ba19-f60a3ed2f652/library/4a97b129-9744-49f8-97ff-3e0b3f5f9bab/details

[4] Agora Energiewende, "Die Energiewende in Deutschland: Stand der Dinge 2024.: Rückblick auf die wesentlichen Entwicklungen sowie Ausblick auf 2025.," Jan. 2025. Accessed: Jan. 12 2025. [Online]. Available: https://www.agora-energiewende.de/fileadmin/Projekte/2025/2024-18_DE_JAW24/A-EW_351_JAW24_WEB.pdf

[5] Boston Consulting Group (BCG), "Klimapfade 2.0 - Ein Wirtschaftsprogramm für Klima und Zukunft," Oct. 2021. Accessed: Jan. 12 2025. [Online]. Available: https://web-assets.bcg.com/58/57/2042392542079ff8c9ee2cb74278/klimapfade-study-german.pdf

[6] A. A. Carmona-Martínez *et al.,* "Charting the Course: Navigating Decarbonisation Pathways in Greece, Germany, The Netherlands, and Spain's Industrial Sectors," *Sustainability*, vol. 16, no. 14, p. 6176, 2024, doi: 10.3390/su16146176.

[7] J. Ramsebner, R. Haas, A. Ajanovic, and M. Wietschel, "The sector coupling concept: A critical review," *WIREs Energy & Environment*, vol. 10, no. 4, 2021, doi: 10.1002/wene.396.

[8] Fraunhofer Institute for Solar Energy Systems (ISE), "Levelized Cost of Electricity-Renewable Energy Technologies," Jul. 2024. Accessed: Nov. 2 2024. [Online]. Available: https://www.ise.fraunhofer.de/content/dam/ise/en/documents/publications/studies/EN2024_ISE_Study_Levelized_Cost_of_Electricity_Renewable_Energy_Technologies.pdf

[9] L. Pedretti and M. Kanellakopoulou, "European PPA Market Outlook 2024: Preparing for impact: The silver lining after the clouds," Accessed: Nov. 7 2024. [Online]. Available: https://pexapark.com/european-ppa-market/

[10] Deutsche Energie-Agentur (DENA), "PPA-Marktanalyse Deutschland 2023," Apr. 2024. Accessed: Nov. 7 2024. [Online]. Available: https://www.dena.de/fileadmin/dena/Publikationen/PDFs/2024/PPA-Marktanalyse_Deutschland_2023.pdfhttps://www.dena.de/fileadmin/dena/Publikationen/PDFs/2024/PPA-Marktanalyse_Deutschland_2023.pdf

[11] J. Figgener, C. Hecht, J. van Ouwerkerk, and J. Brucksch, *Battery Charts.* [Online]. Available: https://battery-charts.rwth-aachen.de/

[12] J. Figgener *et al., The development of battery storage systems in Germany: A market review (status 2023).* [Online]. Available: https://www.researchgate.net/publication/369479477_The_development_of_battery_storage_systems_in_Germany_A_market_review_status_2023

[13] S. Englberger, A. Jossen, and H. Hesse, "Unlocking the Potential of Battery Storage with the Dynamic Stacking of Multiple Applications," *Cell Reports Physical Science*, vol. 1, no. 11, 2020, doi: 10.1016/j.xcrp.2020.100238.

[14] S. P. Englberger, "Optimized energy management for battery energy storage via multi-use and multi-storage operation," Technische Universität München, 2022.

[15] M. Fleschutz, M. Bohlayer, M. Braun, and M. D. Murphy, "From prosumer to flexumer: Case study on the value of flexibility in decarbonizing the multi-energy system of a manufacturing company," *Applied Energy*, vol. 347, p. 121430, 2023, doi: 10.1016/j.apenergy.2023.121430.

[16] L. Miserocchi, A. Franco, and D. Testi, "Status and prospects of energy efficiency in the glass industry: Measuring, assessing and improving energy performance," *Energy Conversion and Management: X*, vol. 24, p. 100720, 2024, doi: 10.1016/j.ecmx.2024.100720.

[17] D. Jost, S. Kanzurova, B. Nilges, C. Reinert, and N. v. d. Assen, "Life cycle assessment of measures towards a low-carbon flat glass production," *Journal of Cleaner Production*, vol. 501, p. 145294, 2025, doi: 10.1016/j.jclepro.2025.145294.

[18] M. Zier, N. Pflugradt, P. Stenzel, L. Kotzur, and D. Stolten, "Industrial decarbonization pathways: The example of the German glass industry," *Energy Conversion and Management: X*, vol. 17, p. 100336, 2023, doi: 10.1016/j.ecmx.2022.100336.

[19] M. Wei, C. A. McMillan, and S. de La Rue Can, "Electrification of Industry: Potential, Challenges and Outlook," *Current Sustainable/Renewable Energy Reports*, vol. 6, no. 4, pp. 140–148, 2019, doi: 10.1007/s40518-019-00136-1.

[20] Federal Network Agency (BNetzA), "Approval of a hydrogen core network," Oct. 2024. Accessed: Oct. 30 2024. [Online]. Available: https://www.bundesnetzagentur.de/SharedDocs/Downloads/DE/Sachgebiete/Energie/Unternehmen_Institutionen/Wasserstoff/Genehmigung.pdf?__blob=publicationFile&v=6

[21] G. Erbach and S. Svensson, "EU rules for renewable hydrogen: Delegated regulations on a methodology for renewable fuels of non-biological origin," Apr. 2023. Accessed: 23.10.24. [Online]. Available: https://www.europarl.europa.eu/RegData/etudes/BRIE/2023/747085/EPRS_BRI(2023)747085_EN.pdf

[22] *Renewable Energy Directive III: RED III*, 2023. [Online]. Available: https://eur-lex.europa.eu/legal-content/EN/TXT/?uri=CELEX%3A32023L2413&qid=1699364355105

[23] P. Gabrielli, R. Aboutalebi, and G. Sansavini, "Mitigating financial risk of corporate power purchase agreements via portfolio optimization," *Energy Economics*, vol. 109, p. 105980, 2022, doi: 10.1016/j.eneco.2022.105980.

[24] J. Brucksch, J. van Ouwerkerk, and D. U. Sauer, *Evaluating Cost and Emission Reduction Potentials with Stochastic Ppa Portfolio Optimization for Green Hydrogen Production in a Decarbonized Glassworks*, 2025. Accessed: May 9 2025. [Online]. Available: https://papers.ssrn.com/sol3/papers.cfm?abstract_id=5217708

[25] M. G. Prina, G. Manzolini, D. Moser, B. Nastasi, and W. Sparber, "Classification and challenges of bottom-up energy system models - A review," *Renewable and Sustainable Energy Reviews*, vol. 129, p. 109917, 2020, doi: 10.1016/j.rser.2020.109917.

[26] H. C. Gils *et al.,* "Model-related outcome differences in power system models with sector coupling—Quantification and drivers," *Renewable and Sustainable Energy Reviews*, vol. 159, p. 112177, 2022, doi: 10.1016/j.rser.2022.112177.

[27] C. Klemm and P. Vennemann, "Modeling and optimization of multi-energy systems in mixed-use districts: A review of existing methods and approaches," *Renewable and Sustainable Energy Reviews*, vol. 135, p. 110206, 2021, doi: 10.1016/j.rser.2020.110206.

[28] M. Chang *et al.,* "Trends in tools and approaches for modelling the energy transition," *Applied Energy*, vol. 290, p. 116731, 2021, doi: 10.1016/j.apenergy.2021.116731.

[29] J. Silvente, G. M. Kopanos, E. N. Pistikopoulos, and A. Espuña, "A rolling horizon optimization framework for the simultaneous energy supply and demand planning in microgrids," *Applied Energy*, vol. 155, pp. 485–501, 2015, doi: 10.1016/j.apenergy.2015.05.090.

[30] G. Savvidis and K. Hufendiek, "Variable Time Resolution in LP Electricity Market and Investment Models," in *2018 15th International Conference on the European Energy Market (EEM)*, 2018, pp. 1–5.

[31] J. F. Marquant, R. Evins, and J. Carmeliet, "Reducing Computation Time with a Rolling Horizon Approach Applied to a MILP Formulation of Multiple Urban Energy Hub System," *Procedia Computer Science*, vol. 51, pp. 2137–2146, 2015, doi: 10.1016/j.procs.2015.05.486.

[32] P. Gabrielli, P. Hilsheimer, and G. Sansavini, "Storage power purchase agreements to enable the deployment of energy storage in Europe," *iScience*, vol. 25, no. 8, 2022, doi: 10.1016/j.isci.2022.104701.

[33] M. G. Prina, B. Nastasi, D. Groppi, S. Misconel, D. A. Garcia, and W. Sparber, "Comparison methods of energy system frameworks, models and scenario results," *Renewable and Sustainable Energy Reviews*, vol. 167, p. 112719, 2022, doi: 10.1016/j.rser.2022.112719.

[34] D. P. van Vuuren *et al.,* "Comparison of top-down and bottom-up estimates of sectoral and regional greenhouse gas emission reduction potentials," *Energy Policy*, vol. 37, no. 12, pp. 5125–5139, 2009, doi: 10.1016/j.enpol.2009.07.024.

[35] C. Bußar, "Untersuchung optimaler Transformationspfade bis 2050 für die erfolgreiche Umsetzung einer nachhaltigen Reduzierung der Kohlendioxidemissionen im Bereich der Stromerzeugung," RWTH Aachen University, 2019.

[36] H.-K. Ringkjøb, P. M. Haugan, and I. M. Solbrekke, "A review of modelling tools for energy and electricity systems with large shares of variable renewables," *Renewable and Sustainable Energy Reviews*, vol. 96, pp. 440–459, 2018, doi: 10.1016/j.rser.2018.08.002.

[37] H. M. Dietz, *Mathematik für Wirtschaftswissenschaftler*. Berlin, Heidelberg: Springer Berlin Heidelberg, 2019.

[38] F. Cebulla and T. Fichter, "Merit order or unit-commitment: How does thermal power plant modeling affect storage demand in energy system models?," *Renewable Energy*, vol. 105, pp. 117–132, 2017, doi: 10.1016/j.renene.2016.12.043.

[39] L. Moretti, E. Martelli, and G. Manzolini, "An efficient robust optimization model for the unit commitment and dispatch of multi-energy systems and microgrids," *Applied Energy*, vol. 261, p. 113859, 2020, doi: 10.1016/j.apenergy.2019.113859.

[40] T. G. Paul, S. J. Hossain, S. Ghosh, P. Mandal, and S. Kamalasadan, "A Quadratic Programming Based Optimal Power and Battery Dispatch for Grid-Connected Microgrid," *IEEE Transactions on Industry Applications*, vol. 54, no. 2, pp. 1793–1805, 2018, doi: 10.1109/TIA.2017.2782671.

[41] M. Killian, M. Zauner, and M. Kozek, "Comprehensive smart home energy management system using mixed-integer quadratic-programming," *Applied Energy*, vol. 222, pp. 662–672, 2018, doi: 10.1016/j.apenergy.2018.03.179.

[42] Q. Sun, Z. Wu, W. Gu, T. Zhu, L. Zhong, and T. Gao, "Flexible expansion planning of distribution system integrating multiple renewable energy sources: An approximate dynamic programming approach," *Energy*, vol. 226, p. 120367, 2021, doi: 10.1016/j.energy.2021.120367.

[43] H. Shuai, X. Ai, J. Fang, T. Ding, Z. Chen, and J. Wen, "Real-time optimization of the integrated gas and power systems using hybrid approximate dynamic programming," *International Journal of Electrical Power & Energy Systems*, vol. 118, p. 105776, 2020, doi: 10.1016/j.ijepes.2019.105776.

[44] C. Bussar *et al.,* "Large-scale integration of renewable energies and impact on storage demand in a European renewable power system of 2050—Sensitivity study," *Journal of Energy Storage*, vol. 6, pp. 1–10, 2016, doi: 10.1016/j.est.2016.02.004.

[45] S. Abar, G. K. Theodoropoulos, P. Lemarinier, and G. M. P. O'Hare, "Agent Based Modelling and Simulation tools: A review of the state-of-art software," *Computer Science Review*, vol. 24, pp. 13–33, 2017, doi: 10.1016/j.cosrev.2017.03.001.

[46] X. Yue, S. Pye, J. DeCarolis, F. G. N. Li, F. Rogan, and B. Ó. Gallachóir, "A review of approaches to uncertainty assessment in energy system optimization models," *Energy Strategy Reviews*, vol. 21, pp. 204–217, 2018, doi: 10.1016/j.esr.2018.06.003.

[47] P. Lopion, P. Markewitz, M. Robinius, and D. Stolten, "A review of current challenges and trends in energy systems modeling," *Renewable and Sustainable Energy Reviews*, vol. 96, pp. 156–166, 2018, doi: 10.1016/j.rser.2018.07.045.

[48] T. Falke, S. Krengel, A.-K. Meinerzhagen, and A. Schnettler, "Multi-objective optimization and simulation model for the design of distributed energy systems," *Applied Energy*, vol. 184, pp. 1508–1516, 2016, doi: 10.1016/j.apenergy.2016.03.044.

[49] J. Priesmann, L. Nolting, and A. Praktiknjo, "Are complex energy system models more accurate? An intra-model comparison of power system optimization models," *Applied Energy*, vol. 255, p. 113783, 2019, doi: 10.1016/j.apenergy.2019.113783.

[50] D. L. Summerbell, D. Khripko, C. Barlow, and J. Hesselbach, "Cost and carbon reductions from industrial demand-side management: Study of potential savings at a cement plant," *Applied Energy*, vol. 197, pp. 100–113, 2017, doi: 10.1016/j.apenergy.2017.03.083.

[51] F. T. C. Röben, D. Liu, M. A. Reuter, M. Dahmen, and A. Bardow, "The demand response potential in copper production," *Journal of Cleaner Production*, vol. 362, p. 132221, 2022, doi: 10.1016/j.jclepro.2022.132221.

[52] H. C. Gils, T. Pregger, F. Flachsbarth, M. Jentsch, and C. Dierstein, "Comparison of spatially and temporally resolved energy system models with a focus on Germany's future power supply," *Applied Energy*, vol. 255, p. 113889, 2019, doi: 10.1016/j.apenergy.2019.113889.

[53] H. C. Gils *et al.,* "Modeling flexibility in energy systems — comparison of power sector models based on simplified test cases," *Renewable and Sustainable Energy Reviews*, vol. 158, p. 111995, 2022, doi: 10.1016/j.rser.2021.111995.

[54] J. van Ouwerkerk *et al.,* "Impacts of power sector model features on optimal capacity expansion: A comparative study," *Renewable and Sustainable Energy Reviews*, vol. 157, p. 112004, 2022, doi: 10.1016/j.rser.2021.112004.

[55] J. van Ouwerkerk *et al.,* "Comparing open source power system models - A case study focusing on fundamental modeling parameters for the German energy transition," *Renewable and Sustainable Energy Reviews*, vol. 161, p. 112331, 2022, doi: 10.1016/j.rser.2022.112331.

[56] T. Ommen, W. B. Markussen, and B. Elmegaard, "Comparison of linear, mixed integer and non-linear programming methods in energy system dispatch modelling," *Energy*, vol. 74, pp. 109–118, 2014, doi: 10.1016/j.energy.2014.04.023.

[57] R. Palma-Behnke *et al.,* "A Microgrid Energy Management System Based on the Rolling Horizon Strategy," *IEEE Transactions on Smart Grid*, vol. 4, no. 2, pp. 996–1006, 2013, doi: 10.1109/TSG.2012.2231440.

[58] S. Pfenninger *et al.,* "Opening the black box of energy modelling: Strategies and lessons learned," *Energy Strategy Reviews*, vol. 19, pp. 63–71, 2018, doi: 10.1016/j.esr.2017.12.002.

[59] open energy modelling initiative (openmod), *Welcome to the openmod initiative's Wiki.* [Online]. Available: https://wiki.openmod-initiative.org/wiki/Open_Models (accessed: Oct. 26 2024).

[60] S. Candas *et al.,* "Code exposed: Review of five open-source frameworks for modeling renewable energy systems," *Renewable and Sustainable Energy Reviews*, vol. 161, p. 112272, 2022, doi: 10.1016/j.rser.2022.112272.

[61] S. Berendes *et al.,* "Evaluating the usability of open source frameworks in energy system modelling," *Renewable and Sustainable Energy Reviews*, vol. 159, p. 112174, 2022, doi: 10.1016/j.rser.2022.112174.

[62] J. Schmalstieg, C. Rahe, M. Ecker, and D. U. Sauer, "Full Cell Parameterization of a High-Power Lithium-Ion Battery for a Physico-Chemical Model: Part I. Physical and Electrochemical Parameters," *J. Electrochem. Soc.*, vol. 165, no. 16, A3799-A3810, 2018, doi: 10.1149/2.0321816jes.

[63] J. M. Reniers, G. Mulder, and D. A. Howey, "Review and Performance Comparison of Mechanical-Chemical Degradation Models for Lithium-Ion Batteries," *J. Electrochem. Soc.*, vol. 166, no. 14, A3189-A3200, 2019, doi: 10.1149/2.0281914jes.

[64] W. Li, J. Chen, K. Quade, D. Luder, J. Gong, and D. U. Sauer, "Battery degradation diagnosis with field data, impedance-based modeling and artificial intelligence," *Energy Storage Materials*, vol. 53, pp. 391–403, 2022, doi: 10.1016/j.ensm.2022.08.021.

[65] T. M. Alabi, L. Lu, and Z. Yang, "A novel multi-objective stochastic risk co-optimization model of a zero-carbon multi-energy system (ZCMES) incorporating energy storage aging model and integrated demand response," *Energy*, vol. 226, p. 120258, 2021, doi: 10.1016/j.energy.2021.120258.

[66] B. Tepe, N. Collath, H. Hesse, M. Rosenthal, and U. Windelen, "Stationäre Batteriespeicher in Deutschland: Aktuelle Entwicklungen und Trends in 2021," *Energiewirtschaftliche Tagesfragen*, 11/2021, 2021. https://mediatum.ub.tum.de/doc/1601843/ijdqy4jcweympb206zr65pg8j.Tepe,%20Collath%20et%20al.%20-%20Station%C3%A4re%20Batteriespeicher%20in%20Deutschland-%20Aktuelle%20Entwicklungen%20und%20Trends%20in%202021.pdf (accessed: 18.10.24).

[67] R. Korthauer, Ed., *Handbook Lithium-Ion Batteries: Basics and applications*. Berlin, Heidelberg: Springer, 2018. [Online]. Available: https://ebookcentral.proquest.com/lib/kxp/detail.action?docID=5490811

[68] M. Sterner and I. Stadler, *Energiespeicher - Bedarf, Technologien, Integration*. Berlin, Heidelberg: Springer Berlin Heidelberg, 2017.

[69] Y. Ding, Z. P. Cano, A. Yu, J. Lu, and Z. Chen, "Automotive Li-Ion Batteries: Current Status and Future Perspectives," *Electrochemical Energy Reviews*, vol. 2, no. 1, pp. 1–28, 2019, doi: 10.1007/s41918-018-0022-z.

[70] M. Junker, S. Bihn, and D. U. Sauer, "Analyse von neuen Zell-Technologien und deren Auswirkungen auf das Gesamtsystem Batteriepack: FAT-Schriftenreihe," 2020. [Online]. Available: https://www.vda.de/dam/jcr:83261b79-9746-4938-8c12-ef7f58d3b352/V2%20FAT-Schriftenreihe_337.pdf?mode=view

[71] Bielewski M *et al.,* "Clean Energy Technology Observatory: Batteries for Energy Storage in the European Union – 2022 Status Report on Technology Development, Trends, Value Chains and Markets," *1831-9424*, KJ-NA-31-220-EN-N (online), 2022, doi: 10.2760/808352.

[72] J. Schmalstieg, S. Käbitz, M. Ecker, and D. U. Sauer, "From accelerated aging tests to a lifetime prediction model: Analyzing lithium-ion batteries," in *2013 World Electric Vehicle Symposium and Exhibition (EVS27)*, 2013, pp. 1–12.

[73] P. A. Schröer, "Entwicklung einer adaptiven Leistungsprognosefunktion für Starterbatterien mit Lithium-Titanat-Oxid-Anode als Grundlage zur sicheren Energieversorgung im Fahrzeug," Dissertation, Rheinisch-Westfälische Technische Hochschule Aachen, Aachen, 2021. [Online]. Available: https://publications.rwth-aachen.de/record/835784

[74] A. Malhotra, B. Battke, M. Beuse, A. Stephan, and T. Schmidt, "Use cases for stationary battery technologies: A review of the literature and existing projects," *Renewable and Sustainable Energy Reviews*, vol. 56, pp. 705–721, 2016, doi: 10.1016/j.rser.2015.11.085.

[75] M. Aneke and M. Wang, "Energy storage technologies and real life applications – A state of the art review," *Applied Energy*, vol. 179, pp. 350–377, 2016, doi: 10.1016/j.apenergy.2016.06.097.

[76] S. Bentke and B. Hennig, "Hindernisse für Multi-Use-Speicher – Teil 2: Weitere Unsicherheiten und Gesetzesvorschläge," *ZNER - Zeitschrift für neues Energierecht*, 28 Jan., 2024. https://www.vbvh.de/wp-content/uploads/2024/03/Hindernisse-fuer-Multi-Use-Speicher.pdf (accessed: Feb. 11 2025).

[77] *Gesetz für den Ausbau erneuerbarer Energien (Erneuerbare-Energien-Gesetz) - § 19 Zahlungsanspruch: EEG 2023.* Accessed: Feb. 11 2025. [Online]. Available: https://www.gesetze-im-internet.de/eeg_2014/__19.html

[78] J. Figgener *et al.,* "Multi-year field measurements of home storage systems and their use in capacity estimation," *Nat Energy*, vol. 9, no. 11, pp. 1438–1447, 2024, doi: 10.1038/s41560-024-01620-9.

[79] Jan Figgener *et al.,* "Wissenschaftliches Mess- und Evaluierungsprogramm Solarstromspeicher 2.0. Jahresbericht 2017," 2017.

[80] Regionetz, "Entgelte für Netznutzung für 2024," 2024. Accessed: Nov. 11 2024. [Online]. Available: https://www.regionetz.de/fileadmin/regionetz/content/Dokumente/Preisbl%C3%A4tter/Preisbl%C3%A4tter_Strom_2024.pdf

[81] *Verordnung über die Entgelte für den Zugang zu Elektrizitätsversorgungsnetzen (Stromnetzentgeltverordnung) - § 19 Sonderformen der Netznutzung: StromNEV*, 2023. Accessed: Feb. 7 2025. [Online]. Available: https://www.gesetze-im-internet.de/stromnev/__19.html

[82] P. H. Tiemann, A. Bensmann, V. Stuke, and R. Hanke-Rauschenbach, "Electrical energy storage for industrial grid fee reduction – A large scale analysis," *Energy Conversion and Management*, vol. 208, p. 112539, 2020, doi: 10.1016/j.enconman.2020.112539.

[83] S. Henni, J. Becker, P. Staudt, F. vom Scheidt, and C. Weinhardt, "Industrial peak shaving with battery storage using a probabilistic forecasting approach: Economic evaluation of risk attitude," *Applied Energy*, vol. 327, p. 120088, 2022, doi: 10.1016/j.apenergy.2022.120088.

[84] Monopolkommision, "Competition between electricity exchanges in Germany: Chapter III of the 8th Energy Sector Report of the Monopolies Commission pursuant to § 62 EnWG," 2021. [Online]. Available: https://www.monopolkommission.de/images/PDF/SG/chapter-3-competition-between-electricity-exchanges.pdf

[85] B. B. Belmonte, P. Mouratidis, G. Franke, and S. Rinderknecht, "Developments in the cost of grid balancing services and the design of the European balancing market," *Energy Reports*, vol. 10, pp. 910–931, 2023, doi: 10.1016/j.egyr.2023.07.045.

[86] J. Siemer, "Trades against the machine," Jun. 2024. Accessed: Feb. 11 2025. [Online]. Available: https://www.pv-magazine.com/2024/06/22/trades-against-the-machine/

[87] K. Westphal, M. Pastukhova, and J. M. Pepe, "Geopolitics of electricity: grids, space and (political) power," *1863-1053*, 6/2022, 2022, doi: 10.18449/2022RP06.

[88] European Network of Transmission System Operators for Electricity (ENTSO-E), "Data & Standardisation - Grid Map," Accessed: 17.10.24. [Online]. Available: https://www.entsoe.eu/data/map/

[89] ENTSO-E, "European Transmission System Operators Association," Accessed: Mar. 30 2025. [Online]. Available: https://www.entsoe.eu/

[90] 50Hertz Transmission GmbH, Amprion GmbH, TenneT TSO GmbH, TransnetBW GmbH, "Regelleistung.net - Internet platform for the allocation of control power - General Information," Accessed: 17.10.24. [Online]. Available: https://www.regelleistung.net/en-us/General-info/What-is-balancing-energy

[91] M. Celi Cortés, L. Koltermann, T. D. Dang, J. Figgener, S. Zurmühlen, and D. U. Sauer, "Deterministic grid frequency deviations and the provision of frequency containment reserve with battery storage systems," *Energy Reports*, vol. 13, pp. 1029–1040, 2025, doi: 10.1016/j.egyr.2024.12.057.

[92] ENTSO-E, "Impact of merit order activation of automatic Frequency Restoration Reserves and harmonised Full Activation times," Feb. 2016. Accessed: Feb. 11 2025. [Online]. Available: https://eepublicdownloads.entsoe.eu/clean-documents/mc-documents/balancing_ancillary/160229_Report_aFRR_study_merit_order_and_harmonising_FAT_%28vs_1.2%29.pdf

[93] TenneT TSO B.V., "Manual aFRR for BSPs - Rules and procedures for aFRR delivery," Feb. 2022. Accessed: Feb. 11 2025. [Online]. Available: https://netztransparenz.tennet.eu/fileadmin/user_upload/SO_NL/aFRR_manual_for_BSPs_en.pdf

[94] 50Hertz Transmission GmbH, Amprion GmbH, TenneT TSO GmbH, TransnetBW GmbH, "Prequalification Process for Balancing Service Providers (FCR, aFRR, mFRR) in Germany ("PQ conditions"): Status: 05 July 2024," Jul. 2024. Accessed: 15.10.24. [Online]. Available: https://www.regelleistung.net/xspproxy/api/StaticFiles/Regelleistung/Infos_f%C3%BCr_Anbieter/Wie_werde_ich_Regelenergieanbieter_Pr%C3%A4qualifikation/Pr%C3%A4qualifikationsbedingungen_FCR_aFRR_mFRR/PQ-Bedingungen-2024_07_05_(englisch).pdf

[95] 50Hertz Transmission GmbH, Amprion GmbH, TenneT TSO GmbH, TransnetBW GmbH, "Prequalified control power in Germany," Mar. 2024. Accessed: 18.10.24. [Online]. Available: https://www.regelleistung.net/xspproxy/api/staticfiles/regelleistung/startseite/pq-leistung-in%20deutschland.pdf

[96] E. G. Hertwich and R. Wood, "The growing importance of scope 3 greenhouse gas emissions from industry," *Environmental Research Letters*, vol. 13, no. 10, p. 104013, 2018, doi: 10.1088/1748-9326/aae19a.

[97] P. Gerbert *et al.,* "Climate Paths for Germany," Jan. 2018. Accessed: 20.10.24. [Online]. Available: https://web-assets.bcg.com/img-src/Climate-paths-for-Germany-english_tcm9-183770.pdf

[98] J. Burchardt *et al.,* "Climate Paths 2.0: A Program for Climate and Germany's Future Development," Oct. 2021. Accessed: 20.10.24. [Online]. Available: https://web-assets.bcg.com/02/a6/91958a6f4287a0490e24ef56d2b5/climate-paths2-summary-offindings-en.pdf

[99] Prognos, Öko-Institut and Wuppertal Institut, "Towards a Climate-Neutral Germany by 2045: How Germany can reach its climate targets before 2050 - Executive Summary conducted for Stiftung Klimaneutralität, Agora Energiewende and Agora Verkehrswende.," Accessed: 20.10.24. [Online]. Available: https://www.agora-energiewende.org/fileadmin/Projekte/2021/2021_04_KNDE45/A-EW_213_KNDE2045_Summary_EN_WEB.pdf

[100] K. Witkowski, P. Haering, S. Seidelt, and N. Pini, "Role of thermal technologies for enhancing flexibility in multi-energy systems through sector coupling: technical suitability and expected developments," *IET Energy Systems Integration*, vol. 2, no. 2, pp. 69–79, 2020, doi: 10.1049/iet-esi.2019.0061.

[101] A. Marina, S. Spoelstra, H. A. Zondag, and A. K. Wemmers, "An estimation of the European industrial heat pump market potential," *Renewable and Sustainable Energy Reviews*, vol. 139, p. 110545, 2021, doi: 10.1016/j.rser.2020.110545.

[102] Saint-Gobain Research Germany, "Data/Information from the site operator," Herzogenrath, 2024.

[103] J. Pelda, F. Stelter, and S. Holler, "Potential of integrating industrial waste heat and solar thermal energy into district heating networks in Germany," *Energy*, vol. 203, p. 117812, 2020, doi: 10.1016/j.energy.2020.117812.

[104] S. Meyers, B. Schmitt, and K. Vajen, "The future of low carbon industrial process heat: A comparison between solar thermal and heat pumps," *Solar Energy*, vol. 173, pp. 893–904, 2018, doi: 10.1016/j.solener.2018.08.011.

[105] A. Crespo, C. Barreneche, M. Ibarra, and W. Platzer, "Latent thermal energy storage for solar process heat applications at medium-high temperatures – A review," *Solar Energy*, vol. 192, pp. 3–34, 2019, doi: 10.1016/j.solener.2018.06.101.

[106] M. P. Islam and T. Morimoto, "Advances in low to medium temperature non-concentrating solar thermal technology," *Renewable and Sustainable Energy Reviews*, vol. 82, pp. 2066–2093, 2018, doi: 10.1016/j.rser.2017.08.030.

[107] J. Töpler and J. Lehmann, Eds., *Hydrogen and fuel cell: Technologies and market perspectives,* 1st ed. Berlin, Heidelberg: Springer Berlin Heidelberg; Imprint Springer, 2016.

[108] M. David, C. Ocampo-Martínez, and R. Sánchez-Peña, "Advances in alkaline water electrolyzers: A review," *Journal of Energy Storage*, vol. 23, pp. 392–403, 2019, doi: 10.1016/j.est.2019.03.001.

[109] S. S. Kumar and H. Lim, "An overview of water electrolysis technologies for green hydrogen production," *Energy Reports*, vol. 8, pp. 13793–13813, 2022, doi: 10.1016/j.egyr.2022.10.127.

[110] K. Chaudhary, K. Bhardvaj, and A. Chaudhary, "A qualitative assessment of hydrogen generation techniques for fuel cell applications," *Fuel*, vol. 358, p. 130090, 2024, doi: 10.1016/j.fuel.2023.130090.

[111] H. Böhm, S. Goers, and A. Zauner, "Estimating future costs of power-to-gas – a component-based approach for technological learning," *International Journal of Hydrogen Energy*, vol. 44, no. 59, pp. 30789–30805, 2019, doi: 10.1016/j.ijhydene.2019.09.230.

[112] International Energy Agency (IEA), "The Future of Hydrogen - Seizing today's opportunities: Report prepared by the IEA for the G20, Japan," Jun. 2019. Accessed: Nov. 3 2024. [Online]. Available: https://iea.blob.core.windows.net/assets/9e3a3493-b9a6-4b7d-b499-7ca48e357561/The_Future_of_Hydrogen.pdf

[113] Nationale Organisation Wasserstoff- und Brennstoffzellentechnologie – NOW GmbH, "Studie IndWEDe: Industrialisierung der Wasserelektrolyse in Deutschland: Chancen und Herausforderungen für nachhaltigen Wasserstoff für Verkehr, Strom und Wärme," 2018. Accessed: Nov. 4 2024. [Online]. Available: https://www.now-gmbh.de/wp-content/uploads/2020/09/indwede-studie_v04.1.pdf

[114] Y. Xia, H. Cheng, H. He, and W. Wei, "Efficiency and consistency enhancement for alkaline electrolyzers driven by renewable energy sources," *Commun Eng*, vol. 2, no. 1, 2023, doi: 10.1038/s44172-023-00070-7.

[115] D. Virah-Sawmy, F. J. Beck, and B. Sturmberg, "Ignore variability, overestimate hydrogen production – Quantifying the effects of electrolyzer efficiency curves on

hydrogen production from renewable energy sources," *International Journal of Hydrogen Energy*, vol. 72, pp. 49–59, 2024, doi: 10.1016/j.ijhydene.2024.05.360.

[116] R. Moradi and K. M. Groth, "Hydrogen storage and delivery: Review of the state of the art technologies and risk and reliability analysis," *International Journal of Hydrogen Energy*, vol. 44, no. 23, pp. 12254–12269, 2019, doi: 10.1016/j.ijhydene.2019.03.041.

[117] I. A. Hassan, H. S. Ramadan, M. A. Saleh, and D. Hissel, "Hydrogen storage technologies for stationary and mobile applications: Review, analysis and perspectives," *Renewable and Sustainable Energy Reviews*, vol. 149, p. 111311, 2021, doi: 10.1016/j.rser.2021.111311.

[118] R. Bhandari and R. R. Shah, "Hydrogen as energy carrier: Techno-economic assessment of decentralized hydrogen production in Germany," *Renewable Energy*, vol. 177, pp. 915–931, 2021, doi: 10.1016/j.renene.2021.05.149.

[119] G. Correa, F. Volpe, P. Marocco, P. Muñoz, T. Falagüerra, and M. Santarelli, "Evaluation of levelized cost of hydrogen produced by wind electrolysis: Argentine and Italian production scenarios," *Journal of Energy Storage*, vol. 52, p. 105014, 2022, doi: 10.1016/j.est.2022.105014.

[120] *Renewable Energy Sources Act 2023: EEG 2023*, 2023. [Online]. Available: https://www.gesetze-im-internet.de/eeg_2014/BJNR106610014.html

[121] N. Thie, *Risk Management in Direct Marketing of Renewable Energies*: RWTH Aachen University, 2020.

[122] 50Hertz Transmission GmbH, Amprion GmbH, TenneT TSO GmbH, TransnetBW GmbH, *Netztransparenz.de (network transparancy plattform): Market value overview.* [Online]. Available: https://www.netztransparenz.de/en/Renewable-energies-and-levies/EEG/Transparency-requirements/Market-premium/Market-value-overview (accessed: Nov. 2 2024).

[123] J. van Ouwerkerk *et al.,* "Quantifying benefits of renewable investments for German residential Prosumers in times of volatile energy markets," *Nature Communications*, vol. 15, no. 1, p. 8206, 2024, doi: 10.1038/s41467-024-51967-6.

[124] A. Ajanovic, M. Sayer, and R. Haas, "The economics and the environmental benignity of different colors of hydrogen," *International Journal of Hydrogen Energy*, vol. 47, no. 57, pp. 24136–24154, 2022, doi: 10.1016/j.ijhydene.2022.02.094.

[125] S. Mohr, *Minimal quota for green hydrogen in industry: The consequences of the RED III.* [Online]. Available: https://www.ffe.de/en/publications/consequences-of-the-red-iii/

[126] Zentrum für Sonnenenergie- und Wasserstoff-Forschung (ZSW), "Power-Purchase-Agreements (PPA) zur Belieferung von Elektrolyseanlagen zur Herstellung synthetischer Kraftstoffe aus erneuerbare Energien," Jul. 2021. [Online]. Available: https://vm.baden-wuerttemberg.de/fileadmin/redaktion/m-mvi/intern/Dateien/PDF/211020_PPA_zur_EE_Stromversorgung_von_reFuels.pdf

[127] C. Fraunholz, D. Hladik, D. Keles, D. Möst, and W. Fichtner, "On the long-term efficiency of market splitting in Germany," *Energy Policy*, vol. 149, p. 111833, 2021, doi: 10.1016/j.enpol.2020.111833.

[128] J. Arellano and M. Carrión, "Electricity procurement of large consumers considering power-purchase agreements," *Energy Reports*, vol. 9, pp. 5384–5396, 2023, doi: 10.1016/j.egyr.2023.04.371.

[129] Deutsche Energie-Agentur (DENA), "Preisleitfaden Green PPA: Ein Leitfaden für Stromerzeuger und -abnehmer sowie Projektfinanzierer," 2022. Accessed: Oct. 24 2024. [Online]. Available: https://www.dena.de/fileadmin/dena/Publikationen/PDFs/2022/Preisleitfaden_Green_PPA_.pdf

[130] L. Mendicino, D. Menniti, A. Pinnarelli, and N. Sorrentino, "Corporate power purchase agreement: Formulation of the related levelized cost of energy and its application to a real life case study," *Applied Energy*, vol. 253, p. 113577, 2019, doi: 10.1016/j.apenergy.2019.113577.

[131] M. L. Bynum *et al.,* "Pyomo - Optimization Modeling in Python: Pyomo Documentation 6.8.1," 2021. Accessed: Feb. 11 2025. [Online]. Available: https://pyomo.readthedocs.io/en/stable/

[132] J. Gong *et al.,* "FOCUS : A framework for energy system optimization from prosumer to district and city scale," https://arxiv.org/abs/2304.07150

[133] L. L. Gurobi Optimization, *Gurobi Optimizer Reference Manual.* [Online]. Available: https://www.gurobi.com/

[134] C. Li, A. J. Conejo, P. Liu, B. P. Omell, J. D. Siirola, and I. E. Grossmann, "Mixed-integer linear programming models and algorithms for generation and transmission expansion planning of power systems," *European Journal of Operational Research*, vol. 297, no. 3, pp. 1071–1082, 2022, doi: 10.1016/j.ejor.2021.06.024.

[135] M. T. Baumhof, E. Raheli, A. G. Johnsen, and J. Kazempour, "Optimization of Hybrid Power Plants: When is a Detailed Electrolyzer Model Necessary?," in *2023 IEEE Belgrade PowerTech*, 2023, pp. 1–10.

[136] J. van Ouwerkerk, J. Brucksch, C. Bussar, and D. U. Sauer, "Facing the energy crisis: implementing short-term measures to reduce costs and emissions at industrial manufacturing sites," in *NEIS 2023; Conference on Sustainable Energy Supply and Energy Storage Systems*, 2023, pp. 86–91. Accessed: Mar. 28 2025. [Online]. Available: https://ieeexplore.ieee.org/abstract/document/10556675

[137] D. Jost, S. Kanzurova, C. Reinert, and N. von der Aßen, "Decarbonization potential of the glass melting process via energy efficiency measures and fuel switching," in *13. Internationale Energiewirtschaftstagung (IEWT 2023).* Accessed: May 8 2025. [Online]. Available: https://iewt2023.eeg.tuwien.ac.at/download/contribution/fullpaper/45/45_fullpaper_20230210_155922.pdf

[138] Fraunhofer Institute for Solar Energy Systems (ISE), "Paths to a Climate-Neutral Energy System: The German Energy Transition in its Social Context," Feb. 2020. Accessed: 28.10.24. [Online]. Available: https://www.ise.fraunhofer.de/content/dam/ise/en/documents/publications/studies/Fraunhofer-ISE-Study-Paths-to-a-Climate-Neutral-Energy-System.pdf

[139] Federal Network Agency (BNetzA), "Bedarfsermittlung 2023-2037/2045: Bestätigung Netzentwicklungsplan Strom," Mar. 2024. Accessed: Oct. 28 2024. [Online]. Available: https://www.netzentwicklungsplan.de/sites/default/files/2024-03/NEP_2037_2045_Bestaetigung.pdf

[140] "Gesetz über die Elektrizitäts- und Gasversorgung (Energiewirtschaftsgesetz): EnWG," in *§ 118 Übergangsregelungen, (6)*, 2024. Accessed: 25.01.25. [Online]. Available: https://www.gesetze-im-internet.de/enwg_2005/__118.html

[141] *Gesetz zur Finanzierung der Energiewende im Stromsektor durch Zahlungen des Bundes und Erhebung von Umlagen - (Energiefinanzierungsgesetz) - § 36 Herstellung von Wasserstoff in stromkostenintensiven Unternehmen: EnFG*, 2023. [Online]. Available: https://www.gesetze-im-internet.de/enfg/__36.html

[142] "Stromsteuergesetz: StromStG," in *§ 9a Erlass, Erstattung oder Vergütung der Steuer für bestimmte Prozesse und Verfahren*, 2024. Accessed: 25.01.25. [Online]. Available: https://www.gesetze-im-internet.de/stromstg/__9a.html

[143] German Federal Ministry of Finance, Ed., "Gesetzentwurf der Bundesregierung: Entwurf eines Gesetzes zur Modernisierung und zum Bürokratieabbau im Strom- und Energiesteuerrecht," May. 2024. Accessed: Jan. 19 2025. [Online]. Available: https://www.bundesfinanzministerium.de/Content/DE/Gesetzestexte/Gesetze_Gesetzesvorhaben/Abteilungen/Abteilung_III/20_Legislaturperiode/2024-04-12-Strom-und-Energiesteuerrecht/2-Regierungsentwurf.pdf?__blob=publicationFile&v=2

[144] *§ 118 Übergangsregelungen, (6)*.

[145] *§ 9a Erlass, Erstattung oder Vergütung der Steuer für bestimmte Prozesse und Verfahren*.

[146] European Central Bank (ECB), *ECB Data Portal: Harmonised Index of Consumer Prices (HICP).* [Online]. Available: https://data.ecb.europa.eu/data/data-categories/prices-macroeconomic-and-sectoral-statistics/measuring-inflation-harmonised-index-consumer-prices-hicp/harmonised-index-consumer-prices-hicp/goods (accessed: Nov. 2 2024).

[147] European Central Bank (ECB), *ECB Data Portal: US dollar/Euro, Annual.* [Online]. Available: https://data.ecb.europa.eu/data/datasets/EXR/EXR.A.USD.EUR.SP00.A (accessed: Nov. 3 2024).

[148] T. Badouard, D. de Oliveira, J. Yearwood, and P. Torres, "Final Report Cost of Energy (LCOE): Energy costs, taxes and the impact of government interventions on investments,"

Jul. 2020. Accessed: Nov. 7 2024. [Online]. Available: https://energy.ec.europa.eu/system/files/2020-10/final_report_levelised_costs_0.pdf

[149] International Renewable Energy Agency (IRENA), "Renewable power generation costs in 2023," Abu Dhabi, 2024. Accessed: Nov. 7 2024. [Online]. Available: https://www.irena.org/-/media/Files/IRENA/Agency/Publication/2024/Sep/IRENA_Renewable_power_generation_costs_in_2023.pdf

[150] prognos, "Strompreisprognose bis 2045," 2024. Accessed: 27.10.25. [Online]. Available: https://www.vbw-bayern.de/Redaktion/Frei-zugaengliche-Medien/Abteilungen-GS/Wirtschaftspolitik/2024/Downloads/Strompreisprognose_2024_v4-(002).pdf

[151] Institute of Energy Economics at the University of Cologne (EWI), "Scenarios for the Price Development of Energy Commodities: English summary," Jul. 2022. [Online]. Available: https://www.ewi.uni-koeln.de/cms/wp-content/uploads/2022/09/EWI-Study-Scenarios-for-the-price-development-of-energy-commodities_English-Summary.pdf

[152] C. Hank *et al.,* "Power-to-X Country Analysis: Site-specific, Comparative Analysis for Suitable Power-to-X Pathways and Products in Developing and Emerging Countries," May. 2023. Accessed: 27.10.24. [Online]. Available: https://www.ise.fraunhofer.de/content/dam/ise/en/documents/publications/studies/Fraunhofer-ISE-H2Global-Study-Power-to-X-Country%20Analysis.pdf

[153] acatech – National Academy of Science and Engineering, *H2-Compass: Pathfinder for a future hydrogen economy.* [Online]. Available: https://www.wasserstoff-kompass.de/en/ (accessed: 27.10.24).

[154] BDEW Bundesverband der Energie- und Wasserwirtschaft e.V., "BDEW-Strompreisanalyse Juli 2024: Haushalte und Industrie," Jul. 2024. Accessed: Nov. 7 2024. [Online]. Available: https://www.bdew.de/media/documents/240703_BDEW-Strompreisanalyse_Juli_2024_Korrektur.pdf

[155] Vereinigung der Bayerischen Wirtschaft e. V. (vbw), "Internationaler Energiepreisvergleich für die Industrie," Oct. 2023. Accessed: Nov. 7 2024. [Online]. Available: https://www.vbw-bayern.de/Redaktion/Frei-zugaengliche-Medien/Abteilungen-GS/Wirtschaftspolitik/2023/Downloads/vbw-Studie_Internationaler-Energiepreisvergleich_Oktober-2023.pdf

[156] Federal Statistical Office, *GENESIS-Online: The database of the Federal Statistical Office.* [Online]. Available: https://www-genesis.destatis.de/datenbank/online

[157] Federal Environmental Agency (UBA), "CO2 Emission Factors for Fossil Fuels," 2016. Accessed: Nov. 7 2024. [Online]. Available: https://www.umweltbundesamt.de/sites/default/files/medien/1968/publikationen/co2_emission_factors_for_fossil_fuels_correction.pdf

[158] KPMG, "Cost of capital study 2024," 2024. Accessed: Nov. 7 2024. [Online]. Available: https://kpmg.com/de/en/home/insights/overview/cost-of-capital.study.html

[159] European Hydrogen Backbone, "Implementation Roadmap - Cross Border Projects and Cost Update," Nov. 2023. Accessed: Oct. 30 2024. [Online]. Available: https://ehb.eu/files/downloads/EHB-2023-Implementation-Roadmap-Part-1.pdf

[160] D. Then, C. Spalthoff, J. Bauer, T. M. Kneiske, and M. Braun, "Impact of Natural Gas Distribution Network Structure and Operator Strategies on Grid Economy in Face of Decreasing Demand," *Energies*, vol. 13, no. 3, p. 664, 2020, doi: 10.3390/en13030664.

[161] Deutscher Wetterdienst (DWD), "CDC - Climate Data Center," 2025. Accessed: Mar. 2 2025. [Online]. Available: https://cdc.dwd.de/portal/

[162] R. Lochhead, O. Donnelly, and J. Carroll, "System-Level Offshore Wind Energy and Hydrogen Generation Availability and Operations and Maintenance Costs," *Wind*, vol. 4, no. 2, pp. 135–154, 2024, doi: 10.3390/wind4020007.

[163] Fraunhofer Institute for Solar Energy Systems (ISE), *Energy-Charts.* [Online]. Available: https://www.energy-charts.info/index.html?l=en&c=DE (accessed: Oct. 28 2024).

[164] EPEX SPOT, "Continuous price indices," 2024. Accessed: Mar. 28 2025. [Online]. Available: https://www.epexspot.com/en/indices#continuous-price-indices

[165] Fraunhofer Institute for Solar Energy Systems (ISE), "Current and Future Cost of Photovoltaics: Long-term Scenarios for Market Development, System Prices and LCOE of Utility-Scale PV Systems," Feb. 2015. Accessed: Nov. 2 2024. [Online]. Available: https://www.ise.fraunhofer.de/content/dam/ise/de/documents/publications/studies/AgoraEnergiewende_Current_and_Future_Cost_of_PV_Feb2015_web.pdf

[166] Dirk Uwe Sauer *et al.,* "Energiespeicher - Technologiesteckbrief zur Analyse „Flexibilitätskonzepte für die Stromversorgung 2050“," 2015.

[167] A. Sangwongwanich, Y. Yang, D. Sera, F. Blaabjerg, and D. Zhou, "On the Impacts of PV Array Sizing on the Inverter Reliability and Lifetime," *IEEE Transactions on Industry Applications*, vol. 54, no. 4, pp. 3656–3667, 2018, doi: 10.1109/TIA.2018.2825955.

[168] C. Bucher, J. Wandel, and D. Joss, "Life Expectancy of PV Inverters and Optimizers in Residential PV Systems," 2022, doi: 10.4229/WCPEC-82022-3DV.1.46.

[169] L. Koltermann, M. C. Cortés, N. Nsir, J. van Ouwerkerk, and D. U. Sauer, "Performance Testing of a Megawatt-Scale Battery Storage for Energy Trading," in *Atlantis Highlights in Engineering, Proceedings of the International Renewable Energy Storage and Systems Conference (IRES 2023)*, P. Droege and L. Quint, Eds., Dordrecht: Springer Nature, 2024, pp. 4–11.

[170] T. Roth, L. Streck, A. Graule, P. Niehoff, and A. Jossen, "Relaxation Effects in Self-Discharge Measurements of Lithium-Ion Batteries," *J. Electrochem. Soc.*, vol. 170, no. 2, p. 20502, 2023, doi: 10.1149/1945-7111/acb669.

[171] A. de Almeida, B. Santos, and F. Martins, "Energy-efficient distribution transformers in Europe: impact of Ecodesign regulation," *Energy Efficiency*, vol. 9, no. 2, pp. 401–424, 2016, doi: 10.1007/s12053-015-9365-z.

[172] Federal State Office for Nature, the Environment and Consumer Protection in North Rhine Westphalia (LANUV), *Energie Atlas: Solarkataster NRW.* [Online]. Available: https://www.energieatlas.nrw.de/site/karte_solarkataster (accessed: Nov. 8 2024).

[173] E. van der Roest, R. Bol, T. Fens, and A. van Wijk, "Utilisation of waste heat from PEM electrolysers – Unlocking local optimisation," *International Journal of Hydrogen Energy*, vol. 48, no. 72, pp. 27872–27891, 2023, doi: 10.1016/j.ijhydene.2023.03.374.

[174] A. Meriläinen, A. Kosonen, J. Jokisalo, R. Kosonen, P. Kauranen, and J. Ahola, "Techno-economic evaluation of waste heat recovery from an off-grid alkaline water electrolyzer plant and its application in a district heating network in Finland," *Energy*, vol. 306, p. 132181, 2024, doi: 10.1016/j.energy.2024.132181.

[175] H. van ’t Noordende and P. Ripson, "A One-GigaWatt Green-Hydrogen Plant: Advanced Design and Total Installed-Capital Costs," Jan. 2022. Accessed: Nov. 3 2024. [Online]. Available: https://ispt.eu/media/Public-report-gigawatt-advanced-green-electrolyser-design.pdf

[176] O. Schmidt, A. Gambhir, I. Staffell, A. Hawkes, J. Nelson, and S. Few, "Future cost and performance of water electrolysis: An expert elicitation study," *International Journal of Hydrogen Energy*, vol. 42, no. 52, pp. 30470–30492, 2017, doi: 10.1016/j.ijhydene.2017.10.045.

[177] S. Krishnan *et al.,* "Present and future cost of alkaline and PEM electrolyser stacks," *International Journal of Hydrogen Energy*, vol. 48, no. 83, pp. 32313–32330, 2023, doi: 10.1016/j.ijhydene.2023.05.031.

[178] A. Ibáñez-Rioja *et al.,* "Off-grid solar PV–wind power–battery–water electrolyzer plant: Simultaneous optimization of component capacities and system control," *Applied Energy*, vol. 345, p. 121277, 2023, doi: 10.1016/j.apenergy.2023.121277.

[179] T. Roeder, A. Rosenstiel, N. Monnerie, and C. Sattler, "Impact of expected cost reduction and lifetime extension of electrolysis stacks on hydrogen production costs," *International Journal of Hydrogen Energy*, 2024, doi: 10.1016/j.ijhydene.2024.08.015.

[180] J. Wang, J. Wen, J. Wang, B. Yang, and L. Jiang, "Water electrolyzer operation scheduling for green hydrogen production: A review," *Renewable and Sustainable Energy Reviews*, vol. 203, p. 114779, 2024, doi: 10.1016/j.rser.2024.114779.

[181] *Zwölfte Verordnung zur Durchführung des Bundes-Immissionsschutzgesetzes (Störfall-Verordnung) - Anhang I Mengenschwellen: BImSchV*, 2024. Accessed: Feb. 6 2025. [Online]. Available: https://www.gesetze-im-internet.de/bimschv_12_2000/anhang_i.html

[182] Ø. Ulleberg, T. Nakken, and A. Eté, "The wind/hydrogen demonstration system at Utsira in Norway: Evaluation of system performance using operational data and updated hydrogen energy system modeling tools," *International Journal of Hydrogen Energy*, vol. 35, no. 5, pp. 1841–1852, 2010, doi: 10.1016/j.ijhydene.2009.10.077.

[183] G. Sdanghi, G. Maranzana, A. Celzard, and V. Fierro, "Review of the current technologies and performances of hydrogen compression for stationary and automotive applications," *Renewable and Sustainable Energy Reviews*, vol. 102, pp. 150–170, 2019, doi: 10.1016/j.rser.2018.11.028.

[184] Z. Abdin, C. Tang, Y. Liu, and K. Catchpole, "Large-scale stationary hydrogen storage via liquid organic hydrogen carriers," *iScience*, vol. 24, no. 9, p. 102966, 2021, doi: 10.1016/j.isci.2021.102966.

[185] M.-R. Tahan, "Recent advances in hydrogen compressors for use in large-scale renewable energy integration," *International Journal of Hydrogen Energy*, vol. 47, no. 83, pp. 35275–35292, 2022, doi: 10.1016/j.ijhydene.2022.08.128.

[186] Y. Wang, J. Kowal, M. Leuthold, and D. U. Sauer, "Storage System of Renewable Energy Generated Hydrogen for Chemical Industry," *Energy Procedia*, vol. 29, pp. 657–667, 2012, doi: 10.1016/j.egypro.2012.09.076.

[187] P. C. Ghosh, B. Emonts, H. Janßen, J. Mergel, and D. Stolten, "Ten years of operational experience with a hydrogen-based renewable energy supply system," *Solar Energy*, vol. 75, no. 6, pp. 469–478, 2003, doi: 10.1016/j.solener.2003.09.006.

[188] K. Reddi, A. Elgowainy, N. Rustagi, and E. Gupta, "Impact of hydrogen refueling configurations and market parameters on the refueling cost of hydrogen," *International Journal of Hydrogen Energy*, vol. 42, no. 34, pp. 21855–21865, 2017, doi: 10.1016/j.ijhydene.2017.05.122.

[189] C. Wulf *et al.,* "Life Cycle Assessment of hydrogen transport and distribution options," *Journal of Cleaner Production*, vol. 199, pp. 431–443, 2018, doi: 10.1016/j.jclepro.2018.07.180.

[190] Department for Energy Security and Net Zero and Department for Business, Energy & Industrial Strategy, "Fugitive hydrogen emissions in a future hydrogen economy," Apr. 2022. Accessed: 26.01.25. [Online]. Available: https://www.gov.uk/government/publications/fugitive-hydrogen-emissions-in-a-future-hydrogen-economy

[191] R. Grosse, B. Christopher, W. Stefan, R. Greyer, and S. Robbi, *Long term (2050) projections of techno-economic performance of large-scale heating and cooling in the EU*. Luxembourg: Publications Office of the European Union, 2017. Accessed: Nov. 4 2024. [Online]. Available: https://publications.jrc.ec.europa.eu/repository/bitstream/JRC109006/kjna28859enn.pdf

[192] M. M. Rahman, A. O. Oni, E. Gemechu, and A. Kumar, "Assessment of energy storage technologies: A review," *Energy Conversion and Management*, vol. 223, p. 113295, 2020, doi: 10.1016/j.enconman.2020.113295.

[193] H. Thomas, A. Marian, A. Chervyakov, S. Stückrad, and C. Rubbia, "Efficiency of superconducting transmission lines: An analysis with respect to the load factor and capacity rating," *Electric Power Systems Research*, vol. 141, pp. 381–391, 2016, doi: 10.1016/j.epsr.2016.07.007.

[194] Federal Network Agency (BNetzA), *Beendete Ausschreibungen / Statistiken.* [Online]. Available: https://www.bundesnetzagentur.de/DE/Fachthemen/ElektrizitaetundGas/Ausschreibungen/Solaranlagen2/BeendeteAusschreibungen/start.html (accessed: Nov. 2 2024).

[195] T. Thien, D. Schweer, D. vom Stein, A. Moser, and D. U. Sauer, "Real-world operating strategy and sensitivity analysis of frequency containment reserve provision with battery energy storage systems in the german market," *Journal of Energy Storage*, vol. 13, pp. 143–163, 2017, doi: 10.1016/j.est.2017.06.012.

[196] Regionetz, "Entgelte für Netznutzung für 2021," 2021. Accessed: Feb. 7 2025. [Online]. Available: https://www.regionetz.de/fileadmin/regionetz/content/Dokumente/Preisbl%C3%A4tter/Preisbl%C3%A4tter_Strom_2021_Regionetz.pdf

[197] J. van Ouwerkerk and J. Brucksch, "Battery Revenue Index (Beta-Version): Revenue potential for Grid-scale batteries," 2025. Accessed: Feb. 9 2025. [Online]. Available: https://battery-charts.rwth-aachen.de/battery-revenue-index-beta-version-2/

[198] D. Kucevic *et al.,* "Standard battery energy storage system profiles: Analysis of various applications for stationary energy storage systems using a holistic simulation framework," *Journal of Energy Storage*, vol. 28, p. 101077, 2020, doi: 10.1016/j.est.2019.101077.

[199] *VDI 2067 - Economic efficiency of building installations - Fundamentals and economic calculation,* VDI – The Association of German Engineers, Sep. 2012. [Online]. Available: https://www.vdi.de/richtlinien/details/vdi-2067-blatt-1-wirtschaftlichkeit-gebaeudetechnischer-anlagen-grundlagen-und-kostenberechnung-1

Curriculum Vitae

Name	Jonas van Ouwerkerk
Year of birth	1992
Place of birth	Malsch Kreis Karlsruhe (Germany)

Education

10.07.2025	Doctoral Examination for Dr.-Ing., Faculty for Electrical Engineering, RWTH Aachen University, Germany
2019-2025	Research Assistant and Doctoral Candidate, Institute for Power Electronics and Electrical Drives (ISEA) / Institute for Power Generation and Storage Systems (PGS), Supervisor: Prof. Dirk Uwe Sauer, RWTH Aachen University, Germany
March 2019	Master of Science, Electrical Engineering, Information Technology and Computer Engineering, RWTH Aachen University, Germany
2018	Internship at Sonnen Inc., Atlanta, Georgia, USA
2016-2017	ERASMUS Semester at University College Cork, Cork, Ireland
April 2016	Bachelor of Science, Electrical Engineering, Information Technology and Computer Engineering, RWTH Aachen University, Germany
2009-2012	General Higher Education Entrance Qualification (Abitur) Berufskolleg Uerdingen, Krefeld, Germany

Professional career

2023-2025	Head of Grid Integration and Storage System Analysis, Institute for Power Electronics and Electrical Drives (ISEA) / Institute for Power Generation and Storage Systems (PGS), RWTH Aachen University
2020-2025	Battery Expert and Co-Founder, ACCURE Battery Intelligence GmbH, Aachen, Germany
2024 and 2025	Leading the Seminar by Haus der Technik (HDT): Stationäre Lithium-Ionen-Speichersysteme, Aachen, Germany

ABISEA Band 1
Eßer, Albert
Berührungslose, kombinierte Energie- und Informationsübertragung für bewegliche Systeme
1. Aufl. 1992, 129 S.
ISBN 3-86073-046-0

ABISEA Band 2
Vogel, Ulrich
Entwurf und Beurteilung von Verfahren zur Hochausnutzung des Rad-Schiene-Kraftschlusses durch Triebfahrzeuge
1. Aufl. 1992, 131 S.
ISBN 3-86073-060-6

ABISEA Band 3
Reckhorn, Thomas
Stromeinprägendes Antriebssystem mit fremderregter Synchronmaschine
1. Aufl. 1992, 128 S.
ISBN 3-86073-061-4

ABISEA Band 4
Ackva, Ansgar
Spannungseinprägendes Antriebssystem mit Synchronmaschine und direkter Stromregelung
1. Aufl. 1992, 137 S.
ISBN 3-86073-062-2

ABISEA Band 5
Mertens, Axel
Analyse des Oberschwingungsverhaltens von taktsynchronen Delta - Modulationsverfahren zur Steuerung von Pulsstromrichtern bei hoher Taktzahl
1. Aufl. 1992, 178 S.
ISBN 3-86073-069-X

ABISEA Band 6
Geuer, Wolfgang
Untersuchungen über das Alterungsverhalten von Blei-Akkumulatoren
1. Aufl. 1993, 97 S.
ISBN 3-86073-097-5

ABISEA Band 7
Langheim, Jochen
Einzelradantrieb für Elektrostraßenfahrzeuge
1. Aufl. 1993, 213 S.
ISBN 3-86073-123-8
(vergriffen)

ABISEA Band 8
Fetz, Joachim
Fehlertolerante Regelung eines Asynchron-Doppelantriebes für ein Elektrospeicherfahrzeug
1. Aufl. 1993, 136 S.
ISBN 3-86073-124-6
(vergriffen)

ABISEA Band 9
Schülting, Ludger
Optimierte Auslegung induktiver Bauelemente für den Mittelfrequenzbereich
1. Aufl. 1993, 126 S.
ISBN 3-86073-174-2
(vergriffen)

ABISEA Band 10
Skudelny, H.-Ch.
Stromrichtertechnik
4. Aufl. 1997, 259 S.
ISBN 3-86073-189-0

ABISEA Band 11
Skudelny, H.-Ch.
Elektrische Antriebe
3. Aufl. 1997, 124 S.
ISBN 3-86073-231-5

ABISEA Band 12
Schöpe, Friedhelm
Batterie-Management für Nickel-Cadmium Akkumulatoren
1. Aufl. 1994, 148 S.
ISBN 3-86073-232-3
(vergriffen)

ABISEA Band 13
v. d. Weem, Jürgen
Schmalbandige aktive Filter für Schienentriebfahrzeuge am Gleichspannungsfahrdraht
1. Aufl. 1995, 126 S.
ISBN 3-86073-233-1

ABISEA Band 14
Backhaus, Klaus
Spannungseinprägendes Direktantriebssystem mit schnelllaufender geschalteter Reluktanzmaschine
1. Aufl. 1995, 146 S.
ISBN 3-86073-234-X
(vergriffen)

ABISEA Band 15
Reinold, Harry
Optimierung dreiphasiger Pulsdauermodulationsverfahren
1. Aufl. 1996, 107 S.
ISBN 3-86073-235-8

ABISEA Band 16
Köpken, Hans-Georg
Regelverfahren für Parallelschwingkreisumrichter
1. Aufl. 1996, 125 S.
ISBN 3-86073-236-6

ABISEA Band 17
Mauracher, Peter
Modellbildung und Verbundoptimierung bei Elektrostraßenfahrzeugen
1. Aufl. 1996, 192 S.
ISBN 3-86073-237-4

ABISEA Band 18
Protiwa, Franz-Ferdinand
Vergleich dreiphasiger Resonanz-Wechselrichter in Simulation und Messung
1. Aufl. 1997, 178 S.
ISBN 3-86073-238-2

ABISEA Band 19
Brockmeyer, Ansgar
Dimensionierungswerkzeug für magnetische Bauelemente in Stromrichteranwendungen
1. Aufl. 1997, 175 S.
ISBN 3-86073-239-0

Aachener Beiträge des ISEA

ABISEA Band 20
Apeldoorn, Oscar
Simulationsgestützte Bewertung von Steuerverfahren für netzgeführte Stromrichter mit verringerter Netzrückwirkung
1. Aufl. 1997, 134 S.
ISBN 3-86073-680-9

ABISEA Band 21
Lohner, Andreas
Batteriemanagement für verschlossene Blei-Batterien am Beispiel von Unterbrechungsfreien Stromversorgungen
1. Aufl. 1998, 126 S.
ISBN 3-86073-681-7

ABISEA Band 22
Reinert, Jürgen
Optimierung der Betriebseigenschaften von Antrieben mit geschalteter Reluktanzmaschine
1. Aufl. 1998, 153 S.
ISBN 3-86073-682-5

ABISEA Band 23
Nagel, Andreas
Leitungsgebundene Störungen in der Leistungselektronik: Entstehung, Ausbreitung und Filterung
1. Aufl. 1999, 140 S.
ISBN 3-86073-683-3

ABISEA Band 24
Menne, Marcus
Drehschwingungen im Antriebsstrang von Elektrostraßenfahrzeugen - Analyse und aktive Dämpfung
1. Aufl. 2001, 169 S.
ISBN 3-86073-684-1

ABISEA Band 25
von Bloh, Jochen
Multilevel-Umrichter zum Einsatz in Mittelspannungs-Gleichspannungs-Übertragungen
1. Aufl. 2001, 137 S.
ISBN 3-86073-685-X

ABISEA Band 26
Karden, Eckhard
Using low-frequency impedance spectroscopy for characterization, monitoring, and modeling of industrial batteries
1. Aufl. 2002, 137 S.
ISBN 3-8265-9766-4

ABISEA Band 27
Karipidis, Claus-Ulrich
A Versatile DSP/ FPGA Structure optimized for Rapid Prototyping and Digital Real-Time Simulation of Power Electronic and Electrical Drive Systems
1. Aufl. 2001, 164 S.
ISBN 3-8265-9738-9

ABISEA Band 28
Kahlen, Klemens
Regelungsstrategien für permanentmagnetische Direktantriebe mit mehreren Freiheitsgraden
1. Aufl. 2002, 154 S.
ISBN 3-8322-1222-1

ABISEA Band 29
Inderka, Robert B.
Direkte Drehmomentregelung Geschalteter Reluktanzantriebe
1. Aufl. 2003, 182 S.
ISBN 3-8322-1175-6

ABISEA Band 30
Schröder, Stefan
Circuit-Simulation Models of High-Power Devices Based on Semiconductor Physics
1. Aufl. 2003, 123 S.
ISBN 3-8322-1250-7

ABISEA Band 31
Buller, Stephan
Impedance-Based Simulation Models for Energy Storage Devices in Advanced Automotive Power Systems
1. Aufl. 2003, 138 S.
ISBN 3-8322-1225-6

ABISEA Band 32
Schönknecht, Andreas
Topologien und Regelungsstrategien für das induktive Erwärmen mit hohen Frequenz-Leistungsprodukten
1. Aufl. 2004, 157 S.
ISBN 3-8322-2408-4

ABISEA Band 33
Tolle, Tobias
Konvertertopologien für ein aufwandsarmes, zweistufiges Schaltnetzteil zum Laden von Batterien aus dem Netz
1. Aufl. 2004, 148 S.
ISBN 3-8322-2676-1

ABISEA Band 34
Götting, Gunther
Dynamische Antriebsregelung von Elektrostraßenfahrzeugen unter Berücksichtigung eines schwingungsfähigen Antriebsstrangs
1. Aufl. 2004, 157 S.
ISBN 3-8322-2804-7

ABISEA Band 35
Dieckerhoff, Sibylle
Transformatorlose Stromrichterschaltungen für Bahnfahrzeuge am 16 2/3Hz Netz
1. Aufl. 2004, 147 S.
ISBN 3-8322-3094-7

ABISEA Band 36
Hu, Jing
Bewertung von DC-DC-Topologien und Optimierung eines DC-DC-Leistungsmoduls für das 42-V-Kfz-Bordnetz
1. Aufl. 2004, 148 S.
ISBN 3-8322-3201-X

ABISEA Band 37
Detjen, Dirk-Oliver
Characterization and Modeling of Si-Si Bonded Hydrophobie Interfaces for Novel High-Power BIMOS Devices
1. Aufl. 2004, 135 S.
ISBN 3-8322-2963-9

ABISEA Band 38
Walter, Jörg
Simulationsbasierte Zuverlässigkeitsanalyse in der modernen Leistungselektronik
1. Aufl. 2004, 121 S.
ISBN 3-8322-3481-0

ABISEA Band 39
Schwarzer, Ulrich
IGBT versus GCT in der Mittelspannungsanwendung - ein experimenteller und simulativer Vergleich
1. Aufl. 2005, 170 S.
ISBN 3-8322-4489-1

ABISEA Band 40
Bartram, Markus
IGBT-Umrichtersysteme für Windkraftanlagen: Analyse der Zyklenbelastung, Modellbildung, Optimierung und Lebensdauervorhersage
1. Aufl. 2006, 185 S.
ISBN 3-8322-5039-5

ABISEA Band 41
Ponnaluri, Srinivas
Generalized Design, Analysis and Control of Grid side converters with integrated UPS or Islanding functionality
1. Aufl. 2006, 163 S.
ISBN 3-8322-5281-9

ABISEA Band 42
Jacobs, Joseph
Multi-Phase Series Resonant DC-to-DC Converters
1. Aufl. 2006, 185 S.
ISBN 3-8322-5532-X

ABISEA Band 43
Linzen, Dirk
Impedance-Based Loss Calculation and Thermal Modeling of Electrochemical Energy Storage Devices for Design Considerations of Automotive Power Systems
1. Aufl. 2006, 185 S.
ISBN 3-8322-5706-3

ABISEA Band 44
Fiedler, Jens
Design of Low-Noise Switched Reluctance Drives
1. Aufl. 2007, 176 S.
ISBN 978-3-8322-5864-1

ABISEA Band 45
Fuengwarodsakul, Nisai
Predictive PWM-based Direct Instantaneous Torque Control for Switched Reluctance Machines
1. Aufl. 2007, 141 S.
ISBN 978-3-8322-6210-5

ABISEA Band 46
Meyer, Christoph
Key Components for Future Offshore DC Grids
1. Aufl. 2007, 187 S.
ISBN 978-3-8322-6571-7

ABISEA Band 47
Fujii, Kansuke
Characterization and Optimization of Soft-Switched Multi-Level Converters for STATCOMs
1. Aufl. 2008, 199 S.
ISBN 978-3-8322-6981-4

ABISEA Band 48
Carstensen, Christian
Eddy Currents in Windings of Switched Reluctance Machines
1. Aufl. 2008, 179 S.
ISBN 978-3-8322-7118-3

ABISEA Band 49
Bohlen, Oliver
Impedance-based battery monitoring
1. Aufl. 2008, 190 S.
ISBN 978-3-8322-7606-5

ABISEA Band 50
Thele, Marc
A contribution to the modelling of the charge acceptance of lead-acid batteries - using frequency and time domain based concepts
1. Aufl. 2008, 165 S.
ISBN 978-3-8322-7659-1

ABISEA Band 51
König, Andreas
High Temperature DC-to-DC Converters for Downhole Applications
1. Aufl. 2009, 154 S.
ISBN 978-3-8322-8489-3

ABISEA Band 52
Dick, Christian Peter
Multi-Resonant Converters as Photovoltaic Module-Integrated Maximum Power Point Tracker
1. Aufl. 2010, 182 S.
ISBN 978-3-8322-9199-0

ABISEA Band 53
Kowal, Julia
Spatially resolved impedance of nonlinear inhomogeneous devices: using the example of lead-acid batteries
1. Aufl. 2010, 203 S.
ISBN 978-3-8322-9483-0

ABISEA Band 54
Roscher, Michael Andreas
Zustandserkennung von LiFeP04-Batterien für Hybrid- und Elektrofahrzeuge
1. Aufl. 2011, 186 S.
ISBN 978-3-8322-9738-1

ABISEA Band 55
Hirschmann, Dirk
Highly Dynamic Piezoelectric Positioning
1. Aufl. 2011, 146 S.
ISBN 978-3-8322-9746-6

ABISEA Band 56
Rigbers, Klaus
Highly Efficient Inverter Architectures for Three-Phase Grid Connection of Photovoltaic Generators
1. Aufl. 2011, 244 S.
ISBN 978-3-8322-9816-9

ABISEA Band 57
Kasper, Knut
Analysis and Control of the Acoustic Behavior of Switched Reluctance Drives
1. Aufl. 2011, 205 S.
ISBN 978-3-8322-9869-2

Aachener Beiträge des ISEA

ABISEA Band 58
Köllensperger, Peter
The Internally Commutated Thyristor - Concept, Design and Application
1. Aufl. 2011, 214 S.
ISBN 978-3-8322-9909-5

ABISEA Band 59
Schoenen, Timo
Einsatz eines DC/DC-Wandlers zur Spannungsanpassung zwischen Antrieb und Energiespeicher in Elektro-und Hybridfahrzeugen
1. Aufl. 2011, 128 S.
ISBN 978-3-8440-0622-3

ABISEA Band 60
Hennen, Martin
Switched Reluctance Direct Drive with Integrated Distributed Inverter
1. Aufl. 2012, 141 S.
ISBN 978-3-8440-0731-2

ABISEA Band 61
van Treek, Daniel
Position Sensorless Torque Control of Switched Reluctance Machines
1. Aufl. 2012, 144 S.
ISBN 978-3-8440-1014-5

ABISEA Band 62
Bragard, Michael
The Integrated Emitter Turn-Off Thyristor. An Innovative MOS-Gated High-Power Device
1. Aufl. 2012, 164 S.
ISBN 978-3-8440-1152-4

ABISEA Band 63
Gerschler, Jochen B.
Ortsaufgelöste Modellbildung von Lithium-Ionen-Systemen unter spezieller Berücksichtigung der Batteriealterung
1. Aufl. 2012, 334 S.
ISBN 978-3-8440-1307-8

ABISEA Band 64
Neuhaus, Christoph R.
Schaltstrategien für Geschaltete Reluktanzantriebe mit kleinem Zwischenkreis
1. Aufl. 2012, 133 S.
ISBN 978-3-8440-1487-7

ABISEA Band 65
Butschen, Thomas
Dual-ICT- A Clever Way to Unite Conduction and Switching Optimized Properties in a Single Wafer
1. Aufl. 2012, 168 S.
ISBN 978-3-8440-1771-7

ABISEA Band 66
Plum, Thomas
Design and Realization of High-Power MOS Turn-Off Thyristors
1. Aufl. 2013, 113 S.
ISBN 978-3-8440-1884-4

ABISEA Band 67
Kiel, Martin
Impedanzspektroskopie an Batterien unter besonderer Berücksichtigung von Batteriesensoren für den Feldeinsatz
1. Aufl. 2013, 226 S.
ISBN 978-3-8440-1973-5

ABISEA Band 68
Brauer, Helge
Schnelldrehender Geschalteter Reluktanzantrieb mit extremem Längendurchmesserverhältnis
1. Aufl. 2013, 192 S.
ISBN 978-3-8440-2345-9

ABISEA Band 69
Thomas, Stephan
A Medium-Voltage Multi-Level DC/DC Converter with High Voltage Transformation Ratio
1. Aufl. 2014, 226 S.
ISBN 978-3-8440-2605-4

ABISEA Band 70
Richter, Sebastian
Digitale Regelung von PWM Wechselrichtern mit niedrigen Trägerfrequenzen
1. Aufl. 2014, 126 S.
ISBN 978-3-8440-2641-2

ABISEA Band 71
Bösing, Matthias
Acoustic Modeling of Electrical Drives - Noise and Vibration Synthesis based on Force Response Superposition
1. Aufl. 2014, 188 S.
ISBN 978-3-8440-2752-5

ABISEA Band 72
Waag, Wladislaw
Adaptive algorithms for monitoring of lithium-ion batteries in electric vehicles
1. Aufl. 2014, 232 S.
ISBN 978-3-8440-2976-5

ABISEA Band 73
Sanders, Tilman
Spatially Resolved Electrical In-Situ Measurement Techniques for Fuel Cells
1. Aufl. 2014, 126 S.
ISBN 978-3-8440-3121-8

ABISEA Band 74
Baumhöfer, Thorsten
Statistische Betrachtung experimenteller Alterungsuntersuchungen an Lithium-Ionen Batterien
1. Aufl. 2015, 157 S.
ISBN 978-3-8440-3423-3

ABISEA Band 75
Andre, Dave
Systematic Characterization of Ageing Factors for High-Energy Lithium-Ion Cells and Approaches for Lifetime Modelling Regarding an Optimized Operating Strategy in Automotive Applications
1. Aufl. 2015, 196 S.
ISBN 978-3-8440-3587-2

ABISEA Band 76
Merei, Ghada
Optimization of off-grid hybrid PV-wind-diesel power supplies with multi-technology battery systems taking into account battery aging
1. Aufl. 2015, 184 S.
ISBN 978-3-8440-4148-4

ABISEA Band 77
Schulte, Dominik
Modellierung und experimentelle Validierung der Alterung von Blei-Säure Batterien durch inhomogene Stromverteilung und Säureschichtung
1. Aufl. 2016, 165 S.
ISBN 978-3-8440-4216-0

ABISEA Band 78
Schenk, Mareike
Simulative Untersuchung der Wicklungsverluste in Geschalteten Reluktanzmaschinen
1. Aufl. 2016, 126 S.
ISBN 978-3-8440-4282-5

ABISEA Band 79
Wang, Yu
Development of Dynamic Models with Spatial Resolution for Electrochemical Energy Converters as Basis for Control and Management Strategies
1. Aufl. 2016, 188 S.
ISBN 978-3-8440-4303-7

ABISEA Band 80
Ecker, Madeleine
Lithium Plating in Lithium-Ion Batteries:
An Experimental and Simulation Approach
1. Aufl. 2016, 154 S.
ISBN 978-3-8440-4525-3

ABISEA Band 81
Zhou, Wei
Modellbasierte Auslegungsmethode von Temperierungssystemen für Hochvolt-Batterien in Personenkraftfahrzeugen
1. Aufl. 2016, 175 S.
ISBN 978-3-8440-4589-5

ABISEA Band 82
Lunz, Benedikt
Deutschlands Stromversorgung im Jahr 2050
Ein szenariobasiertes Verfahren zur vergleichenden Bewertung von Systemvarianten und Flexibilitätsoptionen
1. Aufl. 2016, 187 S.
ISBN 978-3-8440-4627-4

ABISEA Band 83
Hofmann, Andreas G.
Direct Instantaneous Force Control: Key to Low-Noise Switched Reluctance Traction Drives
1. Aufl. 2016, 228 S.
ISBN 978-3-8440-4715-8

ABISEA Band 84
Budde-Meiwes, Heide
Dynamic Charge Acceptance of Lead-Acid Batteries for Micro-Hybrid Automotive Applications
1. Aufl. 2016, 157 S.
ISBN 978-3-8440-4733-2

ABISEA Band 85
Engel, Stefan P.
Thyristor-Based High-Power On-Load Tap Changers Control under Harsh Load Conditions
1. Aufl. 2016, 156 S.
ISBN 978-3-8440-4986-2

ABISEA Band 86
Van Hoek, Hauke
Design and Operation Considerations of Three-Phase Dual Active Bridge Converters for Low-Power Applications with Wide Voltage Ranges
1. Aufl. 2017, 231 S.
ISBN 978-3-8440-5011-0

ABISEA Band 87
Diekhans, Tobias
Wireless Charging of Electric Vehicles - a Pareto-Based Comparison of Power Electronic Topologies
1. Aufl. 2017, 151 S.
ISBN 978-3-8440-5048-6

ABISEA Band 88
Lehner, Susanne
Reliability Assessment of Lithium-Ion Battery Systems with Special Emphasis on Cell Performance Distribution
1. Aufl. 2017, 184 S.
ISBN 978-3-8440-5090-5

ABISEA Band 89
Käbitz, Stefan
Untersuchung der Alterung von Lithium-Ionen-Batterien mittels Elektroanalytik und elektrochemischer Impedanzspektroskopie
1. Aufl. 2016, 258 S.
DOI: 10.18154/RWTH-2016-12094

ABISEA Band 90
Witzenhausen, Heiko
Elektrische Batteriespeichermodelle: Modellbildung, Parameteridentifikation und Modellreduktion
1. Aufl. 2017, 266 S.
DOI: 10.18154/RWTH-2017-03437

ABISEA Band 91
Münnix, Jens
Einfluss von Stromstärke und Zyklentiefe auf graphitische Anoden
1. Aufl. 2017, 171 S.
DOI: 10.18154/RWTH-2017-01915

ABISEA Band 92
Pilatowicz, Grzegorz
Failure Detection and Battery Management Systems of Lead-Acid Batteries for Micro-Hybrid Vehicles
1. Aufl. 2017, 212 S.
DOI: 10.18154/RWTH-2017-09156

ABISEA Band 93
Drillkens, Julia
Aging in Electrochemical Double Layer Capacitors: An Experimental and Modeling Approach
1. Aufl. 2017, 179 S.
DOI: 10.18154/RWTH-2018-223434

Aachener Beiträge des ISEA

ABISEA Band 94
Magnor, Dirk
Globale Optimierung netzgekoppelter PV-Batteriesysteme unter besonderer Berücksichtigung der Batteriealterung
1. Aufl. 2017, 210 S.
DOI: 10.18154/RWTH-2017-06592

ABISEA Band 95
Iliksu, Merve
Elucidation and Comparison of the Effects of Lithium Salts on Discharge Chemistry of Nonaqueous Li-O_2 Batteries
1. Aufl. 2018, 160 S.
DOI: 10.18154/RWTH-2018-223782

ABISEA Band 96
Schmalstieg, Johannes
Physikalisch-elektrochemische Simulation von Lithium-Ionen-Batterien: Implementierung, Parametrierung und Anwendung
1. Aufl. 2017, 168 S.
DOI: 10.18154/RWTH-2017-04693

ABISEA Band 97
Soltau, Nils
High-Power Medium-Voltage DC-DC Converters: Design, Control and Demonstration
1. Aufl. 2017, 176 S.
DOI: 10.18154/RWTH-2017-04084

ABISEA Band 98
Stieneker, Marco
Analysis of Medium-Voltage Direct-Current Collector Grids in Offshore Wind Parks
1. Aufl. 2017, 144 S.
DOI: 10.18154/RWTH-2017-04667

ABISEA Band 99
Masomtob, Manop
A New Conceptual Design of Battery Cell with an Internal Cooling Channel
1. Aufl. 2017, 167 S.
DOI: 10.18154/RWTH-2018-223281

ABISEA Band 100
Marongiu, Andrea
Performance and Aging Diagnostic on Lithium Iron Phosphate Batteries for Electric Vehicles and Vehicle-to-Grid Strategies
1. Aufl. 2017, 222 S.
DOI: 10.18154/RWTH-2017-09944

ABISEA Band 101
Gitis, Alexander
Flaw detection in the coating process of lithium-ion battery electrodes with acoustic guided waves
1. Aufl. 2017, 109 S.
DOI: 10.18154/RWTH-2017-099519

ABISEA Band 102
Neeb, Christoph
Packaging Technologies for Power Electronics in Automotive Applications
1. Aufl. 2017, 132 S.
DOI: 10.18154/RWTH-2018-224569

ABISEA Band 103
Adler, Felix
A Digital Hardware Platform for Distributed Real-Time Simulation of Power Electronic Systems
1. Aufl. 2017, 156 S.
DOI: 10.18154/RWTH-2017-10761

ABISEA Band 104
Becker, Jan
Flexible Dimensionierung und Optimierung hybrider Lithium-Ionenbatterie-speichersysteme mit verschiedenen Auslegungs-zielen
1. Aufl., 2017, 157 S.
DOI: 10.18154/RWTH-2017-09278

ABISEA Band 105
Warnecke, Alexander J.
Degradation Mechanisms in NMC Based Lithium-Ion Batteries
1. Aufl. 2017, 158 S.
DOI: 10.18154/RWTH-2017-09646

ABISEA Band 106
Taraborrelli, Silvano
Bidirectional Dual Active Bridge Converter using a Tap Changer for Extended Voltage Ranges
1. Aufl. 2017, 94 S.
DOI: 10.18154/RWTH-2018-228242

ABISEA Band 107
Sarriegi, Garikoitz
SiC and GaN Semiconductors: The Future Enablers of Compact and Efficient Converters for Electromobility
1. Aufl. 2017, 106 S.
DOI: 10.18154/RWTH-2018-227548

ABISEA Band 108
Senol, Murat
Drivetrain Integrated Dc-Dc Converters utilizing Zero Sequence Currents
1. Aufl. 2017, 134 S.
DOI: 10.18154/RWTH-2018-226170

ABISEA Band 109
Kojima, Tetsuya
Efficiency Optimized Control of Switched Reluctance Machines
1. Aufl. 2017, 142 S.
DOI: 10.18154/RWTH-2018-226697

ABISEA Band 110
Lewerenz, Meinert
Dissection and Quantitative Description of Aging of Lithium-Ion Batteries Using Non-Destructive Methods Validated by Post-Mortem-Analyses
1. Aufl. 2018, 139 S.
DOI: 10.18154/RWTH-2018-228663

ABISEA Band 111
Büngeler, Johannes
Optimierung der Verfügbarkeit und der Lebensdauer von Traktionsbatterien für den Einsatz in Flurförderfahrzeugen
1. Aufl. 2018, 171 S.
DOI: 10.18154/RWTH-2018-226569

ABISEA Band 112
Wegmann, Raphael
Betriebsstrategien und Potentialbewertung hybrider Batteriespeichersysteme in Elektrofahrzeugen
1. Auflage 2018, 184 S.
DOI: 10.18154/RWTH-2018-228833

ABISEA Band 113
Nordmann, Hannes
Batteriemanagementsysteme unter besonderer Berücksichtigung von Fehlererkennung und Peripherieanalyse
1. Aufl. 2018, 222 S.
DOI: 10.18154/RWTH-2018-228763

ABISEA Band 114
Engelmann, Georges
Reducing Device Stress and Switching Losses Using Active Gate Drivers and Improved Switching Cell Design
1. Aufl. 2018, 195 S.
DOI: 10.18154/RWTH-2018-228973

ABISEA Band 115
Klein-Heßling, Annegret
Active DC-Power Filters for Switched Reluctance Drives during Single-Pulse Operation
1. Aufl. 2018, 166 S.
DOI: 10.18154/RWTH-2018-231030

ABISEA Band 116
Burkhart, Bernhard
Switched Reluctance Generator for Range Extender Applications - Design, Control and Evaluation
1. Aufl. 2018, 194 S.
DOI: 10.18154/RWTH-2019-00025

ABISEA Band 117
Biskoping, Matthias
Discrete Modeling and Control of a versatile Power Electronic Test Bench with Special Focus on Central Photovoltaic Inverter Testing
1. Aufl. 2018, 236 S.
DOI: 10.18154/RWTH-2019-03346

ABISEA Band 118
Schubert, Michael
High-Precision Torque Control of Inverter-Fed Induction Machines with Instantaneous Phase Voltage Sensing
1. Aufl. 2019, 221 S.
DOI: 10.18154/RWTH-2018-231364

ABISEA Band 119
Van der Broeck, Christoph
Methodology for Thermal Modeling, Monitoring and Control of Power Electronic Modules
1. Aufl. 2019, 290 S.
DOI: 10.18154/RWTH-2019-01370

ABISEA Band 120
Hust, Friedrich Emanuel
Physico-chemically motivated parameterization and modelling of real-time capable lithium-ion battery models – a case study on the Tesla Model S battery
1. Aufl. 2019, 203 S.
DOI: 10.18154/RWTH-2019-00249

ABISEA Band 121
Ralev, Iliya
Accurate Torque Control of Position Sensorless Switched Reluctance Drives
1. Aufl. 2019, 154 S.
DOI: 10.18154/RWTH-2019-03071

ABISEA Band 122
Ayeng'o, Sarah Paul
Optimization of number of PV cells connected in series for a direct-coupled PV system with lead-acid and lithium-ion batteries
1. Aufl. 2019, 114 S.
DOI: 10.18154/RWTH-2019-01843

ABISEA Band 123
Koschik, Stefan Andreas
Permanenterregte Synchronmaschinen mit verteilter Einzelzahnsteuerung - Regelkonzepte und Betriebsstrategien für hochintegrierte Antriebssysteme
1. Aufl. 2019, 158 S.
DOI: 10.18154/RWTH-2019-03446

ABISEA Band 124
Farmann, Alexander
A comparative study of reduced-order equivalent circuit models for state-of-available-power prediction of lithium-ion batteries in electric vehicles
1. Aufl. 2019, 214 S.
DOI: 10.18154/RWTH-2019-04700

ABISEA Band 125
Mareev, Ivan
Analyse und Bewertung von batteriegetriebenen, oberleitungsversorgten und brennstoffzellengetriebenen Lastkraftwagen für den Einsatz im Güterfernverkehr in Deutschland
1. Aufl. 2019, 158 S.
DOI: 10.18154/RWTH-2019-04698

ABISEA Band 126
Qi, Fang
Online Model-predictive Thermal Management of Inverter-fed Electrical Machines
1. Aufl. 2019, 154 S.
DOI: 10.18154/RWTH-2019-08304

ABISEA Band 127
Kairies, Kai-Philipp
Auswirkungen dezentraler Solarstromspeicher auf Netzbetreiber und Energieversorger
1. Aufl. 2019, 140 S.
DOI: 10.18154/RWTH-2019-06706

Aachener Beiträge des ISEA

ABISEA Band 128
Fleischer, Michael
Traction control for Railway Vehicles
1. Aufl. 2019, 162 S.
DOI: 10.18154/RWTH-2019-10570

ABISEA Band 129
Teuber, Moritz
Lifetime Assessment and Degradation Mechanisms in Electric Double-Layer Capacitors
1. Aufl. 2019, 150 S.
DOI: 10.18154/RWTH-2019-10071

ABISEA Band 130
Bußar, Christian
Investigation of Optimal Transformation Pathways towards 2050 for the Successful Implementation of a Sustainable Reduction of Carbon Emissions from Power Generation
1. Aufl. 2019, 204 S.
DOI: 10.18154/RWTH-2019-09975

ABISEA Band 131
Wienhausen, Arne Hendrik
High Integration of Power Electronic Converters enabled by 3D Printing
1. Aufl. 2019, 146 S.
DOI: 10.18154/RWTH-2019-08746

ABISEA Band 132
Kwiecien, Monika
Electrochemical Impedance Spectroscopy on Lead-Acid Cells during Aging
1. Aufl. 2019, 138 S.
DOI: 10.18154/RWTH-2019-09480

ABISEA Band 133
Titiz, Furkan Kaan
A Three-phase Low-voltage Grid-connected Current Source Inverter
1. Aufl. 2019, 128 S.
DOI: 10.18154/RWTH-2020-00458

ABISEA Band 134
Wünsch, Martin
Separation der Kathoden-alterung in Lithium-Ionen-Batteriezellen mittels elektrochemischer Impedanzspektroskopie
1. Aufl. 2019, 177 S.
DOI: 10.18154/RWTH-2019-11017

ABISEA Band 135
Badeda, Julia
Modeling and Steering of Multi-Use Operation with Uninterruptible Power Supply Systems - utilizing the example of lead-acid batteries
1. Aufl. 2020, 282 S.
DOI: 10.18154/RWTH-2020-05456

ABISEA Band 136
Kleinsteinberg, Björn
Energy Efficiency Increase of a Vanadium Redox Flow Battery with a Power-Based Model
1. Aufl. 2020, 163 S.
DOI: 10.18154/RWTH-2020-06092

ABISEA Band 137
Cai, Zhuang
Optimization of dimension and operation strategy for a wind-battery energy system in German electricity market under consideration of battery ageing process
1. Aufl. 2020, 144 S.
DOI: 10.18154/RWTH-2020-06525

ABISEA Band 138
Sabet, Pouyan Shafiei
Analysis of Predominant Processes in Electrochemical Impedance Spectra and Investigation of Aging Processes of Lithium-Ion Batteries with Layered Oxide Cathodes and Graphitic Anodes
1. Aufl. 2020, 136 S.
DOI: 10.18154/RWTH-2020-07683

ABISEA Band 139
Angenendt, Georg
Operation, Optimization and Additional Market Participation of Households with PV Battery Storage System and Power-to-Heat Application
1. Aufl. 2020, 221 S.
DOI: 10.18154/RWTH-2020-05200

ABISEA Band 140
Oberdieck, Karl Friedrich
Measurement and Mitigation of Electromagnetic Emissions of Propulsion Inverters for Electric Vehicles
1. Aufl. 2020, 181 S.
DOI: 10.18154/RWTH-2020-09215

ABISEA Band 141
Bubert, Andreas Martin
Optimierung des elektrischen Antriebsstrangs von Elektrofahrzeugen mit Betrachtung parasitärer Ströme innerhalb der elektrischen Maschine
1. Aufl. 2020, 215 S.
DOI: 10.18154/RWTH-2020-09556

ABISEA Band 142
Fleischer, Christian Georg
Model-Driven Software Development and Verification Solutions for Safety Critical Battery Management Systems
1. Aufl. 2021, 356 S.
DOI: 10.18154/RWTH-2021-00436

ABISEA Band 143
Arzberger, Arno
Thermografische Methoden zur zerstörungsfreien Messung der anisotropen Wärmeleitfähigkeit von Lithium-Ionen Zellen
1. Aufl. 2020, 131 S.
DOI: 10.18154/RWTH-2021-00479

ABISEA Band 144
Lange, Tobias
Oberwellenbasierte Modellierung, Regelung und Auslegung von Permanentmagnet- und Reluktanz-Synchronmaschinen
1. Aufl. 2020, S.
DOI: 10.18154/RWTH-2021-02537

ABISEA Band 145
Weiss, Claude
Fault Tolerant Switched Reluctance Machines with Distributed Inverters – Modeling and Control
1. Aufl. 2020, S.
DOI: 10.18154/RWTH-2021-02327

ABISEA Band 146
Huck, Moritz
Modelling the Transient Behaviour of Lead-Acid Batteries: Electrochemical Impedance of Adsorbed Species
1. Aufl. 2020, 151 S.
DOI: 10.18154/RWTH-2020-08362

ABISEA Band 147
Willenberg, Lisa
Volumenausdehnung und ihre Auswirkungen auf die Alterung einer zylindrischen Lithium-Ionen-Batterie
1. Aufl. 2020, S.
DOI: 10.18154/RWTH-2021-01906

ABISEA Band 148
Rogge, Matthias
Electrification of Public Transport Bus Fleets with Battery Electric Busses
1. Aufl. 2020, 161 S.
DOI: 10.18154/RWTH-2021-02146

ABISEA Band 149
Münderlein, Jeanette
Numerische Methodik zur Auslegung eines Hybriden Speichersystems mit Multinutzen“
1. Aufl. 2020, 221 S.
DOI: 10.18154/RWTH-2021-00867

ABISEA Band 150
Merten, Michael
Participation of Battery Storage Systems in the Secondary Control Reserve Market
1. Aufl. 2020, 187 S.
DOI: 10.18154/RWTH-2021-01029

ABISEA Band 151
Ge, Lefei
Performance Enhancement of Switched Reluctance Machines for High-speed Back-up Generators
1. Aufl. 2020, 152 S.
DOI: 10.18154/RWTH-2020-11546

ABISEA Band 152
Neubert, Markus
Modeling, Synthesis and Operation of Multiport-Active Bridge Converters
1. Aufl. 2020, 227 S.
DOI: 10.18154/RWTH-2020-10814

ABISEA Band 153
Schülting, Philipp
Optimierte Auslegung von hochintegrierten und bidirektionalen Onboard GaN-Ladegeräten
1. Aufl. 2020, 158 S.
DOI: 10.18154/RWTH-2020-09771

ABISEA Band 154
Sewergin, Alexander
Design Challenges and Solutions for the Practical Application of SiC Power Moduls – Exemplified by an Automotive DC-DC Converter. 1. Aufl. 2021, 154 S.
DOI: 10.18154/RWTH-2021-04498

ABISEA Band 155
Stippich, Alexander
Exploiting the Full Potential of Silicon Carbide Devices via Optimized Highly Integrated Power Modules
1. Aufl. 2021, 188 S.
DOI: 10.18154/RWTH-2021-08122

ABISEA Band 156
Gottschlich, Jan
Hilfsspannungsversorgungskonzepte für Mittelspannungs-DC/DC-Wandler
1. Aufl. 2021, 178 S.
DOI: 10.18154/RWTH-2021-11881

ABISEA Band 157
Hollstegge, Philipp
Injektion raumzeigerzerlegter Stromharmonischer zur Minderung tonaler Geräuschanteile in asymmetrisch sechsphasigen Permanentmagnetsynchronmaschinen
1. Aufl. 2021, 191 S.
DOI: 10.18154/RWTH-2021-11040

ABISEA Band 158
Grau, Vivien
Development of a Test Bench to Investigate the Impact of Steep Voltage Slopes on the Lifetime of Insulation Systems for Coil Windings
1. Aufl. 2021, 182 S.
DOI: 10.18154/RWTH-2021-09577

ABISEA Band 159
Ringbeck, Florian
Optimized Charging of Lithium-Ion Batteries with Physico-Chemical Models
1. Aufl. 2021, 174 S.
DOI: 10.18154/RWTH-2021-11038

ABISEA Band 160
Bank, Thomas
Performance and Aging Analysis of High-Power Lithium Titanate Oxide Cells for Low-Voltage Vehicle Applications
1. Aufl. 2021, 148 S.
DOI: 10.18154/RWTH-2021-10369

Aachener Beiträge des ISEA

ABISEA Band 161
Aupperle, Felix
Realizing High-Performance Silicon-Based Lithium-Ion Batteries
1. Aufl. 2022, 138 S.
DOI: 10.18154/RWTH-2022-05155

ABISEA Band 162
Schröer, Philipp A.
Entwicklung einer adaptiven Leistungsprognosefunktion für Starterbatterien mit Lithium-Titanat-Oxid-Anode als Grundlage zur sicheren Energieversorgung im Fahrzeug
1. Aufl. 2021, 187 S.
DOI: 10.18154/RWTH-2021-10819

ABISEA Band 163
Dechent, Philipp
Simulation and Real-Life assessment of cell-to-cell variation of ageing lithium-ion batteries
1. Aufl. 2022, 149 S.
DOI: 10.18154/RWTH-2022-09298

ABISEA Band 164
Li, Weihan
Battery Digital Twin with Physics-Based Modeling, Battery Data and Machine Learning
1. Aufl. 2022, 234 S.
DOI: 10.18154/RWTH-2022-02292

ABISEA Band 165
Thien, Tjark G. C.
Optimaler Betrieb von stationären Hybrid-Batteriespeichern am Beispiel des Projekts M5BAT
1. Aufl. 2022, 172 S.
DOI: 10.18154/RWTH-2022-00997

ABISEA Band 166
Lüdecke, Christoph
Compensating Asymmetries of Parallel-Connected SiC MOSFETs Using Intelligent Gate Drivers
1. Aufl. 2022, 166 S.
DOI: 10.18154/RWTH-2022-09587

ABISEA Band 167
Rahe, Christiane
Untersuchung von Batterieelektroden mit optischen Verfahren
1. Aufl. 2022, 214 S.
DOI: 10.18154/RWTH-2022-08794

ABISEA Band 168
Weber, Felix Martin
Stability of lithium electrolyte interphase enabling rechargeable lithium-metal batteries
1. Aufl. 2023, 168 S.
DOI: 10.18154/RWTH-2023-03565

ABISEA Band 169
Henn, Jochen
Gate Driver Integrated Closed-Loop Control for Electromagnetic Emissions and Switching Losses of Wide Bandgap Power Electronic Converters
1. Aufl. 2023, 169 S.
DOI: 10.18154/RWTH-2023-07726

ABISEA Band 170
Quabeck, Stefan
Modeling of Parasitic Currents and Fault Detection in Electrical Traction Drives
1. Aufl. 2023, 133 S.
DOI: 10.18154/RWTH-2023-10920

ABISEA Band 171
Hecht, Christopher
Usage overview, prediction, and siting optimization for electric vehicles public charging infrastructure with machine learning and big data methods
1. Aufl. 2023, 185 S.
DOI: 10.18154/RWTH-2024-01156

ABISEA Band 172
Kuipers, Matthias L. U.
Development of a Virtual Cell Design Tool for Objective Comparisons between State-of-the-Art Battery Cells and Next Generation Technologies
1. Aufl. 2023, 203 S.
DOI: 10.18154/RWTH-2023-11897

ABISEA Band 173
Brieske, Daniel Martin
Anwendungsbezogene Modellierung und Zustandsbestimmung von Lithium-Schwefel-Batterien
1. Aufl. 2023, 146 S.
DOI: 10.18154/RWTH-2023-10905

ABISEA Band 174
Teichert, Philipp
Einfluss der Degradation von nickelreichen $Li[Ni_xMn_yCo_z]O_2$ (NMC) Elektroden (mit $x \geq 0.6$) auf Vollzellalterung von Lithium-Ionen-Zellen
1. Aufl. 2023, 159 S.
DOI: 10.18154/RWTH-2024-01059

ABISEA Band 175
Kühnle, Hannes Sebastian
Optical and electrochemical investigations of fundamental lithium metal deposition processes on lithium surfaces
1. Aufl. 2023, 218S.
DOI: 10.18154/RWTH-2024-05806

ABISEA Band 176
Epp, Alexander
Multiphysical Models and Optimization for Conceptual Design of High-Voltage Battery Systems
1. Aufl. 2024, 256 S.
DOI: 10.18154/RWTH-2024-00430

ABISEA Band 177
Figgener, Jan
Data-driven battery aging analysis of home storage systems based on high-resolution field measurements
1. Aufl. 2024, 208 S.
DOI: 10.18154/RWTH-2024-10709

ABISEA Band 178
Meishner, Fabian
Untersuchung eines direktnetzgekoppelten stationären LTO-Speichersystems in einem 750 V DC Stadtbahnnetz
1. Aufl. 2024, 116 S.
DOI: 10.18154/RWTH-2024-06358

ABISEA Band 179
Frambach, Tobias
Anwendungsgerechte Dimensionierung und Betriebsstrategien von 48 V Plug-In-Hybridfahrzeugen
1. Aufl. 2024, 154 S.
DOI: 10.18154/RWTH-2024-03411

ABISEA Band 180
Goldbeck, Rafael
Model-Based Control of Three-Phase Dual-Active Bridge Converters for Dynamic Operation and Adaptive Compensation of Parameter Deviations
1. Aufl. 2024, 194 S.
DOI: 10.18154/RWTH-2025-00288

ABISEA Band 181
Götz, Georg Tobias
Bidirectional DC-to-DC Converter with Integrated Switched Reluctance Generator
1. Aufl. 2024, 192 S.
DOI: 10.18154/RWTH-2024-03854

ABISEA Band 182
Harries, Martin
Aktive Reduzierung der Vibrationen von Permanentmagnet-Synchronmaschinen durch adaptive Regler
1. Aufl. 2024, 144 S.
DOI: 10.18154/RWTH-2025-00626

ABISEA Band 183
Börner, Martin Florian
Ein prozessbasiertes Modell zur Berechnung der Kosten von Lithium-Ionen-Batteriezellen
1. Aufl. 2024, 163 S.
DOI: 10.18154/RWTH-2024-07853

ABISEA Band 184
Bihn, Stephan
Automatic Parameterisation of Electrical Equivalent Circuit Models for Virtual Battery Cell Design
1. Aufl. 2024, 226 S.
DOI: 10.18154/RWTH-2024-10636

ABISEA Band 185
Xu, Huihui
Thermal Modeling and Control of an Oil-Cooled Permanent Magnet Synchronous Machine: Initialization, Nonlinearity, and Controllability
1. Aufl. 2025, 156 S.
10.18154/RWTH-2025-01683

ABISEA Band 186
Fritz, Niklas
Generalized Control Methodology for Modular DC-DC Converters
1. Aufl. 2025, 222 S.
DOI: 10.18154/RWTH-2025-04395

ABISEA Band 187
Kalker, Sven
Toward Robust Monitoring of Power Electronic Devices: Challenges and Efficient Solutions
1. Aufl. 2025, 167 S.
DOI: 10.18154/RWTH-2025-06121

ABISEA Band 188
Wasylowski, David
Accelerating Battery Cell Design, Manufacturing, and Testing through Ultrasound Imaging
1. Aufl. 2025, 116 S.
DOI: 10.18154/RWTH-2025-00940

ABISEA Band 189
Steininger, Valentin
Aging analysis of lithium-ion batteries with field data
1. Aufl. 2025, 136 S.
DOI: 10.18154/RWTH-2025-00625

ABISEA Band 190
Jacqué, Kevin
Analyse der Belastungsprofile, der Alterung und der Wirtschaft-lichkeit eines Batteriespeichers im Primärregelleistungsmarkt aus realen Feldmessdaten
1. Aufl. 2025, 244 S.
DOI: 10.18154/RWTH-2025-04328

ABISEA Band 191
Hamzelui, Niloofar
Investigation of active materials and polymeric binders in silicon-based negative electrodes for lithium-ion batteries
1. Aufl. 2025, 148 S.
DOI: 10.18154/RWTH-2025-06437

ABISEA Band 192
Klever, Severin
High-Bandwidth Current Probing Techniques for the Dynamic Characterization of Wide-Bandgap Semiconductor Devices
1. Aufl. 2025, 158 S.
DOI: 10.18154/RWTH-2025-03518

ABISEA Band 193
von Hoegen, Anne
Precise and Instantaneous Flux-Linkage Sensing Methods in PWM Voltage-Source Inverters
1. Aufl. 2025, S.
DOI: 10.18154/RWTH-2026-

Aachener Beiträge des ISEA

ABISEA Band 194
Koltermann, Lucas
Analyse und Optimierung der Zuverlässigkeit und Effizienz von hybriden Batteriespeichern am Beispiel von M5BAT
1. Aufl. 2025, 229 S.
DOI: 10.18154/RWTH-2025-06200

ABISEA Band 195
Jöst, Dominik
Modellbasierte Bewertung von Algorithmen zur Zustandsbestimmung von Batterien: Analyse von Betriebs-, Zell- und Messtechnik-Parametern
1. Aufl. 2025, S.
DOI: 10.18154/RWTH-2026-

ABISEA Band 196
Pegel, Hendrik
Optimal Concept Design of Battery Systems with Tabless Cylindrical Lithium-Ion Cells
1. Aufl. 2025, 309 S.
DOI: 10.18154/RWTH-2025-05204

ABISEA Band 197
Ünlübayir, Cem
Intelligent operating methods and their influence on components for hybrid marine propulsion systems
1. Aufl. 2025, S.
DOI: 10.18154/RWTH-2026-

Achieving climate neutrality requires decarbonisation across all sectors, with the industry sector particularly lagging behind. Especially, energy-intensive applications requiring high-temperature process heat are challenging for decarbonisation. The primary strategy involves maximising electrification and substituting fossil energy with renewable hydrogen or its derivatives. This requires redesigning existing industrial plants, increasing variable renewable power installations, and potentially incorporating battery storage systems.
A notable challenge is decarbonising glassworks for automotive products, focusing on electrifying furnaces and replacing natural gas with hydrogen. Renewable hydrogen can be produced on-site using electrolysis powered by green electricity from power purchase agreements. To identify cost-efficient solutions, a sophisticated energy system modelling framework is developed and applied to a local German glassworks site. This includes a value stacking approach for battery storage to demonstrate the cost-reduction potential enabled by enhanced flexibility.
The results indicate that decarbonisation choices for the local glassworks site incur higher annual costs than rebuilding a natural gas furnace by at least 18.3%. However, high electrification reduces hydrogen demand and utilising low-cost renewable generation can make on-site electrolysis competitive compared to a future pipeline connection. In addition, substantial cost reductions of up to 30.1% are achieved by leveraging electrolyser flexibility and multi-use battery storage operation. These findings serve as a blueprint for decarbonisation strategies across other industrial sites.

ISSN 1437-675X